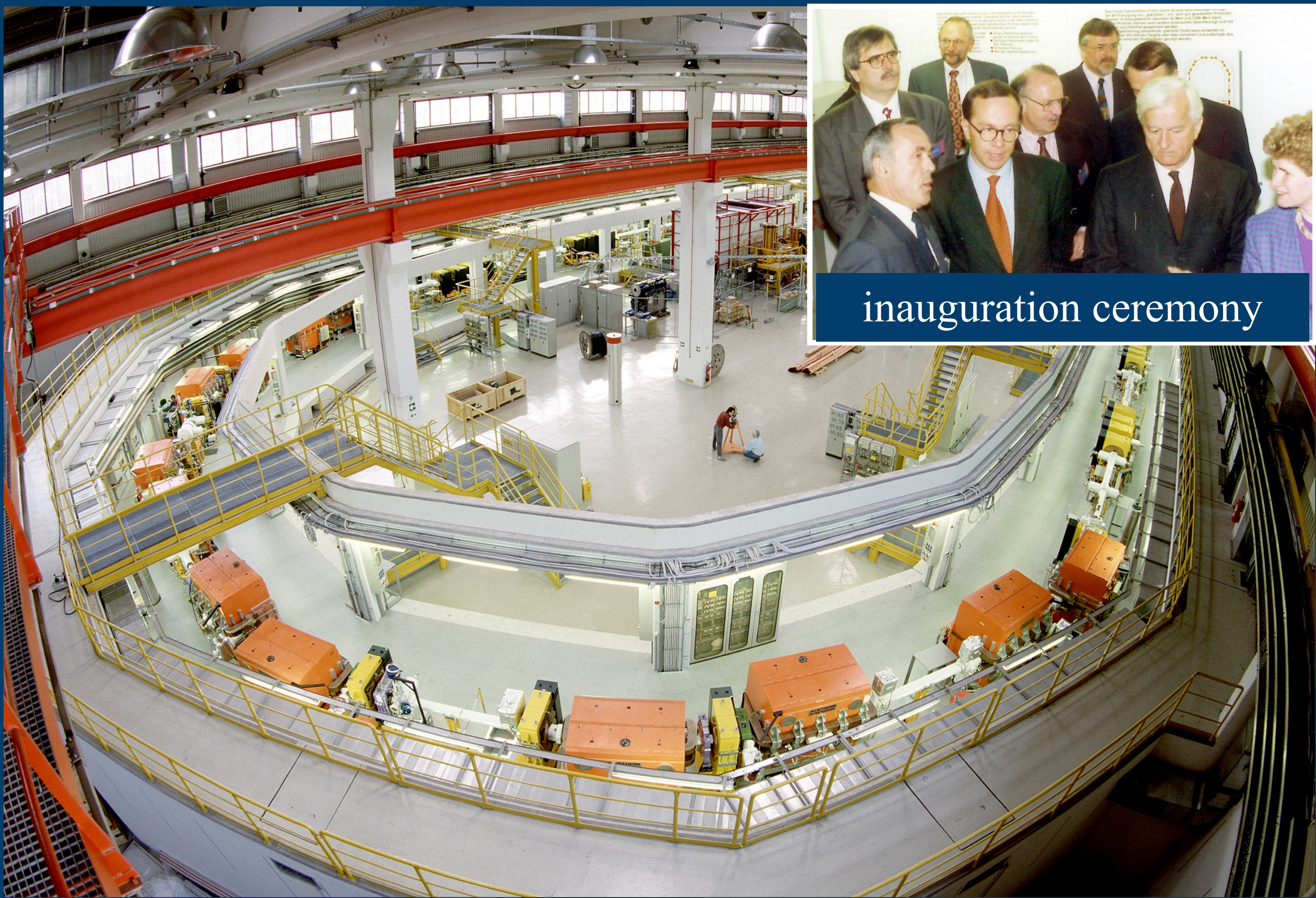

inauguration ceremony

1993 COSY 2023

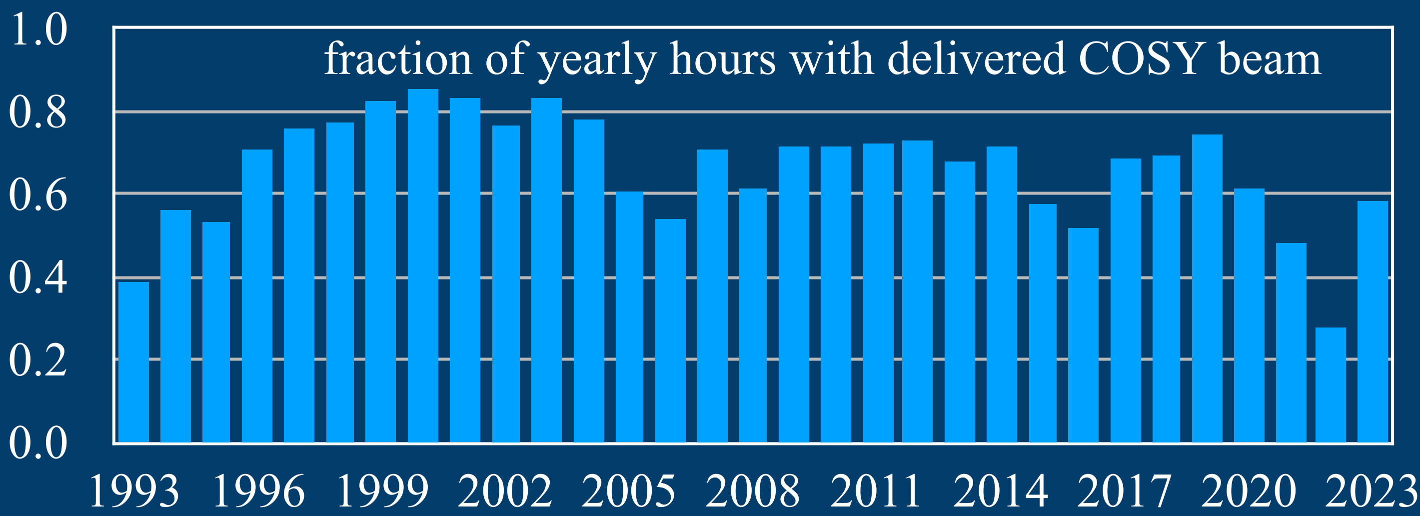

Annual Report 2023

Institut für Kernphysik · COSY

Jül-4442

Annual Report 2023

Institut für Kernphysik / COSY

Cover picture: The cover picture shows the cooler synchrotron COSY which was in operation for 30 years from 1993 until 2023 with a reliability of more than 90% taking into account the scheduled shutdown periods. The bar chart gives the yearly uptime of COSY which delivered beam for up to about 7500 hours/year. In the upper right corner a photo from the inauguration ceremony is shown, which took place on April 1st 1993 in the presence of the German President Richard v. Weizsäcker.
During the COSY operation time many different experiments were served with about 500 visiting users from more than 50 institutions from about 25 different countries resulting in a large number of scientific publications and more than 200 PhD theses based on the data achieved in COSY experiments. Until 2015 the scientific focus was on hadron physics experiments which changed then to precision experiments and preparatory measurement for FAIR until it was decided to stop the COSY operation end of 2023.

Contents

Preface

We are pleased to present the Annual Report of the Institute for Nuclear Physics for the past year. This report provides an overview of our activities, achievements, and challenges as we reflect on the recent developments within our institute.

As we review the past year, we acknowledge the significant milestone of the conclusion of the accelerator operation, which has been integral to our institute's identity for over three decades. This transition prompts us to consider the future directions and opportunities.

We extend our heartfelt gratitude to our dedicated team of researchers, technicians, administrators, and support staff whose unwavering commitment and hard work have contributed to the success of our institute. Their passion for science and dedication to excellence have driven our research endeavors forward.

We also express our appreciation to our esteemed partners and collaborators, both local and international, whose valuable contributions and collaborative efforts have enriched our scientific endeavors and fostered meaningful discoveries.

To our supporters, we extend our sincere thanks for your continued investment in our mission. Your contributions have enabled us to pursue innovative research, foster academic growth, and maintain our commitment to excellence.

This report invites you to explore our institute's key highlights and initiatives. Your ongoing engagement and partnership remain essential as we navigate the evolving landscape of nuclear and accelerator physics.

Thank you for your dedication and support.

Jülich, March 2024

Ralf Gebel, Ulf-G. Meißner, Jim Ritman

1 Experimental Activities for FAIR

1.1 The PANDA Experiment

1.1.1 Software

One of the most challenging aspects in the reconstruction of the data of the future PANDA detector is the finding and fitting of tracks of charged particles in the solenoidal magnetic field of the barrel spectrometer. This task can be simplified by assuming that a track is coming from the known primary interaction point and many tracking algorithms have been developed for this purpose in PANDA. This works well for most physics cases but breaks down if one is studying hyperons, baryons with at least on open strange quark. The ground state of these particles can only decay via the week force which makes these particles quite long living and their decay products are displaced by several centimeters from the primary interaction point and the existing tracking algorithms can only poorly reconstruct these tracks. Therefore, a new algorithm called the Apollonius-Triplet-Track Finder was developed focusing especially on tracks originating several centimeters away from the origin. The algorithm makes use of the special geometry of the Straw Tube Tracker (STT) with its densely packed drift tubes and the measurement of the drift times in each tube. To evaluate the performance of the new track finder in comparison with the existing ones the benchmark channel $\overline{p}p \to \Xi(1820)\Xi$ was selected which decays into one prompt kaon and 5 delayed protons and pions which makes it an ideal test case for secondary track finders. Fig.1 shows the change in the reconstructed $\Xi(1820)$ with the two primary track finders of PANDA and the improvement by combining them with the Apollonius Triplet Track Finder. One can clearly see the improvement of the reconstruction efficiency by using the secondary track finder. The best performance is achieved by using the Standard Track finder with the Apollonius Track finder. The full reconstruction efficiency could be improved by more than a factor 4, from 2.4% to 9.9%. This work was awarded the 2023 PANDA outstanding achievement award.

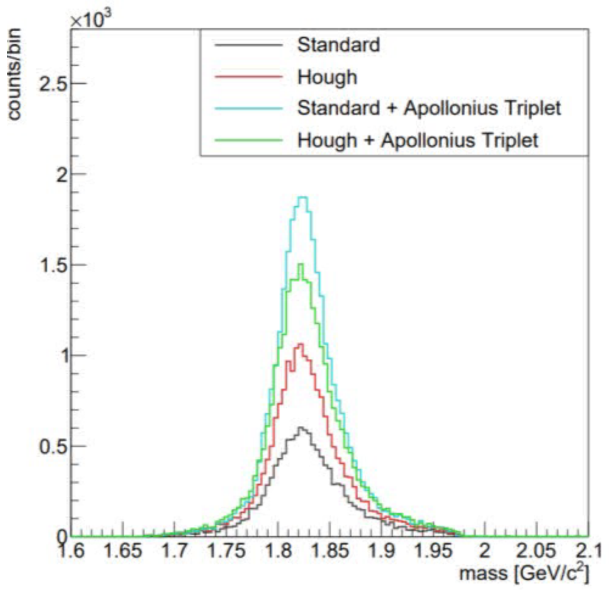

Figure 1: Reconstructed $\Xi(1820)$ with two primary track finders (Standard and Hough) and in combination with the newly developed secondary track finder (Apollonius Triplet).

1.1.2 STT

The next step for the STT system will be to set up one complete STT hexagon sector with connected electronic readout system, gas and high voltage supply system. The system performance of spatial track resolution in 3D-space and particle identification (PID) by the particle specific energy-loss via a measurement of the straw analogue signal time-over-threshold will be determined and optimized. All single straws for the STT have been assembled and are available to be arranged and glued together into multi-layer sector modules. All components of the final electronic readout system, consisting of PASTTREC-ASIC front-end boards and TRB5sc time readout boards, will be soon available. This joint project will be done together with partner groups at the Jagiellonian University and AGH in Krakow and the IFIN-HH institute in Bucharest.

1.1.3 KOALA

One goal of KOALA is to measure the differential cross section of the antiproton-proton elastic scattering down to the Coulomb region, in which the Coulomb scattering can be fixed to normalize the absolute luminosity. KOALA is a fixed target experiment and consists of a hydrogen cluster jet target, a semiconductor recoil detector as well as a forward scintillator detector. The energy and angle of the recoil protons can be measured by single sided silicon or germanium strip detectors located at 90°. The forward detector is placed into the beam pipe close to the beam axis in order to measure the scattered beam particles with small scattering angles. The commissioning of the KOALA experiment has been performed at COSY by measuring proton-proton elastic scattering. The tests clearly verified the experiment concept as well as the detector performance. It is also noted that the finite size of the target thickness and the beam imperfection limit to achieve the desired precision for KOALA and PANDA.
To pursue the best precision some efforts have been paid to solve those constraints. On the one hand, it is needed to understand the evaporation of the hydrogen cluster jet beam, which causes a low vacuum performance as well as high residual gas in the scattering chamber. On the other hand, the investigation on the target thickness, residual gas and the beam misalignment should also be carried out in order to learn how those aspects will impact the measurement precision. As shown in the Fig. 2, with an ideal

Figure 2: Hit rate distribution on forward detector at a beam momentum of 3.0 GeV/c.

beam, the four scintillator detectors, which are symmetrically located to the beam axis, indicate almost the same hits rate on each of them as foreseen, since the elastic scattering is isotropically uniform around the beam axis. However this was not always the case as observed during the commissioning. The beam condition could significantly change. As a consequence, it requires that the forward detector must have a larger acceptance than the ideal case, in order not to lose acceptance.
Recently, a working group has been built to investigate those challenges. The simulation study on the target evaporation is being carried out. After that a proper solution should be taken in order to improve the vacuum performance and reduce the residual gas in the scattering chamber. The concept of a new cluster jet target for KOALA measurement is under discussion. Meanwhile, it is proposed to increase the dimension of the forward detector in order to tolerate relatively big beam profile and beam misalignment. The simulation study on the target and the beam with the KoalaSoft is ongoing to learn the achievable precision of the experiment.

1.2 The CBM Experiment

1.2.1 Proposed Proton-Proton Program at CBM

Proton beams from SIS100 enables a hadron physics program complementary to the foreseen heavy-ion program with CBM. These beams impinging on a liquid hydrogen target enable systems with center-of-mass energies up to $\sqrt{s} = 7.5$ GeV to be produced. The CBM detector acts as a suitable instrument to reconstruct (exclusively) the final state products from these reactions. In this context, the proton-proton studies with CBM at SIS100 will be a natural extension of the ongoing physics studies using proton and secondary pion beams with HADES at SIS18.
In order to develop an inspiring physics program with SIS100 protons, a one-day satellite event connected to the MESON2022 conference was organized in June 2023.

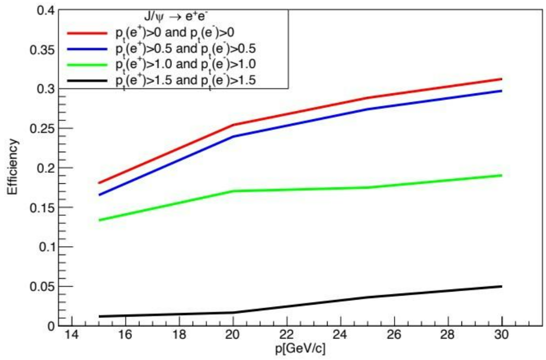

Figure 3: Signal reconstruction efficiency for the channel $pp \to ppJ/\psi$ for $J/\psi \to ee$ decays as a function of the lab momentum for the CBM detector using fast simulations (HepFastSim package). The different colors represent different p_t cuts i.e. cuts on the transverse momentum applied separately on the electrons and positrons.

This event will be followed-up by a dedicated workshop that will be held in Wuppertal in February 2024. Moreover, various Monte Carlo studies based on fast-simulation tools were performed to review the feasibility of some of the key reaction channels of interest. So far, we identified promising opportunities in the field of spectroscopy and structure with hyperons with strangeness |S|=2,3 and in the domain of near-threshold hidden- and open-charm production. The production rates of double and triple hyperons are expected to be very competitive with respect to other facilities. Together with a high-resolution charged-particle detector, such as provided by CBM, it would allow precision line-shape measurements of excited hyperons and it gives access to electromagnetic transition form factors of excited hyperons that have not been studied so far. Such measurements maybe a smoking gun revealing their exotic nature.

The near-threshold charm production can be exploited to study the charm-nucleon interaction which in turn gives access to the intrinsic charm contribution of the proton and to the emergent hadron mass contribution. The near-threshold production of hidden-charm vector mesons in proton-proton collisions, *e.g.,* via reactions like pp $\to$ ppJ/ψ with dileptonic decays of the J/ψ, are of particular interest. Since the proton and the J/ψ do not share valence quarks, a pure gluonic exchange is expected to dominate and it is, albeit speculatively, possible to access gluonic gravitational form factors based on a hadroproduction scenario.

Assuming a cross section of ~ 1 nb for J/ψ production, a 6% branching fraction of J/ψ dileptonic decays, and 10^{10} to 10^{11} protons on target per 10 seconds (spill) one can expect about $1,100$ to $11,000$ reconstructed events with CBM per day, respectively. Figure 3 shows the reconstruction efficiency versus the proton beam momentum.

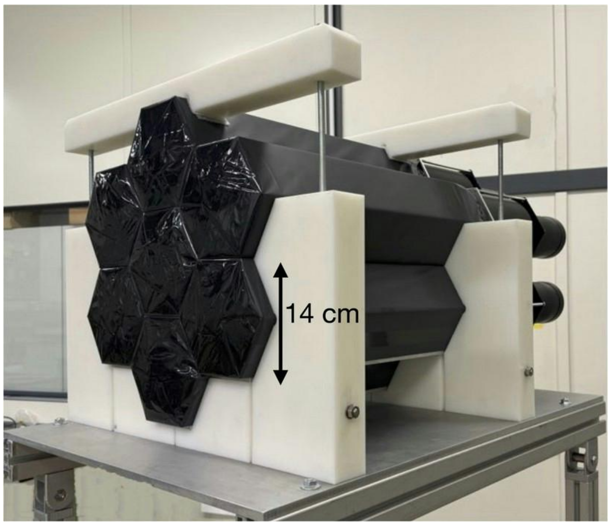

Figure 4: Detector element with 7 hexagonal shaped scintillator modules.

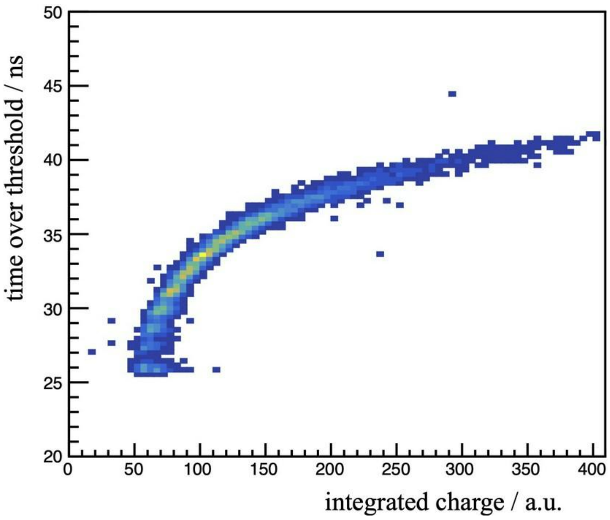

Figure 5: Correlation between integrated signal charge and ToT-value achieved in first tests.

The p_t cuts in Fig. 3 are used in heavy ion collisions and automatically imply a smaller reconstruction efficiency the higher the cut value is. A proton-proton collision program significantly improves the efficiency *e.g.*, by up to a factor of ~ 6 for a lab momentum of 30 GeV/c compared to a CBM heavy ion program which has a 5% efficiency (Fig. 3, black line, 30 GeV/c). Provided that the treatment of background is under control, it is possible to access the interactions of protons and J/ψ mesons by studying the differential cross section as a function of momentum transfer.

1.2.2 Development for the FSD

An extension of the Forward Spectator Detector (FSD), which will consist of a segmented plastic scintillator wall, by an additional neutron detector is considered. Neutron detection will improve the determination of collision centrality and reaction plane in heavy ion reactions and will be important for the analysis of various proton induced reaction channels. Directly downstream of the FSD it is planned to install an array of long plastic scintillator modules coupled to photomultipliers, thus providing a neutron detection efficiency of about 30%. In order to investigate the performance of such a detector component, two detector elements consisting of 7 scintillator modules each, have been prepared to be installed at mCBM for the test measurements in 2024, see Fig. 4. The scintillator modules have a hexagonal shape with a side length of about 14 cm and a length of 45 cm resulting in an area of about 1200 cm^2 for each detector element. One detector element will be positioned behind the TOF-detector of mCBM to correlate the particle tracks with the scintillator signals and the other element will be combined with FSD scintillator modules and placed close to the beam line.

Presently the read-out of the scintillator signals is being integrated into the CBM data acquisition system. The signal amplitude is determined by a time over threshold (ToT) method and first tests give a reasonable correlation between signal charge and ToT value as shown in Fig. 5.

1.2.3 Gas system for the TRD

The CBM Transition Radiation Detector (TRD) is essential to achieve strong background suppression for the identification of electrons/positrons at and above the GeV scale. The produced x-ray radiation is converted in a Xenon based gas detector. Our group has started to take over the task to build this gas system. A main design criterion is the very high level of pressure stability/regulation relative to the ambient atmospheric pressure over the large detector volume.

1.2.4 Outlook for 2024

The physics perspective with proton beams from SIS100 at CBM will be further developed in 2024. For instance, in February we are hosting a 1-week workshop on this topic at the University of Wuppertal. Data will be taken with the FSD modules during the mCBM test measurements and will be used to determine the performance of the detector elements for neutron and charged particle detection. Those data will be compared to simulation studies. Based on the results a neutron detector will be designed for the full CBM detector as an extension of the FSD detector component.

1.3 The HADES Experiment

1.3.1 Evaluation of proton-proton reactions to investigate hyperon production

We are exploring the production mechanisms and spectroscopy of baryons with strangeness contents, *i.e.,* hyperons, using the SIS18 beam at HADES, which is an excellent facility to study hyperons in proton-proton and pion-proton scattering. In the past years, HADES has been upgraded with a forward detector composed of straw-tube trackers (STS1/STS2) and a forward RPC (fRPC), which significantly improve the acceptance for hyperons. Furthermore, a trigger scintillator (iTOF) consisting of 6 plastic scintillating modules with SiPM read-out, covering the first MDC plane was added.

Most of the activities in 2023 were dedicated to the analysis of proton-proton scattering data taken in 2022 with a proton beam of T=4.5 GeV kinetic energy impinging on a 5 cm thick liquid hydrogen target (Feb22 run). This includes the alignment, particle identification, and track reconstruction of the detector (particularly related to the Forward Detector (FD)), luminosity determination, the (exclusive) event selection of channels of interest, the development and usage of high-level analysis tools, and the first preliminary physics analysis of various channels of interest.

To support the analysis of exclusive channels, a kinematic fitting library based on Lagrange multipliers and utilizing different constraints, *e.g.*, geometrical vertex or momentum conservation at a decay vertex has been successfully implemented and rigorously tested as an external library for HYDRA, the HADES software package. Meanwhile this library is used extensively within the HADES collaboration.

Another important technological development supporting the reconstruction analysis of HADES involves novel machine-learning algorithms for particle identification. The conventional approach used in HADES is to apply so-called "graphical cuts" around the theoretical Bethe-Bloch curves. A promising and more powerful alternative approach is to utilize deep learning algorithms. For this, we developed a neural network algorithm that has been trained in a semi-supervised way simultaneously on simulated and real data to accommodate for the discrepancies between the two data domains (simulated data and unlabeled experimental data). With Domain Adversarial Neural Networks (DANN) we have significantly improved the classification of particle species in the experimental data.

Various physics channels are presently being studied using the proton data collected by HADES. Some of these studies make use of the developed kinematic fitter and PID methods described above and were, thereby, used to demonstrate the excellent potential of these methods allowing high purity event selection. More specifically, the following reactions are presently being studied by the HADES-FFN group:

- $p+p \to \Lambda + K_S + p + \pi^+$. This channel allows for a study of, and search for, new baryon resonance coupling to hyperon final states complementary to earlier partial-wave analysis studies of the $p+p \to \Sigma^0/\Lambda + K^+ + p$ reaction. The preliminary analysis revealed a clean signature of the final state of interest with various intermediate baryon and meson resonances playing a role.

- $p+p \to \Xi^- + K^+ + K^+ + p$. The objective is a first cross section measurement or upper limit determination for the elementary production of cascade hyperons. The aim is to use such measurement to shed light on the striking enhancement of the near-threshold cascade production observed in heavy-ion reactions. Next to the cascade channel, the control channel $p+p \to \Sigma^-(1385) + K^+ + \pi^- + p$ is being analyzed whereby the $\Xi^-$and $\Sigma^-(1385)$ share the same final state, namely $\pi^-\Lambda$. A clear signature of the $\Sigma^-(1385)$ has been identified in the analysis and cut-sensitivity studies for the Ξ^- decay identification have been carried out with the aim to optimize the statistical significance.

- $p+p \to p+p+K^+ + K^-(+\pi^0)$. This channel is exploited to study the hidden-strangeness production (*i.e.*, $\phi \to K^+K^-$) and to search for intermediate resonances that couple to Kπ and pK. A clear signature of the $p+p \to \phi + p + p$ reaction has been observed with the help of the kinematic fitter and the PID method based on machine learning outlined above.

- $p+p \to p+p+e^+ + e^- + \pi^0$. The ultimate goal is to probe the electromagnetic properties of the Δ^+ via form factor studies of radiative transitions, *e.g.*, $\Delta \to \gamma^*\Delta$. The objective of this work is a feasibility study demonstrating the capabilities of low-mass virtual photon detection in elementary reactions. A dedicated event generator that incorporates the radiative transition process has been developed in 2023 by extending the PLUTO library.

- $p+p \to p+p$. This channel is used to determine the time-integrated luminosity of the Feb22 run. Moreover, it provides information on the underlying dynamics that take place in this elementary process as a reference to heavy-ion reactions. Differential cross sections have been extracted from the data and are close to being published. The figure below shows some of the preliminary results of this measurement in comparison with data obtained at Argonne at similar energies.

Besides the HADES-data analysis activities, the group has been involved in future developments that potentially connect to the challenges of the next generation experiments such as CBM and PANDA. Particularly, the development of artificial intelligence (AI) techniques for experiment control started in the framework of the NRW-FAIR network with HADES data as a proof-of-principle. As the first step, calibration constants (gains) of HADES' drift chambers were predicted for Feb22 experiment. Predictions are based on a neural-network with Long-Short-Term-Memory cells (LSTM) and graph structure to enhance regularization and to account for correlations between multiple channels. The developed method demonstrated the ability to provide fast and stable calibration predictions with a precision comparable

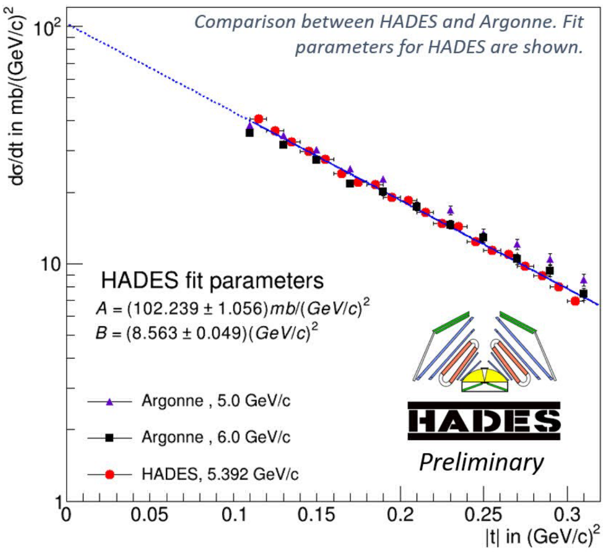

Figure 6: Differential cross-section of p-p elastic scattering from HADES at p_{beam} = 5.392 GeV/c as a function of the 4-momentum transfer |t| and compared with data from Argonne. The measured cross-section is well described by a function of the form $\frac{d\sigma}{dt} = A\exp[-B|t|]$, from which the optical point parameter A and the nuclear slope parameter B are obtained.

to that obtained using traditional offline, time-consuming approaches. With slight changes in the network, predictions can be used to dynamically tune high voltages on the wires of the drift chambers to achieve stable gain during experiments.

1.3.2 Partial Wave Analysis tools and application to pion induced reactions

Preparation studies are ongoing for the upcoming pion-beam at HADES. The pion beam offers a unique opportunity to study baryonic resonances generated at a fixed center of mass energy ($\sqrt{s}$). Moreover, they are complementary to photo-induced studies and possess a significant advantage over proton-induced reactions. We employ a Partial Wave Analysis (PWA) to investigate how these resonances couple to various final states, with a keen interest in the role of the in-medium effects of vector mesons in baryon-rich heavy-ion collisions. In-depth elementary pion-induced studies on protons, coupled with a PWA, are expected to shed light on the intricate couplings of baryonic resonances to ρN and ωN final states. These studies are particularly crucial for understanding the ρ meson's behavior in heavy ion collisions and the role of intermediate vector mesons in dilepton production. With a view towards a more exhaustive exploration in pion-proton collisions, the team is developing a K-Matrix & N/D frameworks implementation in a modular software package. This advancement aims to precisely map the resonance regions, facilitating the extraction of resonance parameters such as mass, width, and contributions to various channels. We have conducted a sensitivity case study of the double resonance behavior of the N(1720) hinted by the CLAS collaboration using Monte Carlo simulated events. This study demonstrated the feasibility of the upcoming pion-beam experiment with HADES to confirm and disentangle the double resonance behavior.

1.3.3 HADES STS as input to DRD1

The DRD1 Collaboration at CERN has been formed in 2023. According to the 2021 ECFA detector research and development roadmap, the DRD1 collaboration will be devoted to detector research and developments in the broad range of gaseous detector technologies, such as Micro-Pattern Gas Detectors (MPGD), Resistive Plate Chambers (RPC), Time Projection Chambers (TPC), large drift chambers, straw tube chambers, and other wire-based detectors like Thin-Gap Chambers and Cathode Strip Chambers. The addressed field of applications ranges from future accelerator and non-accelerator-based particle physics experiments, nuclear and neutrino physics, Dark matter, and rare decays to medical, industrial, and civil security applications.

A comprehensive collaboration proposal document was worked out in a series of symposium and workshop meetings and submitted to CERN by the end of 2023. The document gives a detailed overview of the current state-of-the-art, the challenges, and future perspectives related to the various gaseous detector concepts and technologies. It also describes the proposed scientific organisation with, at current, nine explicit R&D work packages for different gaseous detector technologies and common R&D topics which are addressed by various work groups. After a review process in late 2023 by the CERN DRDC committee the DRD1 collaboration proposal has been fully approved by CERN in December 2023. To date, the collaboration consists of about 700 members from 157 institutes and 33 countries.

Within the new DRD1 collaboration, the FFN group (IKP in FZ Jülich, RU Bochum, and GSI) together with partners in the Jagiellonian University Krakow and IFIN-HH Bucharest, will carry out a research and development project for Straw chamber technologies in hadron physics applications. One focus of this work package project is the development and optimization of a 4D+PID central tracker with track reconstruction in 3D-space, t0 track time extraction and dE/dx measurement for particle identification, combined with a very low material budget. The latter is essential for clean and background-suppressed particle tracking in hadron physics experiments in the GeV/c momentum region. Another topic is the development of small diameter straws for higher particle rate applications in hadron physics.

1.3.4 Outlook for 2024

We plan to test our online calibration prediction methodology in a real-time experimental setting during the next

HADES beam time scheduled for Feb-Mar 2024. Afterwards, the study will be broadened for other detectors and generalized. Additionally, development of an AI-based tool for quick detection and classification of malfunctions in the detector's systems during the beam times is planned for 2024-2025 years. Furthermore, we will extend the PWA framework to proton-proton reaction channels, which are pertinent to the research areas highlighted in this report.

2 Storage Ring Based EDM Search

Electric Dipole Moments (EDMs) of elementary particles are one of the most sensitive tools for studying physics beyond the Standard Model (BSM), since they violate both parity (P) and time-reversal invariance (T) — and, assuming the CPT theorem holds, charge parity (CP) as well. The latter is one of the key requirements for understanding the apparent asymmetry between matter and antimatter in the universe. Non-zero EDMs exist within the Standard Model, but they are too small to explain the observed dominance. Therefore, a measurement of EDMs larger than predicted by the Standard Model would provide a clue to the physics behind the SM and contribute to our understanding of our universe.
The JEDI and CPEDM collaborations continued their investigations and measurements with the goal of providing a scientific infrastructure to search for the electric dipole moments of charged particles with unprecedented sensitivity. The results of the Axion search using this technique for the detection of oscillating EDMs were published in 2023, and the analysis of the precursor runs for the first electric dipole measurement of the deuteron with the waveguide RF Wien filter continued. A final beam time in June 2023 was dedicated to the identification of possible sources of systematic errors.

2.1 Axion Searches (update)

In 2019 the JEDI Collaboration performed a first measurement at COSY exploring a new method to search for axions or axion-like particles (ALPs) in storage rings by using an in-plane polarized deuteron beam. The experiment scanned momenta near 970 MeV/c and entailed a scan of the spin precession frequency. At resonance between the spin precession frequency of deuterons and the ALP-induced EDM oscillation frequency, there should be an accumulation of the polarization component out of the ring plane. The beam momentum and, consequently, the spin precession frequency were ramped to search for a vertical polarization change. During 2022 the data analysis has been finalised, and a corresponding paper was published in Physical Review X[1]. No ALP resonance was observed and upper limits of the oscillating EDM component of the deuteron and the corresponding axion coupling constants are provided.

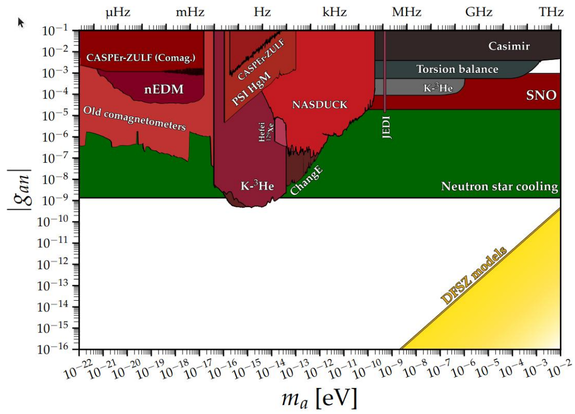

Figure 7: Limits on axion/ALP neutron coupling from the particle data group including the recent result from the JEDI collaboration obtained at COSY.

The JEDI collaboration for the first time have established a new complementary method to search for axion/ALPS. This method could be employed at other storage rings like the ESR or CRYRING at GSI. The JEDI result shown in Fig. 7, already appeared in the latest Review of particle physics (PDG 2023, Fig. 90.3)[2].

2.2 Electric Dipole Moment (EDM) Searches (progress report)

During the previous years the JEDI collaboration aimed to conduct a direct measurement of the deuteron electric dipole moment (EDM) as part of a staged approach towards developing a high-precision, all-electric storage ring for protons. In a magnetic ring like COSY, the spin motion is characterized by the invariant spin axis and the spin tune. In the absence of an EDM, the invariant spin axis is vertical, causing the spin to precess within the ring plane. A non-zero EDM results in a tilt of the invariant spin axis, causing a small oscillation of the vertical spin component. The experimental approach involves using an RF Wien filter to accumulate EDM-induced spin rotations. This concept has been implemented in experimental runs (precursor runs) at COSY in 2018 and 2021, involving a phase-lock feedback, intentional variations of the spin axis, and measurements of polarization build-up using different methods. The obtained data are going to be used to determine a first upper limit of the deuteron EDM by comparing with simulations assuming no EDM. Analysis of the data showed that the tilt of the invariant spin axis is much larger than predicted by the simulation, including all known misalignments and machine imperfections. Therefore, during a dedicated beam time in June 2023, several sources of additional systematic errors

[1] First Search for Axionlike Particles in a Storage Ring Using a Polarized Deuteron Beam, https://doi.org/10.1103/PhysRevX.13.031004 Physical Review X 13, 031004 (2023).

[2] Axions and Other Similar Particles, https://pdg.lbl.gov/2023/reviews/rpp2022-rev-axions.pdf PDG, 2023.

were investigated, including the orbit response to various steerer, field and frequency variations, as well as the alignment of the Wien filter field oscillation plane with the betatron oscillation planes. The data are currently being analyzed. The goal is to complete data analysis of the precursor runs and publish the results in 2024. (see contribution A. Andres, page 65).

2.3 Pilot bunch and co-magnetometry of polarized particles stored in a ring

In polarization experiments at storage rings, one of the challenges is to maintain the spin-resonance condition of a radio-frequency spin rotator with the spin-precessions of the orbiting particles. Time- dependent variations of the magnetic fields of ring elements lead to unwanted variations of the spin precession frequency. We report in the corresponding publication[3] on a solution to this problem by shielding (or masking) one of the bunches stored in the ring from the high-frequency fields of the spin rotator, so that the masked pilot bunch acts as a co-magnetometer for the other signal bunch, tracking fluctuations in the ring on a time scale of about one second. While the new method was developed primarily for searches of electric dipole moments of charged particles, it may have far-reaching implications for future spin physics facilities, such as the EIC and NICA.

The basic demonstration of the pilot-bunch approach was carried out with deuterons at a flattop momentum of 970 MeV/c. In each cycle (fill) the vector polarized deuterons were injected, bunched in two packages, each containing about 10^9 particles, electron-cooled for about a minute at 76 MeV down to a momentum spread of $\Delta p/p \approx 10^{-4}$, and then accelerated to flattop. The beam is stochastically extracted on flattop onto a carbon block target at the JEPO polarimeter, which is used to monitor the horizontal, p_x, and vertical, p_y, polarization components of the beam.

Prior to the experiments, the initially vertical spins of the stored deuterons were rotated once into the horizontal plane by an LC-resonant RF solenoid, operated at a fixed frequency. The frequency needed to accomplish that is determined by observing the vanishing of p_y in the polarimeter. In the further course of the experiment, the spin-precession frequency f_s of the in-plane polarization, determined only rather roughly in this way, was used as the starting frequency for the operation of the RF Wien filter to ensure the resonance condition $f_{WF} = f_s + K f_{rev}$, where $K \in \mathbb{Z}$ is the sideband and f_{rev} the beam revolution frequency. In the present experiment, the Wien filter was run at $K = -1$. In an ideal storage ring, free of magnetic imperfections, the spin-precession frequency $f_s = G\gamma f_{rev}$, G the magnetic anomaly and γ the relativistic factor of the particle, but in practice the magnetic ring imperfection effects might be substantial. The experiment starts with two back-to-back bunches orbiting in the machine with their spins aligned along the vertical axis, perpendicular to the ring plane. After electron cooling is switched off at $t_{cyc} = 77$ s, the periphery of the beam is brought into interaction with the carbon polarimeter target by stochastic heating using a stripline. The time distribution of the events recorded in the polarimeter is mapped into the revolution phase ϕ, given by

$$\phi = 2\pi \left[f_{rev} t_{cyc} - \text{int}(f_{rev} t_{cyc}) \right] \in [0, 2\pi], \tag{1}$$

where 2π corresponds to the ring circumference. The time evolution of the two bunches, pilot (p) and signal (s), is plotted as a function of cycle time t_{cyc} in Fig. 8. The observed longitudinal beam profiles of pilot (p) and signal (s) bunches are shown in Fig. 9. The bunch length is increasing due to emittance growth. An example of the longitudinal beam profile of both bunches near the mid point of the cycle at $t_{cyc} = 122$ s is depicted in Fig. 9 as a function of the revolution phase ϕ. The gate width is well sufficient to fully shield the pilot bunch from the RF field of the Wien filter.

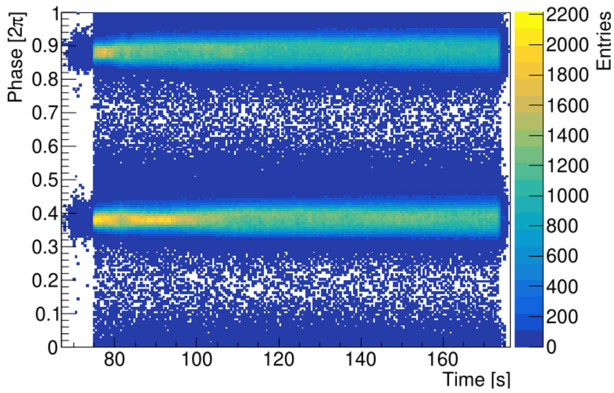

Figure 8: Panel shows a 2D plot of the evolution of two bunches stored in the ring as function of time. The pilot bunch is located near a phase of $\phi_p \simeq 2.4$ rad and the signal bunch near $\phi_p \simeq 5.6$ rad (2π denotes the ring circumference).

The pilot bunch is gated out by fast RF switches in the input and output lines of the Wien filter. The function of these switches is to render the RF of the WF invisible to one of the bunches orbiting in the ring, while the signal bunches are subjected to RF-driven multiple spin flips. The function of the pilot bunch as a co-magnetometer derives from its insensitivity to the operation of the Wien filter, so that its polarization continues to idly precess in the ring plane, thus *continuously* collecting information about the spin precession. This information is used to correct the frequency of the Wien filter in a feedback system to maintain the resonance condition.

The experimental result of the test of the pilot bunch principle is illustrated in Fig. 10. Recording the time stamp of the interactions in the detectors of the polarimeter allows for a concurrent measurement of the left-right asymmetries caused by the pilot and signal bunches. It should be

[3]Pilot bunch and co-magnetometry of polarized particles stored in a ring, arXiv:2309.06561 (2023), submitted to PRL.

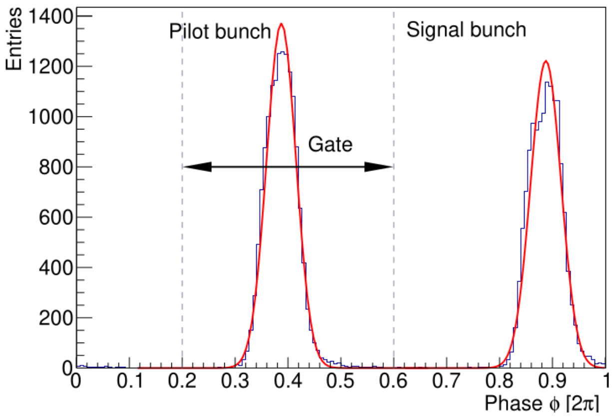

Figure 9: Entries (counts) recorded in the detector system during a time interval of 1 s, plotted as a function of revolution phase, reflect the longitudinal beam profiles of the two back-to-back deuteron bunches in the ring at a cycle time of $t_{\mathrm{cyc}} = 122\,\mathrm{s}$. The total number of entries in the spectrum corresponds to about 38 000 events. The vertical lines indicate the width of the gate that is used to mask the pilot bunch from the RF of the Wien filter.

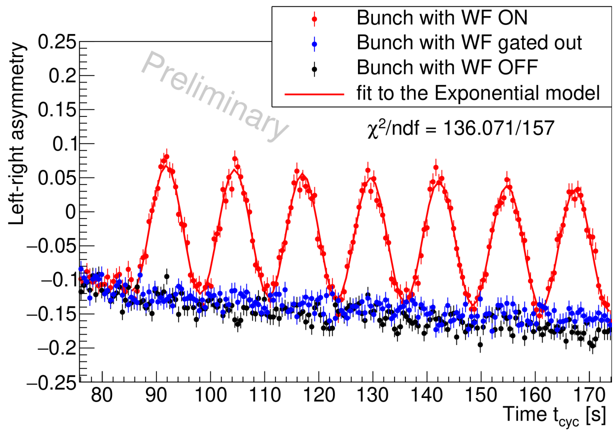

Figure 10: The measured left-right asymmetry induced by RF Wien filter in the polarimeter is presented as a vertical oscillation of the beam polarization for a cycle with two bunches stored in the machine, as depicted in Fig. 9. (The dC analyzing power is not yet applied.) The red points indicate the vertical polarization when at $t_0 = 85.55\,\mathrm{s}$ the RF Wien filter is switched ON (signal bunch) with an additional $\pm 2\sigma$ cut on the signal bunch distribution. The blue points reflect the case for the pilot bunch, *i.e.*, when the RF of the Wien filter is gated out, as indicated in Fig. 9. The black points indicate the situation when, during a different cycle, the Wien filter is completely switched OFF. The red line indicates a fit with Eq. (2), using events from within the $\pm 2\sigma_s$ boundary of the signal bunch distribution.

noted that for the experimental proof of the pilot-bunch technique aimed at here, only asymmetries need to be taken into account; calibrated polarizations are not required. As the target intercepts the periphery of the beam, the off-centered interactions may induce a finite offset of the measured asymmetries and also exhibit a slow time-dependence caused by the enhanced beam heating to maintain a constant count rate, but these are arguably independent of the beam polarization and would not affect the principal distinction between the pilot and signal bunches.

The signal bunch (red symbols) exhibits the expected multiple continuous spin flips (SF). In striking contrast, the asymmetry measured for the pilot bunch (blue symbols) shows no oscillation signal at the spin-flip frequency f_{SF} and perfectly matches that measured in a cycle where the Wien filter was off (black symbols), with the caveat that here we are forced to compare data recorded in different fills.

In the phenomenological analysis, the observed asymmetries shall be described by function

$$A(t) = a(t-t_0) + b + c\exp\left(-\Gamma(t-t_0)\right)\cos\left[2\pi f_{\mathrm{SF}}(t-t_0)\right], \tag{2}$$

where an allowance is made for the spin decoherence caused damping in terms of a time constant $\tau = 1/\Gamma$. The oscillations of the beam-spin asymmetries of the signal bunch are shown in Fig. 10 and were fitted using Eq. (2), which yields the spin-flip amplitude c and the frequency f_{SF}. The results of the spin flip analysis are discussed in the submitted paper[4]. We demonstrated the feasibility of the pilot bunch based co-magnetometry for storage ring experiments which is imperative for high-precision spin experiments. The pilot-bunch technique has been primarily proposed in the first place for precision spin experiments that involve testing of fundamental symmetries, such as searches for the parity- and time-reversal-invariance violating permanent EDMs of charged particles, but it may find other applications in the field of spin physics at storage rings.

2.4 Simulation of the Invariant Spin Axis in COSY

Detailed beam and spin dynamics simulations have been performed with Bmad to understand experimental results with polarized deuterons at COSY. The focus of the investigation was the analysis of correction factors for the determination of the Invariant Spin Axis (ISA) in a Bmad COSY model for deuterons.

The simulation model uses predefined quadrupole settings to produce sixfold optical symmetry at a beam energy of 0.97 GeV/c. All the magnetic and electrical elements implemented in the simulation model have been to match their counterparts in the real COSY storage ring as it was used in the JEDI beamtime in early 2021. Within the last year, a study was started to investigate how a con-

[4] Pilot bunch and co-magnetometry of polarized particles stored in a ring, arXiv:2309.06561 (2023), submitted to PRL.

trolled orbit affects the determination of the ISA. For this purpose, a set of perturbed closed-orbits has been using vertical and horizontal dipole corrector magnets in the COSY lattice. A Gaussian distribution centred on zero was used to generate random beam kick values for the corrector magnets. Its width was chosen conservatively so that all randomly kicked trajectories could result in a closed trajectory. The long tilt n_z of the ISA can be measured in an experiment using a using a solenoid or a Radio Frequency (RF) Wien filter plus a solenoid. These experimental conditions have been implemented in the simulation model and their results were compared with the directly calculated ISA at the position of the devices. The result for the RF Wien filter are shown in Fig. 11.

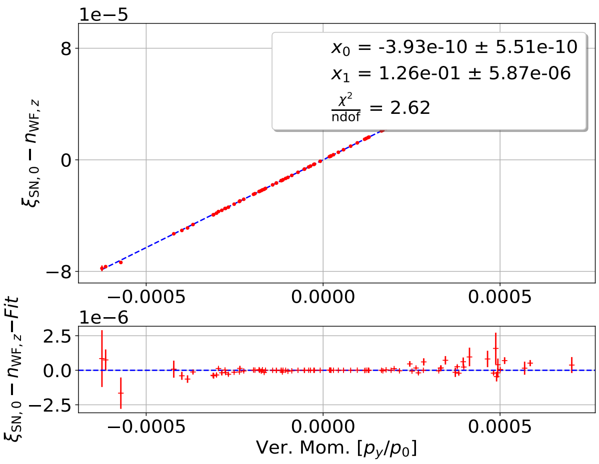

Figure 11: Dependency of difference between Wien filter Minimum ξ_{SN} and long. ISA at the position of RF Wien filter on the vertical momentum when passing the device.

The dependency of difference between solenoidal field and long. ISA at the position of the solenoid for different vertical momenta when passing the device has also been investigated. The outcome of these investigations indicate a linear dependency of the difference in between simulated ISA and experimentally obtained ISA on the vertical beam momentum, when passing a device and the vertical tilt of the device with respect to the nominal orbit (see contribution M. Vitz, page 68).

2.5 Investigation of a Polarimeter Setup for a Prototype EDM Ring

Further beam and spin dynamics simulations for a prototype proton EDM ring were carried out. The main focus was the simulation of the interaction between the stored proton beam and a pellet target. This setup has been proposed as an beam extraction mechanism to measure beam polarization. The pellet target, typically placed just before the bending arc, scatters a portion of the primary beam. As the scattered beam passes through bending elements, it diverges from the original beam, and a second target at the polarimeter is used to measure beam polarization.

Analytical calculations have been performed to estimate the impact of the pellet target on beam losses, followed by simulations with a detailed description of the pellet distribution, to to optimize the target size and position. For example, with 50 μm pellets from the target approximately 96% of the particles were lost at the electrostatic bending plates, leaving only a few to reach the straight section for detection (see Fig. 12).

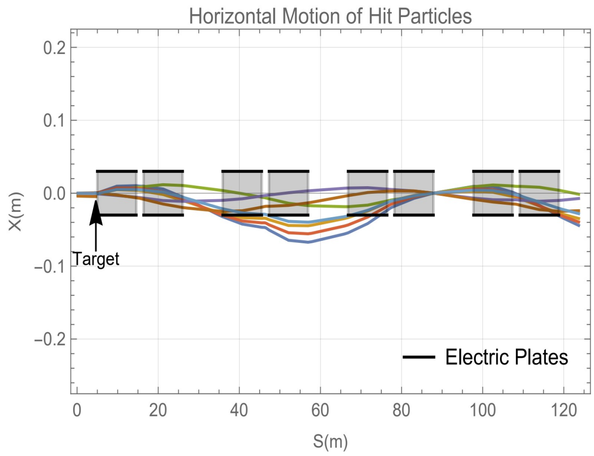

Figure 12: Horizontal motion of survived particles from electrostatic bending plates after scattering with 50μm pellets from a target.

Positioning the pellet target at the center of an arc (between the bending plates) proves far more practical than locating it at the arc's entrance. This position of the pellet target is critical for an effective separation of scattered particles from the original beam (see contribution S. Siddique, page 69).

2.6 Outlook: Experiments with Polarized Beams and Targets at the GSI/FAIR Storage Rings

As already reported a Letter of Intent (LoI) entitled "Towards Experiments with polarized beams and targets at the GSI/FAIR storage rings" was well received by the GSI/FAIR GPAC. Among the proposed physics topics are the axion/ALP search and the measurement of parity-even time-reversal-odd analyzing power in polarized proton tensor-polarized deuteron scattering.[5]

The main goal for the coming years is the preparation of a complete proposal for experiments with polarized beams and at the GSI/FAIR storage rings.

[5] Towards experiments with polarized beams and targets at the GSI/FAIR storage rings, 19th Workshop on Polarized Sources, Targets and Polarimetry, Mainz, Germany, 26-30 September, 2022.

3 Neutrino Physics

The neutrino group is specialized in low-energy neutrino physics with liquid-scintillator (LS) based detectors. Borexino, described in Sec. 3.1, was the world's radio-purest 280 ton LS detector. It was located in the Laboratori Nazionali del Gran Sasso in Italy and taking data from May 2007 until October 2021. The focus of Borexino was on solar neutrinos, but it measured also geoneutrinos and searched for rare processes. JUNO (Jiangmen Underground Neutrino Observatory), described in Sec. 3.2, is going to be the first multi-kton LS detector ever built. It is currently under construction in Jiangmen in South China. Its completion and start of data taking is expected in 2024. The main goal of JUNO is determination of the neutrino mass ordering, but it also has a vast potential in other areas of neutrino and astroparticle physics. The success of JUNO strongly depends on the levels of radiopurity that will be achieved. German groups are leading the construction of a 20 ton satellite detector called OSIRIS (Online Scintillator Internal Radioactivity Investigation System). It will monitor the level of radio-purity of the LS during several months long period of filling the 20 ton JUNO central detector, see Sec. 3.3.

3.1 Borexino

Borexino was a ∼280 ton LS experiment designed for real-time detection of low-energy neutrinos. It was located at the underground Gran Sasso laboratory in Italy, beneath approximately 1400 meters of rock. During more than ten years of data taking, it has measured all the solar neutrino fluxes produced in the proton-proton (*pp*) chain, the main fusion process responsible for approximately 99% of the solar luminosity. Moreover, in the last stages of the data-taking, Borexino has discovered solar neutrinos emitted from the Carbon-Nitrogen-Oxygen (CNO) cycle[6], in which the hydrogen-to-helium fusion is catalyzed by carbon (C), nitrogen (N), and oxygen (O).

3.1.1 Final results of Borexino on CNO solar neutrinos

In 2023, Borexino measured CNO neutrinos using the so-called Correlated and Integrated Directionality (CID) method, which relies on the detection of fast sub-dominant Cherenkov light in a LS detector. This work was published in Physical Review Letters[7] and selected as Editor's suggestion. The CID method relies on the definition of the angular distribution α for the individual hits (typically representing signals from single photons) of both solar-neutrino and background events. The CID method exploits the correlation between the known direction of solar neutrinos originating from the Sun and the direction of the earliest PMT hits of each event. The directional information is preserved by Cherenkov photons and can be exploited to discriminate solar neutrino events from isotropic backgrounds, uncorrelated with the Sun's position. This is possible since the largely sub-dominant Cherenkov light is much faster with the respect to the dominant scintillation light. Borexino applied this novel technique to determine the number of solar neutrino events (N_ν) in a specific energy region of interest. The directional CNO measurement uses the complete Borexino data-taking period and was applied separately for the Phase-I (2007-2021) and for the Phase-II+III (2011-2021). No a-priori knowledge of the backgrounds in the detector is required. In particular, the analysis does not rely on any external constraint on the ^{210}Bi contamination of the LS, a critical aspect in the spectral analysis approach used the first CNO measurements.

Signal and background events are selected in the region of interest (RoI) from 0.85 up to 1.3 MeV, chosen to optimize the signal-to-background ratio. The number of solar neutrino events in the RoI consists of $pep-\nu$ (∼64%), CNO$-\nu$ (∼33%), and ^{8}B-ν (∼3%). The detected PMT hits of each event are relatively ordered in time after subtracting their time of flight, and their corresponding $\cos\alpha$ distributions are fitted with Monte Carlo probability density functions (PDFs), using a χ^2 fit. N_ν in the RoI is extracted simultaneously fitting the first 15 (17) hits for the Phase-I (Phase-II+III) analysis. The fit includes two nuisance parameters to take into account the two major systematics of the CID analysis. The first, known as position reconstruction bias (Δr_{dir}), accounts for the fact that in Borexino the reconstructed position of the event is slightly biased in the direction of the Cherenkov light, e.g. true direction of the electron. Since the Δr_{dir} could not be calibrated, it is treated as a free nuisance parameter of the fit. The second systematic effect arises from the fact that the Cherenkov and scintillation photons have different wavelength distributions and the precision of the MC is wavelength-dependent. This means that effective group velocities, and thus the relative timing of Cherenkov and scintillation photons, are different in data and MC. To mitigate this sub-ns effect, a correction of the effective group velocity of Cherenkov photons ($\mathrm{gv_{ch}}$) is added in the MC simulations. To calibrate $\mathrm{gv_{ch}}$, the CID analysis is performed on an independent energy region (0.54-0.74 MeV) dominated by ^{7}Be solar ν, constraining the number of solar neutrinos to the Standard Solar Model prediction.

In Fig. 13 an illustrative example of the measured $\cos\alpha$ distribution for all phases is shown, alongside the best fit (red) and a pure background hypothesis (blue). To aid comprehension, the first four PMT hits of all selected events are summed. The N_ν best-fit results, obtained with the two parallel analyses for the Phase-I and Phase-II+III datasets, are combined and converted to interaction rate (R), yielding the CNO rate $R_{\mathrm{CID}}(\mathrm{CNO}) = 7.2^{+2.8}_{-2.7}$ (stat. + syst.) counts per day over 100 ton of LS (cpd/100 t). This result includes additional systematic uncertainties arising

[6] Experimental evidence of neutrinos produced in the CNO fusion cycle in the Sun, Nature (2020) 587.

[7] Final results of Borexino on CNO solar neutrinos, Phys. Rev. D (2023) 108.

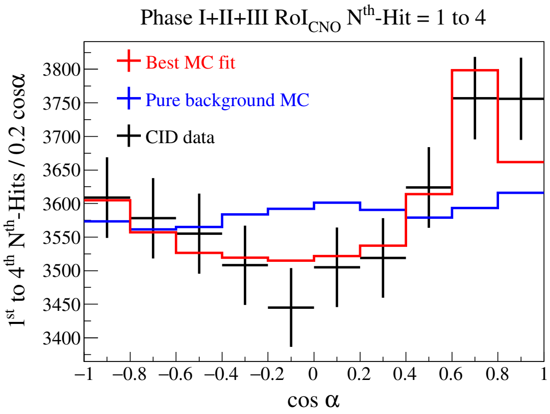

Figure 13: Borexino CNO solar neutrino analysis with the CID method: $\cos\alpha$ distribution of data from the RoI of 0.85 up to 1.3 MeV combining Phase-I+II+III and summing the first four PMT hits is depicted in black. The best-fit results and the background-only hypothesis are shown in red and blue, respectively.[7]

from PMT properties. With this result, the zero-CNO hypothesis is rejected with a significance greater than 5σ, for the first time without any assumption on the backgrounds present in the detector.

Moreover, the result obtained with the CID method can be used as an external constraint for the spectral analysis, based on scintillation light, used in Borexino to detect CNO neutrinos in 2020[6] and 2022[8]. This analysis involves a likelihood fit of the energy and radial distributions of the events to extract CNO$-\nu$ interaction rate. A key aspect of this analysis is an independent constraint of the ^{210}Bi background. The N_ν posterior distribution obtained with CID analysis is used as an additional likelihood term leading to $R(\mathrm{CNO}) = 6.7^{+1.2}_{-0.8}$ (stat. + syst.) cpd/100 t, disfavouring the zero-CNO hypothesis at $\sim 8\sigma$ C.L. This result provides the final and most precise Borexino CNO measurement. This result is combined with $\Phi(^8\mathrm{B})$ from the global analysis of all solar data to estimate the C+N abundance with respect to Hydrogen in the Sun: $\mathrm{N_{CN}} = 5.81^{1.22}_{-0.94} \cdot 10^{-4}$. This result exhibits a mild $\sim 2\sigma$ tension with low metallicity photospheric measurements.

Within the Borexino collaboration, the IKP-2 neutrino group has had a leading role in this analysis. This effort resulted in a collaboration paper published by Physical Review D in 2023 that was selected as the Editors' suggestion. During 2023, the findings of the analysis have been presented at three important international conferences by the members of our group : the European Physical Society Conference on High Energy Physics (EPS-HEP), Topics in Astroparticle and Underground Physics (TAUP), and XX International Workshop on Neutrino Telescopes (NeuTel).

3.1.2 Novel techniques for alpha/beta pulse shape discrimination in Borexino

Particle α/β discrimination played a crucial role in background identification in Borexino. It is based on intrinsic properties of the scintillator, as different interacting particles generate distinct hit time distributions of scintillation photons as a consequence of different energy loss for unit path (dE/dx). In 2023, a detailed review of the α/β pulse shape discrimination adopted in Borexino was uploaded to arXiv and submitted to Phys. Rev. D.[9] The various implementations used to statistically subtract the α components of the energy spectrum over the complete data-taking period are discussed. Optimal discrimination was achieved with a Multi-Layer Perceptron (MLP) neural network, a binary classifier based on neural network training. This discriminator enabled an event-by-event selection of ^{210}Po events. As ^{210}Po is produced in decays of ^{210}Bi, this discrimination was important for placing an upper limit constraint on the ^{210}Bi contamination of the LS - a key element in the spectral measurement of the CNO solar neutrinos.

3.1.3 Borexino's search for low-energy neutrinos associated with gravitational wave events from GWTC-3 database

Borexino searched for signals of neutrino-electron scattering and inverse beta-decay events correlated with gravitational waves observed in the period from September 2015 to March 2020. The analysis considered 74 gravitational wave candidates, arising from merging binaries of black holes, neutron stars, and neutron stars and black holes. However, no statistically significant increase in the number of Borexino events with visible energies above 250 keV was observed. As a result, a new upper limit on the fluence of neutrinos and anti-neutrinos of all flavors was established within the 0.5-5 MeV neutrino energy range.[10]

3.1.4 Independent determination of the Earth's orbital parameters with solar neutrinos

Borexino collaboration has performed for the first time a precise measurement of the Earth's orbital parameters based solely on solar neutrinos,[11] proving once more the solar origin of the Borexino signal. Since the distance between the Sun and the Earth changes in time due to the non-circular shape of the Earth's orbit, the expected solar

[8] Improved Measurement of Solar Neutrinos from the Carbon-Nitrogen-Oxygen Cycle by Borexino and Its Implications for the Standard Solar Model, Phys. Rev. L (2022) 129.

[9] Novel techniques for alpha/beta pulse shape discrimination in Borexino, arXiv:2310.11826 (2023), submitted to Phys. Rev. D.

[10] Borexino's search for low-energy neutrinos associated with gravitational wave events from GWTC-3 database., Eur. Phys. J. C (2023) 83.

[11] Independent determination of the Earth's orbital parameters with solar neutrinos in Borexino, Astroparticle Physics 145 (2023) 102778.

neutrino fluxes arriving to us vary in time. This difference is used in the analysis to estimate the Earth's orbit eccentricity. The search for solar neutrino signal modulations in the frequency range between one cycle/year and one cycle/day was performed using a generalized Lomb-Scargle method. The used dataset period ranges from December 11^{th} 2011 to October 3^{rd} 2021, in the energy region of interest dominated by the mono-energetic ^{7}Be solar neutrino contribution (300 - 827 keV). The estimated eccentricity is $\varepsilon = 0.0184 \pm 0.0032$ (stat+sys). The hypothesis of no annual modulation of the solar neutrino signal due to the eccentricity of Earth's orbit is excluded with a significance greater than 5σ. No other significant modulation frequencies are found. Strong constraints are placed on the amplitudes of other frequencies of interest, such as day-night effects and correlations with the Sun's rotation around its axis. The limits for the percent diurnal modulation and the percent solar rotation day are < 1.3% (90% CL) and 1.8% (90% CL), respectively. These updated bounds are relevant in solar modeling and in constraining various non-standard neutrino interactions.

3.2 JUNO

JUNO is a next-generation LS detector being build in South China, the largest and the most innovative detector of its kind.[12] It will have a spherical 20 kton target surrounded by 17,612 20-inch and 25,600 3-inch PMTs covering 78% of its surface. High photon yield, low LS light absorption, and dense arrangement of PMTs will allow to measure neutrino energy with an unprecedented resolution of 3% at 1 MeV. By measuring electron antineutrino produced in two commercial nuclear power plants (Yangjian and Taishan NPPs) at the distance of 52.5 km, JUNO will resolve neutrino mass ordering (NMO) at 3σ significance level and will precisely measure oscillation parameters $\sin^2\theta_{12}, \Delta m^2_{21}$ and Δm^2_{32} (three out of the six independent parameters defining the neutrino oscillations) at sub-percent level,[13] improving their current uncertainty almost by an order of magnitude. These results are expected to be achieved after 6-7 years of data taking. Besides that, JUNO will serve as an observatory for neutrinos of natural origin: from the Sun, from the atmosphere, and the interior of the Earth and the explosions of supernovae, and will be a powerful tool for searches beyond the Standard Model and new physics.

The civil construction was completed in 2021, and by mid of 2022 the stainless steel supporting structure was installed. Since then the construction works have been continuing with assembly of the acrylic sphere and installation of PMTs with their front-end electronics, see Fig. 14. DAQ systems have been installed in a dedicated room. The LS purification plants were built in 2023 as well. In parallel, the commissioning of the PMTs and the electronics have started.

[12] JUNO Physics and Detector, Progr. Part. Nucl. Ph. (2022) 123.

[13] Sub-percent precision measurement of neutrino oscillation parameters with JUNO, Chin. Phys. C (2022) 46.

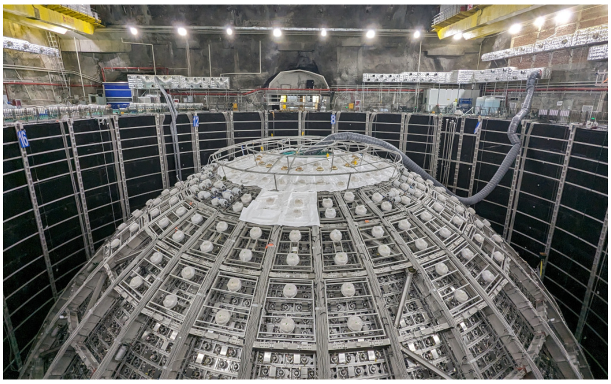

Figure 14: Central detector of JUNO, July 2023.

The design of the Central Detector of JUNO is described in details and published on arXiv.[14]

The central detector and the water pool of JUNO will be partially covered by plastic scintillator planes instrumented with multianode PMTs. The aim of this subsystem is to calibrate the track reconstruction of atmospheric muons and to the evaluate cosmogenic background.[15]

JUNO will be a very powerful tool for observation of a supernova burst in case it happens in our or in the nearby galaxies. A dedicated trigger has been developed in order to collect as much as possible information during a short pulse of neutrinos emitted in the first 10 seconds of the explosion. JUNO will be able not only to measure the energy spectrum and the time profile of the supernova neutrinos, but also to detect neutrinos emitted several hours before the explosion, if it happens within 1 kpc from the Sun. The results of a dedicated study have been summarized in a paper published on arXiv[16] and accepted by Journal of Cosmology and Astroparticle Physics.

The large target mass of the JUNO detector enables searches for rare events. In particular, JUNO will be able to search for proton decay in the $p \to \bar{\nu} K^+$ channel, which will form well-distinguishable three-fold signal. The upper limit is estimated to be 9.6×10^{33} years for a 200 kton-years exposure,[17] competitive to the current best limit from SuperK (5.6×10^{33} years) and complementing it by the use a of a different technology and different decay channel. Another attractive opportunity will be to search for possible annihilation of MeV dark matter particles in the galactic halo.[18] This measurement will be done in the IBD channel and will provide an upper limit for thermally averaged self-annihilation rate of 1.1×10^{-25} cm^3 s^{-1}.

[14] The Design and Technology Development of the JUNO Central Detector, arXiv:2311.17314 (2023).

[15] The JUNO experiment Top Tracker, NIM-A (2023) 1057.

[16] Real-time Monitoring for the Next Core-Collapse Supernova in JUNO, arXiv:2309.07109 (2023), accepted by JCAP.

[17] JUNO sensitivity on proton decay $p \to \bar{\nu} K^+$ searches, Chin. Phys. C (2023) 47.

[18] JUNO sensitivity to the annihilation of MeV dark matter in the galactic halo, arXiv:2306.09567 (2023), submitted to JCAP.

3.2.1 JUNO sensitivity to solar neutrinos

Thanks to its unique features, such as its large active mass, a great PMT geometrical coverage and an unprecedented energy resolution, JUNO will be a perfect candidate to study solar neutrinos. Precision measurements of solar neutrinos fluxes are pivotal for the progress of solar physics: they can, for example, shed light on the abundance of elements heavier than helium inside our star. Furthermore, thanks to the high event statistics that JUNO will collect, it will be possible to search for Beyond Standard Model phenomena in solar neutrinos propagation and interactions.

The JUNO sensitivity to ^{7}Be, *pep*, and CNO solar neutrinos will highly depend on the radio-purity level of the LS. Several radio-purity scenarios were considered in a recent study: from the so-called *Very Low Background* scenario (corresponding to the radio-purity of the last phase of Borexino, the best ever achieved by a LS detector) up to the *High Background* one (the minimum required for the NMO determination). For ^{7}Be neutrinos, as shown in Fig. 15, JUNO can improve the current precision of 2.7% (achieved by Borexino) after less than two years of data-taking. Furthermore, in case of a good radio-purity scenario, a sub-percent measurement of ^{7}Be neutrinos will be possible in the same time span. For the *pep* neutrinos, JUNO can achieve the current best Borexino precision of 17% after two years of data-taking (except for the High radio-purity scenario where 6 years are needed). For a precise measurement of CNO neutrinos, a constraint on the rate of *pep* neutrinos in the spectral fit remains crucial. It can be obtained using the existing data and theoretical models. However, JUNO will be able to detect CNO solar neutrinos without the ^{210}Bi constraint applied in the Borexino spectral analysis and to achieve 20% precision in two to four years (refer to Fig. 16), except for the High scenario. Additionally, in case of a good radio-purity scenario, JUNO will be able to distinguish the ^{13}N and ^{15}O components of the CNO neutrinos for the first time.

The IKP-2 neutrino group has had a leading role in the analysis. A collaboration paper about these studies has been published by JCAP in October 2023.[19] Furthermore, the results of the analysis have been presented at many international conferences throughout the year.

Thanks to the experience gained in Borexino, the IKP-2 neutrino group is performing sensitivity studies to ^{7}Be and CNO solar neutrinos with the directional CID analysis (refer to Sec. 3.1 for further details). Our preliminary results show that the combination of the CID and the spectral analyses may improve the sensitivity to both ^{7}Be and CNO neutrinos. Currently, the analysis strategy is under the first stage of internal review and the future goal is to publish a collaboration paper before the end of the next year.

[19]JUNO sensitivity to ^{7}Be, *pep*, and CNO solar neutrinos JCAP (2023) 10.

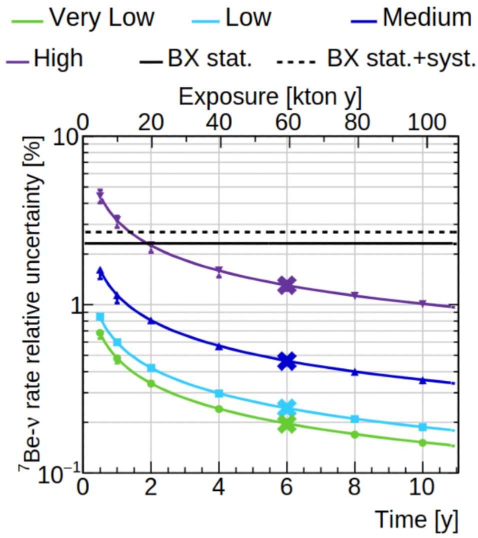

Figure 15: JUNO expected relative uncertainty in the ^{7}Be solar neutrino measurement as a function of the data-taking time in four different radio-purity scenarios[19].

3.2.2 Geoneutrino

Radioactive isotopes present in the interior of the Earth, namely ^{40}K, ^{232}Th, and ^{235,238}U emit electron neutrinos, called *geoneutrinos*. Most of them are $\bar{\nu}_e$ and their flux is proportional to the amount of heat deposited in beta-decays, giving a proxy to investigate the heat budget of the Earth. Geoneutrinos can be detected in the Inverse Beta-Decay (IBD) channel. This way only neutrinos from ^{232}Th and ^{238}U above the energy threshold of 1.8 MeV can be detected. In this measurement, the reactor neutrinos, detected in the same channel, constitute the dominant and irreducible background. This is demonstrated in Fig. 17, where the expected energy spectra of geoneutrino and reactor events are shown together with other relevant backgrounds. Thanks to its large target mass, JUNO will observe about 1 geoneutrino per day in 1 year, collecting more events than the other experiments have collected all together up to date.

The IKP-2 group, together with a group from IHEP (Beijing), plays a leading role in the geoneutrino study in the JUNO collaboration. The JUST software developed by the group for the solar neutrino analysis has been adopted and used for estimation of the JUNO sensitivity to geoneutrinos. The novelty of this analysis with respect to the previous results published by the collaboration back in 2016 include the updated NPP core configuration, new reactor spectral shape input (from a recent Daya Bay measurement), better understanding of detector response, improved muon veto strategy, and the inclusion of uncertainties of the neutrino oscillation parameters. It has been found that the total geoneutrino signal will be measured with a precision of 8% in 10 years assuming fixed Th/U ratio, being a significant improvement

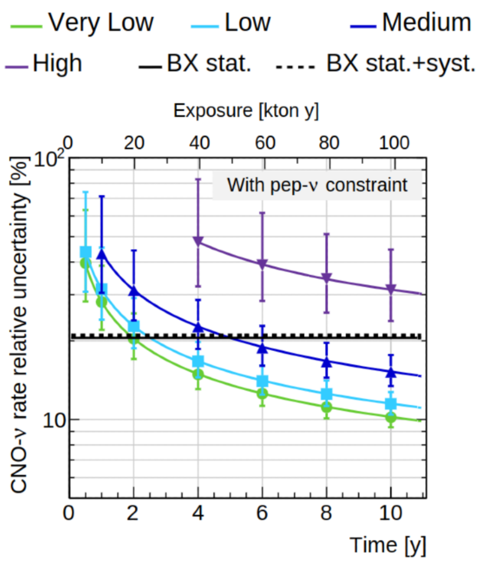

Figure 16: JUNO expected relative uncertainty in the CNO measurement as a function of the data-taking time in four different radio-purity scenarios[19].

compared to the results of Borexino[20] and KamLAND[21] expected (17% and 15%, respectively). Without any constraint on the Th/U ratio, JUNO will measure contributions from Th and U with an accuracy of 35% and 30%, respectively.

A dedicated MC production has been performed for this analysis, which included high-statistics samples of geoneutrino and reactor neutrino signal, as well as Li/He and (α, n) backgrounds.

It is important for the IBD analyses to have an accurate prediction of the geoneutrino signal. It enters as a background to the oscillation analysis, including NMO and precise measurement of oscillation parameters. Besides that, prediction of the geoneutrino signal from the crust, the outermost layer of the Earth, is a key ingredient for observation of the Earth mantle geoneutrino signal. Indeed, the crustal contribution can be predicted with geological and seismic data, while mantle is practically out of reach for exploration. The precious information about it can be obtained by subtraction of the predicted crustal signal from the measured total geoneutrino signal.

The local area near the experimental site contributes to more than a half of the crustal signal. Thus, it is important to have its accurate estimation. A dedicated survey campaign has been undertaking to collect local data and to build an accurate model. The IKP-2 group participates in the evaluation of this model and calculates the geoneutrino signal predicted by this model.

Based on the crustal contribution prediction and its uncertainty one can assess the sensitivity of JUNO to observe the mantle signal. Such calculations have been performed

[20]Comprehensive geoneutrino analysis with Borexino, Phys. Rev. D (2020) 101.

[21]Abundances of Uranium and Thorium Elements in Earth Estimated by Geoneutrino Spectroscopy, Geophys. Res. Lett. (2022) 49.

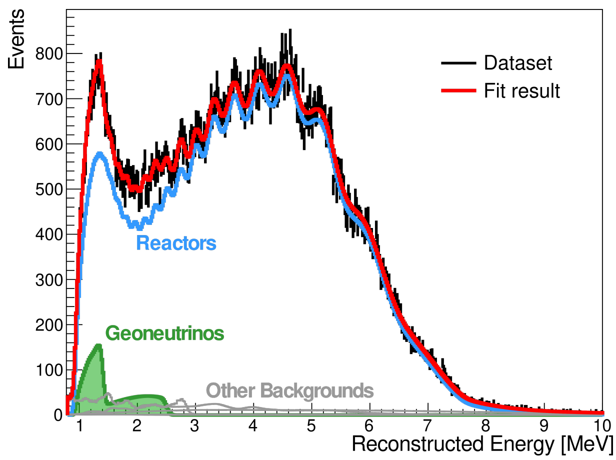

Figure 17: JUNO expected energy spectrum of antineutrino events detected with IBD interaction in 10 years. The contribution of geoneutrinos (green), reactor neutrinos (blue), and other backgrounds (grey) relevant in the IBD analysis is fit with the JUST software, developed by the IKP neutrino group.

by the IKP-2 group and cross-checked with an independent calculation performed by another IHEP group.

The preliminary results of all geoneutrino studies carried out in 2023 were released on several conferences and are planned to be published in a collaboration paper in 2024.

3.3 OSIRIS

The physics potential of JUNO strongly depends on the achievable LS radiopurity levels. A scintillator purification system fulfilling the stringent requirements of JUNO has been built, yielding U/Th radiopurity levels of at least 10^{-15} g/g (NMO determination) and possibly 10^{-16} g/g (solar neutrino measurements). The LS purification chain includes four stages (Al_2O_3 column, distillation, water extraction, and steam stripping) as well as storage and mixing tanks. The obtained LS radiopurities will be validated with the 18 ton detector OSIRIS (Online Scintillator Internal Radioactivity Investigation System). The design of OSIRIS has been optimized to evaluate the contamination of the LS with ^{238}U and ^{232}Th via tagging the ^{214}Bi-^{214}Po and ^{212}Bi-^{212}Po delayed coincidences occurring in the respective decay chains. OSIRIS will continuously monitor the scintillator radiopurity during the months-long filling of JUNO's CD and raise alarms if contaminations are found.

OSIRIS features an 18 ton LS target within an acrylic vessel (AV) of 3 m width and 3 m height. Sixty-four 20-inch Large PMTs (LPMTs), mounted on a stainless steel frame, instrument the watershielded target (see Fig. 18). Twelve additional LPMTs are employed in the water Cherenkov muon veto of OSIRIS, which is optically separated from the inner detector by foils. The LS enters the AV at the top and leaves it at the bottom within roughly

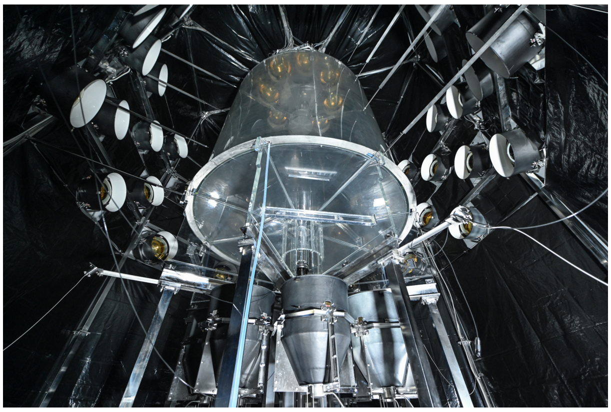

Figure 18: Upward view inside the OSIRIS detector, with the central acrylic vessel instrumented by sixty-four PMTs. The horizontal rods pointing towards the vessel are used for measuring the temperature of the water shield close to the vessel. Image credit: JUNO collaboration.

one day, with diffusors at inlet and outlet ensuring laminar flow speeds.

Within OSIRIS, the IKP-2 neutrino group is responsible for the source insertion calibration system, a refurbished Automated Calibration Unit (ACU, see Fig. 19) provided by the Daya Bay collaboration. It features three independent wheels mounted on a turntable, allowing to lower calibration sources directly into the LS volume. In order to maximise the variation of the detector response at different heights, the ACU is placed 1.2 m off-center to the central axis of OSIRIS. Three calibration sources have been purchased by the IKP-2 group. A multi-gamma source consisting of ^{137}Cs, ^{60}Co, and ^{65}Zn with a combined activity of several kBq is employed for the calibration of energy and vertex reconstructions. A 435 nm LED allows the calibration of LPMT timing and charge responses. By tuning its intensity, also higher p.e. occupancies can be investigated. The third source, a low-activity ^{40}K (≤ 1 Bq) is used to continuously monitor optical LS properties during normal operation.

In 2023, the group members continued to support the commissioning of OSIRIS and prepared the ACU for nominal operation. In order to allow significant progress on both individual PhD theses and the ACU commissioning, the group offered remote support for the Chinese OSIRIS members throughout full 2023. At the same time, the calibration software developed by members of the IKP-2 neutrino group was refined and a calibration knowledge transfer to other German OSIRIS members was initiated.

In September 2023, the ACU hardware and software underwent thorough validations, followed by hardware calibrations ensuring operational safety of the ACU. Subsequently, the calibration sources were installed, and their positioning was calibrated using known reference points within the detector. With these measurements, the accuracy of the source positioning was shown to be around

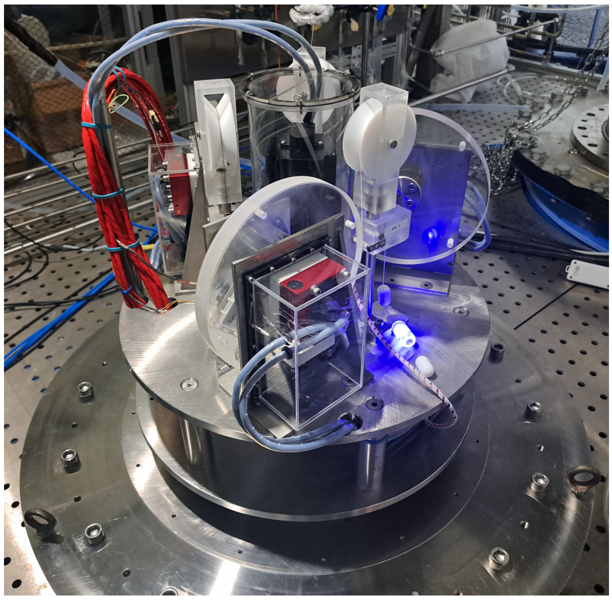

Figure 19: View on the ACU turntable with its three independent source wheels. The LED source, mounted on the foremost wheel and placed on the turntable for a functionality test, can be observed shining brightly. During normal operation, the intensity of the LED will be adjusted such that its light emission is invisible to human eyes.

4 mm, thus confirming the target sub-cm positioning accuracy. Finally, also first LED calibration data was recorded during the commissioning stay. The analysis of the data is ongoing, but preliminary results already confirmed the detector response obtained by detector simulations. The results also allow to perform functionality checks of the full detector, thus helping the overall commissioning efforts to identify issues at an early stage.

4 Accelerator Research

4.1 Developments at COSY

In 2023, the COSY operation was brought to a successful conclusion. In addition to supplying beam to the experiments, COSY has been further developed, and new technologies have been tested and used in regular operations. Highlights include RF Knock-out extraction with spill control, further developments in the area of AI/ML methods, and the acceleration and extraction of polarised beam, which was made possible by precise tune measurement and control during the acceleration ramp.

4.1.1 RF Knock-out extraction

RF-KO extraction will be the main extraction mode for the SIS100 machine at FAIR. It differs from the stochastic slow extraction, which has been used at COSY, as it uses transverse rather than longitudinal noise extraction.

A significant development effort led by the GSI Beam Instrumentation Department supported by IKP and industry partner Cosylab successfully implemented a spill feedback controller based on a software-defined radio. A beam time at COSY was requested and granted by CBAC14 for the implementation of RF-KO extraction with precise spill control.[22] The simulation results were confirmed during the beam time at COSY, and the extraction method was established. The extraction rate could be precisely controlled by feedback independent of extraction time and beam intensity in the ring. As the method proved stable and robust, it was subsequently used as the standard extraction method for all the following beam times. The experimental groups who requested extracted beams could immediately benefit from the newly developed system.

4.1.2 AI/ML

As Bayesian optimisation proved to be a useful tool to optimise the injection beam line already in 2022, further developments were made towards the use of artificial intelligence and machine learning techniques. The existing Bayesian optimiser was extended to use any process variable (PV) related to the injection process as an optimisation target. The optimiser was then used to prepare several beam times, see Fig. 20. Another AI/ML topic covered was the control of the beam as recorded on a scintillating screen by a reinforcement learning agent. The agent was trained on the IBL model. It was demonstrated that it could control the beam according to the operator's demands. For more details see "Injection Optimization via Reinforcement Learning at the Cooler Synchrotron COSY", A. Awal, page 79.

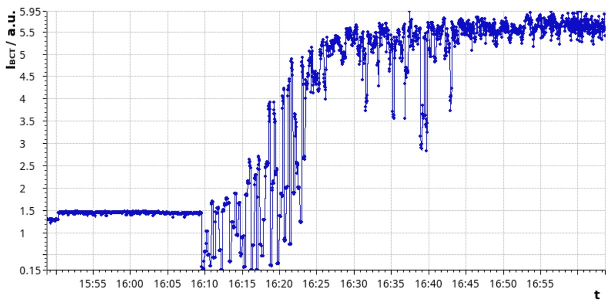

Figure 20: One run of the Bayesian optimiser. The optimisation target was to increase the stored current I_{BCT} in COSY as measured by the BCT. The current was increased by a factor of 3.7 in less than one hour.

Automated positioning of the stripping foil. A programmatic control of the stripping foil position as well as fast switching between the stripping foil and the viewer at the injection location were prerequisites for the AI/ML studies. A stepper motor drive was implemented for this purpose. Controls software developed at iThemba LABS based on the DIAMOND Ethercat EPICS Master was adopted. The system was installed in the COSY tunnel in spring 2023 for the injection beam studies, described in detail in "Extending COSY's Capabilities for Automated Algorithms", J. Hetzel, page 80.

4.1.3 Acceleration and Extraction of Polarised Protons

One of the most challenging beam requests in 2023 was to prepare a polarised proton beam. During the acceleration to a momentum of 1950 MeV/c, several resonances destructive to the polarisation must be crossed. Owing to the recent developments[23] the measurement of the tune during the acceleration ramp with millisecond resolution and the ability of COSY to manipulate the tune accordingly (see Fig. 21) allowed to preserve the polarisation all the way into flat-top (see Fig. 22) and to extract the polarised beam to the external target (see Fig. 23).

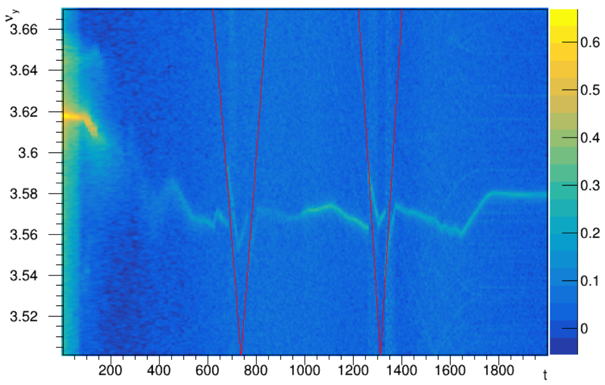

Figure 21: Measurement of the vertical tune during the acceleration ramp. The depolarising resonances are shown as red lines. The tune was manipulated to make fast changes (tune jumps induced by dedicated fast quadrupole magnets) to cross the resonances without losing the polarisation.

4.1.4 Developments at the NESP beamline

The activities of the Jülich Center for Neutron Science (JCNS) towards the development of HBS (see page 18) involved a series of beam times at the COSY accelerator facility. This effort continued in 2023 and amounted to 6 weeks of beam time (see page 20). The ion beam instrumentation at the NESP beamline.[24] providing the beams from the cyclotron to the HBS target station was

[22] P. Niedermayer and R. Singh, "RF Knock Out (KO) extraction", A021, CBAC 14 (2023).

[23] P.Niedermayer et al., A Fast Tune Measurement System for COSY & 4.4 Improved Tune Monitoring, IKP Annual Report 2019, Jül-4423.

[24] Developments at the NESP beamline, page 16, IKP Annual Report 2022; M.Rimmler, O.Felden, Measures at the BigKarl Area for the High Brilliance Neutron Source (HBS), page 73, IKP Annual Report 2021;

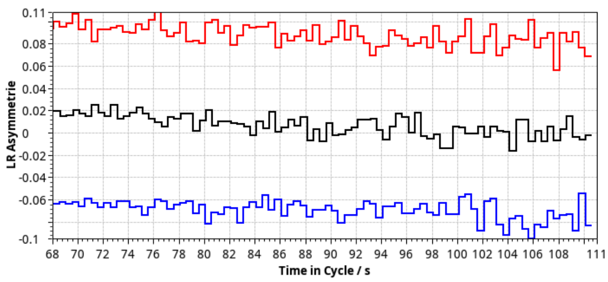

Figure 22: Asymmetry measurement of different polarisation states (red and blue lines) with the JEDI polarimeter. The black curve shows the measurement of the unpolarised proton beam.

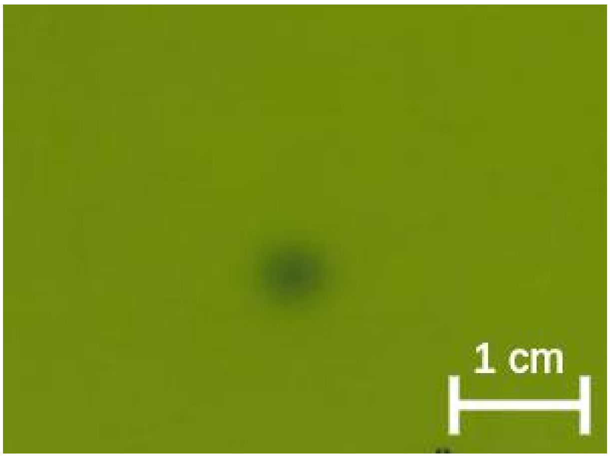

Figure 23: A photograph of a radiation-sensitive film showing the spot of the extracted polarized proton beam. The image was taken during the last experimental beam time at COSY. The film was placed at the exit vacuum window at the end of the COSY-TOF beam line. Courtesy of D. Grzonka.

undergoing improvements. 8 neutron monitor detectors were installed and the signals registered utilizing Red Pitaya data acquisition boards. The loss rate data was published directly to the EPICS system and stored in the IKP EPICS archiver for long-term availability. In addition, 4 scintillation-based beam loss monitors were installed close to the neutron target. Red Pitaya boards also did the readout of these signals. A Red Pitaya also read out two additional gamma radiation monitor systems, and the levels were archived through EPICS. The improved monitoring and control of the ion beam losses helped reducing neutron background in the area.
Furthermore, additional sub-systems were prepared for increased beam intensity in the NESP beamline. For ion beam position monitoring one standard COSY BPM equipped with FEMTO pre-amplifiers and read out by a Libera-system was set up. The beam current was to be measured utilizing a Bergoz fast current transformer in addition to the stripping foil in front of the neutron target. This was done because of the plan to switch from H^- to protons. As an additional system for monitoring the beam position, profile, and current, a beam-induced fluorescence (BIF) monitor was installed along the beamline but still within the cyclotron bunker. This system uses light, sent out by the residual gas while interacting with the ion beam. The light is registered by a multichannel photomultiplier and read out by a multichannel current meter from iThemba LABS. The experiments could not yet benefit from these additional preparations due to still comparatively low ion beam current in the NESP beam line and thus insufficient signal-to-noise ratio.

F. Dahmen et al., Status of the NESP beam line, page 114, IKP Annual Report 2019.

4.2 Progress of the HESR

4.2.1 Freeze

The work on the HESR was governed by the freeze of the HESR project, which the FAIR Council confirmed in March 2023. Consequently, only manufacturing processes started at FZJ or a third-party provider, are to be completed. If a purchasing process has not been started, the corresponding package is on hold and will not be completed until the HESR project is restarted. Major components completed in 2023 are the injection kicker and a prototype of the low-level radio frequency (LLRF) system. All vacuum tests for the tanks of the stochastic cooling system have been carried out. In addition to completing elements, an important step towards the freeze is the delivery of all components available in Jülich to a storage site near the FAIR site. In 2023, one focus was on preparing the transport and transporting the elements to storage in Weiterstadt. In parallel to the freeze activities a restart report was written, documenting all the steps and decisions taken to freeze the project, as well as the resources needed to restart the project at a later stage.

4.2.2 Injection

The manufacture of tank C, the remaining component to complete the injection, has been finished. The FAT/SATs were successfully carried out at the manufacturer's workshop in Vannes, France, in the presence of IKP and GSI staff. The kicker tank, Fig. 24, and its power supply, including the control system for the vacuum and the heating, were then delivered to Weiterstadt.

4.2.3 Beam Instrumentation

All 80 wire arrays for the ionization profile monitors (IPM) have been manufactured at ZEA. The wire arrays will be used not only for the IPMs at the HESR but also for other FAIR beamlines. These wire arrays were delivered to the beam diagnostics group (BEA) of GSI. One HESR IPM has been built at FZJ. Vacuum tests are still to be performed.
All but one of the beam position monitors (BPM) were

Figure 24: Injection tank C is ready for delivery.

delivered to FZJ. They have been successfully tested on the dedicated test bench here.
Both scrapers passed the mechanical and vacuum tests and will be transported to FAIR storage.
Viewer assemblies will not be completed. The vacuum parts, drives and stands will be sent to storage as is.

FESA test system. To advance the understanding of the control system used within the FAIR project - Front-End Software Architecture (FESA) - a stand-alone system was set up at COSY with GSI and Cosylab support a few years ago. The system was meant to be used as a development playground and to test FAIR sub-systems developed and manufactured at IKP within the FAIR controls environment. For proper testing, a minimalistic timing system was set up, utilizing a White Rabbit switch and FAIR Timing Receiver Nodes (FTRN) to provide the functionality of the FAIR General Machine Timing (GMT) system. This environment was used to implement a scaled-down HESR beam loss monitor (BLM) system using 12 of the planned 112 BLM detectors. Being in development for several years, the system became operational in the spring of 2023 and was used for beam loss monitoring during routine COSY operations. The GUI of the operational system is shown in Fig. 25.

4.2.4 Low Level RF System

For the accumulation of antiprotons in the HESR, the concept of longitudinal stacking is planned. This requires a combination of stochastic cooling of the already injected beam and creating space for the next injection by a barrier bucket RF system. This places high demands on the radio frequency (RF) system of the HESR, as it involves the parallel operation of two identical cavities and the need to shift their signals relative to each other in a defined way. As both cavities are used not only for accumulation but also for beam acceleration, this increases the demands on the RF. To generate the necessary signals, an FPGA-driven signal generator was designed and a prototype was built.

4.2.5 Transports

The following main components for the HESR are among the elements delivered from Jülich to the storage site in Weiterstadt:

- all power supplies for the quadrupole magnets and accessories,
- the remaining dipole: all 46 dipoles, including their vacuum tubes, are now stored in Weiterstadt,
- 57 quadrupoles,
- all injection elements and all chicane dipoles.

In addition, the components for the stochastic cooling and for the accelerating RF, which are not subject to tests in the COSY tunnel, and the majority of beam instrumentation elements have been prepared for transport in 2024. Since the manufacture of some elements, in particular vacuum chambers, has been stopped due to the freeze, the stainless steel already purchased for these components has been transported to GSI as well and will now be used for the manufacture of other FAIR components that are not part of the freeze.

4.3 High Brilliance Neutron Source (HBS)

Accelerator-driven high brilliance neutron sources are an attractive alternative to the classical neutron sources of fission reactors and spallation sources to provide scientists with neutrons to study and analyze the structure and dynamics of matter. With the advent of high-current proton accelerator systems, a new class of such neutron facilities can be established referred to as High-Current Accelerator-driven Neutron Sources (HiCANS). The basic features of HiCANS are a medium-energy proton accelerator with tens of MeV and up to 100 mA beam current, a compact neutron production and moderator unit and an optimized neutron transport system to provide

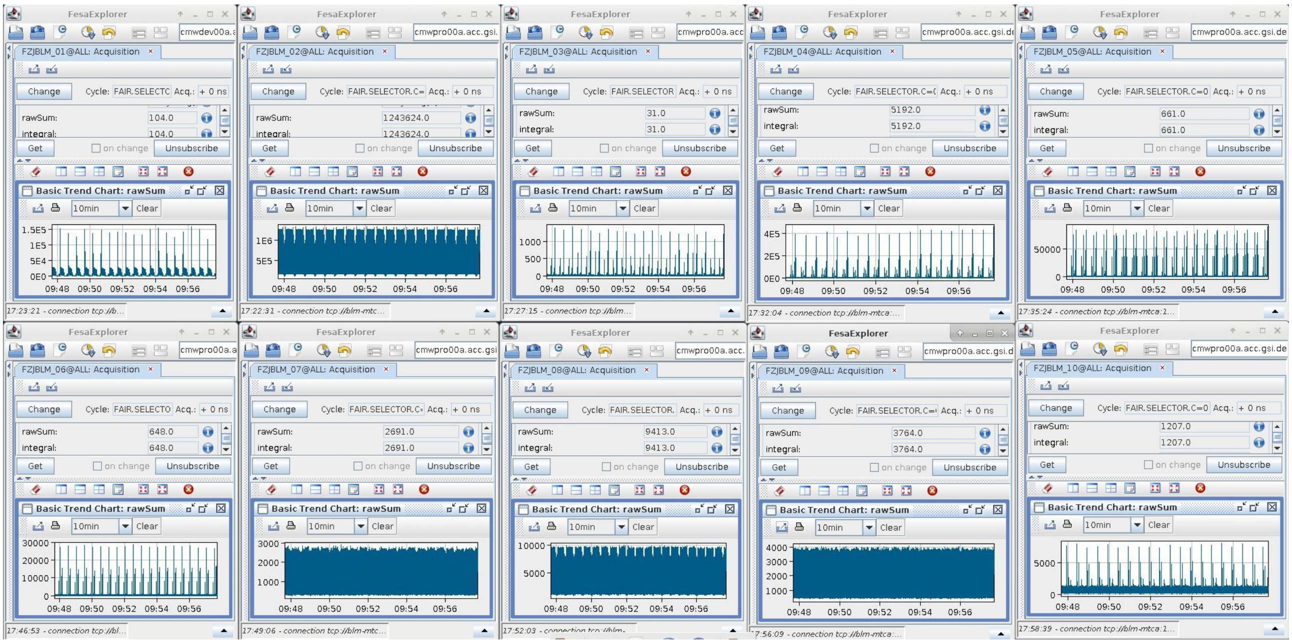

Figure 25: The GUI of the HESR BLM system installed at COSY, utilizing the FESA explorer.

a full suite of high performance, fast, epithermal, thermal and cold neutron instruments. The Jülich Centre for Neutron Science (JCNS) together with partners[25] has established a project to develop, design and demonstrate such a novel accelerator-driven facility termed High Brilliance neutron Sources (HBS).[26] The aim of the project is to build a versatile neutron source as a user facility with open access and service according to the diverse and changing demands of its communities. Embedded in an international collaboration with partners from Germany, Europe and Japan, the Jülich HBS project offers the best flexible solutions for scientific and industrial users. The overall conceptual and technical design of the HBS as a blueprint for the HiCANS facility has been published in a series of recent reports.[27] The full-scale HBS facility is characterized by the simultaneous operation of a suite of neutron instruments distributed around three target stations, each efficiently operated to deliver variable neutron spectra.

4.3.1 Front-End and Linac

The front-end of the HBS-Linac covers the area from the proton source to the Medium Energy Beam Transfer (MEBT) before the injection into the drift-tube Linac. This section has to fulfill several tasks. After the beam creation in the proton source, the beam has to be transported to the entrance of the RFQ using the Low Energy Beam Transfer (LEBT). The LEBT has also to match the transverse phase space to the acceptance of the RFQ. By means of a chopper, the necessary pulse structure is imposed on the DC beam in front of the RFQ. The beam energy at injection into the drift-tube Linac is 2.5 MeV. The Drift Tube Linac (DTL) has to accelerate the proton beam from 2.5 MeV to 70 MeV. The design of the DTL is a complex process between the beam dynamics and cavity design. There are a number of requirements or boundary conditions for the DTL with respect to beam dynamics. The DTL beam dynamics design consists of 45 normal conducting CH-type cavities, of which the second, fifth and eighth are rebunchers. The whole DTL section is 66.7 m long.

4.3.2 High Energy Beam Transport

The High Energy Beam Transport (HEBT) connects the Linac with the individual target stations at HBS. It includes the multiplexer system that is part of the design of the HEBT and a beam dump (s. Fig. 26). To achieve full performance with high beam brilliance at HBS, this facility simultaneously operates three neutron target stations in parallel with multiple neutron instruments attached. Each target station is operated efficiently to deliver different neutron pulse structures, which is achieved by generating an interleaved proton pulse structure that provides three different proton beam timing schemes. The distribution of the different proton pulse sequences to the target stations is accomplished by a proton beam multiplexing system that consists of a kicker magnet and a three-field septum magnet (TFSM). The integration of the multiplexer system at HBS including the design of a septum magnet is based on dedicated developments using a 45 MeV proton beam of the JULIC cyclotron at Forschungszentrum Jülich and scaled for the larger proton beam energy of 70 MeV at the HBS. In connection

[25] IAP of Frankfurt University and IKP-4 at FZ Jülich
[26] EPJ Web of Conf., 286, 02003 (2023)
[27] HBS Technical Design Report

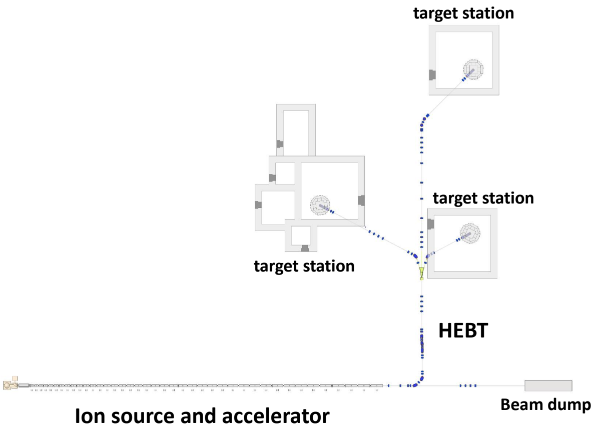

Figure 26: Schematic top view of HBS, including the front end, Linac and High-Energy Beam Transport (HEBT) beamline to the individual target stations.

with the HBS multiplexer system, the HBS High-Energy Beam Transport (HEBT) beamline has been designed and the associated beam dynamics calculations performed. The geometry of the HEBT is determined by the location and arrangement of the HBS target stations in the three experimental halls, based on the space requirements of the neutron targets, instruments and the corresponding building locations and dimensions.

The corresponding beam dynamics calculations for the different beam line sections have been performed using the Bmad library to optimize the optical setting. The dynamic acceptance of the beamline needs to be further optimized, including multipole corrector fields. So far, only estimated multipole errors of the magnets have been implemented without any minimization of the average beam losses in the beamline.

4.4 Neutron Target Station in the Big Karl Area of JULIC

The HBS project developing a High-Current Accelerator-driven Neutron Source (HiCANS) is planning to have up to 25 instruments for neutron scattering, analytics and imaging. Properly tailored neutron beams are provided by three target stations, each optimized for different groups of instruments with their individual proton / neutron pulse structure.

Each target station consists mainly of a Tantalum target which emits neutrons due to nuclear reactions initiated by the 70 MeV proton beam, a moderator / reflector assembly with integrated cryogenic moderators reducing the initial high neutron energy to the thermal or cold energy range, and a shielding structure reducing radiation levels to allowed values.

Figure 27: HBS target station prototype in the Big Karl area of the JULIC cyclotron.

A fully functional target station requires a proper interplay of all described components. This requires further technological development of individual components as well as testing of the whole system. At the Big Karl area at the COSY facility, a target station prototype was thus built as shown in Fig. 27. It uses a 45 MeV proton beam provided directly from the JULIC cyclotron with flexible frequency and pulse length.

The target station prototype is designed to be operated at 10% HBS power level, easing the requirements for target cooling and shielding thickness.[28] An opening mechanism moving a quarter section of the shielding structure allows easy access to the core to modify the moderator / reflector assembly based on a hydrogen-rich polyethylene moderator and a lead reflector with low neutron absorption.

Eight extraction ducts looking at different positions at the moderator / reflector assembly or the target allow simultaneous extraction of fast, epithermal, thermal and cold neutron beams though the shielding. In these ducts, either moderator plugs optimized for the planned experiment or blind plugs for shielding purposes are inserted.

In 2023, six weeks of beamtime have been used by three groups from Germany, one group from France and one from Sweden to perform more than 7 different experiments. Some of these experiments have been reflectometry (CEA), shielding performance validations (JCNS), moderator tests (JCNS), reflector material investigation (ESS), molybdenum and gold irradiation (JCNS), fast neutron imaging (JCNS), thermal neutron imaging (TUM) and detector tests (HEREON, ESS, JCNS).

The target station prototype provides the possibility to test critical components for developing HiCANS sources like target, moderators, shielding, instrumentation, and detectors and the interplay of all components combined. It further allowed to validation Monte Carlo simulations

[28] EPJ Web of Conferences 286, 02004 (2023)

for the shielding layout and target-moderator-reflector performances, as well as to estimate the performances of instruments like imaging or reflectometry.

5 Further Activities

5.1 Plasma Acceleration demonstrates its Capability to produce Polarized Beams

Spin-polarized particle beams are commonly used in nuclear and particle physics to test the Standard Model of particle physics or to map out the hadronic resonance spectrum. Until now, their production relies on conventional particle accelerators, which are generally very large and expensive. The worldwide strategy processes aiming at the realization of next generation's particle accelerators also point at the importance of polarized beams.

Laser-plasma interactions and beam-driven plasma acceleration have been proven to be feasible methods for obtaining high-energy particle beams over much shorter acceleration distances compared to rf-based accelerators. Despite much progress in understanding the phenomena that lead to the particle acceleration, experimental proof of whether polarized beams can be realized with plasma accelerators was still lacking.

Already 10 years ago a group from Forschungszentrum Jülich and Heinrich-Heine University Düsseldorf proposed a concept for producing highly polarized electron, proton, or ion beams through plasma acceleration based on the use of polarized targets.[29] Here the spins of the particles to be accelerated are already aligned before the plasma formation.

Although the method seems simple in principle, it requires careful consideration of various technical challenges associated with maintaining and utilizing polarization in a plasma environment. For example, the typical association of spin alignments is with low temperatures, making it counter-intuitive that they could endure in a 10^8 K plasma long enough to have practical applications. On the other hand, a theoretical study[30] of the scaling laws for the depolarization times revealed the feasibility of polarized particle acceleration in strong plasma fields and stimulated dozens of numerical simulation studies of such processes. These all lead to the conclusion that polarized beams from plasma acceleration should be within reach, probably with a simpler implementation for hadronic beams. This is because these have much smaller magnetic moments and, therefore, their spin alignment in the plasma magnetic fields is much more inert as compared to electrons. Also, from the target point-of-view, polarized nuclei can be provided more easily than electrons.

In an experiment at the PHELIX Petawatt laser of GSI Darmstadt (see Fig. 28), the Jülich-Düsseldorf group could now provide first evidence for an almost complete persistence of nuclear polarization after plasma acceleration to MeV energies.[31] For their experiment, the group used an up to 50% polarized ^{3}He gas jet target which was irradiated by 2.2 ps laser pulses containing about 50 J energy each. The polarization measurement of the accelerated ^{3}He ions was achieved with two identical polarimeters, optimized for short ion bunches from plasma acceleration and mounted at an angle of 90° relative to the laser axis. For those cases that the nuclear spins in the target gas were aligned perpendicular to the flight direction of the helium ions, an angular asymmetry of the scattered particles in the polarimeters is observed which is in line with a transversal polarization of the accelerated ^{3}He ions. No such asymmetries were found for the unpolarized gas.

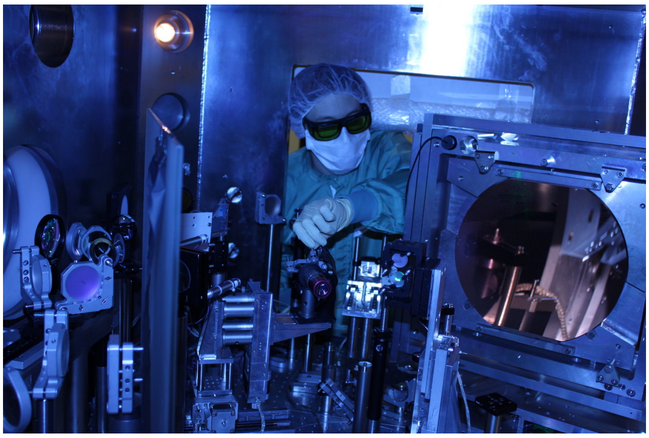

Figure 28: The Petawatt High-Energy Laser for Heavy IOn Experiments (PHELIX) at GSI Darmstadt.

As a next step towards polarized beams, it is planned to repeat the experiments at PHELIX at higher gas polarization and using a shorter (0.5 mm instead of 1.0 mm) gas-jet target. This would have the advantage that the ^{3}He ions are dominantly emitted under 0° and at significantly higher energies (10–15 MeV). For even higher laser intensities (>10 PW) the group has recently proposed a scheme based on shock acceleration to produce >100 MeV polarized ^{3}He beams.[32] A polarized HCl gas target for laser- or beam-driven acceleration of polarized proton and electron beams is also being developed.

5.2 A new Method to generate Hyperpolarization

Particles with a hyperfine structure passing through a static, but oscillating magnetic field of two opposite coils experience in their rest system a monochromatic and coherent incoming electromagnetic pulse. The energy of the corresponding photons is $E_{ph} = h \cdot v/\lambda$, where λ is defined by the distance of the coils and v is the veloc-

[29] Phys. Plasmas 21 023104 (2014), CERN Courier April 2014, High Power Laser Science and Engineering 8, e36 (2020)

[30] Phys. Rev. AB 23, 064401 (2020)

[31] doi: 10.48550/arXiv.2310.04184

[32] doi: 10.48550/arXiv.2309.06271

ity of the beam. This energy is tunable in a wide range from $E_{ph} \sim 10^{-7}$ to 10^{-12} eV. Such photons can induce transitions between the hyperfine substates of the particles which can interfere with each other. By that the occupation numbers of the substates can be manipulated to produce an asymmetry far from thermal equilibrium, i.e. large electron or nuclear polarizations (see Fig. 1). This method is able to generate hyperpolarization to different atoms, molecules and their ions.[33] Meanwhile, an international patent has been applied for under the rules of the Patent Cooperation Treaty (PCT).

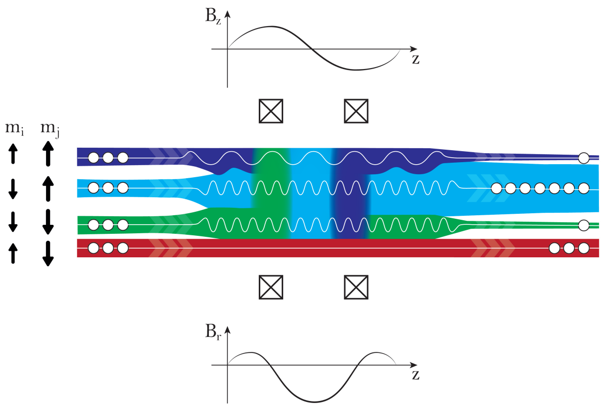

Figure 29: The principle of the new polarization method: An unpolarized atomic hydrogen beam (as a simple example) gets polarized by passing the static magnetic field of two solenoids with opposite field direction. The dominant longitudinal field B_z determines the hyperfine splitting energy in the Breit-Rabi diagram and the radial field B_r induces transitions between the hyperfine substates that can interfere with each other. By that an asymmetry of the occupation numbers can be induced, i.e. a large nuclear or electron polarization.

In the recent months the theoretical understanding of this method was further developed and several aspects that influence the simulations have been investigated experimentally.

1. The occupation numbers of the different hyperfine states in the primary beam have an important influence on the efficiency of the induced transitions, because they can have a constructive or destructive character. Therefore, a resonance can produce a maximum or a minimum of the oscillating occupation numbers when they are measured as function of the magnetic field amplitude.

2. The beam profile has a significant influence on the the strength of the oscillations. The more beam particles are off axis the larger the amplitudes of the oscillations will be. Different beam profiles, a Gaussian or a flat beam profile will produce different structures of the oscillation.

3. This effect can be used to increase the amplitudes of the oscillations even further when the beam and the magnetic field axis are shifted against each other and higher polarization values can be achieved. It should be mentioned that the homogeneity of the magnetic field is decreasing, because in a realistic solenoid the magnetic field strength depends on the radial distance of the beam particles from the magnetic field axes.

4. With different winding numbers of the coils two slightly different wavelengths λ of the radial magnetic field are produced in parallel so that the absorbed photons before and after the zero-crossing can have two different energies. This asymmetric field configuration might allow to induce a nuclear polarization even for different hyperfine structures where the energy-splitting of the substates is equal, e.g. the coupling of the rotational magnetic moment J of a hydrogen/deuterium molecule with the nuclear spins I or the coupling of the nuclear spins of the protons in ortho-water.

The new technique based on radio-wave pumping and quantum interference is theoretically understood and experimentally proven for beams of metastable hydrogen and deuterium atoms. Further tests with beams of $^3He^+$ ions and deuterium atoms in the $1S$ ground state are in progress. In addition, it should be possible to polarize a sample at rest with a corresponding radio wave pulses. A first experiment with molecular hydrogen and deuterium gas and corresponding radio waves at kHz frequencies is being proposed. Here, the hyperfine splitting due to the substates of the nuclear spin coupling with the rotational magnetic moment can be used.
With this rather simple and energy-efficient method several applications are now in range: Besides new types of polarized beams and targets, even for heavy ions, the production of polarized fuel to increase the energy output of fusion reactors is now possible. Another option is the use of hyper-polarized tracers in medicine and maybe a low-field MRI with even better spatial resolution.

6 Theoretical Investigations

6.1 Introduction

The IKP theory group studies the strong interactions in their various settings — spanning topics in hadron structure and dynamics, the nuclear many-body problem, symmetry tests in Quantum Chromodynamics (QCD), physics beyond the Standard Model, strongly correlated electronic systems and brain dynamics. The first focus of the theory group is the formulation and application of effective field theories for precision hadron and nuclear physics based on the symmetries of QCD. The second focus is related to high performance computing in

[33] German Patent: Aktenzeichen DE102022213860.0

nuclear, hadronic and condensed matter physics, spearheaded by the work on nuclear lattice simulations. Since July 2012, the group is heavily involved in the activities of the collaborative research center "Symmetries and the emergence of structure in QCD" (CRC 110) together with researchers from Bonn University, TU München, Ruhr-Universität Bochum, IHEP/CAS (Beijing, China), ITP/CAS (Beijing, China) and Peking University (China). This CRC is presently in its third and final funding period. A further strengthening of the group was achieved through the ERC Advanced Grant "EXOTIC" that began in November 2021. It focuses on precision calculations in nuclear and hypernuclear physics on the lattice as well as exploring fine-tunings in nuclear reactions and the role of anthropic considerations. Since 2022, the IKP theory group is also involved in the NRW-FAIR network funded by the ministry of culture and science of the state of North Rhine-Westphalia. Some of the high-lights of all of these activities are discussed in the following.

6.2 The puzzling ^{4}He transition form factor

The ^{4}He nucleus, the α-particle, is considered to be a benchmark nucleus for our understanding of the nuclear forces and the few-body methods to solve the nuclear A-body problem. The attractive nucleon-nucleon interaction makes this highly symmetric four-nucleon system enormously stable. Furthermore, its first excited state has the same quantum numbers as the ground state, $J^P = 0^+$ with $J(P)$ the spin (parity), but is located about 20 MeV above the ground state. This large energy of the first quantum excitation makes the system difficult to perturb. This isoscalar monopole resonance of the ^{4}He nucleus presents a challenge to our understanding of nuclear few-body systems and the underlying nuclear forces, as the recent precision measurement of the corresponding transition form factor of the first excited state to the ground state at the Mainz Microtrom MAMI compared with *ab initio* calculations based on the Lorentz-integral transformation method using phenomenological potentials as well as potentials based on chiral effective field theory revealed sizeable discrepancies.

Therefore, we used the framework of nuclear lattice effective field theory (NLEFT) to present an *ab initio* solution to the problem. In particular, we addressed the issue whether one possibly misses parts of the nuclear force which, given a simple spin-0 and isospin-0 nucleus like ^{4}He, would be rather striking. To be precise, we utilized the so-called minimal nuclear interaction, that has been successfully used to describe the gross properties of light and medium-mass nuclei and the equation of state of neutron matter to a few percent accuracy. It was also used in nuclear thermodynamics calculations and *ab initio* studies of clusters in hot dilute matter using the method of light-cluster distillation. A similar action was also successfully applied to investigate the emergent geometry and intrinsic cluster structure of the low-lying states of ^{12}C. In particular, the transition form factor from the Hoyle state to the ground state measured at Darmstadt could be excellently reproduced without any parameter adjustment.

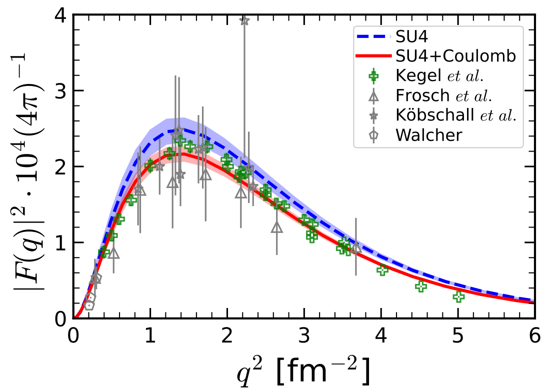

Figure 30: Calculated monople form factor of the $0_2^+ \to 0_1^+$ transition in ^{4}He compared to the recent data from Mainz (green squares) and the older data (grey symbols). Blue dashed line: SU(4) symmetric strong interaction with all parameters determined in 2018. Red solid line: adding the Coulomb interaction perturbatively. The uncertainty bands in the lattice results include stochastic errors and uncertainties in the Euclidean time extrapolation.

The first excited state of ^{4}He is a resonance that sits just above the ^{3}H$+p$ threshold. In order to study this continuum state, we perform calculations using three different cubic periodic boxes with lengths $L = 10, 11, 12$ in lattice units, corresponding to $L = 13.2$ fm, 14.5 fm, 15.7 fm. We can describe the ^{4}He ground state and its first excited state with good precision, which is a prerequisite for calculating the transition form factor. In fact, we find $\Delta E = E(0_2^+) - E(^3\mathrm{H}) = 0.40(9)$ MeV, completely consistent with the experimental value of 0.40 MeV. The transition form factor $F(q)$ was computed using the pinhole algorithm while the Coulomb interaction was treated using perturbation theory. Consider first the SU(4)-symmetric interactions without Coulomb. The resulting form factor is depicted by the blue dashed line in Fig. 30. It somewhat overshoots the data, although the error band associated with stochastic errors and the large L_t extrapolation almost encompasses the data. Including the Coulomb interaction leads to an overall reduction of the transition form factor as shown by the red solid band in Fig. 30. Overall, we achieve a good reproduction of the data and the uncertainty band is also somewhat reduced. This is due to the fact that inclusion of the Coulomb interaction leads to smaller fluctuations in the Monte Carlo data when extrapolating to large L_t. Thus, the nuclear forces relevant to this system are under good control, different to what was speculated by the Mainz people.

6.3 The electromagnetic fine-structure constant in primordial nucleosynthesis revisited

As is well known, primordial or Big Bang nucleosynthesis (BBN) is a fine laboratory to test our understanding of the fundamental physics describing the generation of the light elements. In particular, it sets bounds on the possible variation of the parameters of the Standard Model of particle physics as well as the Standard Model of cosmology. Here, we are interested in bounds on the electromagnetic fine-structure constant α derived from the element abundances in primordial nucleosynthesis. While this has been considered before, we have focussed largely on the nuclear and particle physics underlying the element generation in primordial nucleosynthesis. In particular, we reassess the dependence of the nuclear reactions rates on the fine-structure constant, overcoming on one side certain approximations made in the literature and on the other side providing new and improved parameterizations for the most important reactions in the reaction network, using modern determinations of the ingredients whenever possible, such as the Effective Field Theory (EFT) description of the leading nuclear reaction $n+p\to d+\gamma$ and the calculation of the nuclear Coulomb energies based on Nuclear Lattice Effective Field Theory. For β-decays, we also use up-to-date information on the neutron-proton mass difference $\delta_{mn}^{\mathrm{EM}}$ based on dispersion relations (Cottingham sum rule). Most importantly, we utilize five different publicly available codes for BBN to address the systematic uncertainties related to the modelling of the BBN network. To address the possible variation of α, we went beyond certain approximations done in the literature, in particular using the full S-wave penetarton factors for charged particles in the initial and/or final states as well as the temperature-dependence of the modified reaction rates. All five programs were modified to account for the novel parametrizations of the leading 18 reactions in the network, the new value of the electromagnetic contribution to the neutron-proton mass difference $\delta_{mn}^{\mathrm{EM}}$ and the modifications of the Q-values due to the modified nuclear Coulomb energies. Considering variations of $|\delta\alpha/\alpha| \leq 0.1$, the main findings are: 1) the temperature-dependence of reaction rates at varying α is important, 2) for most elements, the change in the nuclear reaction rates is the biggest effect, 3) the ^{4}He abundance is indeed very sensitive to $\delta_{mn}^{\mathrm{EM}}$, and 4) the so-called lithium problem persists. We find that the α-dependence of the abundances is independent from the five codes and from the ^{4}He mass fraction we can deduce from the 1σ band of the measured value the allowed α-variation, leading to $|\delta\alpha| \leq 1.8\%$, see Fig. 31. These bounds are stronger than the ones found in earler work which can be traced back to 1) the updated experimental values for masses, constants, and the smaller $\delta_{mn}^{\mathrm{EM}}$, 2) different reaction rates due to cross section parametrizations, and 3) the improved treatment of the temperature-dependence of the corrections due to $\delta\alpha$. A similar investigation to assess bounds on variations of the light quark masses from the element abundances in BBN is underway.

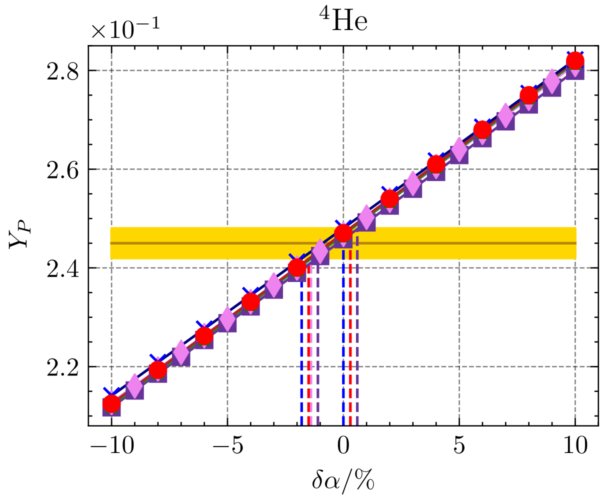

Figure 31: α-dependence of the ^{4}He mass farction Y_p for 5 BBN codes (various symbols) compared to the experimenatlly determined value (black line) and its uncertainty (yellow band).

6.4 Uncertainty of Λ separation energies

For a thorough understanding of neutron matter in, i.e., neutron stars, it is important to get further constraints on their hyperon content. To this aim, additional information on hyperon-nucleon (YN) interactions is needed.
The YN interaction (Y=Λ, Σ) is difficult to determine accurately because there are only very few low-energy scattering data. Fortunately, several bound states of Λ hyperons and nuclei, so called hypernuclei, have been identified. A comparison of theoretical predictions and experiment for these hypernuclei provide important additional information on the YN interaction. In order to fully exploit this information, it is of utmost importance that the uncertainty of the theoretical predictions are carefully examined.
In the previous years, we have developed a set of chiral YN interactions which can be systematically improved in an order by order expansion. So far, YN interactions up to next-to-next-to-leading order (N^{2}LO) have been implemented. In this order, first hyperon-nucleon-nucleon (YNN) three-baryon forces appear which are formulated and currently added to our simulation codes. Corresponding nucleon-nucleon (NN) and three-nucleon (3N) interactions are available up to even higher orders and routinely used.
In a new publication, building up on these interactions, we have now carefully analyzed the uncertainties of our theoretical predictions for light hypernuclei up to $A = 5$. First, we studied the numerical uncertainties and checked the results by benchmarking Jacobi no-core

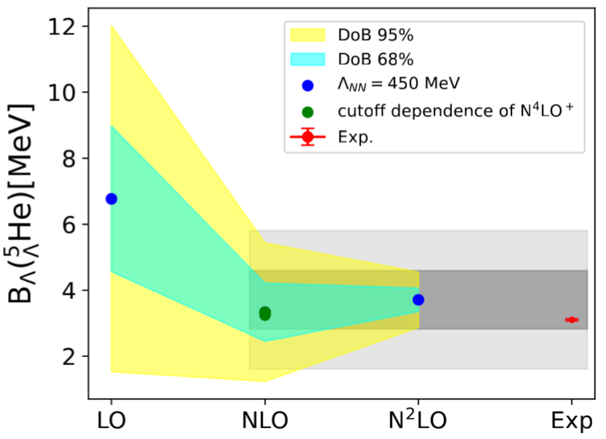

Figure 32: Convergence of the Λ-separation energy of $^{5}_{\Lambda}$He with respect to the chiral order of the YN interaction.

shell model (J-NCSM) and Faddeev-Yakubovsky results. For the J-NCSM, the predictions for the energies are improved by extrapolating to large harmonic oscillator model spaces. The two very different approaches to solve the Schrödinger equation numerically gave very similar results and confirmed that the numerical uncertainties of the solutions are well under control and of minor importance. Especially, we ensured that the extrapolations are reliable.

For the J-NCSM, a Similarity Renormalization Group (SRG) evolution of the interactions is employed to mitigate numerical uncertainties. This step of the calculations could in principle also be a source of uncertainty since we only take induced two- and three-baryon interactions into account. However, based on different choices for the SRG evolution parameters, we showed that also these uncertainties can be safely neglected.

We then quantified the uncertainties due to our limited knowledge on nuclear and hypernuclear interactions by performing calculations in all orders for which NN, 3N and YN interactions are available. Bases on a Bayesian analysis of the results, it was possible to extract reliable uncertainties due to the missing higher order contributions. For the lightest existing hypernucleus, the $^{3}_{\Lambda}$H, these uncertainties are already significantly smaller than the experimental one which justifies to use $^{3}_{\Lambda}$H to determine the spin dependence of YN interactions. For $A = 4$ and $A = 5$ hypernuclei, the uncertainties are larger than the experimental ones as can be seen in Fig. 32. In this case, the N^{2}LO contributions are significant and taking the leading-order YNN interactions into account will be important to make full use of the available experimental information. The results also indicate that uncertainties due to higher order ordinary nuclear interactions are small. Therefore, the hypernuclear binding energies are an excellent source of information on hypernuclear interactions.

6.5 On the nature of N^* and Δ resonances via coupled-channel dynamics

The nature of the inner structure of particles has always been one of the fundamental questions in physics. In hadron physics, the tasks amounts to determining the elementariness or compositeness of an object, i.e. whether it is a compact state formed directly by quarks and gluons, or a hadronic molecule generated from the meson-baryon interaction. Especially in the case of the instable baryonic resonances, the study is complicated by the involved underlying dynamics and the observation that most resonance states are broad and overlapping.

Weinberg's criterion relates the elementariness $Z\,(\varepsilon\,[0,1])$ to the scattering length and the effective range of a state. The experimental determination of those values showed that the deuteron has a small value of Z, i.e. it is a composite state formed by two nucleons. A direct application of Weinberg's criterion to other, excited states, however, is not possible without model assumptions or approximations, because the particle in question has to be an S-wave stable bound state near a two-body threshold, conditions that are not met by the many new hadronic states observed in the last decades. The naive quark model fails to describe certain resonances as, e.g., the Roper $N(1440)$, which indicates a non-trivial and possible molecular nature for some of those states. A generalization of the concept of elementariness or compositeness for excited baryons, however, does not exist but is urgently needed. Several methods have been developed so far, one of them being the "spectral density function" approach, where the spectral density function $w(z)$ is the projection of the physical scattering state (with energy z) on the bare elementary state. The elementariness Z for the resonance can be obtained by collecting the function $w(z)$ near the pole mass M_R of the resonance: $Z \simeq \int_{M_R-\Delta E}^{M_R+\Delta E} w(z)\,dz$ with ΔE a quantity comparable with the pole width.

In a recent work, we adapted and applied the spectral density function method to the framework of the so-called Jülich-Bonn model, a dynamical coupled-channel approach where the baryon resonance states are extracted from simultaneous fits to several pion- and photon-induced reactions based on a large experimental data base (∼100.000 data points). Due to the large numerical effort the corresponding simulations are running on the supercomputer JURECA at JSC. The Jülich-Bonn analysis constitutes one of the theoretically best founded tools to determine the spectrum of light baryons. 13 significant states were studied with respect to the inner composition, for 8 of those it was possible to draw relatively certain conclusions: the $N(1535)1/2^-$, $N(1440)1/2^+$, $N(1710)1/2^+$, and $N(1520)3/2^-$ tend to be composite; whereas the $N(1650)1/2^-$, $N(1900)3/2^+$, $N(1680)5/2^+$, and $\Delta(1600)3/2^+$ tend to be elementary. In Fig. 33 selected results for different spectral density functions are shown.

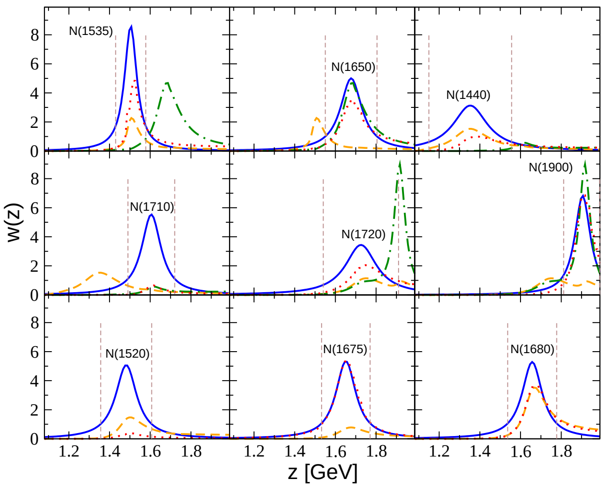

Figure 33: Spectral density functions for selected N^* states. Blue solid line: Breit-Wigner denominator at the pole position. Orange dashed (green dash-dotted) line: spectral density function of the 1st (2nd) bare s-channel resonance from the model. Red dotted line: locally constructed function. A distinct peak structure at the same position in the red, the blue and either the orange or green line indicates a compact state.

6.6 Role of left-hand cut contributions on pole extractions from lattice data: Case study for the $T_{cc}(3875)^+$

Lattice QCD provides a crucial link between QCD and hadron physics in particular for exotic mesons in the heavy quark sector, where direct scattering experiments are not possible. A common approach for those systems is to feed tailor made lattice energy levels into a Lüscher-type formula to extract phase shifts and from those information about the hadronic states present in the system. For the last step often the effective range expansion (ERE) is employed, where the real part of the inverse T-matrix is expanded in a Taylor series according to $p\cot\delta = 1/a + rp^2/2 + O(p^4)$. A bound (virtual) state is contained in the T-matrix, if $p\cot\delta$ equals $-ip$ (ip). This technique was also employed recently to extract information on the $T_{cc}(3875)^+$ from lattice data on DD^* scattering at $M_\pi = 280\,\text{MeV}$. The lattice data as well as the corresponding ERE fit are shown in Fig. 34 as the grey line together with its uncertainty band. Thus, this analysis gave that for that pion mass the T_{cc} appears as a virtual state 9.9 MeV below threshold, which refers to $(p_0/E_{D^*D})^2 = -0.0012$, with E_{D^*D} for the D^*D threshold.

However, at the mentioned unphysical pion mass the D^* has just turned stable, contrary to the physical situation where the D^* can decay into πD. In such a situation the πDD intermediate state, which is part of the D^*D scattering potential, generates a left-hand cut which is located approximately at $(p_{\text{lhc}}^{1\pi})^2 \approx [(\Delta M)^2 - M_\pi^2]/4$, where $\Delta M = M_{D^*} - M_D$. For the given small pion mass it is

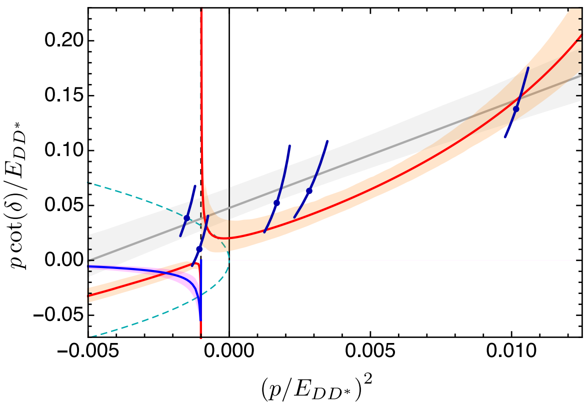

Figure 34: Fit results for the lattice data. The solid and dashed vertical lines indicate the DD^* threshold and the lhc, respectively, while the green dashed curve shows the function $\pm ip$. The gray line and gray band show the fit and its 1σ uncertainty, respectively, using the ERE formula in the entire energy range. The red solid line and the orange band show the best fit and its 1σ uncertainty, respectively, calculated in this work.

thus located very close to the D^*D threshold, namely at $(p_{\text{lhc}}^{1\pi}/E_{D^*D})^2 = -0.0010$. It is shown as the black dashed line in Fig. 34. Thus the left-hand cut is located in between the mentioned T-matrix pole and the threshold! Since this left-hand cut sets the radius of convergence for the ERE (and also prohibits using the Lüscher formula in its standard form), employing it to extract the location of the T-matrix pole is not justified for these kinematics. Instead we employed an amplitude that we developed recently for D^*D scattering in the analysis that contains the full dynamics of the one-pion exchange. Accordingly $p\cot\delta$ is no longer linear in p^2 but can have a pronounced curvature close to the location of the left-hand cut. The result of our fit to those parts of the lattice data that are located above the left-hand cut (including the part of the uncertainty of the second data point from the left that reaches above the cut) are shown as the red line in Fig. 34. Thus, based on the best fit this analysis suggests that instead of one virtual pole the lattice data point at two poles, squeezed in between the left-hand cut and the D^*D threshold. Note that within uncertainties the data are also consistent with the presence of a narrow resonance. Clearly, what is presented here cannot be the final analysis at the given pion mass as it is not clear how the necessary modificatiomss of the Lüscher formula will impact the extracted phase shifts.

6.7 Using the D-wave quantum annealer to simulate gauge theories in the strong coupling limit

Lattice gauge theories in the strong coupling regime can be formulated in dual variables which are integer-valued.

This is especially true for lattice QCD. Theories in this limit can be efficiently simulated at modest finite temperatures and finite densities via the worm algorithm, circumventing the finite density sign problem in this regime. However, the low temperature regime is much more difficult and requires an alternative formulation. Since the partition function is solely expressed in terms of integers, it can be cast as a combinatorial optimization problem that can, in principle, be mapped onto a quantum annealer. During the past year we demonstrated how such a formalism can be achieved using the quadratic binary optimization (QUBO) formalism, which allowed the problem to be setup on a quantum annealer, and in particular the D-Wave Advantage™ system at Forschungszentrum Jülich.

The D-Wave quantum annealer consists of an array of superconducting metal loops with Josephson junctions that act as two-state quantum qubits. The qubits are then inductively paired with other qubits to form D-Wave's quantum processing unit (QPU). The inductances between qubits, as well as the intrinsic inductance within each qubit, can be tuned *in situ*. The array of qubits can then be modelled as an Ising spin glass. By application of an external magnetic field, the D-Wave can evolve a system from the (near) ground state of the transverse Ising model (which is simple to set up) to the target Hamiltonian that represents the system under investigation. If this evolution is done slowly enough, i.e. *adiabatically*, then the system remains in the ground state throughout the evolution. This is known as quantum annealing. On D-Wave the annealing lasts on the order of 100 μsecs.

In practice we find that the quantum annealer rarely evolves to the ground state of the target Hamiltonian. However, it is easy to repeat the annealing thousands of times due to the relatively short annealing profile, thereby generating a distribution of solutions. This distribution of solutions, after appropriate reweighting, follows the desired Boltzman distribution $\sim e^{-Ht}$, which in turn allows us to calculate observables statistically, as is done readily in Monte Carlo calculations

As a proof of concept, we calculated select observables on D-Wave for the gauge groups U(1), U(3), and SU(3). In Fig. 35 we show the results for the chiral condensate and baryon density as a function of chemical pontential $a\mu$ for a small 2x2 SU(3) system. The small size of the lattice allows us to benchmark D-Wave's results with known analytic results. One sees that D-Wave's raw results are nowhere near the analytic results, but after reweighting the results agree extremely well. These results demonstrate how quantum annealing can be used for low-temperature simulations of gauge theories in the strong coupling limit.

Ultimately we will push our simulations to larger lattices and even longer time extents, with the goal of investigating the critical point in the strong coupling regime.

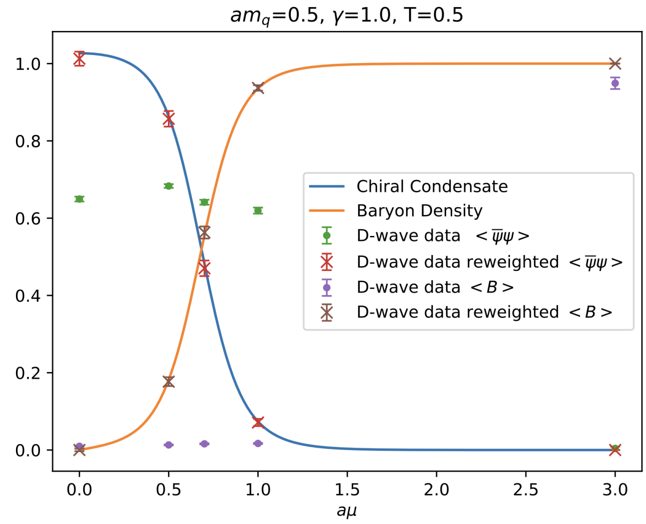

Figure 35: The chiral condensate (blue) and baryon density (orange) as a function of the chemical potential $a\mu$ at quark mass $am_q = 0.5$, and temperature $T = 1.0$ on 2×2 SU(3) lattice. The circle points are D-wave raw data and the cross points are reweighted data.

6.8 Exact lattice chiral symmetry in 2d gauge theory

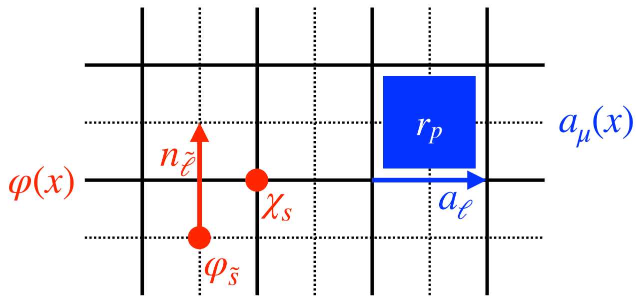

Figure 36: Putting electrodynamics on a two-dimensional grid while maintaining all the desired symmetries entails splitting the bosonic matter φ into three fields (red) and the electromagnetic fields into two fields (blue). Some ingredients live on the vertices of the lattice, while others live on the edges and faces.

The light quarks that comprise protons, neutrons, and other particles, are very nearly massless. Thus, the Standard Model contains approximately massless (chiral) fermions. In the limit that these masses vanish, it is a chiral gauge theory where left- and right-handed fermions behave differently. So, it is important to have numerical methods which can correctly handle light fermions: to make approximation-free computer simulations requires getting chiral symmetry right in the continuum limit where the discretization of spacetime used in the simulations computing is unimportant. The problem of discretizing quantum field theories with fermions in a way that preserves their symmetries has been a key challenge in particle physics, nuclear physics, and condensed matter physics since the 1970s.

Chiral fermions in particular are notoriously difficult to discretize. The Nielsen-Ninomiya no-go theorem asserts that the usual approach to computer simulations must give up either locality, chiral symmetry, or suffer from extra unwanted particles in a way that spoils the anomaly—the way quantum mechanics effects the chiral symmetry.

There are various routes around this roadblock. Different discretizations make different choices, but all agree in the continuum limit, as large-scale computer simulations demonstrate. However, the inability to match the anomaly makes it very difficult to formulate a chiral gauge theory where the left- and right- handed fermions behave differently.

In some special theories, however, it is possible to circumvent the Nielsen-Ninomiya theorem entirely. In particular, we avoid discretizing the fermions at all. In two spacetime dimensions we can completely trade the fermions for bosonic matter with specially-chosen behavior. Because the trade is exact we can imagine simulating the bosons and extracting answers that tell us about systems of fermions.

Most remarkably, by reframing simulations in these terms we found a discretization that enjoys all three desirable features: locality, chiral symmetry, and is free from any extra particles. We had to use recently-developed lattice differential geometry to ensure we maintained all the desired symmetries.

We applied this technique to two-dimensional electrodynamics with one and two species of fermions. But that's not all—we can match the anomaly, even at finite lattice spacing. This opens the door to a construction of chiral gauge theories! We found that we could also construct a large class of two-dimensional chiral gauge theories with all the symmetries that we want in the continuum limit. We also designed algorithms for their simulation.

The success of these techniques unlocks new directions for real computer simulations and the ability to address previously-unanswerable questions about chiral gauge theories. We are excited by the prospects for the future!

A Beam Time at COSY in 2023

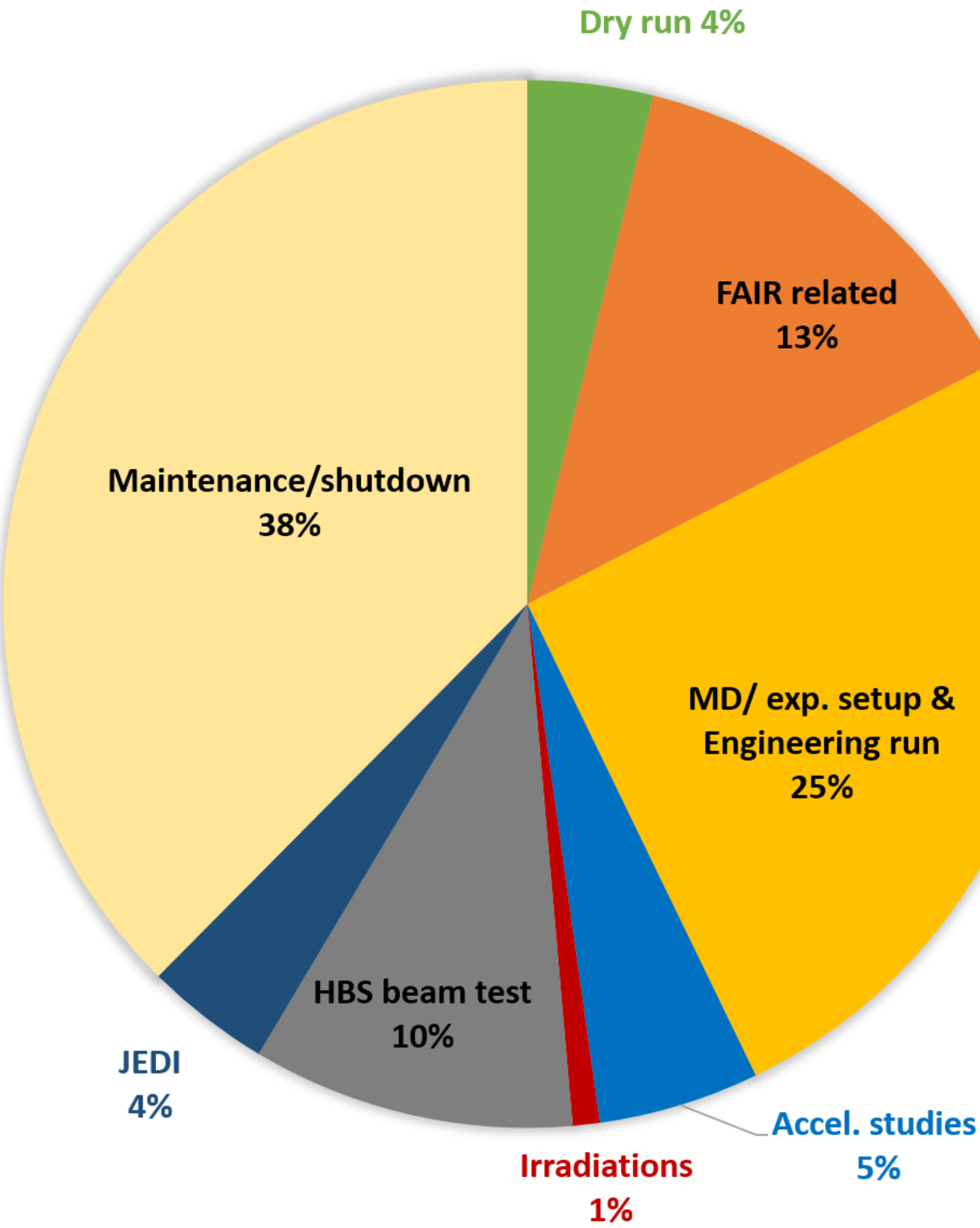

Figure 37: COSY beam-time statistics in 2023.

The distribution of user weeks and maintenance/shutdown periods is listed in Table 1.

Table 1: Overview COSY user beam time and EDM/FAIR weeks in 2023.

Date	Experiment	Duration	Comments
1.01.23–12.03.23	Shutdown	10 weeks	
13.03.–26.03.	Dry run	2 weeks	
27.03.–22.04.	Shutdown & Maintenance	4 weeks	
23.04.–30.04.	Engineering run HBS		
03.05.–03.05.	Proton Irradiation Studies of SiPMs	1 day	H^-, 294 MeV/c from JULIC
04.05.–07.05.	COSY Injection studies	4 days	H^-, p, 294 MeV/c, JULIC -> COSY
08.05.–14.05.	MD Ay measurement of elastic pp-scattering	1 week	unpolarized and polarized p, 1950 MeV/c, COSY ring & T
15.05.–21.05.	HBS	1 week	H^- 294 MeV/c
22.05.–28.05.	RF knock-out extraction & spill control & CBM/HADES	1 week	p, 1000 MeV/c, COSY ring and NEMP area
29.05.–06.06.	MD Ay measurement of elastic pp-scattering	9 days	unpolarized and polarized p, 1950 MeV/c
07.06.–11.06.	HBS	5 days	H^- 294 MeV/c
12.06.–18.07.	MD JEDI	1 weeks	unpolarized p
19.06.–02.07.	JEDI	2 weeks	unpolarized p, 970 MeV/c, 321 MeV/c, e-cooling, Wien fi
03.07.–09.07.	MD SBM/HADES, R3B, PANDA Forward Endcap Calorimeter	1 week	p, 2740 MeV/c
10.07.–16.07.	RF knock-out extraction & spill control	1 week	p, 1000 MeV/c
17.07.–23.07.	R3B/SFRS	1 week	p, 450 MeV/c, 1000 MeV/c, 1700 MeV/c, TOF area
24.07.–24.07.	Irradiation for INM	1 day	H^-, 294 MeV/c
25.07.–06.08.	HBS	2 weeks	H^- 294 MeV/c
07.08.–13.08.	PANDA Forward Endcap Calorimeter	1 week	p, 2740 MeV/c, TOF area
14.08.–20.08.	MD PANDA Cluster Jet Target	1 week	p, 3000 MeV/c, st. cooling
21.08.–28.08.	PANDA Cluster Jet Target	1 week	p, 3000 MeV/c, st. cooling
29.08.–03.09.	HBS	1 week	H^- 294 MeV/c
04.09.–07.09.	PANDA Cluster Jet Target	4 days	p, 3000 MeV/c
08.09.–14.09.	MD & PANDA Forward Endcap Calorimeter	1 week	
15.09.–18.09.	CBM/HADES	4 days	p, 2740 MeV/c
19.09.–28.09.	MD Ay measurement of elastic pp-scattering	1week	unpol. and polazied p, 1950 MeV/c
29.09.–03.10.	Ay measurement of elastic pp-scattering	5 days	polazied p, 1950 MeV/c
04.10. –04.10.	Irradiation		H^-, 294 MeV/c, JULIC
07.10.–12.11.	MD JULIC & 3He+	5.3 weeks	
13.11.–03.12.	Maintenance & Shutdown		
04.12 –15.12	MD & HBS	2 weeks	HH^- 294 MeV/c
16.12.–31.12.2023	Shutdown		
User weeks 2023		17 weeks	
MD/Engineering run		13 weeks	
Shutdown		22 weeks	

B Committees

B.1 CBAC – COSY Beam Time Advisory Committee

Prof. K. Aulenbacher	Universität Mainz, Germany
Prof. O. Kester	TRIUMF, Canada
Prof. C.J. Schmidt	GSI Darmstadt, Germany
Prof. T. Stöhlker	HI-Jena, Jena, Germany
Prof. M. Weber (chair)	KIT, Karlsruhe, Germany

B.2 Committee Service

A. Andres	-	Representative Young Scientists IKP
	-	IKP Internal Steering Committee (ILA), FZ-Jülich GmbH, Germany
C. Böhme	-	Representatives' Assembly (WTV), FZ-Jülich GmbH, Germany
	-	IKP Internal Steering Committee (ILA), FZ-Jülich GmbH, Germany
O. Felden	-	WTR (Scientific and Technical Council), FZ-Jülich GmbH, Germany
	-	Representatives' Assembly (WTV), FZ-Jülich GmbH, Germany
	-	IKP Internal Steering Committee (ILA), FZ-Jülich GmbH, Germany
R. Gebel	-	International Organising Committee (IOC) of the International Conference on Cyclotrons and their Applications (CYC23 - CYC25)
	-	European Physical Society - Accelerator Group (EPS-AG), 2023 - 2029
	-	Organization and Scientific Committee (OC, SC), International Particle Accelerator Conference (IPAC'25), Taipei, Taiwan, June 1 - 6, 2025
	-	TransFAIR delegate, HGF Programme "Matter and Technologies -Accelerator Research and Development MT-ARD"
	-	WTR (Scientific and Technical Council), FZ-Jülich GmbH, Germany
F. Goldenbaum	-	Chair of the PANDA at FAIR collaboration board
	-	WTR (Scientific and Technical Council), FZ-Jülich GmbH, Germany
	-	Representatives' Assembly (WTV), FZ-Jülich GmbH, Germany
	-	IKP Internal Steering Committee (ILA), FZ-Jülich GmbH, Germany
	-	Scientific Secretary of COSY Beam Advisory Committee (CBAC), FZ-Jülich GmbH, Germany
C. Hanhart	-	Theory advisory Group PANDA
	-	Particle Data Group
	-	Task coordinator (Precision calculations in non-perturbative QCD (I): Effective Field Theories, analyticity and dispersion relations) within STRONG2020
	-	Coordinator FZ contribution to NRW-FAIR
	-	Topical convener (decays) of the Quarkonium Working Group
	-	IKP Internal Steering Committee (ILA), FZ-Jülich GmbH, Germany
V. Hejny	-	WTR (Scientific and Technical Council), FZ-Jülich GmbH, Germany
	-	Representatives' Assembly (WTV), FZ-Jülich GmbH, Germany
	-	IKP Internal Steering Committee (ILA), FZ-Jülich GmbH, Germany
V. Kamerdzhiev	-	COSY Beamtime Advisoty Committee (CBAC), FZ-Jülich GmbH, Germany
	-	IKP Internal Steering Committee (ILA), FZ-Jülich GmbH, Germany
T. Lähde	-	Representatives' Assembly (WTV), FZ-Jülich GmbH, Germany
	-	IKP Internal Steering Committee (ILA), FZ-Jülich GmbH, Germany
A. Lehrach	-	Institutional representative, European Network for Novel Accelerators (EuroNNAc)
	-	Coordination, support and enhancement of training activities for accelerators in Europe, EU project ARIES (Accelerator Research and Innovation for European Science and Society)
	-	Institutional representative, MT Executive Board, HGF Programme "Matter and Technologies"
	-	Scientific Advisory Board, 14^{th} International Particle Accelerator Conference (IPAC'23), May 7 - 12, 2023, Venice, Italy
	-	International Advisory Committee, 6^{th} European Advanced Accelerator Concepts workshop

		(EAAC2023), Sept. 17 – 23, 2023, La Biodola Bay, Isola d'Elba, Italy
	-	CA-D Machine Advisory Committee, Brookhaven National Laboratory, Upton (NY), USA
	-	JuDocs Council, FZ Jülich GmbH, Germany
	-	IKP Internal Steering Committee (ILA), FZ-Jülich GmbH, Germany
	-	Representatives' Assembly (WTV), FZ-Jülich GmbH, Germany
L. Ludhova	-	Institutional Board of Borexino
	-	Steering Committee of Borexino
	-	Physics Coordinator of Borexino
	-	Institutional Board of JUNO
	-	Analysis Coordination Comittee of JUNO
	-	International Advisory Committee of Physics In Collision conferences
	-	International Advisory Panel for The European Spallation Source neutrino Super Beam plus
U.-G. Meißner	-	WTR (Scientific and Technical Council), FZ-Jülich GmbH, Germany
	-	Spokesperson DFG Review Board 309 "Particles, Nuclei and Fields"
	-	Gründungsmitglied der Kommission für Ethik in der Forschung am Forschungszentrum Jülich
	-	Scientific Advisory Committee of the Collaborative Research Center (SFB) 1245, "Nuclei: From fundamental interactions to structure and stars", TU Darmstadt
	-	German/DFG delegate of NuPECC
	-	Project coordinator, Regional Doctoral Program in Theoretical and Experimental Particle Physics (Bonn, Jülich, Siegen, Tiflis, Yerevan), funded by Volkswagen Stiftung
	-	Spokesperson of the Colloborative Research Center SFB/TR-110 "Symmetries and the Emergence of Structure in QCD"
	-	Theory advisory Group PANDA
	-	Particle Data Group
A. Nass	-	Representatives' Assembly (WTV), FZ-Jülich GmbH, Germany
	-	IKP Internal Steering Committee (ILA), FZ-Jülich GmbH, Germany
A. Nogga	-	WTR (Scientific and Technical Council), FZ-Jülich GmbH, Germany
	-	Representatives' Assembly (WTV), FZ-Jülich GmbH, Germany
	-	IKP Internal Steering Committee (ILA), FZ-Jülich GmbH, Germany
J. Pretz	-	Representatives' Assembly (WTV), FZ-Jülich GmbH, Germany
	-	IKP Internal Steering Committee (ILA), FZ-Jülich GmbH, Germany
K. Reimers	-	Representatives' Assembly (WTV), FZ-Jülich GmbH, Germany
	-	IKP Internal Steering Committee (ILA), FZ-Jülich GmbH, Germany
J. Ritman	-	WTR (Scientific and Technical Council), FZ-Jülich GmbH, Germany
	-	Scientific Coordinator of COSY
	-	Co-Chair of the MESON biannual conference series
	-	Chair of the Scientific Advisory Committee for FAIR-CZ
	-	Member of FAIR-RO Scientific Advisory Committee
	-	Co-Spokesperson of KLF (K-Long Facility at Jefferson Lab)
G. Roes	-	IKP Internal Steering Committee (ILA), FZ-Jülich GmbH, Germany
T. Sefzick	-	IKP Internal Steering Committee (ILA), FZ-Jülich GmbH, Germany
T. Stockmanns	-	Computing coordinator PANDA
	-	IKP Internal Steering Committee (ILA), FZ-Jülich GmbH, Germany
H. Ströher	-	IAB KIU (International Advisory Board Kutaisi International University, Georgia)
	-	ISPC (International Spin Physics Committee)
	-	PGSB (Palestinian-German Science Bridge) Advisory Committee

C Publications

C.1 Journal Articles

1. A. Abusleme *et al.*
JUNO sensitivity on proton decay $p \to \nu K^+$ searches*
Chinese Phys. C **47** 113002 - (2023)

2. A. Abusleme *et al.*
The JUNO experiment Top Tracker
Nucl. Instr. Meth. Phys. Res. A **1057** 168680 - (2023)

3. A. Abusleme *et al.*
JUNO sensitivity to the annihilation of MeV dark matter in the galactic halo
J. Cosmol. Astropart. P. **2023** 001 - (2023)

4. A. Abusleme *et al.*
JUNO sensitivity to 7 Be, pep, and CNO solar neutrinos
J. Cosmol. Astropart. P. **2023** 022 - (2023)

5. S. Adhikari *et al.*
Measurement of the J/ψ photoproduction cross section over the full near-threshold kinematic region
Phys. Rev. C **108** 025201 (2023)

6. S. Adhikari *et al.*
Measurement of spin-density matrix elements in ρ (770) production with a linearly polarized photon beam at E γ = 8.2 - 8.8 GeV
Phys. Rev. C **108** 055204 (2023)

7. H. Akdag, B. Kubis and A. Wirzba
C and CP violation in effective field theories
J. High Energ. Phys. **2023** 154 (2023)

8. H. Alharazin *et al.*
Local spatial densities for composite spin-3/2 systems
J. High Energ. Phys. **2023** 163 (2023)

9. S. Appel *et al.*
Independent determination of the Earth's orbital parameters with solar neutrinos in Borexino
Astropart. Phys. **145** 102778 (2022)

10. A. Asokan *et al.*
Can the two-pole structure of the $D_0^*(2300)$ be understood from recent lattice data?
Eur. Phys. J. C **83** 850 (2023)

11. H. Avakian *et al.*
Observation of Correlations between Spin and Transverse Momenta in Back-to-Back Dihadron Production at CLAS12
Phys. Rev. Lett. **130** 022501 (2023)

12. A. Awal *et al.*
Optimization of the injection beam line at the Cooler Synchrotron COSY using Bayesian Optimization
J. Instrum. **18** P04010 - (2023)

13. V. Baru *et al.*
Emergence of heavy quark spin symmetry breaking in heavy quarkonium decays
Phys. Rev. D **107** 014027 (2023)

14. D. Basilico *et al.*
Borexino's search for low-energy neutrinos associated with gravitational wave events from GWTC-3 database
Eur. Phys. J. C **83** 538 (2023)

15. D. Basilico *et al.*
Final results of Borexino on CNO solar neutrinos
Phys. Rev. D **108** 102005 (2023)

16. T. Chetry *et al.*
First Measurement of Λ Electroproduction off Nuclei in the Current and Target Fragmentation Regions
Phys. Rev. Lett. **130** 142301 (2023)

17. G. Christiaens *et al.*
First CLAS12 Measurement of Deeply Virtual Compton Scattering Beam-Spin Asymmetries in the Extended Valence Region
Phys. Rev. Lett. **130** 211902 (2023)

18. S. Diehl *et al.*
First Measurement of Hard Exclusive π - Δ + + Electroproduction Beam-Spin Asymmetries off the Proton
Phys. Rev. Lett. **131** 021901 (2023)

19. S. Diehl *et al.*
A multidimensional study of the structure function ratio $\sigma_{LT'}/\sigma_0$ from hard exclusive π^+ electro-production off protons in the GPD regime
Phys. Lett. B **839** 137761 - (2023)

20. M. Du *et al.*
Role of Left-Hand Cut Contributions on Pole Extractions from Lattice Data: Case Study for T c c (3875) +
Phys. Rev. Lett. **131** 131903 (2023)

21. S. Gazagnes *et al.*
Reconstructing charged-particle trajectories in the PANDA Straw Tube Tracker using the LOcal Track Finder (LOTF) algorithm
Eur. Phys. J. A **59** 100 (2023)

22. F. Guo *et al.*
New insights into the nature of the $\Lambda(1380)$ and $\Lambda(1405)$ resonances away from the SU(3) limit
Phys. Lett. B **846** 138264 - (2023)

23. J. Haidenbauer *et al.*
Hyperon-nucleon interaction in chiral effective field theory at next-to-next-to-leading order
Eur. Phys. J. A **59** 63 (2023)

24. J. Haidenbauer and U. Meißner
$\Lambda\bar{\Lambda}$ final-state interaction in the reactions $e^+e^- \to \phi\Lambda\bar{\Lambda}$ and $e^+e^- \to \eta\Lambda\bar{\Lambda}$
Eur. Phys. J. A **59** 136 (2023)

25. F. Hildenbrand and H. Hammer
Pionic final state interactions and the hypertriton lifetime
Eur. Phys. J. A **59** 280 (2023)

26. M. Hoferichter *et al.*
On the role of isospin violation in the pion-nucleon σ-term
Phys. Lett. B **843** 138001 - (2023)

27. S. Karanth *et al.*
First Search for Axionlike Particles in a Storage Ring Using a Polarized Deuteron Beam
Phys. Rev. X **13** 031004 (2023)

28. J. Kim, P. Pattanaik and W. Unger
Nuclear liquid-gas transition in the strong coupling regime of lattice QCD
Phys. Rev. D **107** 094514 (2023)

29. J. Kim, T. Luu and W. Unger
U(N) gauge theory in the strong coupling limit on a quantum annealer
Phys. Rev. D **108** 074501 (2023)

30. I. Korover *et al.*
Observation of large missing-momentum $(e,e'p)$ cross-section scaling and the onset of correlated-pair dominance in nuclei
Phys. Rev. C **107** L061301 (2023)

31. A. Kreisel *et al.*
Neutron and isotope production yield from proton and deuteron beams in the 20-45 MeV range on thick liquid gallium-indium and lithium targets
Eur. Phys. J. A **59** 185 (2023)

32. H. Le *et al.*
Ab initio calculation of charge-symmetry breaking in A = 7 and 8 Λ hypernuclei
Phys. Rev. C **107** 024002 (2023)

33. Y. Lin, H. Hammer and U. Meißner
The electromagnetic Sigma-to-Lambda transition form factors with coupled-channel effects in the space-like region
Eur. Phys. J. A **59** 54 (2023)

34. M. Mai *et al.*
Inclusion of $K\Lambda$ electroproduction data in a coupled channel analysis
Eur. Phys. J. A **59** 286 (2023)

35. M. Mai, U. Meißner and C. Urbach
Towards a theory of hadron resonances
Phys. Rep. **1001** 1 - 66 (2023)

36. P. Maris *et al.*
Uncertainties in ab initio nuclear structure calculations with chiral interactions
Front. Phys. **11** 1098262 (2023)

37. U. Meißner, B.C. Metsch and H. Meyer
The electromagnetic fine-structure constant in primordial nucleosynthesis revisited
Eur. Phys. J. A **59** 223 (2023)

38. J.Y. Panteleeva *et al.*
Definition of gravitational local spatial densities for spin-0 and spin-1/2 systems
Eur. Phys. J. C **83** 617 (2023)

39. J.Y. Panteleeva *et al.*
Electromagnetic and gravitational local spatial densities for spin-1 systems
J. High Energ. Phys. **2023** 237 (2023)

40. S.J. Paul *et al.*
Alignment of the CLAS12 central hybrid tracker with a Kalman Filter
Nucl. Instr. Meth. Phys. Res. A **1049** 168032 - (2023)

41. D. Sadasivan *et al.*
New insights into the pole parameters of the $\Lambda(1380)$, the $\Lambda(1405)$ and the $\Sigma(1385)$
Front. Phys. **11** 1139236 (2023)

42. M. Salajegheh *et al.*
Determination of diffractive PDFs from a global QCD analysis of inclusive diffractive DIS and dijet cross-section measurements at HERA
Phys. Rev. D **107** 094038 (2023)

43. A. Sarkar, D. Lee and U. Meißner
Floating Block Method for Quantum Monte Carlo Simulations
Phys. Rev. Lett. **131** 242503 (2023)

44. D. Severt, M. Mai and U. Meißner
Particle-dimer approach for the Roper resonance in a finite volume
J. High Energ. Phys. **2023** 100 (2023)

45. C. Shen, Y. Lin and U. Meißner
P_{cc}^{N} states in a unitarized coupled-channel approach
Eur. Phys. J. C **83** 70 (2023)

46. S. Shen *et al.*
Emergent geometry and duality in the carbon nucleus
Nat. Commun. **14** 2777 (2023)

47. Y. Shi, Z. Xing and U. Meißner
Weak radiative decay $\Lambda_c^+ \to \Sigma^+\gamma$ using light-cone sum rules
Eur. Phys. J. C **83** 224 (2023)

48. R. Skibiński *et al.*
The nucleon-induced deuteron breakup process as a laboratory for chiral dynamics
Front. Phys. **11** 1084040 (2023)

49. J. Slim *et al.*
Quantum mechanical derivation of radio-frequency-driven coherent beam oscillations in storage rings
Phys. Rev. Accel. Beams **26** 014201 (2023)

50. H. Ströher *et al.*
Precision Storage Rings for Electric Dipole Moment Searches: A Tool En Route to Physics Beyond-the-Standard-Model
Part. **6** 385 - 398 (2023)

51. M. Tang *et al.*
Isospin-conserving hadronic decay of the D s1 (2460) into D s π + π -
Commun. Theor. Phys. **75** 055203 - (2023)

52. Y. Tian *et al.*
Exclusive π - electroproduction off the neutron in deuterium in the resonance region
Phys. Rev. C **107** 015201 (2023)

53. Q. Yang *et al.*
New insights into the oscillations of the nucleon electromagnetic form factors
Sci. Bull. **68** 2729 - 2733 (2023)

54. Z. Zhang *et al.*
Revealing the nature of hidden charm pentaquarks with machine learning
Sci. Bull. **68** 981 - 989 (2023)

C.2 Books

1. P. Bechtle, F. Bernlochner, H. Dreiner, C. Hanhart, J. Pretz, J. Jochum and K. Riebe
   Faszinierende Teilchenphysik: Von Quarks, Neutrinos und Higgs zu den Rätseln des Universums
   Springer Berlin Heidelberg (2023)

2. T. Brückel *et al.*
   Technical Design Report HBS Volume 1 – Accelerator
   Verlag Forschungszentrum Jülich GmbH Zentralbibliothek (2023)

D Talks, Colloquia and Proceedings

D.1 Conference and Workshop Contributions

1. A. Andres
   The Search for Electric Dipole Moments of Charged Particles in Storage Rings
   DPG Spring Meeting, Dresden, Germany: 2023-03-20 - 2023-03-24

2. A. Andres
   The Search for Charged Particle Electric Dipole Moments in Storage Rings
   MU Days 2023, Karlsruhe, Germany: 2023-09-14 - 2023-09-15

3. A. Asokan
   Employing Approximate Symmetries for Hidden Pole Extraction
   20th International Conference on Hadron Spectroscopy and Structure, Genova, Italy: 2023-06-05 - 2023-06-09

4. J. Baggemann *et al.*
   Beam dynamics studies for the target beamlines of the high brilliance neutron source
   14th International Particle Accelerator Conference, Venice, Italy: 2023-05-07 - 2023-05-12

5. E. Berkowitz and N. Warrington
   Fermi Gases in Two Dimensions
   The 40th International Symposium on Lattice Field Theory, Batavia, Illinois, USA: 2023-07-31 - 2023-08-04

6. E. Berkowitz
   Scattering Amplitudes from Lattice QCD
   Lattice Practices 2023, Berlin, Germany: 2023-10-11 - 2023-10-13

7. C. Böhme *et al.*
   Current Status of the HESR Beam Instrumentation
   12th Int. Beam Instrum. Conf., Saskatoon, Canada: 2023-09-10 - 2023-09-14

8. C. Böhme *et al.*
   Challenges of the COSY Synchrotron Control System Upgrade to EPICS
   19th Int. Conf. Accel. Large Exp. Phys. Control Syst., Cape Town, South Africa: 9 Oct 2023 - 13 Oct 2023

9. B. Breitkreutz *et al.*
   Improved waveforms for barrier-bucket systems
   14th International Particle Accelerator Conference, Venice, Italy: 2023-05-07 - 2023-05-12

10. T. Brückel *et al.*
    The High Brilliance Neutron Source (HBS) Project for a Next Generation Neutron Research Facility
    Eighth European Conference on Neutron Scattering, TUM Department of Mechanical Engineering and the new Science Congress Center Munich, Germany: 2023-03-19 - 2023-03-23

11. T. Brückel *et al.*
    The High Brilliance neutron Source (HBS): A project for a next generation neutron research facility
    Eighth European Conference on Neutron Scattering, TUM Department of Mechanical Engineering and the new Science Congress Center Munich, Germany: 2023-03-20 - 2023-03-23

12. F. Cuteri *et al.*
    QCD simulations with stabilized Wilson fermions
    High-Performance Computing in Science & Engineering: 26th Results and Review Workshop of the HLRS, Stuttgart, Germany: 2023-10-12 - 2023-10-13

13. R.W. Engels, K. Grigoryev and O. Bilen
    Storage Cell Tests for the Polarized Target at LHCb
    19th Workshop on Polarized Sources, Targets and Polarimetry, Mainz, Germany: 2022-09-26 - 2022-09-30

14. R.W. Engels *et al.*
    Development of polarized sources based on molecular photodissociation
    19th Workshop on Polarized Sources, Targets and Polarimetry, Mainz, Germany: 2022-09-26 - 2022-09-30

15. N. Faatz *et al.*
First test of a polarized $^{3}He^{+}$ ion source
25th International Spin Symposium, Durham, USA: 2023-09-24 - 2023-09-29

16. K. Grigoryev *et al.*
Development of a combined element with an electric and magnetic fields for the JEDI experiment
14th International Particle Accelerator Conference, Venice, Italy: 2023-05-07 - 2023-05-12

17. C. Hanhart
How to identify hadronic molecules by combining results from Lattice QCD, EFTs and Experiment
Accessing and Understanding the QCD Spectra, Seattle, USA: 2023-03-20 - 2023-03-24

18. C. Kannis *et al.*
A universal method to polarize atoms, molecules, and their ions for accelerators, nuclear fusion, or medical applications
25th International Spin Symposium, Durham, USA: 2023-09-24 - 2023-09-29

19. J. Kim, T. Luu and W. Unger
Testing importance sampling on a quantum annealer for strong coupling SU(3) gauge theory
The 40th International Symposium on Lattice Field Theory, Fermilab, USA: 2023-07-31 - 2023-08-04
arXiv

20. J. Kim, T. Luu and W. Unger
Testing importance sampling on a quantum annealer for strong coupling lattice QCD
The 40th International Symposium on Lattice Field Theory, Fermilab, USA: 2023-07-31 - 2023-08-04

21. J. Kim, G. Pederiva and A. Shindler
Scalar content of nucleon with the gradient flow using machine learning
Arbeitstreffen Kernphysik 2023, Schleching, Germany: 2023-02-23 - 2023-03-02

22. H. Kleines *et al.*
Architecture of the control system for the Jülich High Brilliance Neutron Source
19th Biennial International Conference on Accelerator and Large Experimental Physics Control Systems, South African Radio Astronomy Observatory (SARAO), managed by the National Research Foundation (NRF), South Africa: 2023-10-07 - 2023-10-13

23. A. Lehrach *et al.*
High-current accelerator systems for future HBS: HBS Innovationpool Project
9th annual meeting of the programme "Matter and Technologies", Karlsruhe, Germany: 2023-10-09 - 2023-10-11

24. R. Liu *et al.*
Event builder and online monitoring of OSIRIS pre-detector of JUNO
DPG Spring Meeting 2023, Dresden, Germany: 2023-03-20 - 2023-03-24

25. R. Liu
JUNO Experiment: Current Status and Physics
The 28th International Nuclear Physics Conference (INPC 2022), Journal of physics / Conference Series 2586(1), 012135 - (2023)

26. L. Ludhova
JUNO Status and Physics Potential
Phys. Sci. Forum. 2023 (NuFACT 2022) 8 25

27. L. Ludhova
Overview of experimental results on geoneutrinos
International Workshop on Multi-messenger Tomography of the Earth, Paris, France: 2023-07-04 - 2023-07-07

28. L. Ludhova
Neutrino physics with liquid scintillator detectors: the case of Borexino and JUNO
Arbeitstreffen Kernphysik 2023, Schlechinger Bürgerhaus, Schulstraße 4, Switzerland: 2023-02-28 - 2023-03-02

29. L. Ludhova
Solar neutrinos from the CNO fusion cycle: Borexino discovery and implications for the solar physics
International Cosmic Ray Conference, Nagoya, Japan: 2023-07-26 - 2023-08-03

30. Y. Malyshkin
JUNO's Perspective for Geoneutrinos
International Workshop on Multi-messenger Tomography of the Earth, Paris, France: 2023-07-03 - 2023-07-07

31. Y. Malyshkin
JUNO Status and Prospects
XX International Workshop on Neutrino Telescopes, Venice, Italy: 2023-10-23 - 2023-10-27

32. U. Meißner
Recent developments in nuclear lattice EFT
EMMI Workshop and International Workshop XLIX on Gross Properties of Nuclei and Nuclear Excitations on "Effective field theories for nuclei and nuclear matter,", Hirschegg, Austria: 2023-01-15 - 2023-01-21

33. U. Meißner
Hyperon-nucleon scattering at NNLO in chiral EFT
Third International Workshop on the Extension Project for the J-PARC Hadron Experimental Facility, JPARC, Japan: 2023-02-13 - 2023-02-15

34. U. Meißner
Regional Doctoral Training Program in Theoretical andExperimental Particle Physics
Modernizing Doctoral Education in the Caucasus and Central Asia, Tbilisi, Rep of Georgia: 2023-06-11 - 2023-06-12

35. U. Meißner
Hi-Lites from the German Side
The 7th Symposium on "Symmetries and the emergence of Structure in QCD,", Rizhao, Peoples R China: 2023-07-19 - 2023-07-22

36. U. Meißner
Recent Progress in Nuclear Lattice EFT
The 7th Symposium on "Symmetries and the emergence of Structure in QCD,", Rizhao, Peoples R China: 2023-07-19 - 2023-07-22

37. U. Meißner
The Proton radius and its Relatives A.D. 2023
The 25th European Conference on Few-Body Problems in Physics, Mainz, Germany: 2023-07-30 - 2023-08-01

38. U. Meißner
Life on Earth - an Accident?
RDP School and Workshop on Mathematical Physics, Yerevan, Armenia: 2023-08-19 - 2023-08-24

39. U. Meißner
Theory of Hadron Resonances
Conference on High-Energy Physics, Yerevan, Armenia: 2023-09-11 - 2023-09-14

40. U. Meißner
Two topics in strong interactions physics with electromagneticprobes
The 16th International Conference on Meson-Nucleon Physics and the Structure of the Nucleon, Mainz, Germany: 2023-10-15 - 2023-10-20

41. C.I. Morales Reveco
JUNO Sensitivity to Geoneutrinos
MAYORANA School, Modica, Italy: 2023-07-04 - 2023-07-11

42. C.I. Morales Reveco
JUNO Sensitivity to Geoneutrinos
42nd International Conference on Physics in Collision, Arica, Chile: 2023-10-10 - 2023-10-13

43. C.I. Morales Reveco
JUNO Sensitivity to Geoneutrinos
MAYORANA, Modica, Italy: 2023-07-04 - 2023-07-11

44. L. Pelicci
CNO solar neutrinos measurement with Borexino detector: updated combined analysis with directionality constraint
DPG 2023 Spring Meetings, Dresden, Germany: 2023-03-20 - 2023-03-24

45. L. Pelicci
CNO solar neutrino detection with Borexino: directionality measurement and spectral analysis
XX International Workshop on Neutrino Telescopes, Venice, Italy: 2023-10-23 - 2023-10-27

46. J. Pretz *et al.*
Injection Optimization via Reinforcement Learning at the Cooler Synchrotron COSY
14th International Particle Accelerator Conference, Venice, Italy: 2023-05-07 - 2023-05-12

47. J. Pretz
Precision Experiments at Storage Rings: The Search for Axion- like Particles
GSI Symosium, Darmstadt, Darmstadt: 2023-02-27 - 2023-02-27

48. J. Pretz
Axion Searches at Cooler Synchrotron COSY
MU Days, Karlsruhe, Germany: 2023-09-14 - 2023-09-14

49. J. Pretz
Electric Dipole Moment (EDM) searches for leptons and hadrons
Heavy Quarks and Leptons, Mumbai, India: 2023-11-28 - 2023-12-02

50. J. Pretz
Towards experiments with polarized beams and targets at the GSI/FAIR storage rings
FAIR/GSI Research Retreat, Bensheim, Germany: 2023-02-13 - 2023-02-14

51. M. Rifai *et al.*
Atmospheric neutrino reconstruction for the neutrino mass ordering measurement of JUNO
DPG Spring Meeting 2023, Dresden, Germany: 2023-03-20 - 2023-03-24

52. M. Rifai
Status of the Jiangmen Underground Neutrino Observatory to measure Neutrino Mass Ordering
Blois 2023: 34th Rencontres de Blois on "Particle Physics and Cosmology", Blois, France: 2023-05-14 - 2023-05-19

53. M. Rifai
JUNO's prospects for atmospheric neutrinos
International Workshop on Multi-messenger Tomography of the Earth, Paris, France: 2023-07-04 - 2023-07-07

54. M. Rifai
JUNO NMO's sensitivity
Matter and Universe 2023, Karlsruhe, Germany: 2023-09-14 - 2023-09-15

55. M. Rodekamp *et al.*
From Theory to Practice: Applying Neural Networks to Simulate Real Systems with Sign Problems
The 40th International Symposium on Lattice Field Theory, Batavia, Illinois, USA: 2023-07-31 - 2023-08-04
Proc. Sci., SISSA 453 XXX

56. D. Rönchen
The light baryon resonance spectrum in a coupled-channel approach - recent results of the Jülich-Bonn model
The 16th International Conference on Meson-Nucleon Physics and the Structure of the Nucleon, Mainz, Germany: 2023-10-16 - 2023-10-20

57. D. Rönchen
Coupled-channel analyses to extract the baryon resonance spectrum
ECT*-APCTP joint workshop: exploring resonance structure with transition GPDs, Trento, Italy: 2023-08-21 - 2023-08-25

58. S. Siddique, J. Pretz and A. Lehrach
Simulations of Beam Dynamics and Beam Lifetime for the Prototype EDM Ring
Matter and the Universe, Karlsruhe, Germany: 2023-09-14 - 2023-09-15

59. A. Singhal *et al.*
JUNO's sensitivity to 7Be, pep and CNO solar neutrinos and strategy for directional analysis of CNO solar neutrinos in JUNO
DPG Spring Meeting 2023, Dresden, Germany: 2023-03-20 - 2023-03-24

60. A. Singhal
JUNO's sensitivity to 7Be, pep and CNO solar neutrinos
European Physical Society Conference on High Energy Physics, Hamburg, Germany: 2023-08-21 - 2023-08-25

61. A. Singhal
Combined directional and spectral analysis of solar neutrinos from Carbon-Nitrogen-Oxygen fusion cycle with Borexino Experiment
European Physical Society Conference on High Energy Physics 2023, Hamburg, Germany: 2023-08-21 - 2023-08-25

62. A. Singhal
JUNO's sensitivity to 7Be, pep and CNO solar neutrinos
XX International Workshop on Neutrino Telescopes, Venice, Italy: 2023-10-23 - 2023-10-27

63. A. Singhal
JUNO's sensitivity to 7Be, pep and CNO solar neutrinos
European Physical Society Conference on High Energy Physics 2023, Hamburg, Germany: 2023-08-21 - 2023-08-25

64. R. Stassen *et al.*
Kicker for the CR Stochastic Cooling based on HESR Slot-Ring Coupler
14th international Workshop Cool23, Montreux, Switzerland: 2023-10-08 - 2023-10-14

65. T. Stoehlker *et al.*
Towards experiments with polarized beams and targets at the GSI/FAIR storage rings
19th Workshop on Polarized Sources, Targets and Polarimetry, Mainz, Germany: 2022-09-26 - 2022-09-30

66. R. Suvarna *et al.*
Rogowski Beam Position Monitor
19th Workshop on Polarized Sources, Targets and Polarimetry, Mainz, Germany: 2022-09-26 - 2022-09-30

67. Y. Valdau *et al.*
Design and production of the fast HESR-injection kicker magnets
14th International Particle Accelerator Conference, Venice, Italy: 2023-05-07 - 2023-05-12

68. M.C. Vollbrecht *et al.*
Calibration of the JUNO pre-detector OSIRIS
DPG Spring Meeting 2023, Dresden, Germany: 2023-03-20 - 2023-03-24

69. M.C. Vollbrecht
OSIRIS - The online scintillator internal radioactivity investigation system of JUNO
LOW RADIOACTIVITY TECHNIQUES 2022 (LRT 2022): Proceedings of the 8th International Workshop on Low Radioactivity Techniques, Rapid City, United States: 2022-06-14 - 2022-06-17

70. L. von Detten, C. Hanhart and V. Baru
The Y(4230) as a $D_1\bar{D}$ molecule
17th International Workshop on Meson Physics, Cracow, Poland: 2023-06-22 - 2023-06-27

71. M. Westphal *et al.*
Measurement of the occupation number of metastable atoms in the hyperfine-substate β_3 in an atomic hydrogen beam
19th Workshop on Polarized Sources, Targets and Polarimetry, Mainz, Germany: 2022-09-26 - 2022-09-30

72. P. Zakalek *et al.*
JULIC Neutron Platform - the HBS technology development infrastructure
MT Meeting, Karlsruher Institut für Technologie (KIT), Germany: 2023-10-09 - 2023-10-09

73. P. Zakalek *et al.*
The High Brilliance Neutron Source Target Stations
Eighth European Conference on Neutron Scattering, TUM Department of Mechanical Engineering and the new Science Congress Center Munich, Germany: 2023-03-20 - 2023-03-23

74. P. Zakalek *et al.*
JULIC Neutron Platform, a testbed for HBS
10th Annual Meeting of the Union for Compact Accelerator-driven Neutron Sources, Budapest, Hungary: 2023-10-16 - 2023-10-19

D.2 Colloquia

1. E. Berkowitz and N. Warrington
Finding Vortices in the BKT Transition of 2D Fermi Gases
Emergent Phenomena of Strongly-Interacting CFTS, Aspen, CO, USA: 2023-09-03 - 2023-09-17

2. E. Berkowitz and N. Warrington
Finding Vortices in the BKT Transition of 2D Fermi Gases
New York, NY, USA: 2023-09-20

3. E. Berkowitz and N. Warrington
FINDING VORTICES IN THE BKT TRANSITION OF 2D FERMI GASES
UNC, Chapel Hill, USA: 2023-08-22

4. R.W. Engels
A universal method to polarize atoms, molecules and their ions and possible applications: $^{3}He^{+}$ Ion Source
Seminar, Brookhaven, N.Y., USA: 2023-02-17

5. R.W. Engels
Polarization and Recombination Measurements
LHCspin kick-off meeting, CERN, Switzerland: 2023-12-18 - 2023-12-18

6. V. Hejny
Suche nach Dunkler Materie am Speicherring COSY
Wissenschaft online, Forschungszentrum Jülich, Jülich, Germany: 2023-08-31

7. A. Lehrach
High-Energy Transport Beamline Layout
HBS Accelerator Meeting, Jülich, Germany: 2023-09-19 - 2023-09-20

8. A. Lehrach
High-Energy Beam Transport (HEBT) Layout
HBS Accelerator Workshop, Frankfurt, Germany: 2023-02-14 - 2023-02-15

9. A. Lehrach
High Energy Beam Transport Layout
HBS Accelerator Workshop, Frankfurt, Germany: 2023-02-14 - 2023-02-15

10. L. Ludhova
Solar neutrinos from the CNO fusion cycle: Borexino discovery and implications for the solar physics
Daejeon, South Korea: 2023-08-09 - 2023-08-09

11. U. Meißner
Molecular structures in hadron & nuclear physics
Colloquium, Beijing, Peoples R China: 2024-11-01 - 2024-11-01

12. U. Meißner
The nucleus as a quantum laboratory
Colloquium, Orsay, France: 2023-06-27 - 2023-06-27

13. U. Meißner
    Life on Earth - an accident?
    Colloquium, Bochum, Germany: 2023-11-13 - 2023-11-13

14. A. Nass
    Atomic Beam Sources
    LHCspin kick-off meeting, CERN, Switzerland: 2023-12-18 - 2023-12-18

15. J. Pretz
    Physik und Musik - Vom Gartenschlauch zur Posaune
    Highlights der Physik, Kiel, Kiel, Germany: 2023-09-25 - 2023-09-30

16. J. Pretz
    Spin Polarisation Experiments at Storage Rings: Axion Searches and Electric Dipole Moments
    Quantum Seminar, Mainz, Germany: 2023-12-21 - 2023-12-21

17. S. Siddique, J. Pretz and A. Lehrach
    SIMULATIONS OF BEAM DYNAMICS AND BEAM LIFETIME FOR THE PROTOTYPE EDM RING
    14th International Particle Accelerator Conference, Venice, Italy: 2023-05-07 - 2023-05-12

18. S. Siddique, J. Pretz and A. Lehrach
    Simulations of Beam Dynamics and Beam Lifetime for the Prototype EDM Ring
    86th Annual Conference of the DPG and DPG Spring Meeting, RWTH Aachen: 2023-03-20 - 2023-03-24

19. P. Zakalek *et al.*
    JULIC Neutron Platform - the HBS technology development infrastructure
    MT Meeting, Karlsruher Institut für Technologie (KIT), Germany: 2023-10-09 - 2023-10-09

E Academic Degrees

E.1 Dissertation / PhD Theses

1. A. Alicke
   Development of fast track finding algorithms for densely packed straw tube trackers and its application to Ξ (1820) hyperon reconstruction for the PANDA experiment
   Ruhr-Universität Bochum

2. C. Kannis
   Theoretical and Experimental Investigation of Sona Transitions
   RWTH Aachen University

3. S. Karanth
   Novel method to search for axion-like particles in storage rings
   Jagiellonian University in Kraków

4. G. Perez Andrade
   Measurement of proton-proton elastic scattering to commission the STS tracking stations in the HADES spectrometer
   Ruhr-Universität Bochum

5. R. Shankar
   Optimization of Spin Coherence Time at a Prototype Storage Ring for Electric Dipole Moment Investigations
   University of Ferrara

E.2 Master Theses

1. T.A. El-Kordy
   Storage Cell Tests for the Polarized Target at LHCb/CERN
   FH Aachen - University of Applied Sciences

2. N. Faatz
   Simulations of the occupation numbers of hyperfine substates passing external fields
   RWTH Aachen University

3. J. Gollub
   Sensitivity study for baryon resonances searches in pion-proton collisions with HADES
   Ruhr-Universität Bochum

4. L. Heuser
   The quest to derive plausible lineshapes from resonance parameters
   University of Bonn

5. A. Piccoli
   Beam dynamics simulations at the hybrid storage ring for EDM investigation
   University of Ferrara

6. R.P. Suvarna
   An Investigation of the Signal-to-Noise Ratio of the Rogowski Beam Position Monitor
   RWTH Aachen University

7. M. Westphal
   Design, Construction and Test of a Transition Unit for a Metastable Hydrogen Beam
   FH Aachen - University of Applied Sciences

E.3 Bachelor Theses

1. N.M. Hanold
   Influence of the Radial Magnetic Field of a Sona Transition Unit on Polarization of Particles
   Heinrich Heine University Düsseldorf

2. F.L.M. van Maele
   Optimization of a Sona transition unit to produce polarized hadron beams
   RWTH Aachen University

F Awards

1. Cristobal Morales won the best poster and mini-talk award at the MAYORANA School in Modica, Italy.

2. Recognition of the work of Livia Ludhova on the Borexino experiment in Italy by the social media of the Slovak Embassy in Rome in the occasion of: Event "Solar neutrino physics at LNGS: Borexino and Gallex experiments" organized by Academia Nazionale dei Lincei in Rome.

G Third Party Funded Projects

Project	Responsible/Contact	Funded by
ERC Advanced Grant EXOTIC	U.-G. Meißner	EU
NRW-FAIR	C. Hanhart	MKW NRW
SFB/TRR 110 Quantenchromodynamik TP A02	T. Luu	DFG/NSFC
SFB/TRR 110 Quantenchromodynamik TP A05	U.-G. Meißner	DFG/NSFC
SFB/TRR 110 Quantenchromodynamik TP A10	T. Luu	DFG/NSFC
SFB/TRR 110 Quantenchromodynamik TP B03	C. Hanhart	DFG/NSFC
SFB/TRR 110 Quantenchromodynamik TP B06	A. Nogga	DFG/NSFC
SFB/TRR 110 Quantenchromodynamik TP B09	U.-G. Meißner	DFG/NSFC
SFB/TRR 110 Quantenchromodynamik TP B11	D. Rönchen	DFG/NSFC
SFB/TRR 110 Quantenchromodynamik TP Z01	U.-G. Meißner	DFG/NSFC
SFB/TRR 110 Quantenchromodynamik TP Z02	C. Hanhart	DFG/NSFC
PANDA/ Straw Tube Tracker	J. Ritman	Industrieprojekt mit der GSI GmbH
PANDA/ Micro Vertex Detector	J. Ritman	Industrieprojekt mit der GSI GmbH
HESR - Dipole und Quadrupole	R. Tölle	Industrieprojekt mit der FAIR GmbH
HESR - sonstige Magnete	J. Böker	Industrieprojekt mit der FAIR GmbH
HESR - Netzgeräte	M. Retzlaff	Industrieprojekt mit der FAIR GmbH
HESR - Hochfrequenz	R. Stassen	Industrieprojekt mit der FAIR GmbH
HESR - Injektion	R. Tölle	Industrieprojekt mit der FAIR GmbH
HESR - Strahldiagnose	V. Kamerdzhiev	Industrieprojekt mit der FAIR GmbH
HESR - Vakuum	F. Esser	Industrieprojekt mit der FAIR GmbH
HESR - Stochastische Kühlung	R. Stassen	Industrieprojekt mit der FAIR GmbH
HESR - Panda-Integration	D. Prasuhn	Industrieprojekt mit der FAIR GmbH
HESR - P1SR	R. Tölle	Industrieprojekt mit der GSI GmbH
Transnational Access to COSY TA1	D. Grzonka	EU (STRONG2020)
JRA2-FTE@LHC:	F. Rathmann	EU (STRONG2020)
JRA12-SPINFORFAIR: Spin for FAIR	F. Rathmann	EU (STRONG2020)
Regional Doctoral Program in Particle Physics	U.-G. Meißner	VolkswagenStiftung
Precision neutrino physics with JUNO	L. Ludhova	DFG

H Collaborations

- ATHENA (Accelerator Technology Helmholtz Infrastructure)
- Belle-II (B(meson) to lepton lepton v.2)
- Borexino (Boron solar neutrino experiment, LNGS, Italy)
- CBM (Compressed Baryonic Matter)
- CLAS (CEBAF Large Acceptance Spectrometer, Jefferson Lab, USA)
- CPEDM (Electric Dipole Moments, CERN)
- ELENA (CERN) (Extra Low Energy Antiproton ring)
- EuPRAXIA (European Plasma Research Accelerator with Excellence in Applications)
- GlueX (Gluonic Excitations Experiment, Jefferson Lab, USA)
- HADES (High Acceptance DiElectron Spectrometer)
- HBS (High Brilliance Neutron Source)
- JEDI (Jülich Electric Dipole moment Investigation, COSY)
- JUNO (Jiangmen Underground Neutrino Observatory, Jiangmen, China)
- JuSPARC (Jülich Short-Pulsed Particle and Radiation Center)
- KLF (K-long Facility, Jefferson Lab)
- LENPIC (Low Energy Nuclear Physics International Collaboration)
- PANDA (Anti-Proton Annihilation at Darmstadt, FAIR)
- PAX (Polarized Antiproton eXperiments, COSY)
- PDG (Particle Data Group)
- PREFER (Polarization Research for Fusion Experiments and Reaktors)
- STRONG-2020 (The strong interaction at the frontier of knowledge: fundamental research and applications)
- WASA-FRS (Wide Angle Shower Apparatus at FRS)
- WASA-at-COSY (Wide Angle Shower Apparatus at COSY)

I Conferences and Outreach Activities (Co-)Organized by the IKP

I.1 Georgian-German Science Bridge: Lecture Week in Tbilisi

Within the framework of the “Georgian-German Science Bridge” (GGSB), institutes of Forschungszentrum Jülich (IKP, INM, IEK, and ZEA), representatives of Helmholtz-Zentrum Dresden-Rossendorf (HZDR), GSI Helmholtz-Zentrum, and RWTH Aachen - together with its Georgian partner universities (AUG, GTU, KIU and TSU), have organized the fifth meeting called this time “Lecture week in Tbilisi”, which took place during June 25 to 30, 2023, in Tbilisi (at AUG, GTU, and TSU) (see the corresponding website: http://fz-juelich.gtu.ge/autumn-lectures/2023/).

As part of the GGSB concept, educational programs for Georgian students have been conducted as so-called “Autumn Lectures” at the Georgian Technical University (GTU) in 2013 and 2015. In 2017 and 2019, a new initiative (so-called “QUALI-Start-Up Lectures”) took place in Jülich, in which scientists of FZJ institutes provided theoretical as well as practical trainings to selected Georgian students at experimental and technological facilities of FZJ. The subjects of these training courses were in the fields of basic science and included lectures in experimental and theoretical physics, chemistry, mathematics, life sciences and health as well as engineering science with an emphasis on applications of technologies. In addition, “Workshops and Summer Schools” were held at different locations in Georgia in even years. They started in 2004 with an interruption during the pandemic and were restarted in 2022. This time the GGSB Lecture week 2023 with it’s general topic: “Health as a Global Challenge – From Discovery to Technology / Contributions by the GGSB SMART|Labs in Georgia” - were devoted to the subjects focused on health – in particular cancer – and covered:

- Fundamental Research & Applications in Particle and Nuclear Physics
- Accelerator Research and Applications in Medicine
- Atmospheric Sciences and Environment
- Medical Imaging and Radionuclides for Life Sciences
- Machine Learning and Image Analysis
- Mechanical and Electrical Engineering

This was the first step to prepare the next edition of „QUALI-Start-Up lectures (2025)“ - which are planned as distributed events in Aachen, Darmstadt, Dresden-Rossendorf and Jülich. During the lecture week, the German partner institutions have been introduced their major projects, such that interested Georgian students now well aware about various possibilities in Germany. As part of the event, twenty excellent students were selected from various scientific fields – Physics, Mathematics, Chemistry, Biology and Engineering Technology – which were granted internships of about 6 weeks each in Forschungszentrum Jülich, GSI, Dresden/Rossendorf, and RWTH Aachen. For IKP (and GSI) a total of 4 physics students were identified which will visit the institute in February/March, 2024.

For 2024, the GGSB partners will hold the 10^{th} Georgian-German School and Workshop in Basic Science (GGSWBS), between September 9 - 14, 2024. The event marks the 20^{th} anniversary of the GGSB. It will be conducted under the title: "The First 20 years – achievements of GGSB and its SMART|Labs", celebrating by a one-week Science Fest its development during the first two decades in science, education and personnel and cultural exchange (see the corresponding website: http://collaborations.fz-juelich.de/ikp/cgswhp/cgswhp24/).

Figure 38: Participants of the Lecture Week in Tbilisi (TSU).

I.2 MESON 2023 – 17th International Workshop on Meson Physics

The 17th International Workshop on Meson Physics-Meson 2023, took place in Krakow from 22nd to 27th June 2023. The Meson conference series has a long standing tradition and is organised by the Institute of Physics of Jagiellonian University, GSI Helmholtz Centre for Heavy Ion Research, INFN-LNF Frascati and Institute of Nuclear Physics Polish Academy of Science, in Kraków. It brings together experimentalists and theorists involved in studies of meson production, interactions, internal structure and meson properties in strongly interacting matter (see website: https://indico.meson.if.uj.edu.pl/event/3/). Meson2023

Figure 39: Participants of the MESON2023 in Krakow.

included overviews of new experimental results and theoretical developments in the field of: spectroscopy of heavy flavour mesons, hyperons and light meson production and interactions in hadron and photon induced reactions and presentation of new emerging facilities. A particular highlight of this conference was a session devoted to role of strangeness in neutron star matter with the Laura Tolos (ICE, Barcelona) invited talk selected and sponsored by EPJA.

J Teaching Positions

Institute	Name	University
IKP-1	Prof. Dr. F. Goldenbaum	Bergische Univ. Wuppertal
	Prof. J. Ritman Ph.D.	Ruhr-Univ. Bochum
	Dr. T. Stockmanns	Ruhr-Univ. Bochum
IKP-2	Prof. Dr. L. Ludhova	RWTH Aachen
	Prof. Dr. J. Pretz	RWTH Aachen
IKP-3/IAS-4	Dr. E. Berkowitz	Rheinische Friedrich-Wilhelms-Univ. Bonn
	Prof. Dr. C. Hanhart	Rheinische Friedrich-Wilhelms-Univ. Bonn
	Prof. Dr. T. Luu	Rheinische Friedrich-Wilhelms-Univ. Bonn
	Prof. Dr. Dr. h.c. U.-G. Meißner	Rheinische Friedrich-Wilhelms-Univ. Bonn
	Dr. A. Nogga	Rheinische Friedrich-Wilhelms-Univ. Bonn
	Dr. D. Rönchen	Rheinische Friedrich-Wilhelms-Univ. Bonn
IKP-4	Dr. O. Felden	FH Aachen
	Prof. Dr. A. Lehrach	RWTH Aachen

K Personnel

Dr. A. Alicke (RUB/GSI-FFN)
MSc. A. Andres (IKP-2/ IKP-4)
MSc. A. Asokan (IKP-3/IAS-4)
MSc. A. Awal (GSI-HESR)
C. Berchem (IKP-TA)
Dr. E. Berkowitz (IKP-3/IAS-4)
Dr. C. Böhme (IKP-4)
M. Böhnke (IKP-4)
DI N. Bongers (IKP-4)
Dr. B. Breitkreutz (GSI-HESR)
P. Brittner (IKP-4)
B. Eng. F. Celik (GSI-HESR)
MSc. J. T. Chacko (IKP-3/IAS-4)
MSc. C. Chen (IKP-3/IAS-4 since 7 Nov. 2023)
W. Classen (IKP-4)
M. Comuth-Werner (IKP-TA/IAS-4)
DI F. Dahmen (IKP-4 until 30 April 2023)
C. Deliege (IKP-4)
DI N. Demary (IKP-TA)
MBA A. Derichs (IKP-1)
MSc L. von Detten (IKP-3/IAS-4)
G. D'Orsaneo (IKP-2)
R. Dosdall (IKP-1)
Dr. R. Engels (IKP-2)
T. El-Kordy (GSI-FFN until 30 June 2023)
B. Erkes (IKP-4)
Dr. W. Esmail (GSI-FFN until 31 Oct. 2023)
DI F.-J. Etzkorn (IKP-4)
MSc. N. Faatz (GSI-FFN until 31 March 2023)
Dr. O. Felden (IKP-TA)
H. - W. Firmenich (IKP-TA)
Dr. A. Foda (GSI-FFN)
MSc. C. Gäntgen (IKP-3/IAS-4)
Dr. R. Gebel (IKP-4, GSI-HESR)
J. Göbbels (IKP-TA)
Prof. Dr. F Goldenbaum (IKP-1)
J. Gollub (RUB/GSI-FFN until 30 Sept. 2023)
Dr. K. Grigoryev (GSI-HESR)
Dr. D. Grzonka (IKP-1, GSI-FFN since 1 Nov. 2023)
MSc. D. Gu, (GSI-FFN)
T. Hahnraths-von der Gracht (IKP-TA)
A. Halama (GSI-HESR)
DI S. Hamzic (GSI-HESR)
Prof. Dr. C. Hanhart (IKP-3/IAS-4)
Dr. M. Hartmann (IKP-2)
DI R. Hecker (IKP-TA)
Dr. V. Hejny (IKP-2)
Dr. J. - H. Hetzel (GSI-HESR)
BSc. L. Heuser (IKP-3/IAS-4 until 30 Sept. 2023)
M. Holona (IKP-1)
Dr. A. Kacharava (IKP-2)
M. Kaczmarek (GSI-HESR until 31 May 2023)
Dr. V. Kamerdzhiev (IKP-4, GSI since 1 Feb, 2023)
MSc. J. Kannika (GSI-FFN until 30 April 2023)
Dr. C. Kannis (GSI-FFN until 31 July 2023)
A. Kelleners (IKP-TA)
Dr. I. Keshelashvili (GSI-FFN)
A. Kieven (IKP-4 until 30 June 2023)
Dr. J. Kim (IKP-3/IAS-4)
S. Kistemann (IKP-TA)
MSc. V. Kladov (RUB since 15 Jan. 2023)
Dr. R. Kliemt (RUB/GSI-FFN)
B. Klimczok (IKP-TA)
G. Koch (GSI-HESR)
Dr. A. Kononov (GSI-FFN)
M. Kremer (IKP-TA)
DI T. Krings (IKP-TA)
L. Kunkel, (GSI-FFN since 1 April 2023)
M. Küven (IKP-4, until 31 Dec. 2023)
Dr. T. Lähde (IKP-3/IAS-4)
Dr. K. Laihem (GSI-HESR)
K. - G. Langenberg (IKP-4)
Dr. H. Le Thi (IKP-3/IAS-4)
Prof. Dr. A. Lehrach (IKP-4)
MSc. S. Liebert (GSI-HESR)
MSc. R. Liu (GSI-FFN until 31 Aug. 2023)
Prof. Dr. L. Ludhova (IKP-2)
Dr. S. Lutterer (RUB/GSI-FFN 1 May until 31 Oct. 2023)
Prof. T. Luu (IKP-3/IAS-4)
MSc. M. Malabarba, (GSI-FFN since 1 July 2023)
Dr. Y. Malyshkin, (GSI-FFN since 16 Jan. 2023)
MSc. M. Manerova (GSI-HESR)
MSc. M. Margos, (GSI-FFN, since 1 June 2023)
M. Eng. M. Marzen (GSI-HESR)
Prof. Dr. Dr. h. c. U.-G. Meißner (IKP-3/IAS-4)
MSc. A. Meraviglia (GSI-FFN unitl 28 Feb. 2023)
DI A. Messaaf (GSI-HESR)
Dr. J. Messchendorp (GSI-FFN)
Dr. B. Metsch (IKP-3/IAS-4)
MSc. N. Mohan (GSI-FFN until 31 May 2023)
MSc. C. Morales (GSI-FFN, since 23 Jan. 2023)
Dr. H. Mutuk (IKP-3/IAS-4 until 31 Jan. 2023)
Dr. A. Nass (IKP-2)
MSc. P. Niedermayer (GSI-HESR)
Dr. A. Nogga (IKP-3/IAS-4)
MSc. D. Okropiridze, (GSI-FFN, since 15. Nov. 2023)
MSc. S. Pattnaik (GSI-FFN since 1 Feb. 2023)
MSc. L. Pelicci (IKP-2)
Dr. O. Penek (GSI-FFN, since 1 Feb. 2023)
Dr. G. Perez-Andrade (GSI-FFN)
Dr. A. Pesce (IKP-2 until 31 May 2023)
Prof. Dr. J. Pretz (IKP-2)
V. Priebe (IKP-TA, GSI-FFN until 30 Sept. 2023)
BSc. P. Pütz (IKP-3/IAS-4 since 4 Oct. 2023)
S. Pütz (GSI-FFN until 31 Dec. 2023)
Dr. F. Rathmann (IKP-2, until 30 Sept. 2023)
MSc S. Rawat (IKP-3/IAS-4)
DI K. Reimers (IKP-4, GSI-HESR, since 1 July 2023)
MSc. M. Rifai (IKP-2)

Prof. J. Ritman Ph.D (IKP-1, GSI-FFN)
Dr. D. Rönchen (IKP-3/IAS-4)
G. Roes (IKP-TA)
P. Rottscheidt, (GSI-EPS since 1 April 2023)
D. Ruhrig (IKP-4)
MSc. S. Sahu (RUB, since 1 March 2023)
Dr. A. Saleev, (GSI-FFN)
Ph.D. habil. S. Schadmand (GSI-FFN)
F. Scheiba (IKP-4)
Dr. R Schleichert (IKP-2)
M. Schmühl (IKP-4)
MSc. C. Schneider (IKP-3/IAS-4)
M. Schubert (GSI-HESR)
Dr. T. Sefzick (IKP-TA)
H. Sharma (GSI-FFN)
Dr. S. Shen (IKP-3/IAS-4)
Dr. H. Shi, (GSI-FFN since 20 March 2023)
Dr. V. Shmakova (GSI-FFN until 31 July 2023)
MSc. N. Shurkhno (GSI-HESR)
MSc. S. Siddique (GSI-FFN)
M. Eng. R. Similon (GSI-HESR)
DI M. Simon (IKP-4)
MSc. P. Sinilkov (IKP-3/IAS-4 since 1st Feb. 2023)
MSc. A. Singhal (IKP-2)
J. Spelthann (GSI-HESR)
D. Spölgen (IKP-2)
Dr. R. Stassen (IKP-4)
J. Steinhage, (GSI-FFN)
Dr. T. Stockmanns (IKP-1)
Dr. X.-X. Sun (IKP-3/IAS-4 since 1 Feb. 2023)
MSc. R. Suvarna (GSI-FFN)
Dr. K. Suzuki (RUB until 31 July 2023)
Dr. J. Taylor, (GSI-FFN)
MSc. M. Thelen (IKP-4)
Dr. Y. Valdau (GSI-HESR)
BSc. V. Verhoeven (GSI-FFN until 31 July 2023)
MSc. M. Vitz (IKP-4)
MSc. C. Vollbrecht (IKP-2, until 15 March 2023)
BSc. M. Westphal (GSI-FFN, until 31 March 2023)
Dr. P. Wintz (IKP-1)
D. Wirtz (IKP-TA)
J. Wirtz, (GSI-FFN since 15 April 2023)
Dr. H. Xu (IKP-1)
MSc. R. Yang (Uni Wuppertal since 22 May 2023)
H. Zens (IKP-4)

IKP-1:	Experimental Hadron Structure
IKP-2:	Experimental Hadron Dynamics
IKP-3/IAS-4:	Theory of the Strong Interactions
IKP-4:	Large-Scale Nuclear Physics Equipment
IKP-TA:	Technical Services and Administration
GSI-FFN:	GSI Helmholtzzentrum für Schwerionenforschung, FAIR Forschung NRW
GSI-HESR:	GSI Helmholtzzentrum für Schwerionenforschung, Hochenergiespeicherrig
RUB:	Ruhr-Universität Bochum

L Individual Contributions

Contents

AI for detector control and data analysis for HADES and future FAIR experiments

V. Kladov, J. Messchendorp, J. Ritman, W. Esmail, J. Regina

1 Real-time predictions of calibration constants

The online data processing of the next generation of experiments, such as those conducted at FAIR, requires a reliable reconstruction of event topologies and, therefore, will depend heavily on in-situ calibration procedures. Work in this direction started in our laboratory with building a neural network based tool, designed to provide real-time predictions of calibration constants with the usage of continuously available environmental data.

To efficiently create and test the network, the data from a running experiment at FAIR Phase Zero, i.e. Hades, is being used. Drift chambers (MDC) gains were chosen for this role as they have clear dependence on the environment conditions which were monitored and stored to a database during previous HADES beam times. Additionally, the MDC has a number of channels arranged in a non-trivial structure. This makes it an ideal test subject for the future generalization of the technique.

To enhance regularization of the network, information about previous environmental states was forwarded to a Long Short-Term Memory (LSTM) architecture. LSTM was combined with graph convolution cells to facilitate predictions across multiple channels simultaneously and to account for correlations between the channels. Graphs support regularization by handling information of different kinds of detectors in the same way.

The developed neural network was wrapped into a C++ and ROOT based application. The app is able to access the database with environment information, automatically construct training datasets, perform "offline" calibrations of the MDC, retrain the model or update it using new batches of data. Most importantly, it can use all this to autonomously predict calibration constants during experiment. The code was designed to minimize delays of predictions and to improve their precision at the beginning of the beam time. As such, datasets for retraining are constructed simultaneously with predictions and starting coefficients of the neural network, which are kept from the previous beam time, are adjusted as soon as offline calibration of new batches of data are available.

A proof-of-principle of this approach has been demonstrated using data collected in the February 2022 experiment. Our method showed the ability to provide fast and stable calibration predictions with a precision comparable to that obtained using traditional offline, time-consuming approaches (fig 1.). The readout of the database appeared to be the most time consuming part of predictions. Still, it was far less than both run duration and the period of environmental conditions stability.

The proposed methodology will be tested in a real-time experimental setting during the next HADES beam time in Feb-Mar 2024. The speed of accuracy convergence after the big changes in the system is one of the main concerns of this technique and will, therefore, be measured during this beam time as well.

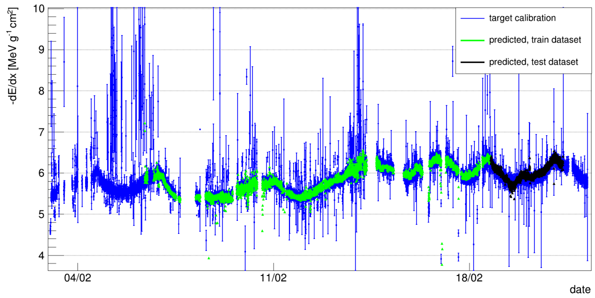

Figure 1: Time variations of the average energy-loss values of the MDC. Targets in blue and predicted by the network in green and black.

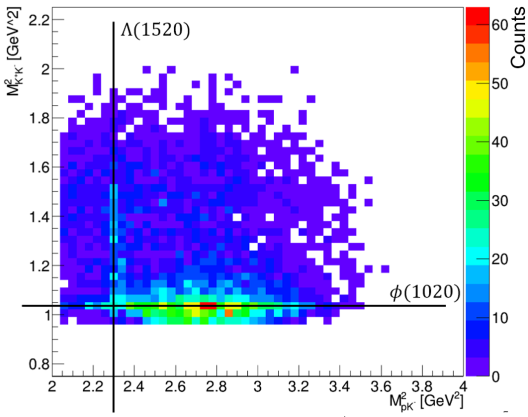

Figure 2: Dalitz distribution for K^+K^- and pK^- pairs.

2 Analysis of the process $pp \to ppKK$

The reaction $pp \to ppKK$ was analysed using the data taken by HADES in 2022 with kinetic beam energy of 4.5GeV. For this analysis, the neural network-based particle identification procedure, developed by the group, was improved and optimized. The network was fine-tuned to separate charged hadrons and trained on the appropriate dataset. Batch and feature normalizations were added as well as smart reweightening of classes, required because of the very unbalanced datasets, in which K^- appear on the order of 50 times less frequently than π^-.

For the selection of events, all final state particles were identified and forwarded to a combinatorial kinematic refitting procedure with 4C constraint, corresponding to the conservation of four momentum in the process. Clear signals from $\phi(1020) \to KK$ and $\Lambda(1520) \to pK$ were observed in the invariant mass distributions (fig. 2) with their parameters consistent with PDG data within one standard deviation. Developed event selection techniques will be used as a basis for a partial wave analysis with the goal to determine the contributions of various baryonic resonances in the initial step of the reaction. Additionally, the analysis will be extended to the $ppKK\pi^0$ final state.

Preparation of test modules for neutron detection at mCBM

D. Okropiridze, F. Goldenbaum, D. Grzonka, J. Ritman

One component of the CBM-experiment [1] will be the Forward Spectator Detector (FSD) which will allow to determine the reaction plane and the collision centrality in heavy ion reactions. It will consist of a segmented plastic scintillator wall with a thickness of about 5 cm for the detection of charged particles. In order to extend the performance an additional neutron detector is considered to be placed behind the FSD. Neutron detection will improve the determination of collision centrality and collective flow in heavy ion reactions and will be important for the analysis of various proton induced reaction channels. It is planned to cover the FSD scintillator wall at the backside by an array of long plastic scintillator modules coupled to photomultipliers using the energy-detector of the COSY-TOF-experiment [2]. For the modules BC-416 was chosen as scintillator material and photomultipliers of the type XP4592/PA from Photonis with an outer diameter of about 130 mm are used for the read out. In an analysis of the $pp \rightarrow pn\pi^+$ reaction channel at 2.7 GeV/c beam momentum a detection efficiency for neutrons of up to about 40% was achieved [3].

In order to investigate the performance of such a detector component two detector assemblies consisting of seven scintillator modules each, have been prepared to be installed at mCBM for test measurements in 2024. The scintillator modules have a hexagonal shape with a side length of about 8cm and a length of 45 cm resulting in an area of about 1200 cm^2 for each detector assembly. For the preparation of the detector assemblies the COSY-TOF detector was disassembled and separate scintillator modules packed in light tight black foil were prepared. One detector assembly will be positioned behind the TOF-detector of mCBM to correlate the particle tracks with the scintillator signals and the other assembly will be combined with FSD scintillator modules and placed close to the beam line to investigate the response to very high multiplicities and rates as expected in the CBM experiments. In Fig.1 a photo of such a detector assembly is shown.

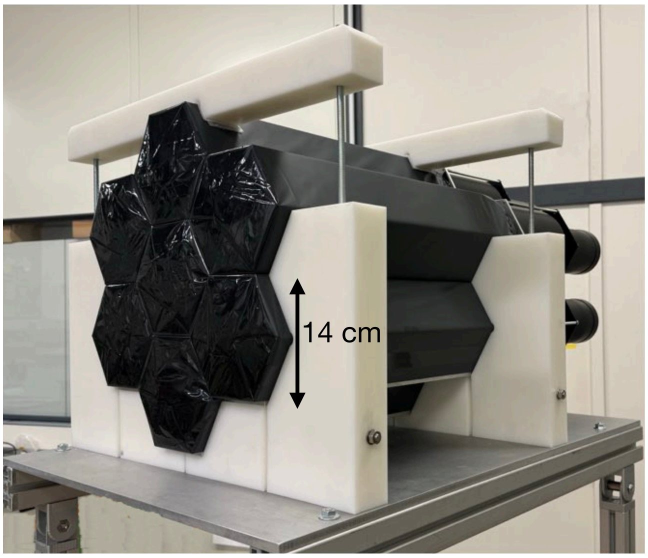

Fig. 1: Neutron detector assembly consisting of seven scintillator modules with a length of 45 cm read out by XP-4592/PA PMTs.

The measurement of the signal amplitude will be performed by a time over threshold (ToT) measurement in the mCBM data aquisition system and presently possible solutions for the integration of the scintillator signals are under analysis. In Fig.2 a typical signal induced by a cosmic particle passage through the scintillator and the result of a test with cosmic data showing the correlation between the measured ToT-value and the integrated signal charge is shown. For the test, which was done with C. Pauly at the university of Wuppertal, the scintillator signal is splitted and connected simultaneously to an oscilloscope and a DAQ-system producing a ToT-value. For each event the area of the scope trace below a certain threshold as indicated by the red line in Fig.2 is integrated and compared to the ToT-value for this event. A very good correlation is achieved which will result in a sufficiently precise determination of the energy deposited in a scintillator module.

Presently the read out of the scintillator signals with the integration into the CBM data acquisition system is prepared.

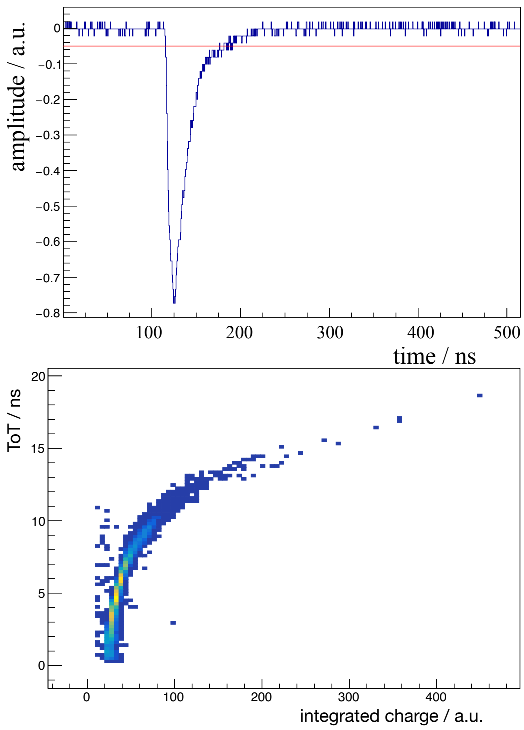

Fig. 2: Typical signal induced by a cosmic particle passing through the scintillator (left side) and correlation between ToT-value and integrated signal charge (right side).

References:

[1] https://www.gsi.de/work/forschung/cbmnqm/cbm
[2] J. Kreß, PhD thesis, University Tübingen, 2003.
[3] E. Roderburg, IKP annual report 2011.

Luminosity Determination via p-p Elastic Scattering with the Upgraded HADES Spectrometer

G. Perez-Andrade, P. Wintz and J. Ritman

The upgraded HADES Spectrometer, including new Forward Detector components (FD) [1], was used in 2022 to investigate hyperon production using a proton beam of p_{beam} = 5.3 GeV/c, impinging onto a fixed LH_2 target. P-p elastic scattering events were used to determine the integrated luminosity $\mathcal{L}$. In particular, coincidences with one proton detected in the FD ($\theta_{FD} < 6°$) and the other proton measured in the main HADES acceptance ($18° < \theta_H < 85°$) were considered. The event selection criteria is based on kinematic constraints defined for the p-p elastic scattering and the reconstructed polar and azimuthal angles, including: i) $|\phi_H - \phi_{FD} - 180°| < 7°$, ii) $|tan\theta_H \times tan\theta_{FD} - 1/\gamma^2_{cm}| < 0.1$, and iii) $|p_{el} - p_H| <$ 500 MeV/c, where p_{el} is the theoretical momentum calculated for an elastically scattered proton, emitted at θ_H. A detailed description of the kinematics and selection process of the p-p elastic processes is discussed in [2]. The reaction kinematics and detector acceptance constrain the event selection to the window -0.318 GeV^2 $< t <$ -0.093 GeV^2, where t is the square of the four-momentum transfer, calculated from θ_H, the proton mass and p_{beam} [3].

The elastic scattering yield dN_{el} was obtained by integrating the $\Delta\phi$ distribution, which showed minimal background present under the peak after the final selection cuts [2]. dN_{el} is shown as a function of t in Fig. 1 (a). The $\mathcal{L}$ was determined as:

$$\mathcal{L} = \frac{DS}{\sigma_{el}} \int \frac{dN_{el}}{d\varepsilon} \times d\eta \quad dt, \tag{1}$$

where $d\eta$ is a correction factor that compares the simulation and data reconstruction efficiency in the FD, and $d\varepsilon$ accounts for the reconstruction efficiency calculated from simulation, by comparing the total number of generated events to the number of reconstructed events after applying the same selection criteria as in the data [2]. These factors are strongly t-dependent, as shown in Fig. 1 (b) and (c). Since there are no available data for the p-p elastic scattering reaction cross-section σ_{el} at p_{beam} = 5.3 GeV/c, for Eq. 1 an interpolation using existing data measured at beam momenta of 5.0 and 6.0 GeV/c [4] was used, resulting in σ_{el} = (4.69 ± 0.04) mb for the selected t-range. Finally, DS = 64 is a scaling factor of the HADES trigger. The preliminary result is $\mathcal{L} = (6.47 \pm 0.06)\ pb^{-1}$, where the uncertainty is statistical.

The p-p elastic scattering differential cross-section $d\sigma_{el}/dt$ is obtained by:

$$\frac{d\sigma_{el}}{dt} = \frac{1}{\mathcal{L}} \frac{dN}{dt}, \tag{2}$$

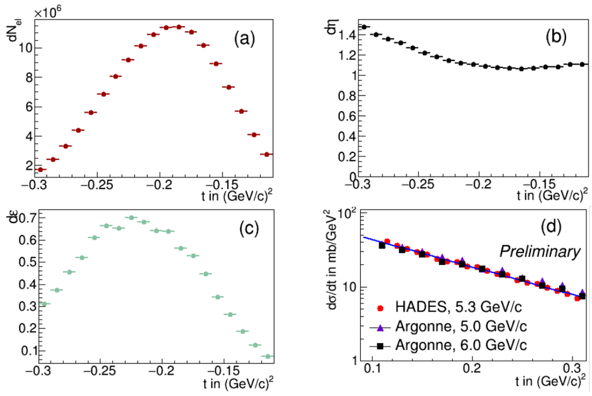

Figure 1: (a), (b) and (c) show the differential distributions of the dN_{el}, $d\eta$ and $d\varepsilon$ from Eq. 1. (d) $d\sigma_{el}/dt$ of HADES compared with data from [4]. The HADES data is plotted together with its corresponding exponential function, marked by the blue line.

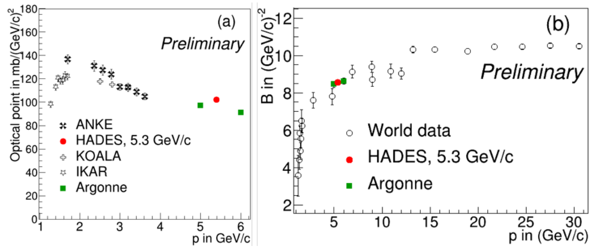

Figure 2: Overview of the optical point (a) and nuclear slope parameter (b) from different experiments.

where dN denotes the efficiency-corrected number of reconstructed elastic-scattering events. The result is shown in Fig. 1 (d) as a function of $|t|$. The data in this figure are well described by a function of the form $d\sigma_{el}/dt = Ae^{-B|t|}$ [3], from which the optical point parameter A = (102.24 ± 1.06) mb/(GeV/c)^2 and the nuclear slope parameter B = (8.56 ± 0.05) (GeV/c)$^{-2}$ are obtained. Preliminary results of A and B show a good agreement with existing data for p_{beam} = 5.0 GeV/c and 6.0 GeV/c, shown in the same Figure. Figure 2 shows a compilation of values of the optical point parameter (a) and the nuclear slope parameter (b), obtained by different experiments at different beam momenta, showing that the values obtained for HADES agree well with the existing world data.

References

[1] J. Adamczewski-Musch, *et al.*, Eur. Phys. J. A. (2021) 57:138 `https://doi.org/10.1140/epja/s10050-021-00388-w`.

[2] G. Perez-Andrade, PhD thesis, RU Bochum, (2023) `https://doi.org/10.13154/294-10810`.

[3] H. Xu, *et al.*, Phys. Lett. B, 812, 136022 (2021) `https://doi.org/10.1016/j.physletb.2020.136022`.

[4] I. Ambats, *et al.*, Phys. Rev. D, 9(5), 1179 `https://doi.org/10.1103/PhysRevD.9.1179`

Development of Machine Learning Algorithms to Optimise the Detection of Low-mass Dileptons

Saket Sahu, Johan Messchendorp and James Ritman

Radiative transitions and decays of hadrons provide valuable information on their electromagnetic structure. The radiative internal transition of the $\Delta \rightarrow \Delta\gamma'$ can be exploited to extract its magnetic moment μ_{Δ^+}. The Particle Data Group (PDG) currently reports the magnetic moment of the Δ^+ (1232) as $\mu_{\Delta^+} = 2.7^{+1.0}_{-1.3}$ (stat) ± 1.5 (syst) ± 3.0 (theo) μ_N, which has large theoretical uncertainty due to model ambiguities. The virtual photon (dileptons) transition of the Δ^+ is promising since it allows to extract observables, such as spin-density matrix elements (SDMEs), that are not accessible using real photons and thus can provide a less model dependent extraction of the magnetic moment. The experimental challenges lie in the identification of (mostly) low-mass dilepton pairs and separating the physics channels of interest from bremsstrahlung and external conversion processes. Thus, studying exclusive reactions using elementary beams can be used to suppress the contribution of (virtual) bremsstrahlung. The exclusive channel $p+p \rightarrow p+p+e^+ +e^- +\pi^0$ is

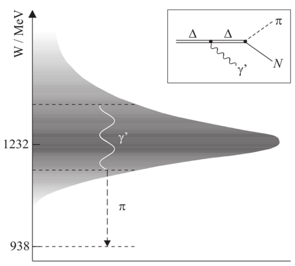

Figure 1: $\Delta \rightarrow \Delta\gamma'$ transition within the resonance width [1]

being analysed using the February 2022 proton proton collision data using the **H**igh **A**cceptance **Di**-**E**lectron **S**pectrometer (HADES) at GSI Darmstadt for such form factor studies of radiative transitions as outlined above. HADES is equipped with a hadron blind Ring Imaging Cherenkov Detector (RICH) to probe various rare dilepton pairs. The current reconstruction algorithm fails to efficiently identify dilepton pairs with very small opening angles[2]. A dedicated event generator that incorporates the radiative transition process for the Δ^+ has been developed in 2023 by extending the PLUTO library. Preliminary phase space studies show that $\approx 64\%$ of the dileptons have e^+e^- opening angles$< 4°$ and $\approx 78\%$ of the dileptons have e^+e^- opening angles $< 9°$.

Convolutional Neural Networks (CNN) are known to show great performance in image analysis and thus can be used for ring reconstruction. The CNN will be trained on both real and simulated pixel hits information of the Multi Anode Photo Multipliers

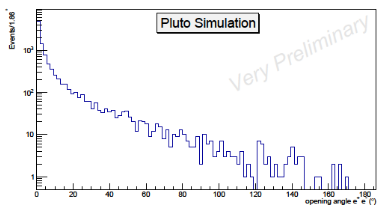

Figure 2: e^+e^- opening angle distribution for the exclusive channel

(MAPMT) of the HADES RICH. Machine Learning models are usually created using various frameworks like PyTorch, scikit-learn or TensorFlow that are not directly compatible with each other. Open Neural Network Exchange (ONNX), is an open-source format for representing and sharing machine learning models. ONNX provides a common format allowing you to move models between different frameworks seamlessly. This provides the option to use the algorithm for online monitoring for future experiments by training the model during the experiment.

References

[1] S. Schumann et al. (The European Physical Journal A 43.3 (2010), pp. 269–282).

[2] J.H.Otto (PhD Thesis, Justus-Liebig-Universität Gießen, 2022, http://dx.doi.org/10.22029/jlupub-7207).

Ξ^- and $\Sigma^*(1382)$ Reconstruction in p(4.5 GeV)+p Reactions with HADES

J. Taylor, J. Messchendorp and J. Ritman

This report covers the analysis of the Ξ^- and $\Sigma^*(1382)$ hyperons in data taken with the HADES (High Acceptance Di-Electron Spectrometer) in 2022 using a proton beam with a kinetic energy of 4.5 GeV impinging on a liquid-hydrogen target.

One of the main motivations to study the Ξ^- production in proton-proton scattering is to determine the production cross section for the first time. Such a measurement might shed light on the striking near-threshold cross section enhancement observed in heavy-ion (pA) reactions [1]. For the elementary proton-proton reaction, one expects a cross section ranging between 0.35 and 3.6 at 4.5 GeV [2] .

The Ξ^- hyperons are searched for via the reaction $pp \to \Xi^- K^+ K^+ p + X$, where the Ξ^- decays into $\Lambda\pi^-$ with a branching fraction of close to 100% and the Λ further decays into $p\pi^-$ with a branching fraction of 64%. About 25% of the full experimental data set were analyzed together with corresponding Monte Carlo data simulated for the reaction channel of interest.

For the 2022 beam time, HADES was upgraded with a forward detector covering polar angles less than 7°. The forward detector consists of straw tracking stations and an RPC detector for time-of-flight measurements. Since protons from hyperon decays are mostly scattered towards small angles, the current analysis assumes that all the tracks in this detector originate from protons.

To select protons and pions in the main HADES spectrometer, a relative fime-of-flight procedure is used. Two pions are selected. For each pion, Δ_t is calculated as the difference between the measured TOF and the expected TOF calculated from the flight path. The difference of the Δ_t is taken for the pions and only those pairs where the difference is less than $\pm$ 0.5 ns are selected. Protons are selected if the difference between the measured TOF of the positive and one of the negative particles is within $\pm$ 0.5 ns of the expected TOF difference for a π^- and proton hypothesis. Protons and π^- are combined to form a Λ. All combinations of protons from the forward detector after the selection are combined with an additional π^- to form an inclusive Ξ^-.

From the data analyzed so-far, no significant signature of the Ξ^- decay is observed. The expected statistical significance is therefore evaluated as a function of cross section. Monte Carlo simulations were used to estimate the expected number of reconstructed events of the signal channel, scaled according to the cross section and accounting for luminosity, branching fractions, acceptances, and efficiencies (S). The experimental data in the mass range around the expected Ξ^- mass is used as a measure

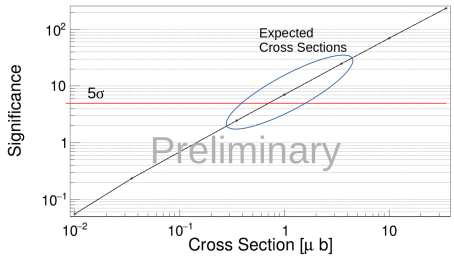

Figure 1: Calculated significance as a function of cross section. The red line indicates a 5σ significance at 0.7 μb and the blue ellipse marks the region of predicted cross sections.

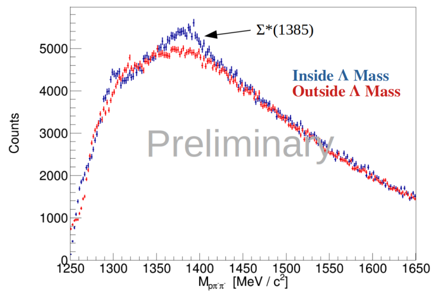

Figure 2: $\Sigma^*(1385)$ mass peak in the spectrum of the invariant mass M($p\pi^-\pi^-$). The red line corresponds to events outside the Λ mass peak and the blue line corresponds to events within the Λ mass peak.

of the background (B). The statistical significance is calculated by $S/\sqrt{S+B}$ and the corresponding results are depicted in Fig. 1. Preliminary, one might speculate that with the data analyzed so-far, that one can exclude a cross section that is larger than 0.7 μb with a significance of 5σ.

The decay of the $\Sigma^*(1385)$ to the same final-state as the Ξ^- is used as a control channel to verify the analysis procedure and as a calibration source for the reconstructed mass spectrum. Currently, protons from the main HADES spectrometer are used. After applying a selection around the π^-p invariant mass in the vicinity of the expected Λ mass together with a selection on the missing mass of the initial four-momentum minus the reconstructed four momentum of the $\Sigma^*(1385)$ candidate, a clear structure around the expected $\Sigma^*(1385)$ mass starts appearing (see Fig. 2).

References

[1] *The HADES and PANDA @ HADES Collaborations*, Eur. Phys. J. A 57 (2021) 138.

[2] *The HADES Collaboration*, Phys. Rev. Lett. 114 (2015) 212301.

Hyperon-Production Studies in $\mathbf{p+p \to \Lambda + K^0_S + p + \pi^+}$ at $\mathbf{T = 4.5}$ GeV with HADES at GSI

S. Pattnaik, J. Messchendorp, J. Ritman

Proton-induced hyperon production studies can provide valuable insights into the field of baryon spectroscopy [1]. In particular, a study of the coupling strengths of intermediate baryons to hyperon final states will be important to understand their internal structure and to search for new baryon resonances. A proton beam with 7.5×10^7 particles/s and kinetic energy of T = 4.5 GeV was incident on a liquid-hydrogen target and around 1.5×10^9 events were recorded with HADES [2]. We analyzed the exclusive process $p + p \to \Lambda + K^0_S + p + \pi^+$.

Intermediate kaons and hyperons are reconstructed via decay channels, $K^0_S \to \pi^+\pi^-$ and $\Lambda \to p + \pi^-$. Selection criteria included time information, a reconstructed global event vertex, and four-momentum conservation. A time-of-flight technique was used for particle identification that exploited the relative time-of-flight between particle candidates. This was shown to be an effective method to separate between pion and proton tracks particularly for high momenta and when combined with an invariant mass reconstruction of particle pairs, it provided a clean identification of Λ and K^0_S.

To enhance the selection of long-lived hyperons, we deployed a kinematic fitter based on vertex constraints. Subsequently, under the exclusive condition of detecting a primary pion and a proton, we extracted approximately 15,000 candidate events with Λ and K^0_S in coincidence. Similar results were obtained with an estimate of the distance of closest approach (DCA) between the daughters of neutrally charged particle candidates and applied an optimized cut on the corresponding value of χ^2_{DCA}.

With this data sample we studied intermediate resonances decaying into, e.g., ΛK^0_S and $p\pi^+$ pairs by inspecting the correlation between the invariant masses of $M^2(\Lambda K^0_S)$ against the $M^2(p\pi^+)$. The result of this study is illustrated in the corresponding Dalitz plot distribution along with their projections as shown in Fig. 1. We subtracted uncorrelated ΛK_S background events with a sideband analysis.

We generated phase space distributed Monte Carlo data of the $p + p \to \Lambda + K^0_S + p + \pi^+$ reaction using Pluto [4]. The response of the detector was modeled with Geant3 [5] and the resulting data were analyzed using the same conditions as applied to the experimental data. For a comparison between these signal Monte Carlo events and the experimental data, the projections from their respective Dalitz plot distributions are shown in Fig. 1. The bottom right figure strongly suggests the presence of the $\Delta^{++}(p\pi^+)$ at the nominal mass squared of 1.5 $(\mathrm{GeV}/c^2)^2$. A conclusive study of the dynamics between ΛK^0_S still requires a correction for acceptance x efficiency.

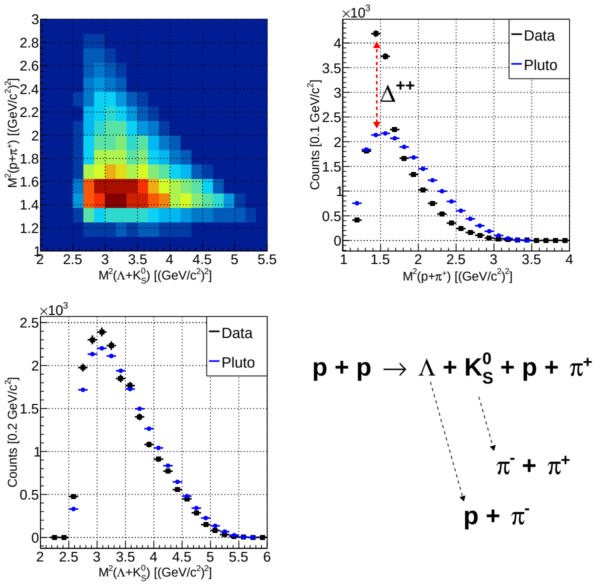

Figure 1: Reconstructed invariant mass distribution of $M^2(\Lambda K^0_S)$ against $M^2(p\pi^+)$ along with their projections. The projections compare the experimental data (black) to phase space generated events (blue).

In conclusion, we observed clear dynamics in the Dalitz plot distribution of the reaction $p + p \to \Lambda + K^0_S + p + \pi^+$ pointing to intermediate resonances. From this preliminary analysis, we observed the decay of $\Delta^{++} \to p\pi^+$. This gives us the possibility to study the role of intermediate baryon resonances via the $pp \to \Lambda K^0_S \Delta^{++}$ process as a complementary probe to earlier studies based upon the $pp \to \Lambda K^+ p$ and $pp \to \Sigma^0 K^+ p$ channels [6]. This study will be followed up by a more detailed and quantitative analysis using a partial wave amplitude analysis.

References

[1] J. Adamczewski-Musch *et al.*, Eur. Phys. J. A **57**, 138 (2021).

[2] G. Agakichiev *et al.*, Eur. Phys. J. A **41**, 243–277 (2009).

[3] P.A. Zyla *et al.*, (Particle Data Group), Prog. Theor. Exp. Phys. **2020**, 083C01 (2020).

[4] I. Fröhlich *et al.*, J. Phys Conf. Ser. **219** 032039 (2010).

[5] Y. Zeng-Yun *et al.*, Chinese Phys. C **32** 572 (2008).

[6] R. Abou Yassine *et al.*, Eur. Phys. J. A **60**, 18 (2024).

Partial Wave Analyses for the HADES Experiment

A. M. Foda, J. Gollub, J. Messchendorp, J. Ritman

The High Acceptance Di-Electron Spectrometer (HADES) experiment, situated at GSI Helmholtzzentrum für Schwerionenforschung, is dedicated to the exploration of of the structure strongly-interacting matter. One of the powerful methods employed in this pursuit is Partial Wave Amplitude (PWA) analysis. The efforts for PWA analyses in HADES are motivated by the analysis of the upcoming pion-beam data. Particularly, they encompass the study of the two-pion final state and the extraction of Electromagnetic Time-like Form Factors (ETFF) of baryonic resonances using dilepton decay channels. HADES data will complement global data on single and double pion production from photon induced reactions [1].

PWA analyses within HADES have been conducted using the BnGa framework, a FORTRAN-based software that employs unbinned maximum likelihood fitting techniques, including K-Matrix and D-Matrix techniques [2]. Our current focus is directed towards presenting an analysis framework in a modular setup with a user-friendly interface. To accomplish this, we are collaborating with the BnGa group to integrate the K-Matrix and D-Matrix analysis models into AmpTools [4]. Our initial milestone involves establishing a PWA analysis framework for final states originating from pion-induced reactions investigated with HADES. This will serve as a proof of concept, allowing us to compare our results with previous fits obtained using BnGa and prepare for PWA analysis endeavors with upcoming pion-beam data. Subsequently, we intend to expand the framework to encompass other reactions of interest, including proton-beam reactions.

Also, a study has been done to investigate the sensitivity of the HADES experiment to disentangle the N(1720) double resonance proposed by the CLAS collaboration [6]. The study examined the effects of varying branching fractions for the decay of N(1720) and N'(1720) resonances into $\Delta\pi$ and Nρ final states, along with the yield ratio between these resonances and the impact of the number of events. The analysis was conducted within both 4π and estimated HADES acceptance, comparing the polar angle distribution of the N(1720) resonance alone with that of the combined N(1720) and N'(1720) resonances, quantifying differences through a χ^2 value. An example partial wave fit within 4π acceptance is presented in Fig. 1. The fit with a two-state model results in the expected χ^2 value, whereas the fit with a one-state model shows a significantly larger χ^2 value and can thereby be excluded. The required number of events for a significant observation varies based on branching fraction cases within the HADES acceptance. The comparison indicates that the HADES experiment is capable of identifying the N'(1720) resonance. In the future, a more detailed study could include the N(1720) resonance decay into the Nσ final state, background contributions from other N* resonances, and exploring the decay of N(1720) and N'(1720) resonances into $\Delta\pi$ and Nρ as a spin-3/2 F-wave. Different partial wave amplitude models might be considered. A more detailed simulation of the HADES detector could provide an improved estimate of the acceptances and account for reconstruction effects.

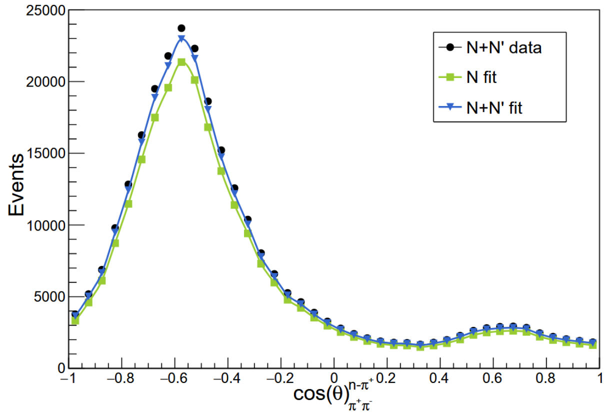

Figure 1: An example fit of a single baryon resonance (green squares) and a fit accounting for two states (blue triangles) of the generated N(1720) double resonance spectrum at $\sqrt{s}$=1.76 GeV within 4π acceptance [5].

References

[1] HADES Collaboration, Baryon couplings to mesons and virtual photons in the third resonance region: vacuum and cold matter studies, internal document, 2022.

[2] 'Bonn-Gatchina' Webpage https://pwa.hiskp.uni-bonn.de

[3] Anisovich, A. V. et. al., Phys. Rev. D, 84, 7 076001, 2011, 10.1103/PhysRevD.84.076001.

[4] M. Shepherd *et al.*, 'AmpTools' https://doi.org/10.5281/zenodo.7336113

[5] J. Gollub, Sensitivity study for baryon resonances searches in pion-proton collisions with HADES, 2023.

[6] V.I. Mokeev *et al.*, *Physics Letters B*, vol. 805, p. 135457, 2020.

Accessing the Proton Structure via Charm Production in Proton-Proton Interactions with the Compressed Baryonic Matter Experiment

Ömer Penek

This report discusses prospects of charm-production studies with a proton beam by the Schwerionensynchrotron 100 (SIS100) impinging on a fixed proton target and using the Compressed Baryonic Matter (CBM) experiment at the Facility for Anti-proton and Ion Research (FAIR). The charm-nucleon interaction can be experimentally studied exploiting the reaction $pp \to ppJ/\psi$ whereby the J/ψ is identified via its dileptonic decay $J/\psi \to ee, \mu\mu$ with branching fractions of about 6% each. Hereby, it is expected that the exchange between the protons and the J/ψs are purely based on gluonic nature enabling the possibilty to determine and access the gluonic gravitational form factors (GFFs) [1] based on hadroproduction. In these studies, we assume a liquid hydrogen (LH_2) target with a thickness of 5 cm. The reachable maximum proton momentum is 30 GeV/c corresponding to a center-of-mass energy of $\sqrt{s} = 7.6$ GeV. The CBM detector is a suitable site for the reconstruction of exclusive final state events. Thus, the proton-proton program can be seen as an extension of the heavy-ion program with CBM at FAIR. Assuming the J/ψ production cross section to be $\sim$ 1 nb and 10^{10} to 10^{11} protons-on-target (POT) per 10 seconds (spill), the expected production rate with CBM is about 1100 to 11000 events per day. Figure 1 represents the signal efficiency using the geometrical acceptance of the CBM detector versus the proton lab momentum based on fast simulations (PANDAROOT-FastSim package).

The fast simulation results presented in Fig. 1 are compatible with earlier studies that were done with a full simulation using CBMROOT [2] and reported in [3]. For the heavy-ion feasibility studies, an explicit cut on p_t was used resulting to a total efficiency of 5 % (Fig. 1 red circle). To validate our fast simulation results, we studied the effect of the reconstruction efficiency for proton collisions on LH_2 target with different p_t cuts. It turns out that the independent simulation method based on fast simulations is in agreement when looking at a lab momentum of 30 GeV/c and using a p_t cut applied separately on the electrons and positrons at 1.5 GeV/c. For the proposed proton-proton studies, it will be possible to exclude an explicit p_t cut leading to an efficiency gain by a factor of almost $\sim$ 6 to 30 % (red line, no p_t cut). Besides the efficiency studies, we also studied the background yield and evaluated the maximum statistical significance one will be able to obtain. The main background source will be due to the pionic channel via e.g. $pp \to pp\pi^+\pi^-$ with a cross section of about 1 mb. Taking into account the expected capabilities of CBM and by making use of kinematic constraints (energy-momentum conservation), we expect to be able to reach a high signal-to-background ratio of about $s/\sqrt{s+b} \sim 100$ within 1 month of beam time (30 days) with **10^{11} POT**. Figure 2 illustrates the corresponding invariant-mass spectrum of the dilepton pair under these conditions using a product of duty cycle and reconstruction efficiency to be 10 %. In conclusion, the proton beam foreseen with SIS100 in combination with the CBM detector opens a window towards accessing the $p - J/\psi$ final state interaction strength. Cross section measurements near the hidden-charm production threshold are linked to various key topics in the field of strong QCD, namely the intrinsic charm component of the proton, the mass radius of the proton, GFFs and the emergent hadron mass puzzle.

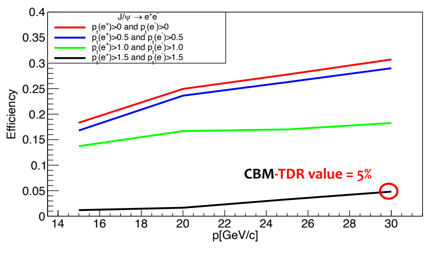

Figure 1: Signal reconstruction efficiency using CBM acceptance for the channel $pp \to ppJ/\psi$ for $J/\psi \to ee, \mu\mu$ decays as a function of the lab momentum for the CBM detector using fast simulations. The different colors represent different p_t cuts i.e. cuts on the transverse momentum applied separately on the electrons and positrons.

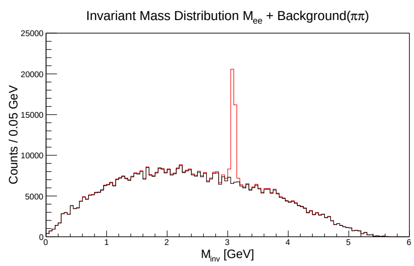

Figure 2: Invariant mass distribution of $M_{inv}(J/\psi \to ee) + M_{inv}(\pi^+\pi^-)$ (red) versus $M_{inv}(\pi^+\pi^-)$ (black).

References

[1] Nature 615, 813816 (2023)
[2] https://git.cbm.gsi.de/computing/cbmroot
[3] https://repository.gsi.de/record/237432

Polarization amplitude estimation based on confidence intervals and Bayes' theorem

V. Tempel for the JEDI Collaboration

While examining the data for the spin coherence time measurement, it was observed that a bias arises when fitting the amplitude P of a sine-wave, particularly when dealing with small amplitudes [1].
In application to the precursor data from COSY the argument of the sine-wave is directly related with the spin tune and the turn number, while the amplitude represents the amount of Polarization, corresponding to a probability density for observation in the detectors. This probability density is of the type:

$$f(x) \propto (1 + A\sin(x) + B\cos(x)) = (1 + P\cos(x-\phi)) \quad (1)$$

For a simple least squares χ^2 fit the estimated value for P tends to be consistently larger than the actual amplitude. This discrepancy is apparent, especially for the special case $P = 0$, where the fit still finds a signal amplitude, because of the statistically fluctuating data. The uncertainty parameter of the fitted amplitude σ_P is decreasing with the number of events N in the sample considered for the fit $\sigma_P \approx \sqrt{2/N}$.

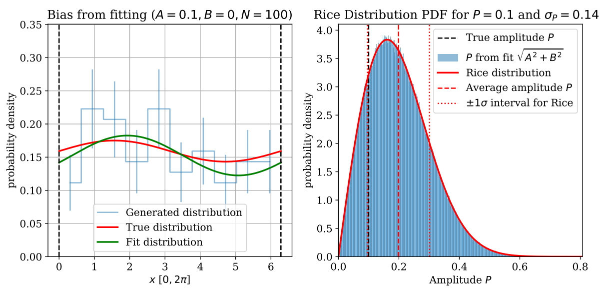

Figure 1: The data for fitting is generated with a true amplitude of $P = 0.1$. In a least squares fit the average result is $P = 0.2$, introducing a notable bias.

The resulting distribution for the fit of P (see Figure 1) is the so called Rice distribution, and its probability density is zero for vanishing amplitudes [1].
For small relative uncertainties regarding the amplitude $\sigma_P/P \ll 1$ the Rice distribution approaches a Gaussian, where the complications described below are negligible. If however σ_P is of the order of the amplitude P (large fluctuations per bin), a naive interpretation of the fit result $\pm 1\sigma$ as a (Gaussian) 68 % confidence interval is wrong. It may even lead to coverage in the unphysical region below zero. To avoid such effects in the analysis of COSY data, the fitting procedures have to be studied carefully.
An approach based on the Feldman-Cousins algorithm of likelihood ratios can be used to construct improved confidence intervals with coverage only in the allowed region $P \geq 0$. In an application of Bayes' theorem a probability density $\tilde{f}(P|\hat{P})$ for the true P, given a measured $\hat{P}$, finally leads to better estimates of the true amplitude compared to simple fitting procedures. In the experimental data the decreasing horizontal polarization due to decoherence has to be considered as well. In a simple model it can be approximated by an exponential function with a decay constant τ, which is the spin-decoherence-time.
In Figure 2 an example for a fit regarding simulated data is given. Again a least squares fit clearly overestimates τ, if small polarization amplitudes are to be included in the fit. With the likelihood function

$$L = \prod_{i=1}^{N_{\text{bin}}} \tilde{f}\left(P_0 \exp\left(\frac{-t_i}{\tau}\right) \middle| \hat{P}_i \right) \quad (2)$$

using the proper probability distribution $\tilde{f}$, the fit typically gives a result closer to the true input values.

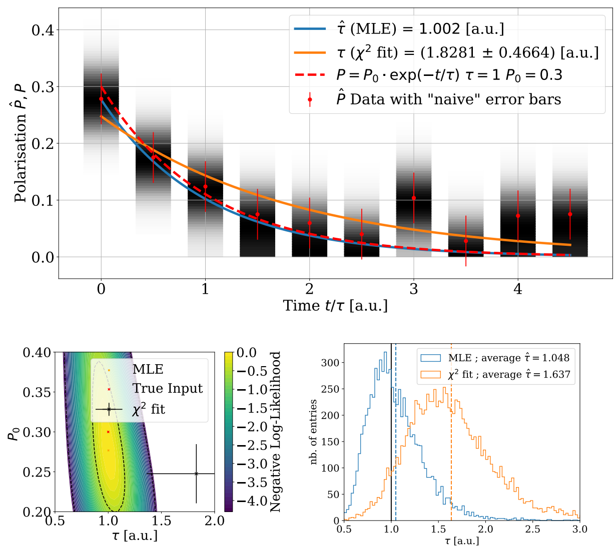

Figure 2: Example for improved fitting procedures. The dashed red line represents the true distribution, i.e. the input for the simulation. The vertical bands at each time bin show the probability density $\tilde{f}(P|\hat{P})$ as a function of P, where $\hat{P}$ is the generated value.

The uncertainties and correlation for the parameters of the MLE in each fit can be investigated by examining the environment around the minimum of the likelihood function. Repeating the fit shows: While the uncertainty regarding the starting amplitude P_0 remains similar, the bias for τ is significantly reduced.

References

[1] D. Eversmann et. al., "Amplitude estimation of a sine function based on confidence intervals and Bayes' theorem" JINST (2016) 11 arXiv:1512.08715.

Progress towards a direct measurement of the deuteron Electric Dipole Moment at COSY

A. Andres for the JEDI Collaboration

The Standard Model of elementary particle physics fails in explaining the observed imbalance between matter and antimatter in the universe. To comprehend the matter-antimatter asymmetry, additional phenomena violating CP symmetry are required according to A. Sakharov. Subatomic particles' Permanent Electric Dipole Moments (EDM) show a break in CP violation if the CPT theorem is valid. This report summarizes the ongoing analysis of the Precursor I (2018) and II (2021) experiments, which aim to measure the deuteron EDM at COSY.

Within a storage ring, the spin motion can be characterized by the invariant spin axis, denoted as $\vec{n}$. This axis is defined by the rotation axis around which the in-plane component of the spin vector precesses. In the presence of a non-zero EDM within an ideal storage ring, the invariant spin axis experiences a tilt in the radial direction ($\vec{n}_x$). The primary objective of the experiment is to determine the direction of the invariant spin axis. However, magnetic misalignments introduce additional tilts in both the longitudinal and radial directions. Consequently, comparing the results to a comprehensive simulation model of COSY becomes crucial to distinguish the genuine EDM signal from misalignments. The longitudinal component of the invariant spin axis can be measured at three different location in the COSY storage ring, namely the Siberian Snake, the 2MV Solenoid and the rf Wien filter. The radial component, containing a potential EDM signal, can only be measured at the rf Wien filter. The location of the devices is shown in Figure 1. The findings that were already presented in previous reports are summarized in Table 1 [1].

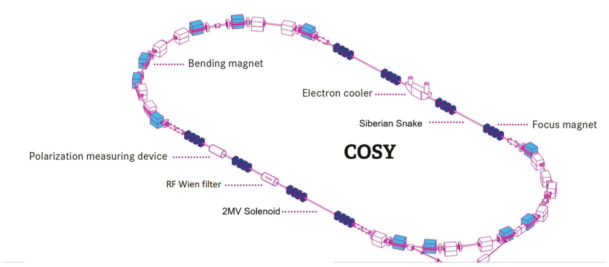

Figure 1: Schematic of the COSY storage ring. The longitudinal component $\vec{n}_z$ of the invariant spin axis can be measured at the Siberian Snake, 2 MV Solenoid and rf Wien filter. The radial component $\vec{n}_x$ can only be measured at the rf Wien filter.

Ongoing analyses are concentrated on comprehending the obtained experimental outcomes. In an ideal scenario, the longitudinal component $\vec{n}_z$ would consistently equal zero throughout the entire ring. Alignment initiatives undertaken between the two

Table 1: Summary of experimental results.

Device	Obs.	Prec. I	Prec. II
rf WF	$\vec{n}_x$/mrad	$-3.36(4)$	$-1.78(8)$
	$\vec{n}_z$/mrad	$4.12(3)$	$-3.24(8)$
Sib. Snake	$\vec{n}_z$/mrad	$0.54(5)$	$-0.0612(9)$
2 MV Sol.	$\vec{n}_z$/mrad		$-0.0585(5)$

experiments have notably enhanced the results at the Siberian Snake by a factor of ten. The order of magnitude for the longitudinal component of the invariant spin axis at the Siberian snake and the 2 MV Solenoid can be covered by spin-tracking simulations including the knowledge about all COSY parameters. Although the order of magnitude of $\vec{n}_z$ at the 2MV Solenoid and the Siberian Snake remains the same during Precursor 2, the corresponding value at the rf Wien filter is unexpectedly two orders of magnitude larger, given that they are only 8 m apart. The reason for this mismatch remains unclear. During the year many systematic studies were conducted:

Beam Time 2023: During the last JEDI beam time in 2023 many orbits for different steerer settings were measured to support the COSY simulation group with experimental data. In addition, the direction of the electro magnetic fields were tried to measure. An unknown rotation of the electromagnetic fields in the rf Wien filter leads to a bias in the determination of the invariant spin axis. Unfortunately, these measurements didn't come to a conclusion.

Event Studies: By systematically filtering events inside the bunch structure, the bunch itself was probed for inconsistencies in polarization. It was found that all particles are behaving consistently.

Inductivity of the rf Solenoid: The idea was raised whether the rf Solenoid resonance circuit might pick up rf signals from the rf Wien filter leading to undesired spin kicks. A measurement at the circuit when running the Wien filter disregarded the idea.

New methods: In 2021 a new method for measuring the invariant spin axis was conducted using two bunches while only the signal bunch is affected by the rf Wien filter. The so-called unaffected pilot bunch can be used to probe systematics. While the method worked the findings of the large tilts of the invariant spin axis remain unclear.

References

[1] A. Andres, The Search for Electric Dipole Moments of Charged Particles in Storage Rings, 20th Conference on Flavor Physics and CP Violation, Oxford, MS, (2022).

Spin tracking simulations of polarized hadron beams at GSI/FAIR storage rings

Daoning Gu on behalf of the JEDI Collaboration

The axion/axion-like-particle (ALP) field has an effect on the spin motion of particles in storage rings, which leads, among other effects, to an oscillating Electric Dipole Moment (oEDM). This report covers preliminary simulations of possible axion/ALP searches that can be performed at existing GSI/FAIR accelerators with polarized hadron beams[1]. The lattices used for the investigation were converted from MAD-X to BMAD format.

The preservation of a long polarization is a prerequisite for such experiments. The spin tune is energy dependent $\Delta\nu_s = G\Delta\gamma$. The momentum of particles slightly varies, which lead to spin tune changes. The 1st order effect can be canceled by bunching the beam using RF cavities. Sextupole magnets can be used to correct the 2nd order effect, and thus minimize the spin tune spread $\Delta\nu_s$. It has been shown in[2, 3] that the reciprocal of the Spin Coherence Time (SCT) has a relationship with sextupole magnet currents as follows:

$$\frac{1}{\tau} = |A + a_i I_i| \cdot (\Delta x)^2 + |B + b_j I_j| \cdot (\Delta y)^2 + |C + c_k I_k| \cdot \left(\frac{\Delta p}{p_0}\right)^2, \tag{1}$$

where τ is the SCT. Δx and Δy are deviations of the particle in the x and y directions. $\Delta p/p$ is the relative momentum deviation. A, B and C are natural chromaticities. I_i, I_j and I_k are currents applied to sextupoles. In Figure 1, the $\Delta\nu_s$ of low energy and high energy deuterons are shown separately. It can be seen that quadratic relations between $\Delta\nu_s$ and $\Delta p/p$ are also followed in ESR.

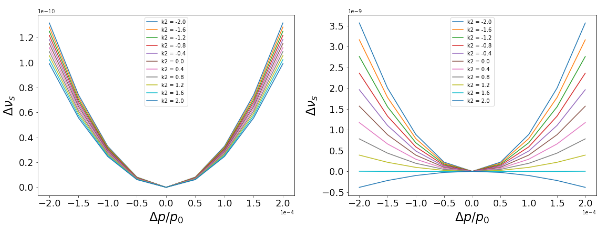

Figure 1: Simulated spin tune spreads $\Delta\nu_s$ of a single particle with different momentum deviations $\Delta p/p$ for ESR. The energies of the deuteron were set to 100 MeV (left) and 1000 MeV (right). Different colors represent normalized sextupole strengths k_2.

The optimized setting for minimum $\Delta\nu_s$ can be obtained by flattening those parabolas. For low energy particles, the 2nd order effect is negligible because the velocity β_0 is small: $\gamma = \gamma_0 + \gamma_0\beta_0^2\Delta\delta$. As shown in the left panel of Figure 1, sextupoles will not be able to correct effectively.

Since the oscillation frequency of the axion/ALP is unknown, the entire energy range must be scanned. In an ideal lattice, intrinsic spin resonances arising from vertical betatron motions dominates. The resonance condition is given by[4]: $\gamma G = nP \pm Q_y$, where P is the superperiodicity of the accelerator. For ESR, $P = 6$. n is integer number. Q_y is the vertical betatron tune. Simulated $\Delta\nu_s$ results are shown in Figure 2. For deuterons, $\Delta\nu_s$ increases slowly with energy and no resonance occurs. For protons, two intrinsic resonances are located at Q_y and $6 - Q_y$ respectively. Varying quadruple settings will result in different betatron tunes, which in turn changes the energy of resonances. The parameter space for such an optimization would include 5 groups of quadruples and up to 4 groups of sextuples, which would be time consuming for brute force simulations using classical algorithms. A new multi-parameter optimization method is still under investigation.

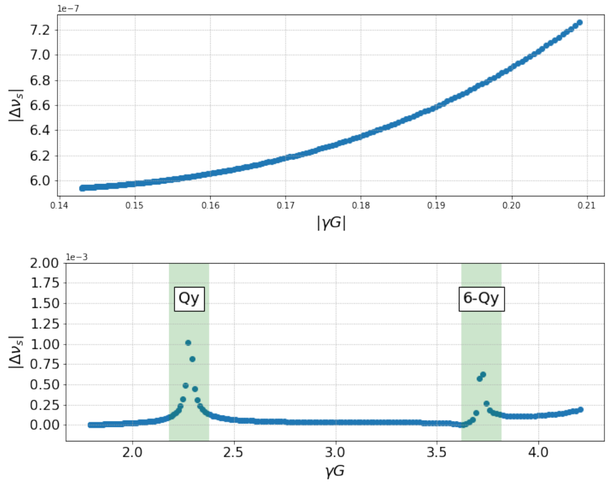

Figure 2: Simulated spin tune spreads $\Delta\nu_s$ for a single deuteron (top) or proton (bottom) with vertical offset in the full energy range. Absolute values were taken to make the results sorted by their energies. The two intrinsic resonance regions of the proton are marked in green.

[1] T. Stoehlker et al., Towards experiments with polarized beams and targets at the GSI/FAIR storage rings, 19th Workshop on Polarized Sources, 2022.

[2] D. Gu, Master thesis, RWTH Aachen University, 2022.

[3] G. Guidoboni et al., Phys. Rev. Accel. Beams 21, 024201, 2018.

[4] S.Y. Lee, Spin dynamics and snakes in synchrotrons, World Scientific, 1997.

Optimization of Spin Coherence Time at the Prototype Storage Ring

Rahul Shankar, on behalf of the JEDI collaboration

In this report, the recent progress in the optimization of spin coherence time at the prototype storage ring is discussed. In previous work [1], optimization was performed by simulating roughly 1000 protons in the BMAD prototype lattice [2]. However, moving forward, efforts were made to understand spin behaviour in frozen-spin lattices at a fundamental level, starting with modelling the spin tune of single particles.

1 Spin Tune Model

It is well known that the spin tune in a pure magnetic ring is given by $\nu_s = \gamma G$. But in a storage ring using both magnetic and electric fields for bending, the spin tune is given by:

$$\nu_s = \gamma G - \frac{r(G+1)}{\gamma(\beta + r)} \qquad (1)$$

It is more useful to rewrite this in terms of phase-space coordinates of the particle, which in this case would be $\delta = {}^{\Delta p}/_{p}$. A very good approximation of the resulting function would be:

$$\nu_s = \sigma_0 \delta + \sigma_1 \delta^2 \qquad (2)$$

These so-called "spin-tune factors" σ_0 and σ_1 (first and second order respectively) can be calculated from eq(1) or measured through simulations. The current study focuses on the empirical approach of measurement of factors from simulation data.

The model described by eq(2) does not take into account the presence of transverse and longitudinal focusing which can be present in the ring. When investigated, the data showed that spin tune changes linearly with the transverse emittances, and also proportionally with the square of the steady-state momentum offset of the particle, which can be thought of as the "longitudinal emittance".

Furthermore, chromaticity and phase slip (momentum compaction) of the second order present in the ring was also observed to proportionally influence spin tune by an amount proportional to the particle's corresponding emittance [2].

Combining all these factors, the model proposed for the time-averaged spin tune $\langle \nu_s \rangle$ now becomes:

$$\langle \nu_s \rangle = \epsilon_i a^i + \epsilon_i M^i{}_j \xi^j \qquad (3)$$

Here, the indices $i, j \in \{1,2,3\}$, and the Einstein summation convention is followed for repeated indices. The arrays ϵ_i and ξ^j are assigned as follows:

$$[\epsilon_i] = \begin{bmatrix} \epsilon_x & \epsilon_y & \frac{\delta_a^2}{2} \end{bmatrix} \quad [\xi^j] = \begin{bmatrix} \xi_x \\ \xi_y \\ \eta_1 \end{bmatrix} \qquad (4)$$

…where ϵ_x and ϵ_y are the horizontal and vertical emittances, ξ_x and ξ_y are the horizontal and vertical chromaticities, and η_1 is the second-order phase-slip factor. The three parameters arranged in the vector a^i and the nine matrix elements $V^i{}_j$ are free parameters which set the strengths/couplings of the respective contributions to the spin tune.

These parameters were simultaneously fit to spin tune data gathered from simulations of particles with various emittances stored in lattices with various second-order optical settings, using the model described by eq(3). The complete model was then used to calculate the spin tunes of a fresh set of samples whose spin tunes were also measured using BMAD. The result of a comparison between the measured and calculated values is shown in Figure 1.

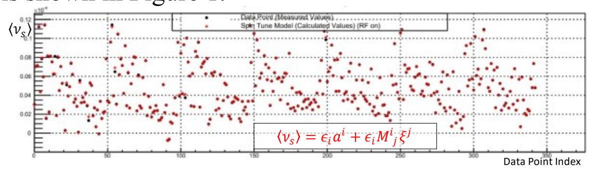

Figure 1: A plot comparing the spin tunes as measured by BMAD and those determined by the spin tune model of eq(3).

The agreement between the measured and calculated values demonstrates the accuracy of the model.

2 Using the spin tune model in SCT optimization

If eq(3) were re-written as…

$$\langle \nu_s \rangle = \langle \epsilon \rangle_i \left(a^i + M^i{}_j \xi^j \right) \qquad (5)$$

…it is intuitive to understand that there can exist a particular optical setting such that:

$$a^i + M^i{}_j \xi^j = 0 \qquad (6)$$

In such a setting, it is clear that the time averaged spin tune of a particle would essentially be zero regardless of its emittance or momentum offset amplitude. Therefore, it can be seen that in principle, all the particles in a bunch should exhibit close to zero spin tune and so the bunch as a whole would have a very high spin coherence time.

Given that the model be highly accurate, this special setting is simply estimated by:

$$\xi^j = -(M^{-1})^j{}_i a^i \qquad (7)$$

This way the optimized point can be determined through single particle simulations alone. However, the optimized setting for SCTs higher than 1000s is highly sensitive to the sextupole settings. Thus, as seen from recent attempts, determining this from the single-particle model demands a much higher precision from the model. This is currently the primary focus of this ongoing work.

3 References

[1] R. Shankar, P. Lenisa and A. Lehrach, "Optimization of spin-coherence time for electric dipole moment measurements," in *19th Workshop on Polarized Sources, Targets and Polarimetry (PSTP2022)*, Mainz, Germany, 2022.

[2] CPEDM Collaboration, "Storage ring to search for electric dipole moments for charged particles: Feasibility study," CERN Yellow Reports: Monographs, Geneva, 2021.

[3] Yoshihiko Shoji, "Dependence of average path length betatron motion in a storage ring," *Physical Review Special Topics - Accelerators and Beams,* vol. 8, p. 094001, 2005.

Determination of ISA correction factors

M. Vitz on behalf of the JEDI Collaboration

This report covers the analysis of correction factors for the determination of the Invariant Spin Axis (ISA) in a Bmad COSY model for deuterons. The simulation model uses predefined quadrupole settings to create a sixfold optical symmetry at an energy of 0.97 GeV/c. All magnetic and electric elements implemented in the simulation model were designed to match their counterparts in the real COSY storage ring as it was used in the beginning of 2021. Within the last year an investigation was started how a steered orbit impacts the determination of the ISA [1]. For this reason, a set of perturbated orbits was created by using vertical and horizontal correctors. A Gaussian distribution centered around zero was used to generate random kick values for the correctors. Its width was chosen in a conservative way so that all randonmly steered orbits could yield a closed orbit. The long. tilt n_z of the ISA can be measured in an experiment using a solenoid (see c_{sol} in formula 1) or a Radiofrequency (RF) Wien filter plus a solenoid (see $\xi_{SN,0}$ in formula 2). These experimental conditions were implemented in the simulation model and their results had been compared to the directly calculated ISA at the position of the devices. The results are sketched in figure (1) and figure (2).

$$\Delta\nu_s = \frac{1}{\pi}\Bigg(\cot\pi\nu_s\cdot\cos\left(\frac{B_{sol}k_{sol}}{2}-1\right) \\ -c_{sol}\cdot\sin\left(\frac{B_{sol}k_{sol}}{2}\right)\Bigg) \tag{1}$$

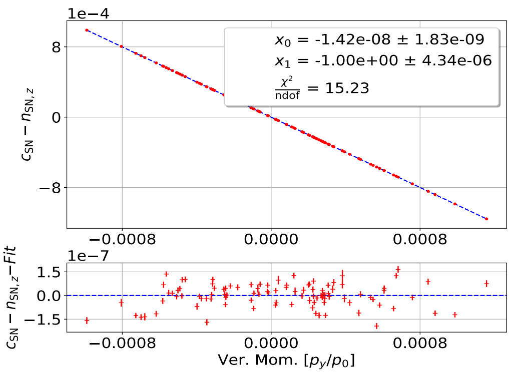

Figure 1: Dependency of difference between Snake fitparameter c_{sol} and long. ISA at the position of Snake solenoid on the vertical momentum when passing the device.

$$\epsilon_{EDM} = \Bigg[A_{WF}^2\left(\phi_{WF}-\phi_{WF,0}\right)^2 \\ +A_{SN}^2\left(\frac{\xi_{SN}}{2\sin\left(\pi\nu_{s,0}\right)}-\xi_{SN,0}\right)^2\Bigg]^{1/2}+\epsilon_0 \tag{2}$$

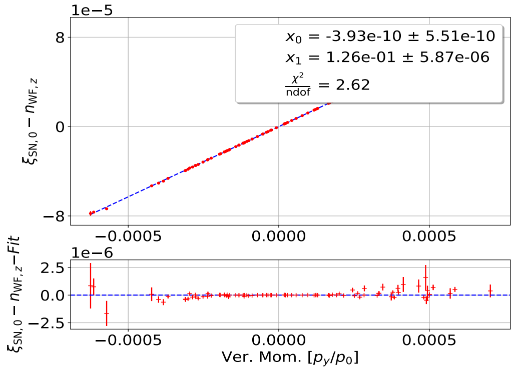

Figure 2: Dependency of difference between Wien filter Minimum ξ_{SN} and long. ISA at the position of RF Wien filter on the vertical momentum when passing the device.

The outcome of this investigation indicates a linear dependency of the difference in between directly calculated ISA and experimentally obtained ISA on the vertical momentum $p_{y,i}$, when passing a device and the vertical tilt of the device $n_{y,WF}$ against the nominal orbit. A summary of the results in shown below:

$$\xi_{SN} = n_z(s_{WF}) - A\cdot p_{y,WF} - B\cdot n_{y,WF} \tag{3}$$

$$c_{sol} = n_z(s_{sol}) - C\cdot p_{y,sol} \tag{4}$$

It has been found that the fit paramter A corresponds to $\gamma-1$ by changing the particle energy within the simulation model. All other fit parameter correspond to a value of 1, which reflects a transformation into the particles reference frame. The dependency of the difference on the tilt of the solenoid $n_{y,sol}$ is very weak and can be neglected. A correction factor needed for the radial determination of the ISA (see $\phi_{WF,0}$ in formula 2) could not be observed. This procedure is under further development to fit the experimental conditions even better. Therefore the idealized RF Wien filter field was replaced with a simulated grid field of the device. This might change the fit parameter A and B in the near future.

[1] M. Vitz, A Lehrach, J Pretz, *Determination of the Invariant Spin Axis in a COSY model using Bmad*, Proc. 14th Int. Particle Acc. Conf., TUPM076, 2023 DOI:10.18429/JACoW-IPAC2023-TUPM076

Study of Beam-Target Simulations for Prototype Electric Dipole Moment Storage Ring

S.Siddique for the JEDI and CPEDM Collaboration

This report focuses on simulations of the interaction between a proton beam and pellet target of prototype EDM storage ring. To measure polarization, a pellet target scatters the beam at the ring's bending arc, directing it towards polarimetry for polarization measurement. Analytical calculations [1] highlighted the pellet target's impact on beam losses, necessitating simulations to optimize the target size and position, aiming to minimize these losses. The pellet target, strategically placed just before the bending arc, scatters a portion of the primary beam. As the scattered beam passes through bending elements, it diverges from the original beam, and a second target at the polarimeter is introduced to measure polarization. Parameters for both the beam and target are detailed in Table 1.

Beam		**Target**	
Energy	30 MeV	Density	3.52 g/cm^3
Particles	10^5	Diameter	50 μm
$\epsilon_{x,y}$	1μ mrad	velocity	60 m/s
$\delta p/p_0$	10^{-4}	Gap	60 mm
$< E >_{loss}$	0.23 MeV	Θ_{rms}	3.5 mrad

Table 1: Beam Target parameters, where $< E >_{loss}$ = Average loss, Θ_{rms}= RMS scattering angle.

Using Wolfram Mathematica, simulations employed transfer matrices to observe the post-collision behavior of particles. Initially, two vertically moving spherical pellets, positioned with a fixed gap at the center of the beam-pipe, caused scattering upon interaction. As these targets traversed the beam, multiple particles were hit and deflected. For instance, with 50μm pellets, out of 411 particles hit, approximately 96% were lost at the bending plates, leaving only a few to reach to the straight section for detection.(see Figure 1).

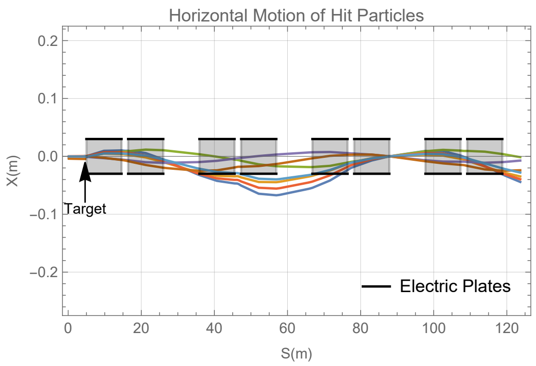

Figure 1: Horizontal motion of survived particles from bending plates after scattering with 50μm targets.

Simulations were run by varying pellet sizes ($40\mu m, 30\mu m, 20\mu m$) and comparison between outputs can be seen in Table 2.

Diameter(μm)	Hits	Lost*	Survived
50	411	394(96%)	17
40	275	252(92%)	23
30	148	134(90%)	14
20	50	35(70%)	15

Table 2: Comparison of different pellet targets sizes. * Particles which lost due to bending plates.

It is much clear that less particles are losing due to bending plates as pellet size gets thinner but below 20μm cannot be considered due to technical limits. However, a hung chunk of particles lost due to bending plates. This compelled to shift pellet target between bending plates and results with all sizes are encouraging and comparison can be observed in table 3. For 50μm pellets, scattered beam horizontal motion can also be seen in figure 2.

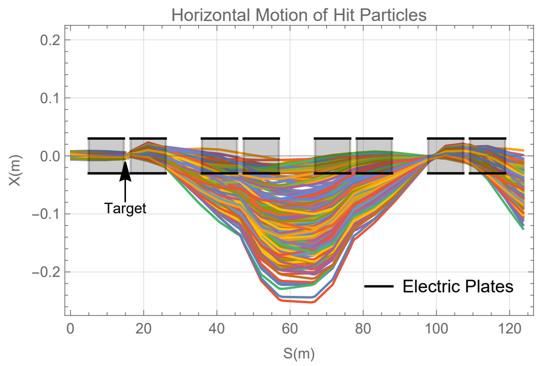

Figure 2: Horizontal motion of survived particles with target's impact at center of the arc

Diameter(μm)	Hits	Lost*	Survived
50	504	326(64%)	178
40	326	175(54%)	151
30	172	61(35%)	111
20	78	21(27%)	57

Table 3: Comparison of different pellet targets sizes. * Particles which lost due to bending plate.

In summary, positioning the pellet target at the center of the arc (between the bending plates) proves far more practical than locating it at the arc's start. This placement is crucial for effectively separating scattered particles from the original beam immediately after beam-target interaction.

References

[1] S. S. et al., *Simulations of beam dynamics and beam lifetime for the prototype EDM ring*, in Proc. IPAC'23.

Determining quadrupole magnetic length shortening in COSY using a Bmad model

M. Margos on behalf of the JEDI collaboration

The JEDI collaboration aims to measure the electric dipole moment (EDM) of deuterons. EDMs of subatomic particles violate time reversal and parity symmetries. Assuming that the CPT theorem holds, they also violate CP, and thus help explain matter-antimatter-asymmetry in the universe. EDMs of charged particles can be measured in storage rings like COSY. Simulations of COSY are required to support the analysis and understand systematic effects. Betatron oscillations are an important characteristic of accelerators and describe the transverse oscillation of a particle beam around the nominal orbit. The betatron tune denotes the number of oscillations per revolution. Measurements and simulations in Bmad show significant deviation. Since quadrupole magnets have the greatest effect on betatron tunes, the possibility of magnetic shortening of quadrupole magnets shall be investigated.

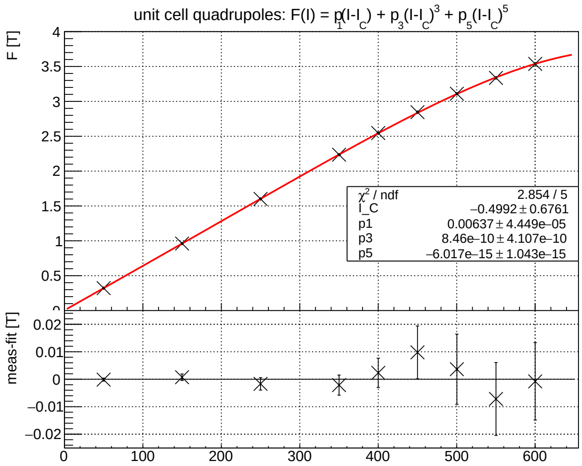

Figure 1: fitting focus strength over current with odd polynomial, shifted by coecitive current I_C.

In a first step, measurements of the focus strength F vs. current I for 34 telescope quadrupoles and 26 unit cell quadrupoles are analysed. The focus strength F is defined as [1]

$$F(I)\,[\mathrm{T}] = \int \frac{dB_y(I,s)}{dx}\,ds = g(I)\,\ell_{\mathrm{eff}}.$$

Those measurements are scanned, digitized via optical character recognition (OCR), plotted, and an odd polynomial, shifted by coercitive current I_C, fitted to telescope and unit cell quadrupoles respectively. Using the effective magnetic length ℓ_{eff} from V. Poncza's measurement[2], the current-dependent gradient g can be inserted into Bmad's description of quadrupoles in COSY.

During the operation of COSY, the betatron tune is measured by reading the difference signals at

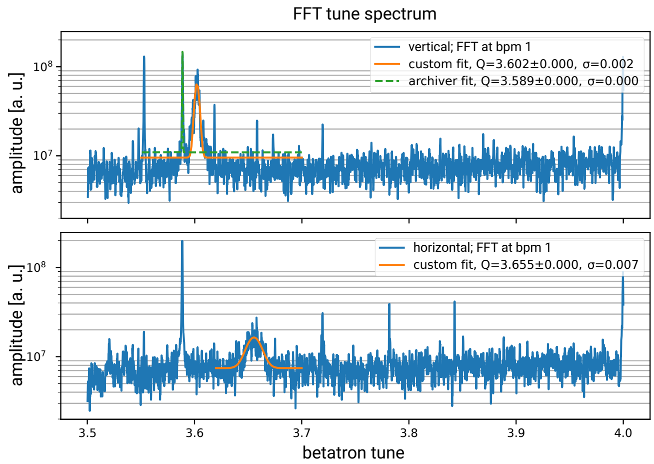

Figure 2: The online tune measurement, as saved in the archiver, may fit the wrong tune peak, or find no tune at all.

beam position monitors (BPMs) at revolution frequency, fast-fourier-transforming these, and re-mapping them to betatron tune range of $[3.5, 4.0]$, as shown in Figure 2. A gauss+background fit is made for each active BPM for both horizontal and vertical direction, and a weighted average of gaussian peaks among the BPMs and their uncertainties is used to determine both horizontal and vertical betatron tunes. The FFT spectra, the corresponding fit range, the fit results and the tunes are then saved in the archiver.

This automatic tune measurement is prone to errors, as it may fit the wrong peak on a noisy BPM, or the fit fails for small signals. Some peaks are due to coupling of horizontal betatron oscillation into the vertical plane and vice versa. Also, previous calculations restrict the tunes with a precision of ≈ 0.1. Therefore the tune is re-calculated by re-fitting the FFT spectra, while dynamically restricting the fit range and discarding data from a noisy BPM.

References

[1] G. Schnell, Magnete, Grundlagen - Aufbau - Anwendungen, Verlag Karl Thiemig, 204 (1973)

[2] V. Poncza, PhD Thesis, Extensive Optimization of a Simulation Model for the Electric Dipole Moment Measurement at the Cooler Synchrotron COSY, 67 (2021) DOI: 10.18154/RWTH-2021-04834

Electronic System of OSIRIS

Runxuan Liu

The Jiangmen Underground Neutrino Observatory (JUNO) experiment [1] is a 20 kt liquid scintillator (LS) detector currently under construction in China. Its main goal is to determine the neutrino mass ordering (NMO) by detecting antineutrinos from two nuclear power plants at 53 km baseline. The radiopurity of the LS is crucial in determination of the NMO. The Online Scintillator Internal Radioactivity Investigation System (OSIRIS) pre-detector of JUNO has been designed and installed to monitor the radiopurity of LS during the several months of filling to the main volume of JUNO. The OSIRIS design has been optimized for sensitivity to the ^{238}U/^{232}Th decay rates via tagging of the respective ^{214}Bi-^{214}Po and ^{212}Bi-^{212}Po coincidence decays in the ^{238}U and ^{232}Th decay chains. The contamination levels of ^{210}Po, ^{14}C, and ^{85}Kr in the LS can also be determined by OSIRIS.

OSIRIS is equipped with 76 20-inch Microchannel Plate (MCP) Photomultiplier Tubes (PMTs). There are 64 of them observing the inner detector, which contains the 18-tons LS target, surrounded by water. The remaining 12 PMTs are installed in the water Cherenkov detector, which surrounds the inner detector that is optically separated.

The electronics system design of OSIRIS is similar to the JUNO main detector. As illustrated in Figure 1, every three PMTs are connected to one Under Water Box (UWB) with bellows, which contains three High Voltage Units that power the PMTs and one Global Control Unit (GCU) that realizes several functions as front-end electronics. The GCU can receive the global reference timestamps from the Back End Card (BEC) for data acquisition and processing. There are 6 channels of ADC providing digitized waveform data from both high-gain and low-gain of the three PMTs. All the 27 UWBs of OSIRIS are connected to one BEC, which also provides trigger.

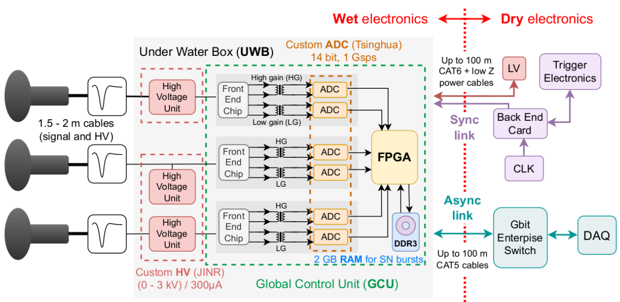

Figure 1: Schematic of the electronics system of both JUNO and OSIRIS. [2]

In 2023, Runxuan Liu from the IKP-2 neutrino group contributed to electronics testing for OSIRIS. All GCUs for OSIRIS PMTs have passed the tests in the Surface Assmbly Building (SAB) at JUNO site. The tests include a ping test, a fake ADC linearity test, and a bert test, for each GCU. One OSIRIS support computer was successfully configured with hardware network connections for GCUs, one BEC, and low voltage power supply (for UWBs), as well as testing software. Later, the configuration was also used for testing the readout chain of PMTs and the electronics of OSIRIS underground after the installation.

A prototype DAQ software was implemented for the first commissioning data of OSIRIS. The first commissioning data from air run with the OSIRIS calibration LED source was acquired in September 2023. The timing signals of the LED pulses are used as external trigger for acquiring the data from the PMTs with a 1008 ns time window. A decoder of the raw data has been developed to validate the data structure and integrity, as well as to extract the useful information, including trigger timestamps with the corresponding PMT pulse shapes in both high-gain and low-gain in all 76 PMT channels. One example of a typical waveform from a single PMT is shown in Figure 2.

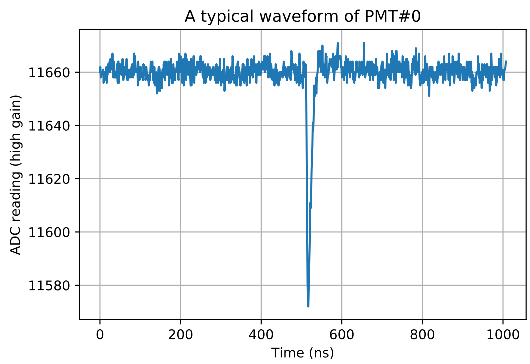

Figure 2: One waveform (high gain) of PMT No. 0 in a LED test run.

Further work on the commissioning data is still in progress, including analysis on the noise level, single photon separation, and time correction for different positions of the LED source.

References

[1] JUNO collaboration. "JUNO physics and detector." Progress in Particle and Nuclear Physics 123 (2022): 103927.

[2] Cerrone, Vanessa, et al. Nuclear Instruments and Methods in Physics Research Section A 1053 (2023): 168322.

Directional solar neutrino analysis in JUNO

M. Malabarba

JUNO (Jiangmen Underground Neutrino Observatory) is a multipurpose neutrino physics experiment currently under construction in China. Its central detector is composed of a 17.7 m acrylic sphere, filled with 20 kton of organic liquid scintillator, and a stainless steel structure, built to sustain 43212 photomultiplier tubes (PMTs) all around the sphere. The main goal of the experiment is to determine, through the detection of antineutrinos from nearby nuclear power plants, the neutrino mass ordering with a 3σ significance in about six years of data-taking.
However, thanks to its unique features, such as its large active mass, a complex strategy for radioactivity control of all its components, and an unprecedented energy resolution, JUNO will be a perfect candidate to study solar neutrinos as well. In JUNO, solar neutrinos mainly interact with the liquid scintillator electrons through elastic scattering reactions. The scattered electrons then deposit their energy and produce scintillation and Cherenkov light that is detected by the PMTs. Since solar neutrinos interactions do not produce multiple signals in temporal coincidence, all the β-like decays of unstable nuclides, in the liquid scintillator and surrounding the central detector, will be backgrounds.
The *Correlated and Integrated Directionality* (CID) analysis can be exploited to statistically separate solar neutrino events from background ones. CID relies on the directionality of the Cherenkov light: when a signal interaction takes place, the angle between the incoming solar neutrino and the scattered electron is small (typically $< 20°$ in the chosen regions of interest). Hence, as shown in Fig. 1, the PMT hits caused by Cherenkov photons exhibit a correlation with the Sun position: the distribution of $\cos\alpha$, where α is the angle between the neutrino direction and the event position - hit PMT vector, has a peak around 0.7. Since scintillation photons are emitted isotropically, their hits do not exhibit any correlation with the Sun position instead. Even though in liquid scintillator detectors the Cherenkov light is heavily sub-dominant ($< 1\%$ of the total emitted photons), it is emitted almost instantaneously ($\sim$ ps); whereas the scintillation light is emitted after a delay that ranges from a few ns to several hundreds of nanoseconds. As a consequence, the Cherenkov light will typically reach the PMTs earlier than the scintillation photons and the earliest PMT hits will retain the directional information. On the other hand, for backgrounds events, the $\cos\alpha$ distributions of Cherenkov and scintillation photons are both flat since the particles produced in nuclear decays are emitted in random direction. The CID technique was developed by the Borexino collaboration [1] and was exploited to obtain the most precise results on CNO neutrinos [2]. In the last year, several studies have been performed to evaluate the potentialities of the CID technique in JUNO as well. In particular, two distinct regions of interest, called ^{7}Be ROI and CNO ROI, were considered and, in both of them, toy Monte Carlo $\cos\alpha$ PDFs were produced for signals and backgrounds. From those, several thousands of pseudodataset were generated, with realistic assumptions about the number of signal and background events, and then fitted to evaluate JUNO precision in reconstructing solar neutrinos events. Finally, the CID results can be used as an external constraint in the spectral analysis [3], which exploits the different energy spectral shapes of signals and backgrounds. The combination of the two analyses allows to improve JUNO sensitivity to the ^{7}Be and CNO solar neutrino species.
In particular, I performed the whole workflow in the ^{7}Be region of interest. The preliminary results show that the combination of the CID and spectral analyses could potentially yield the most precise measurement of ^{7}Be ever achieved. Furthermore, I am working on the implementation of a solar neutrino generator for the official JUNO simulation software. This will allow to produce full Monte Carlo $\cos\alpha$ PDFs and to thoroughly evaluate the impact of various CID systematics on JUNO sensitivity to solar neutrinos.

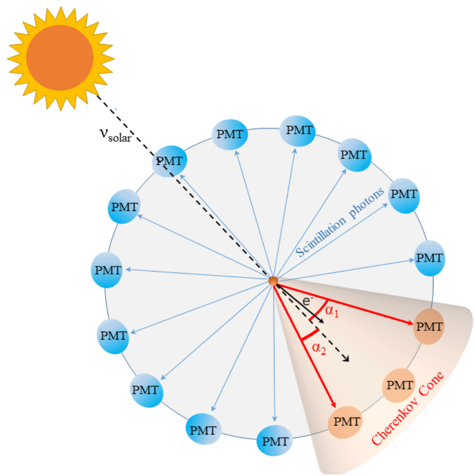

Figure 1: Schematic representation of the angular correlation between Sun position and the Cherenkov hits in a signal event [1].

References

[1] M. Agostini et al., Phys. Rev. L 128, 091803.
[2] D. Basilico et al., Phys. Rev. D 108, 102005.
[3] A. Abusleme et al. JCAP, 2023(10):022.

JUNO Geoneutrino Sensitivity Study

Yu. Malyshkin

JUNO (Jiangmen Underground Neutrino Observatory) is a liquid scintillator detector in China planned to be constructd by the end of 2024. The main goal of the experiment is to probe neutrino oscillations by measuring the signal from reactor electron antineutrinos ($\bar{\nu}_e$): to determine neutrino mass ordering with at least 3σ confidence level and to measure three out of six independent parameters driving the oscillations, namely "solar" mixing angle θ_{12} and mass splitting Δm^2_{21}, and "atmospheric" mass splitting $\Delta m^2_{31(32)}$ with sub-percent precision.

JUNO will be also able to measure neutrinos from various natural sources: supernova bursts, the Sun, and the atmosphere and interior of the Earth. The later ones, called geoneutrinos, are produced by beta-decay of U, Th, and K radioactive isotopes. JUNO will be able to detect those of them with energy above 1.8 MeV (from ^{238}U and ^{232}Th) via the Inverse Beta-Decay (IBD) channel, the same one as used for detection of reactor neutrinos. Thus, for geoneutrinos, the reactor neutrinos constitute an irreducible and dominant background, as one can see from Fig. 1 showing the geoneutrino and reactor spectra together with other backgrounds (including non-IBD ones).

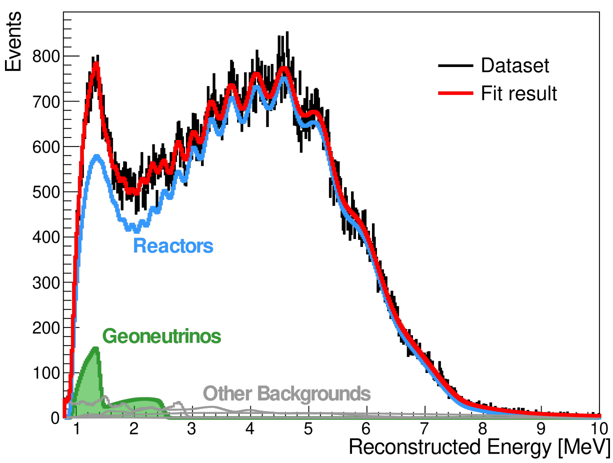

Figure 1: Spectra of geoneutrino, reactor neutrino and other backgrounds for an MC pseudo-dataset.

Although the reactor background is several times larger than the geoneutrino signal in the region of interest, it can be statistically disentangled with a great precision, thanks to the fact that JUNO has been designed for its measurement. JUNO will observe about 1 geoneutrino event per day resulting in 1 year statistics exceeding the number of geoneutrino events accumulated by Borexino [1] and KamLAND [2] together, the only two experiments reporting observing geonuetrinos up to now.

Preliminary geoneutrino sensitivity estimations for JUNO were reported in [3] in 2016. Since then a lot of updates have been made, including changing of the number of nearby nuclear power plants, release of reactor neutrino spectral shape by Daya Bay [4], improvement of the detector response, improved background estimation, and the increase of the exposure thanks to new muon veto strategy.

All the aforementioned updates have been incorporated into a newly setup analysis performed with the fitting tool JUST (Jülich nUsol Sensitivity Tool [5]), adopted for geoneutrino study. It has been found that JUNO will be able to measure the total geoneutrino signal with a precision of 10% (8%) after 6 (10) years of data taking assuming that the Th/U ratio of 3.9, predicted by compositional analysis of chondrites. For comparison, the uncertainty of Borexino and KamLAND measurement was 17% and 15%, respectively. Leaving the Th/U free, JUNO will be able to measure U and Th components separately with a precision of 30% and 35%, respectively, and their sum with a precision of 15% in 10 years. The uncertainties of the neutrino oscillation parameters, making a noticable impact, have been considered for the first time in the geoneutrino analysis of JUNO.

The geoneutrino signal can be split into two components: coming from the lihtopshere and from the mantle. No contribution from the core is expected. The lithospheric signal can be predicted with a precision at the level of 10-15% based on geological and seismic data, while the mantle signal rate predictions differ by an order of magnitude. The mantle's share in the total geoneutrino signal is expected to range from a few percent to about 30% and can only be obtained by subtracting the lithospheric prediction from the measurement of the total geoneutrino signal. A new analysis has been started to estimate JUNO mantle sensitivity. It has been found that the discovery potential will be poor for low mantle signal prediction but can reach $> 3\sigma$ confidence level for high predictions after 6 years of data taking. This analysis has been performed with fixed neutrino oscillation parameters, and their uncertainties are to be included in the future.

Besides that an independent calculation of geoneutrino flux prediction has been performed based on the available geophysical models. Detailed cross-checks with other groups in JUNO are in progress.

References

[1] M. Agostini et al., Phys. Rev. D 101 (2020).
[2] S. Abe, Geophys. Rev. Lett. 49/16 (2022).
[3] F. An, J. Phys. G 43/3 (2016).
[4] F. An, Chin. Phys. C 45 (2021).
[5] A. Göttel et al., Il Nuovo Cimento C 1 (2021)

Sensitivity to intermediate energy solar neutrinos in JUNO experiment

L. Pelicci

JUNO is a 20 kt liquid scintillator detector, currently under construction in Jiangmen, China. Thanks to high statistics and excellent energy resolution of 3% at 1 MeV, it represents a great opportunity for the detection of solar neutrinos. In previous years, I contributed to assessing JUNO's sensitivity to intermediate energy solar neutrinos, namely ^{7}Be, *pep*, and CNO neutrinos. To disentangle neutrino signals from indistinguishable backgrounds, a spectral analysis based on likelihood fit has been implemented. The findings of this analysis demonstrate that JUNO will be able to measure solar neutrino rates with an uncertainty highly competitive in comparison to the current best results. Further details about this analysis are available in [1]. In 2023, I worked on an extension of this analysis, incorporating a novel technique known as *Correlated Integrated Directionality* (CID). This method relies on the detection of sub-dominant, but fast-directional Cherenkov light. In particular, it utilizes the correlation between the direction of the impinging neutrino, defined by the known position of the Sun, and the direction of reconstructed photons. We denote the angle between these two directions as α. Cherenkov hits originated by solar neutrino interactions exhibit a correlation with the position of the Sun, resulting in a characteristic $\cos\alpha$ distribution peaked around $\cos\alpha \sim 0.7$. In contrast, isotropic scintillation and background events do not correlate with the sun, leading to a flat $\cos\alpha$ distribution. This distinctive feature introduces a new powerful tool to differentiate solar neutrino signals from backgrounds. The CID method was originally introduced by the Borexino collaboration, providing a proof of principle to use the sub-dominant Cherenkov information produced by sub-MeV solar neutrinos in a liquid scintillator detector. Additionally, it facilitated the first directional measurement of sub-MeV ^{7}Be [2, 3] and CNO solar neutrinos [4].

My contribution was the development of a C++ code to perform simultaneous χ^2-fits to extract the number of solar neutrino events with a given exposure. The code, based on TMinuit, includes two free parameters (signal and background events) and takes probability density functions (PDFs) from Monte Carlo simulations as input. The code's structure includes the following operations:

- Pseudo-dataset generation: creating random pseudo-datasets by sampling signal and background PDFs, weighted with the expected number of events.
- PDF linear smoothing: implementing a linear function-based smoothing to mitigate statistical fluctuations, with negligible impact as demonstrated by the study.
- Simultaneous fit of N histograms: performing a simultaneous fit on each of the N = 26 histograms comprising each pseudo-dataset using common free parameters.
- Cost function optimization: offering various cost functions, including Pearson χ^2, Neyman χ^2, Combined Neyman-Pearson χ^2_{CNP}, and Likelihood ratio, with χ^2_{CNP} chosen after thorough evaluation.
- Profiling: enabling $\Delta\chi^2$ profiling for a specified parameter of interest.
- Systematic uncertainty: providing the option to incorporate a systematic effect, named position reconstruction bias, as a free nuisance parameter in the fit. This effect, a significant source of systematic error in Borexino, was found to be negligible in JUNO.

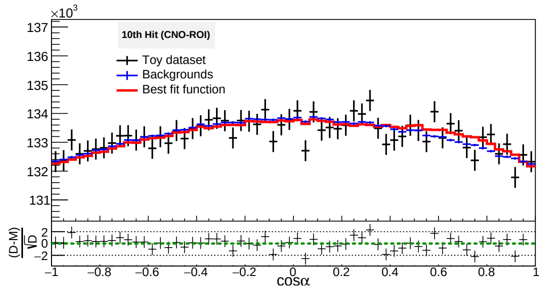

Figure 1: Illustrative example of the Monte Carlo fit of one $\cos\alpha$ spectrum. The pseudo-datasets are shown in black, along with the best-fit functions (red) and background-only hypothesis (blue).

To evaluate JUNO's sensitivity to solar neutrinos, 10^4 psuedo-datasets are generated and subsequently fitted, with an example shown in Fig. 1. Sensitivity is quantified as the median value of the distribution of relative errors on the number of events extracted by the fit. The result can be used as an external constraint in the spectral analysis detailed in [1]. The combined results from both analyses yield a preliminary improvement in the precision of solar neutrino determination with JUNO.

References

[1] A. Abusleme et al. JCAP, 2023(10):022.
[2] M. Agostini et al., Phys. Rev. L 128, 091803.
[3] M. Agostini et al., Phys. Rev. D 105 052002.
[4] D. Basilico et al., Phys. Rev. D 108, 102005.

Simulation of the IBD energy spectra for JUNO

Hexi SHI

The JUNO experiment will measure the reactor anti-neutrino with an energy resolution of 3% at 1 MeV via the Inverse Beta Decay (IBD): $\bar{\nu}_e + p \rightarrow e^+ + n$, The IBD occurs when an electron antineutrino interacts with a proton inside the 20 kton Liquid Scintillator (LS) detector. With a baseline of about 53 km from the closest nuclear reactors, the experiment is optimised to determine the mass ordering of the three neutrino mass eigenstates. The IBD events are characterized by two energy deposition signals separated by a time interval. One promptly after the reaction from the positron and the subsequent back-to-back γ pair after the positron annihilates with an electron. The second "delayed" energy deposition comes from the de-excitation γ from the excited nuclear states, when the neutron is captured by a nucleus in the LS, after an average time of about 200 μs after the reaction.

For the precise analysis of the prompt energy spectrum, a realistic estimation of the spectra shape and the rate for both the IBD signals and the backgrounds is essential. In 2023, the Probability Density Function (PDF) of the prompt energy spectra of the reactor neutrinos and the geo-neutrinos based on the full MC simulation were produced and cross-checked with the analytical models of the detector response. The simulation data sets were produced with the latest JUNO simulation software, which implemented accurate optical models of the LS, the up-to-date geometry models of the Photomultipliers (PMTs), as well as the electronic models of the MPT readout. The data of the MC simulation is also structured in the same way as in real measurement. Then the event reconstruction algorithm and the IBD event selection conditions are applied to the MC data sets, in the same way as to the real measurement data. We obtained the full MC PDF of the expected prompt energy spectra for the reactor antineutrino and the geo-neutrino as shown in Fig. 1 (a) and (b). The comparison between the MC PDFs to the analytically calculated PDFs based on known detector response models shows good agreement. These MC PDFs are used in the on-going sensitivity studies of the geo-neutrino detection in JUNO.

Another key contribution to JUNO is on the simulation of the IBD-like background from the $^{13}C(\alpha,\ n)^{16}O$ reaction, which originates in the α particles from the radioactive contamination in the LS interacting with the ^{13}C ($\sim$1 % abundance in natural carbon) nuclei in the LS material. First, we used an open-source Geant4 based simulation package SaG4n [1] to estimate the neutron yield and to

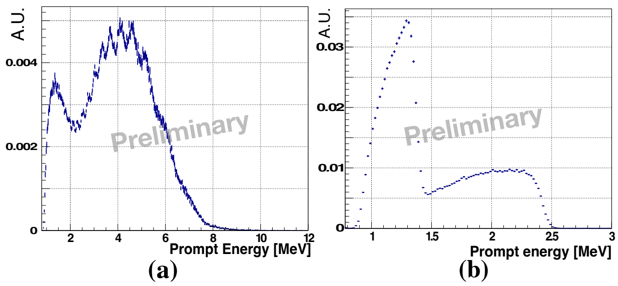

Figure 1: The MC PDFs from the JUNO simulation: (a) reactor anti-neutrino; (b) geo-neutrinos.

simulate the out-going particles from the reaction. We also developed a library within the framework of the JUNO simulation software to transfer the necessary information from the SaG4n simulation results to the JUNO full-detector simulation. After the data production and IBD selection analysis, we produced for the first time the PDF of the $(\alpha,\ n)$ background shape based on the complete JUNO detector as shown in Fig. 2. The contributions from the ^{238}U, ^{232}Th, and ^{210}Po isotopes were taken into account. Until now the PDF from the simulation from the Daya Bay experiment (also shown in Fig. 2) has been used in all sensitivity studies for JUNO.

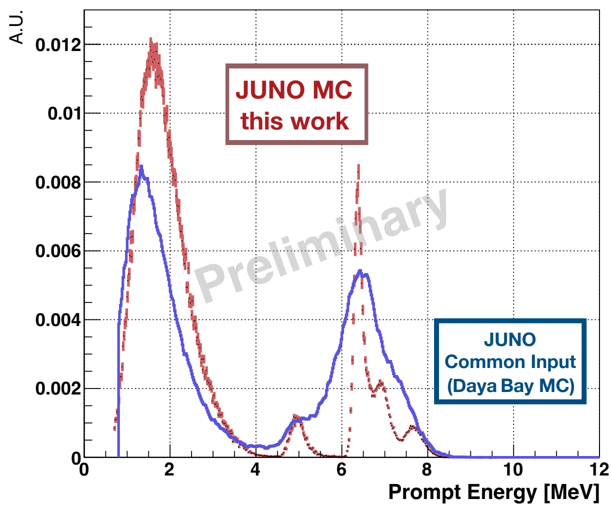

Figure 2: The PDF of the (α, n) backgrounds from the JUNO simulation.

References

[1] E. Mendoza, *et al*, *NIM A* **2020**, *960*, 163659.

Commissioning of the Automated Calibration Unit of the OSIRIS detector

Moritz Cornelius Vollbrecht

The neutrino group of IKP-2 is participating in the JUNO collaboration (Jiangmen Underground Neutrino Observatory) and working on the OSIRIS detector (Online Scintillator Internal Radioactivity Investigation System). This cylindrical detector (Fig. 1) will be used during the months-long filling of the 20 kton JUNO detector to monitor the radiopurity and optical properties of the liquid scintillator (LS), hereby preventing LS contaminations from affecting JUNO's sensitivity. For that purpose, OSIRIS will mainly measure LS contaminations by ^{238}U and ^{232}Th, but also by ^{14}C, ^{210}Po and ^{85}Kr.

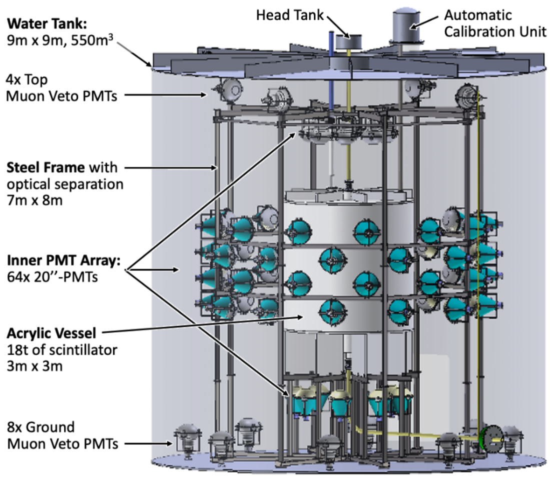

Figure 1: OSIRIS detector overview, modified.[1]

OSIRIS utilises 76 LPMTs (Large PMTs) to analyse signals originating from the 18-ton LS target and the water buffer around it. The LPMTs are a replacement of the planned intelligent PMTs (developed at RWTH Aachen and supported by the IKP-2 neutrino group), which were non-functional after arrival on-site at JUNO.

For PMT timing and charge calibrations, as well as for the calibration of vertex and energy reconstructions, OSIRIS uses a refurbished Automated Calibration Unit (ACU). The ACU, shown in Fig. 2, was kindly provided by the Daya Bay experiment. Featuring a turntable with three independent source deployment assemblies, the ACU can individually lower three calibration sources at an off-centre axis directly into the LS volume. The sources used in OSIRIS include a multi-gamma source (^{137}Cs, ^{65}Zn and ^{60}Co; total activity ≈8.5 kBq; $E_\gamma = 0.66-2.5$ MeV), an LED source ($\lambda = 435$ nm) and a low-radioactive ^{40}K-source (activity <1 Bq, $E_\gamma = 1.46$ MeV).

The commissioning of the ACU started during the first commissioning stay onsite in autumn 2022 and continued remotely until September 2023. The remote support for the Chinese colleagues onsite also included improving existing analyses, performing GEANT4-simulations of different calibration source designs and the development of ACU control software. The commissioning of the ACU was then concluded during another personal stay onsite in September 2023, when both ACU hardware and software were first thoroughly validated for correct functionality. Subsequently, the calibration sources were assembled on their wires, installed in the ACU and tested for mechanical stability. Then, as the last step of the ACU commissioning, the accurate positioning of the calibration sources within OSIRIS was verified utilising known positions in the detector as reference points. An accuracy of ≈4 mm could be achieved, thus confirming the target sub-cm positioning accuracy. At all times, the ACU control software was tested and improved with new functionalities.

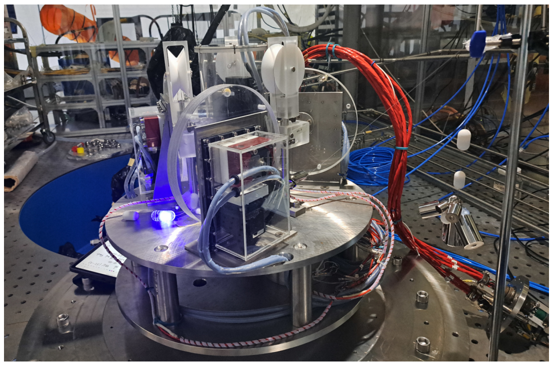

Figure 2: Image of the ACU during a load test of a source assembly (visible as white ellipsoids on the right). In the image, also the LED source for PMT timing and charge calibration can be seen shining brightly. Its intensity during calibration is invisible to the human eye.

Ultimately, first calibration data was successfully acquired after the ACU commissioning, such as shown for one PMT in Fig. 3. The analysis of the data is ongoing, but preliminary results already confirmed expectations obtained via detector simulations. The findings are also used to better understand the detector behaviour in great detail.

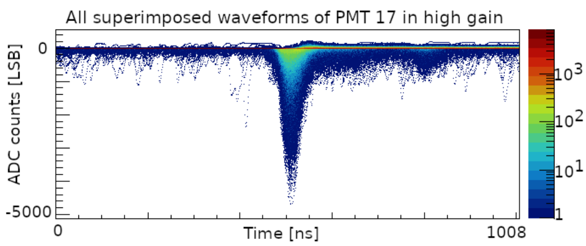

Figure 3: First LED signals recorded by a single PMT (superimposed).

[1] The design and sensitivity of JUNO's scintillator radiopurity pre-detector OSIRIS, published 2021 in Eur.Phys.J.C.

Kicker for the CR stochastic cooling system based on HESR slot-ring couplers

R. Stassen, R. Greven, H. Schneider, J. Wolters, B. Breitkreutz[1]

The stochastic cooling system of Collector Ring (CR) is used to fast reduce the phase space of hot rare isotope beams (RIBs) and antiproton beams [1]. Both operation modes are designed for fixed particle velocities, i.e. 0.83 times the speed of light for RIBs (corresponds to a kinetic energy of 740 MeV/u) and 0.97 times for antiprotons (3 GeV/c). Since stochastic cooling is more sensitive to heavy particles, the kicker is optimized for the latter. The robust slot-ring design of the HESR has been proven [2]. Hence it was decided to use this concept for the CR kicker as well. Therefore, the parameters need to be adapted for the CR cooling system. The aperture was increased to 140 mm while the operating frequency was changed to 1 - 2 GHz.

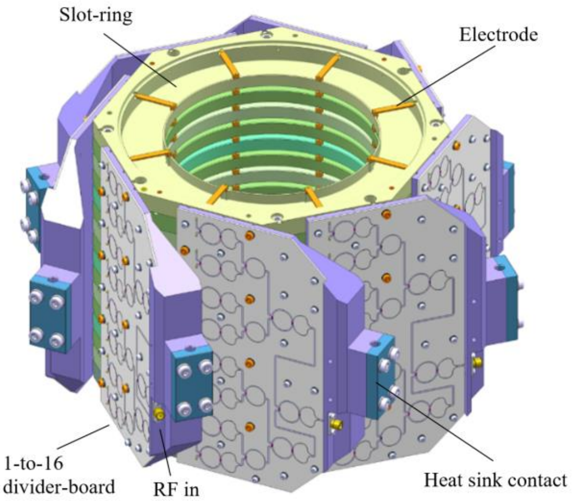

Figure 1: One stack of new CR kicker structure including divider-boards.

The slot-ring structures were optimized with CST Studio Suite for a high shunt impedance of antiprotons at a velocity of $\beta = 0.97$. The impedances are defined according to [3]. The electric fields were simulated for a cell at the centre of a long structure, and the resulting impedances were multiplied by the number of cells to obtain the total impedances shown in Table 1.
Compare to the slotline PUs from GSI, the cooling for both transverse planes can be operated at the same beam position due to the static aperture. Thus, one KI will be used for transvers cooling in both directions and one KI for longitudinal cooling. Each kicker tank contains 128 slot-rings. Every 16 rings are hard-wired with ceramic divider-boards as a stack (see Fig. 1). The main parameters of the new structures are summarized in table 1.

Table 1: CR Kicker parameters

Main parameters	**Value**	**Unit**
RF frequency range	1 - 2	GHz
Particle velocity		
Rare isotope	0.83	c_0
Anti-proton	0.97	c_0
aperture	140	mm
No. of Slot-rings per tank	128	
Total longitudinal shunt impedance for anti-protons	2816	Ω
Total transverse shunt impedance for anti-protons	896	Ω
Total longitudinal shunt impedance for rare isotopes	1280	Ω
Total transverse shunt impedance for rare isotopes	448	Ω
Nominal power loss per divider board	15 (max. 95)	W
Nominal total power loss per tank	960	W

The Wilkinson dividers at the divider-boards use SMD resistors to dissipate the odd-mode signals coming in from the electrode side. Since the electrodes are mostly a pure inductive load, all power applied by the power amplifiers is reflected and must be dissipated in these resistors. Therefore, diamond-based resistors are used. To increase the bandwidth, mostly two-staged Wilkinson dividers are used when possible. Only the third of the four divider levels is one-staged due to space limitations. The much higher power losses at the CR divider-boards compared to the HESR requires a new cooling concept. The copper bands between the divider boards and the water cooling block have been replaced by heat pipes or heat straps respectively and extensive simulations were carried out.
The used simulation model calculates the heat flow from the resistors to the water cooling considering the detailed structure of the boards, including the strip lines and thin layers of Ag past and glue. For a constant resistor power of 15 W the maximum resistor temperature will stay below 60 °C. If the power in the resistors of a circuit board is increased to 95 W for 5 minutes, the temperature in the resistors rises to ~110 $°C$ within 0.1 s (Fig. 2). The subsequent moderate increase, which is determined by the heating of the entire board, goes up to a maximum temperature of almost 174 $°\ C$. This is already at a critical limit. Moderate temperature increase can be handled by a temperature-measurement interlock system, but the fast increase at the beginning not.

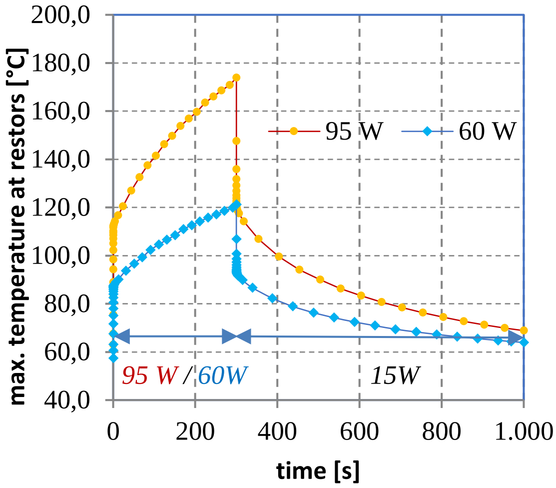

Figure 2: Simulated temperatures at resistors of the divider-boards.

The heat pipes are modelled by simplified solid bodies with high thermal conductivity, which corresponds to the heat removal capability according to the data sheet. This simplification cannot correctly describe the complex non-linear processes in the heat pipes and resulting limitations of the cooling system. This uncertainty in the parameters of the simulations require additional consideration through prototypes.

References

[1] C. Zhang et al., ”A 1-2 GHz stochastic cooling system for antiproton and rare isotopes”, Proceedings of IPAC23, Venezia, Italy, 2023

[2] R. Stassen, B. Breitkreutz, N. Shurkhno, “Recent Results of HESR original stochastic cooling tanks at COSY”, Proceedings of IPAC18, Vancouver, Canada, 2018

[3] Goldberg, D. A., and Lambertson, G. R. “Dynamic devices. A primer on pickups and kickers.” AIP Conference Proceedings, Vol. 249, 1992

[1] GSI Helmholtzzentrum für Schwerionenforschung, Darmstadt, Germany

Injection Optimization via Reinforcement Learning at the Cooler Synchrotron COSY

A. Awal[1,2]

[1]RWTH Aachen University
[2]GSI Helmholtzzentrum für Schwerionenforschung

In accelerator facilities, achieving a high-intensity, low-emittance particle beam quickly is crucial. This research tackles the primary challenges of lengthy optimization processes and injection losses in storage rings. A Reinforcement Learning (RL) framework is introduced to train agents while addressing the sim-to-real transfer challenge and train an agent to optimize the Injection Beam Line (IBL) at the Cooler Synchrotron (COSY) in Forschungszentrum Jülich. This methodology holds potential for application in future accelerators, such as the FAIR facility.

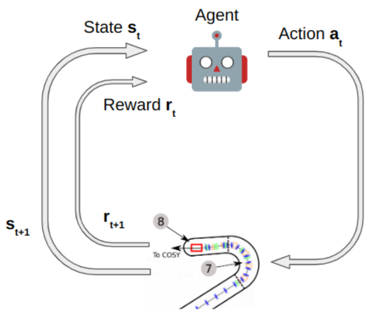

Figure 1: RL agent learning cycle, showing the interaction between the agent, environment, and rewards.

Reinforcement Learning Methodology: The approach lies in utilizing a standard RL framework, where an agent interacts with an environment to maximize a cumulative reward. The state of the environment at each time step t is denoted as $s_t \in S$, and the agent's policy $\pi(a|s)$ determines the action $a \in A$ based on the state. The reward function $r : S \times A \rightarrow \mathbb{R}$ guides the agent's actions. The RL cycle is depicted in a graph (Fig. 1), illustrating the agent's interaction with the environment. The agent's objective is to find an optimal policy π^* that maximizes the expected return, formulated as:

$$J(\pi) = \mathbb{E}[R_0|\pi] = \mathbb{E}\tau \sim p(\tau|\pi)\left[\sum_{t=0}^{T} r(s_t, a_t)\right] \quad (1)$$

where $R_t = \sum_{t'=t}^{T} \gamma^{t'-t} r_{t'}$, $\gamma \in [0, 1]$ is the discount factor, and T is the horizon.

RL Application at COSY: The manual optimization of the IBL injection process was replaced with an RL-based method and integrated it with the EPICS control system [2]. This method focuses on optimizing the transverse space of the beam at the injection point as recorded by a fluorescent screen. The agent's policy is adapted to various goals at the injection point, with the reward function defined as $r(s, a, g)$, considering the stochastic goal g. The goal is defined as μ_x, μ_y, σ_x, σ_y representing the center, width, and height of the beam at the injection point.

Agent Training and Domain Randomization: The training employed the Soft Actor-Critic (SAC) [1] agent, suitable for continuous action spaces. Domain randomization is used to expose the agent to a variety of environmental dynamics, enhancing its ability to adapt to real-world conditions. The agent's training involves selecting actions based on its policy and updating its actor and critic networks, as detailed in the following steps: 1. Initialize dynamic parameters ρ and goal g_t. 2. Observe the current state s_t and goal g_t. 3. Select an action a_t using policy $\pi(a|s_t, g_t)$. 4. Receive a reward $r_t = r(s_t, a_t, g_t)$. 5. Transition to the next state s_{t+1}. 6. Update the critic and actor networks. 7. Repeat until convergence.

Results The agent, trained across diverse and complex environmental dynamics through domain randomization, effectively adapted to the dynamics of the IBL, which presented itself as a different variant of these training dynamics. The agent successfully optimized the IBL in real runs with a mean L2 error of 0.19 mm for the beam's central position (μ) and an L1 error of 0.7 mm for its spread (σ). This degree of accuracy demonstrates the potential of RL in enhancing the efficiency of particle accelerator operations.

Acknowledgements Simulations were performed with computing resources granted by RWTH Aachen University under project rwth0905.

References

[1] T. Haarnoja et al. "Soft Actor-Critic: Off-Policy Maximum Entropy Deep Reinforcement Learning with a Stochastic Actor". *CoRR* abs/1801.01290 (2018). arXiv: `1801.01290`.

[2] *EPICS: Experimental Physics and Industrial Control System*. URL: `http://www.aps.anl.gov/epics/`.

Extending COSY's Capabilities for Automated Algorithms

J. Hetzel, A. Awal, V. Kamerdzhiev, M. Thelen

In 2023, further reseach was carried out to explore the benefits of automated optimisation and operation of accelerators. This included a series of experiments to optimise the accelrator using Machnie Learning and Artificial Intelligence techniques (ML/AI). After the successful optimisation of of the machine with the Bayesian Optimisation algorithm already in 2022 [1], this algorithm was extended and used during several regular machine development weeks. In parallel, a Reinforcement Learning agent was trained and prepared to operate the COSY IBL [2]. Its objective is to control the position and size of the beam, as recorded on a scintillating screen, according to the requirements as defined by an operator. To enable these studies, the existing hardware and sotware was modified such that algorithmic control could be applied to COSY. In adition to the already existing algorithmic access to all magnetic elements of the injection beam line and the ion source beam line, the control and readout of the scintillating viewer screens and their cameras was implemented. This includes access to central quantities as EPICS process variables (PVs) [3]. Another novel development with high relevance for the ML/AI activities is the automated online fit of the signal of the beam current transformer (BCT) of COSY. Both developments have been supported by Cosylab [4].

TUM Drive The measurement of the beam with a scintillating screen is destructive, i.e. the beam is stopped at the position of the screen. Therefore the screen must be moved out of the beam for regular operation of the beam line. An important screen for

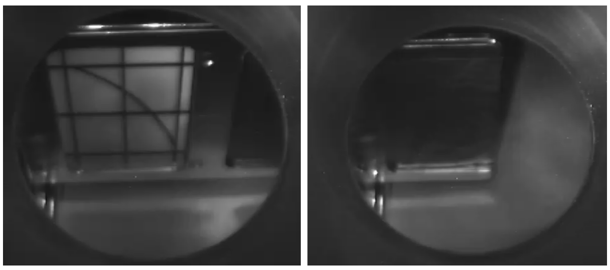

Figure 1: The two positions of the TUM-frame. Left: Viewer screen, right: TUM-foil.

the application of automated algorithms for the IBL is located at the injection point of COSY at the very end of the IBL, see Fig. 1. In normal operation a stripping foil (TUM) is located at this position. The foil is attached to a movable frame which also houses the scintillating screen. By moving the frame to defined positions the beam interacts either with the TUM-foil or with the scintillating screen. The manual adjustment of the positions has been replaced by an automatic one [5]. After calibration, the frame

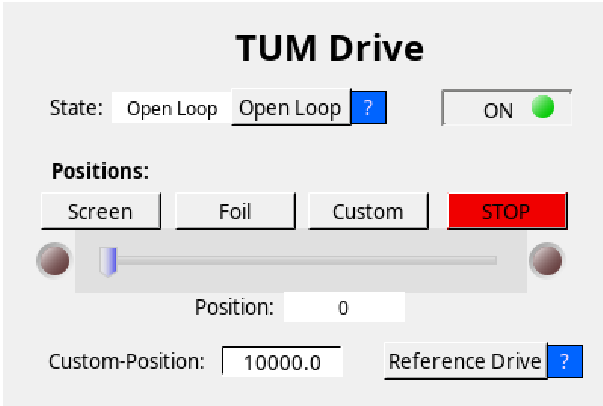

Figure 2: The GUI for the automated TUM-Drive.

can now be moved to three defined positions, cf. Fig. 2: the position for operation, where the beam interacts with the TUM-foil, the screen position, which is used to record the position of the beam, and a custum position which can be entered by the user. Additionally a referencig procedure can be triggered, where the drive slowly seeks its end-position.

Viewer Readout The emmited light from the scintillating screen is recorded by a camera. The area detector module of EPICS is used to provide the recorded image. The following modifications were made to the original module prior to its usage by the ML/AI algorithms:

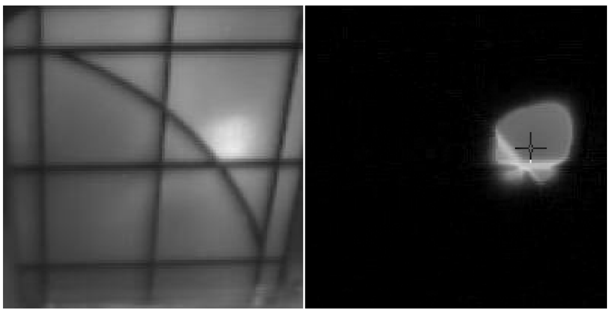

Figure 3: Image of the viewer screen. Left: Raw image with zoom to the region of interest. Right: Processed image after background subtraction. The identified position of the beam is indicated by the black crosshair.

- Automated beam triggering: The module already provides the acquisition and subtraction of background, a region of interest (ROI, see Fig. 3), and the calculation of the integrated brigthness of each frame of the recorded stream. To decide when the beam hits the scintillator, the brightness of the live stream within a specified ROI is evaluated and only images with an integrated brightness above a user-defined threshold are considered to contain beam.

- Average beam position and size, see Fig. 3: The position and size of the beam is calculated for each image of the stream. The result is stored in a circular buffer large enough to contain all the images that are recorded during one passage of the beam, including the afterglow of the screen. All frames with a brightness above the specified threshold are averaged and written to a dedicated PV as soon as the brightness falls below the specified threshold.
- Conversion to beam-pipe coordinates: The original module gives all relevant image information in pixels and refers it to the pixel in the top-left corner of the image. A conversion to a scale in mm with an origin at the centre of the screen has been implemented. In order to maintain the option of recalibration, all scaling factors are implemented as PVs that can be set by the user. The initial calibration was carried out using the scale printed at the viewer screen. A cross-check of the records was performed by moving the beam trasversely to specified positions.

BCT Fit Another target for optimisation, commonly used by both operators and algorithms, is the current of the stored beam at COSY. Depending on the state of COSY and the time window of interest, its evolution over time can usually be described by either an exponential function or a linear (constant) function. An online fit to the recorded data has

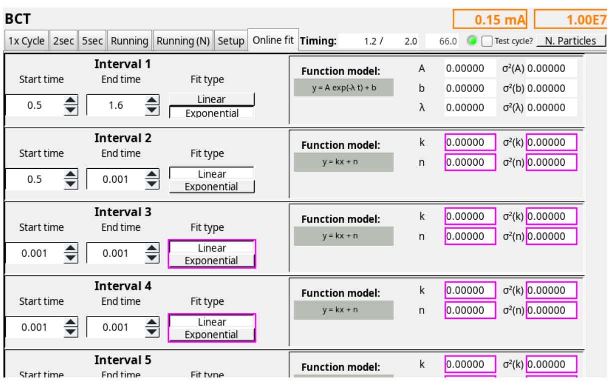

Figure 4: BCT fitting as part of the BCT-GUI. The user can select both linear and exponential fits. The fitting is only triggered if the "Start time" is lower than the "End time".

been implemented. This allows the user to specify a time window relative to the start of each cycle in which a fit is to be performed, and whether an exponential or linear function is to be fitted, cf. Fig. 4. Up to five different time windows for different fits can be selected for each cycle. The result of each fit is provided to the user via a set of PVs.

Both, the camera integration and the BCT fit, extended the capabilities of the AI/ML studies: The reinforcement learning studies would not have been possible without the camera readout, as live control of the beam was the main target of the reinforcement learning agent. The fit functionality on the other hand was used as a valuable input to the Bayesian optimiser. Since the target of the optimiser can be easily adapted to any PV recorded at least once per cycle, the fit results - or any PV based on the fit result - are well suited to serve as input. This extended the usability of the Bayesian optimiser to a standard tool used in the preparation of multiple beam times.

References

[1] A. Awal et al., "Optimisation of the injection beam line at the Cooler Synchrotron COSY using Bayesian Optimisation", J. Instrum., vol. 18, no.4, p. P04010 (2023).

[2] A. Awal et al., "Injection Optimization via Reinforcement Learning at the Cooler Synchreotron COSY", Proc. of IPAC23, p. 2874 (2023).

[3] EPICS: Experimental Physics and Industrial Control System. `https://www.aps.anl.gov/epics/`.

[4] Cosylab, d. d., Control System Laboratory, Ljubljana, Solvenia, `https://cosylab.com/`.

[5] K. Reimers, "Drive controls for beam instrumentation devices at COSY", IKP Annual Report 2023 (2024).

Drive controls for beam instrumentation devices at COSY

K. Reimers*

The controls of beam instrumentation drives in the COSY injection beamline (IBL) and the Quellen, i.e. ion source beamline (QBL) was initially realized using relay based glue logic connected to a digital I/O VME card via a 48channel flat ribbon cable. This hardware came into age after around 30 Years of continuous operation. Furthermore, as the COSY controls have been upgraded to EPICS-based system, the need to integrate the drives of the profile grids and faraday cups in the beamlines became obvious. Additionally, the drive of the stripping foil (TUM) and the corresponding scintillation screen at the injection into COSY was to be remote controlled. This enables script based control of the components and is a prerequisite for the use of this equipment in e.g. the AI/ML studies. To implement the new controls layer to the still flawlessly operating drive hardware, the Beckhoff Ethercat [1] system was chosen. This system delivers various analog and digital I/O modules and digital processing controllers to be assembled to units fitting exactly to their specified task. They are controlled by a Master Controller via daisy-chain ethernet line. This design is inexpensive, highly scalable and fits well into limited spaces. The Ethercat communication protocol ensures deterministic timing which is required in the accelerator environments. This technology is well established at COSY and thus the software know-how is readily available in the controls group.

IBL-Drives of Profile grids and faraday cups At the IBL the digital I/O controlled relays providing power to the pneumatic drives of 8 Profile Grids have been replaced by Ethercat relays. The drives of four Faraday cups are now operated by a second Ethercat unit also providing information on the 8 limit switches.

Faraday cup drives in QBL The QBL transports beams from ion sources to the cyclotron, the main injector of COSY. The Faraday cups, when moved into the beam, measure the beam current. In the QBL two groups of faraday cups are installed. The first group FB0...FB5 already was controlled by a G64 based I/O rack. The second group FB1',FB2' and LR3 was only controlled manually. Now an Ethercat unit handles 8 drives and 16 limit switches. As the GUI already existed, only the middleware had to be adapted. As local control is still required, a combined remote/local setup was implemented. All Ethercat controlled devices have been installed into available spaces in the initial electronics cabinets

New remotely-controlled drive for the stripping foil The stripping foil (TUM) and a scintillation screen are mounted on a holder that can be moved in and out of the beam manually. An Ethercat controlled stepper motor was added in 2023 (see Fig. 1). Two significant constraints effected the mechanical design quite significantly. For reasons of accelerator operational safety venting the vacuum section that includes the stripping foil was not an option. Hence the mechanical design had to be developed around the initial mechanical vacuum feedthrough. Furthermore, the weight of additional components had to be independently supported using non-conductive materials as the initial manual drive is mounted on a ceramic isolator to enable TUM current measurements.

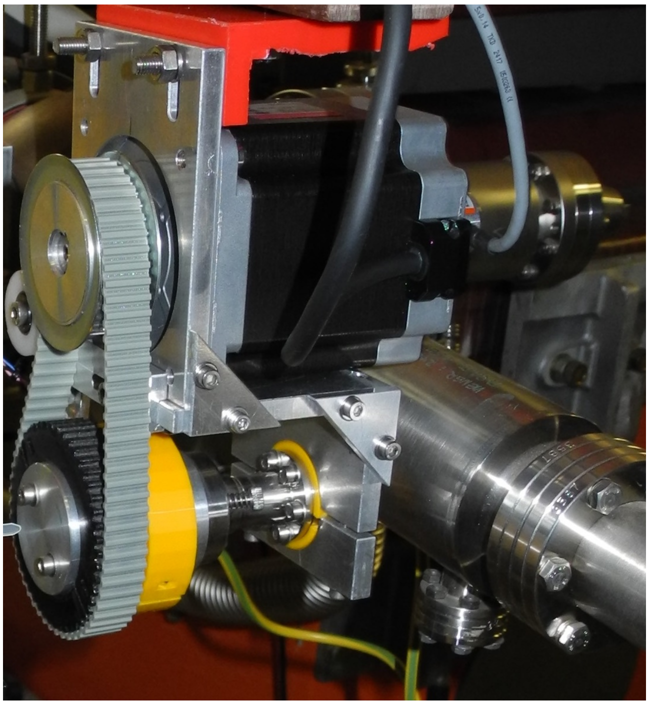

Fig. 1: The initially manual TUM drive is now equipped with a stepper motor.

Summary

In beamlines 6 Ethercat slaves controlled by one common Ethercat master, an application of the Etherlab [2] server were put into operation. This way reliable, cost-effective and maintenance-friendly drive controls were implemented inside EPICS environment of COSY. The remotely controlled TUM drive proved to be of great advantage in setting up the injection of the particle beam into COSY especially for automated optimization of parameters.

Acknowledgements

The author greatly appreciates the support by Berthold Klimczok in designing and installing the new TUM drive as well as Michael Simon and Michael Thelen for Ethercat integration and GUI development. Furthermore, the author acknowledges valuable advise provided by Yury Valdau.

References:

[1] Ethercat is a trademark of Beckhoff automation `https://www.beckhoff.com`

[2] Etherlab is a free Linux based application of a server software for communication with Ethercat devices. `https://etherlab.org/`

* GSI Helmholtzzentrum für Schwerionenforschung GmbH, Planckstraße 1, 64291 Darmstadt

Measurement of the neutron dose rate in the Big Karl area for the HBS project

J. Li, T. H. Randriamalala, J. Chen, N. Schmidt, J. Baggemann, E. Mauerhofer, N. Demary, O. Felden, U. Rücker, P. Zakalek, T. Gutberlet

A innovative biological shielding for a new generation of accelerated based neutron sources has been developed and built as part of the HBS (High Brilliance Neutron Source) target station prototype. The shieding is composed of layers of lead and borated polyethylene. The neutron dose rates were measured at this target station prototype during the beam time in July, August, September and December 2023. Additionally neutron and gamma dose rate in the vicinity of the target station were simulated.

Neutron dose rate meter calibration

A total of eight neutron dose rate meters were used for dose rate measurement on site. The neutron dose rate meters consist of ^3He tube surrounded by a polyethylene cylinder with a diameter of 216 mm to thermalize neutrons. Neutrons can be measured with an energy up to 10 MeV and a saturation of up to 1 Sv/h. The neutron dose rate meters were calibrated for 15 minutes with a 370 MBq AmBe source with a neutron emission of 2.80e+04 per second, leading to an average calibration factor of $(3.3 \pm 0.7\,\mu\mathrm{Svh}^{-1}\mathrm{s})$.

Measurements

The neutron dose rates were measured continuously during the beam time. The location of the dose rate meters is shown in Figure 1. Rate meters 1 and 2 were positioned along the proton beam line, next to the quadrupole magnets and steering magnets to identify the beam loss. Rate meter 3 was located on the outer surface of the target station, but directly above or below the proton beam line. Rate meter 5 was placed directly on the outer surface of the shielding in front of the target exchange. Rate meter 8 was placed at the one of the neutron extraction ports and rate meter 9 was located at the octagonal corner of the shielding. Rate meters 4 and 7 were placed beside the top plate of the shield, at a height of 2.74 m. Rate meters 6 and 11 were positioned 2.40 m from the outer surface of the shielding.

Table 1 shows the measured neutron dose rate normalized to a proton current of 1 mA for the different positions of the dose rate meters. The letters L, M, H and T in table 1 corresponds to the vertical positions of the dose rate meters with heights of 0.70, 1.40, 2.10 and 2.74 m, respectively. The dose rate meter installed at middle height (M) is located at the same height of the target (1.40 m) at which the primary neutrons were generated.

The neutron dose rates at position 3 were measured to $(33.3 \pm 6.7\,\mathrm{Sv/h})$ and $(40.7 \pm 8.1\,\mathrm{Sv/h})$ with the location below or above the proton beam, respectively. These high values are due to the backward neutrons emission of the target.

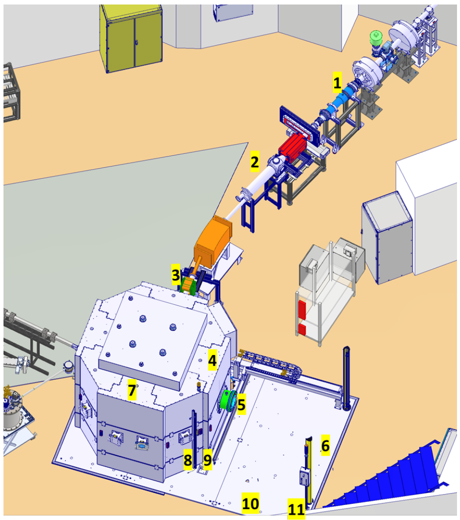

Figure 1: Location of the neutron dose rate meters.

In addition, these neutrons were further scattered from the concrete shielding of the proton beam line, which is not shown in the figure 1. The neutron dose rate meters 5, 6 and 11 were exposed to this scattered neutron field. Therefore the measured neutron dose rates at e.g. the middle height (M) were $(3.86 \pm 0.77\,\mathrm{Sv/h})$, $(1.44 \pm 0.29\,\mathrm{Sv/h})$ and $(2.22 \pm 0.44\,\mathrm{Sv/h})$, respectively.

The rate meter 8 placed in front of the open neutron extraction port showed a dose rate of $(1.44 \pm 0.29\,\mathrm{Sv/h})$, providing a reference for the neutron emission from a surface of 27 by 17 cm^2. It is about 5 times higher than with a closed beam port.

Table 1: Measured neutron dose rate normalized to a proton current of 1 mA, $Sv/h@1mA$.

position	1	2	3	4	5	6	7	8	9	10	11
T	-	-	-	0.15	-	-	0.12	-	-	-	-
H	-	-	33.3	-	5.74	3.95	-	0.29	0.22	0.34	5.48
M	0.33	0.93	-	-	3.86	1.44	-	1.44	0.32	0.36	2.22
L	-	-	40.7	-	2.01	1.45	-	0.22	0.27	0.38	1.84

Simulation

The neutron and gamma dose rates were simulated using Monte Carlo program package PHITS3.24 [1] and the JENDL-4.0 data library [2].

A monoenergetic proton beam with an energy of 42 MeV was applied for the simulation, which impinges uniformly on the tantalum target surface. The target, the polyethylene thermal moderator and the lead reflector as well as the surrounding biological shield-

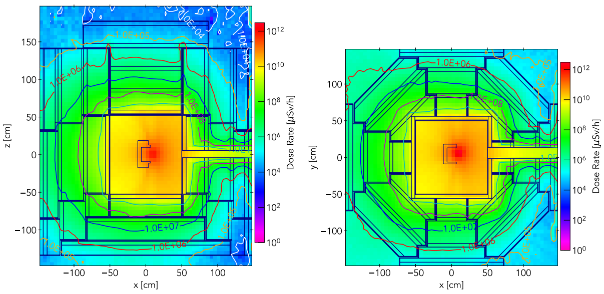

Figure 2: The neutron dose rate map at the vertical cross-section (left) and at the horizontal cross-section (right) of the target station.

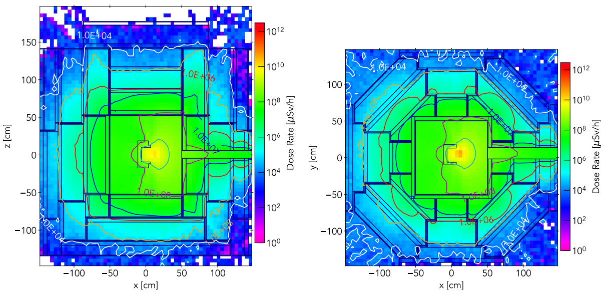

Figure 3: The photon dose rate map at the vertical cross-section (left) and at the horizontal cross-section (right) of the target station.

ing were modeled. The cold moderator, the extraction channels, concrete shielding of the proton line and actual walls of the area were not taken into account. The neutron and photon dose rate distributions normalized to a proton current of 1 mA are shown in Figures 2 and 3.

The dose rate distribution shows the benefits of the layered biological shielding. The highest dose rate is located in the center of the target station with about 500 kSv/h, where the primary neutrons were generated. A each double layers of borated PE and lead reduce the dose rate by about one order of magnitude. Figure 2 demonstrates that the neutron dose rate at a height of 1.40 m is below 1 Sv/h, except at the proton beam side due to the backward neutron emission, which is consistent with the measured value from rate meter 3.

The neutron dose rate at position 5 (see table 1) was measured as $(3.86 \pm 0.77\,\mathrm{Sv/h})$, which is higher than the calculated dose rate. The discrepancy is due to the influence of neutrons scattered from the concrete shielding of the proton beam line and the experiment walls, which were not modeled in the simulation.

Additionally, the simulated gamma dose rate distribution is shown in Figure 3 . The gamma dose rate at the outer surface of the biological shielding is less than 10 mSv/h.

Conclusion

The measured neutron dose rates in the vicinity of the target station were in the range of 1 Sv/h, except at the positions above or below proton beam line. Due to the backscattered neutrons, the neutron dose rate reached up to $(40.7 \pm 8.1\,\mathrm{Sv/h})$. The simulated and measured values agree well with each others. The dose rate distribution from the simulation shows that the biological shielding of the target station can reduce the total dose rate at a proton current of 1 mA below 1 Sv/h.

References

[1] Tatsuhiko Ogawa, Yuho Hirata, Yusuke Matsuya and Takeshi Kai, Development and validation of proton track-structure model applicable to arbitrary materials, Scientific Reports, 11, 24401 (2021) DOI: 10.1038/s41598-021-01822-1.

[2] K. Shibata, O. Iwamoto, T. Nakagawa, N. Iwamoto, A. Ichihara, S. Kunieda, S. Chiba, K. Furutaka, N. Otuka, T. Ohsawa, T. Murata, H. Matsunobu, A. Zukeran, S. Kamada, and J. Katakura: "JENDL-4.0: A New Library for Nuclear Science and Engineering," J. Nucl. Sci. Technol.. 48(1), 1-30 (2011).

A Study of Ethane as a candidate for cold neutron moderation for the HBS project

M. El Barbari, U. Rücker, A. Schwab, J. Chen, P. Zakalek, J. Li, T. Gutberlet, T. Brückel

1 Introduction

The cold neutron moderator is an essential element in neutron scattering instruments, where it significantly contributes to decelerating thermal neutrons. This process enhances the capability of these neutrons to analyze atomic and molecular structures in materials more precisely than with standard thermal neutrons. Selecting an appropriate moderator material requires carefully weighing factors of efficiency, stability, and safety, especially in high-radiation environments. In such settings, ethane is a particularly promising choice, offering distinct advantages in stability and safety.

2 Experimental setup

The moderator material is housed in a cylindrical aluminum vessel, measuring 6 cm in length and 2.2 cm in outer diameter. Surrounding this vessel is a maze-like structure, where cold helium gas circulates to cool the moderator. This vessel is filled with ethane gas, although other gases with similar properties can be used as alternatives. The neutron spectra are recorded using a 7 m long diffractometer. This instrument is located at beamline 2 of the JULIC Neutron Platform [1].

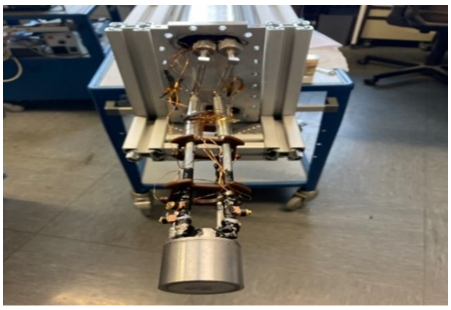

Figure 1: A flexible mounting configuration with the moderator volume and four temperature sensors for adaptive experimental setups at the front of the extraction plug.

The spectra are captured using Time-of-Flight (ToF) methodology, featuring a time resolution of 200 microseconds. The primary neutron pulses are generated through the (p,n) reaction, involving 45 MeV protons interacting with a Tantalum (Ta) target placed in front of the moderator-reflector assembly. For the experiments described, the proton pulse duration is set at 400 microseconds.

3 Measurements and correction processing

Figure 2, shows the results of the cold neutron spectra after correction for a thermal contribution from the PE moderator, normalization to a monitor counter and correction for the wavelength dependent transport properties of the neutron guide. As expected, the spectrum peak undergoes a shift towards higher wavelengths in colder neutron regimes as the temperature decreases. This is in accordance with expectations and indicates an increase in moderation efficiency.

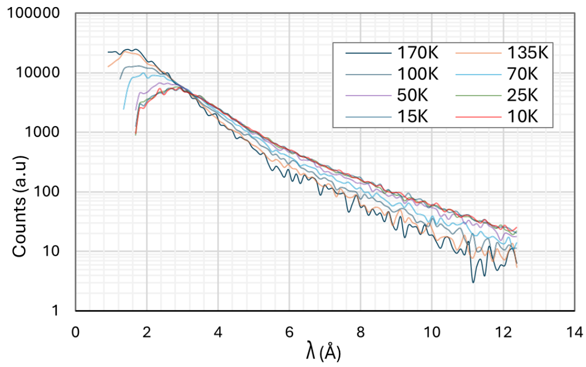

Figure 2: Neutron spectra emitted by the ethane cold neutron moderator as a function of the wavelength for different moderator temperatures.

4 Neutron temperature

To extract neutron temperatures from the preceding neutron spectrum, we employ a fitting process wherein we fit the neutron data to the normalized Maxwell wavelength distribution. Fig.3 illustrates the variation of neutron temperatures noted Tn with respect to the ethane moderator material temperature noted Tm obtained after fitting all temperatures with this method.
As neutrons traverse through the moderator material, interactions with its constituent elements lead to energy transfer and absorption. These interactions result in a thermalization (cooling) process where neutrons lose kinetic energy and, consequently, experience a decrease in temperature, which basically is the role of such moderator materials. This is observed as shown in Fig. 3, where the trend of the neutron temperature shows a decreasing value of temperature proportional to the decreasing of the moderator temperature until it this last one reaches 50 K

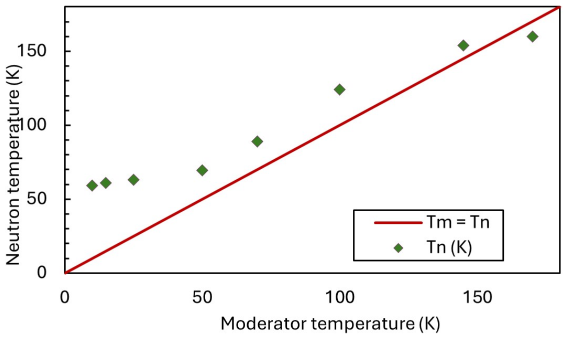

Figure 3: The temperature of the emitted neutron spectrum compared to the moderator temperature.

and below, then the neutron temperature does not decrease further, showing an asymptotic behavior towards 57 K, this indicates that ethane is not perfectly suitable to produce very cold neutrons, but a data analysis and understanding in more depths will be performed.

5 Conclusion

As ethane exhibits superior safety and stability compared to other cold moderator materials [2], it is a suitable choice for future endeavors in this field to a temperature of 50 K. However, it is essential to acknowledge that certain aspects of ethane's behavior as a cold neutron moderator still require more detailed and comprehensive examination which will be addressed in forthcoming studies.

References

[1] T. Brückel et al., EPJ Web Conf. 286, 02003 (2023)

[2] M. H. Parajon et al. Phys. Procedia 60 (2014)

Operation of the HERMES reflectometer at the JULIC Neutron Platform

M.A. Paulin , I. Pechenizkiy, P. Zakalek, K. Lieutenant, P. Kämmerling, A. Steffens, H. Kleines, U. Rücker, T. Gutberlet, S. Gautrot, A. Menelle, and F. Ott

The HERMES reflectometer was installed [1] at the JULIC Neutron Platform (JNP) in December of 2022. The JNP exploits the JULIC (JÜlich Light Ion Cyclotron) accelerator [2] from the Institute for Nuclear Physics (IKP) at Forschungszentrum Jülich (FZJ) to accelerate protons that are conducted to a target-moderator-reflector assembly (TMR) built by the Jülich Centre for Neutron Science (JCNS). HERMES [3, 4, 5] was originally conceived as a time-of-flight horizontal reflectometer (see Fig.1) mainly intended for soft-matter studies and it was in operation at the ORPHEE reactor [6] until its shutdown in 2019.

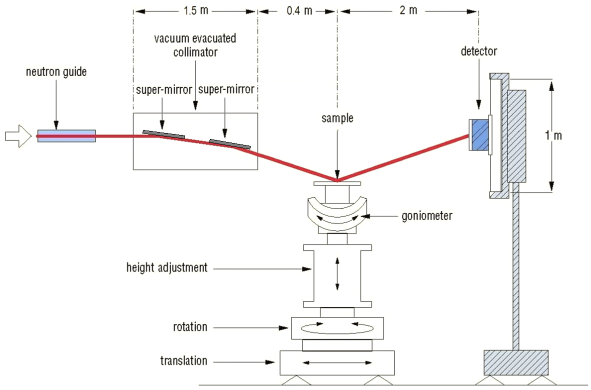

Figure 1: Scheme of the HERMES reflectometer.

Initial HERMES experiments at the JNP [1] in 2022 were performed with a low proton current (Ip ≈ 200 nA) impinging onto the target and with the reflectometer only fed by the polyethylene (PE) thermal moderator. Due to the improvements made in the JULIC accelerator at the beginning of 2023, it was possible to increase the proton current up to Ip = 3.5 µA. In July of 2023, a para-H_2 cold moderator [7] was installed at the extraction channel 3 of the TMR, providing HERMES with a cold spectrum more suited for reflectometry studies. A 2.5 m neutron guide with m = 1.2 on all sides transports the neutrons out of the target shielding and into the collimator of HERMES.

As it is shown in Figure 2, the para-H_2 moderator shifts the neutron flux peak (λ_{peak}) from 1.4 Å to 3.1 Å and increases the total amount of neutrons in the 1-12 Å range from 0.74(1) n/s.cm^2.µA to 1.69(1) n/s.cm^2.µA. This 2.3 gain factor is linked to the directional emission of the para-H_2 cylindrical moderator [7] as well as the better transmission properties of the neutron guide for cold neutrons.

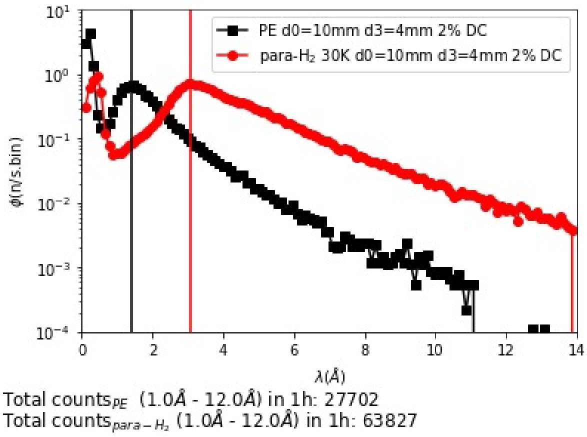

Figure 2: Direct beam measured at the HERMES reflectometer in 2023 with and without a cold moderator, normalised for a proton current of Ip = 3.5 µA.

Taking advantage of the improved performance of the instrument, we measured the reflectivity of a 40 nm (12 cm x 3 cm) Ni layer on Si (see Fig. 3).

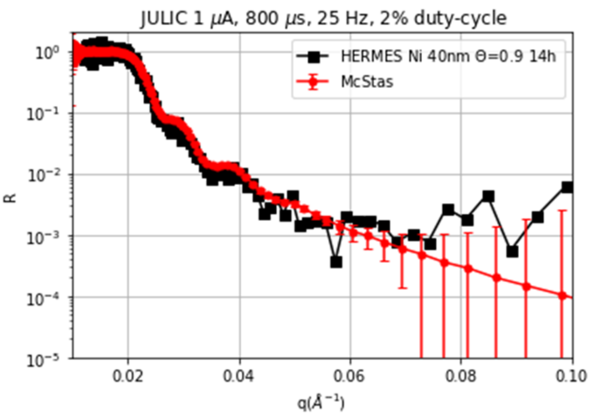

Figure 3: Reflectivity of a 40 nm Ni layer on Si measured at HERMES reflectometer at the JNP without additional detector shielding and the corresponding McStas simulation.

During this experiment, the proton current was only 1 µA and thus, 14h were required to collect enough statistics. We were able to measure reflectivities down to 10^{-3} with approximately 1W of power onto the target. The simulated curve (McStas) fits our experiment, although above Q=0.04Å^{-1} the effects of background become noticeable for the experimental curve.

As the instrument's performance strongly relies on the background-to-signal ratio, efforts must be focused on properly shielding the instrument from external background sources. The HERMES shielding was conceived for its installation at the guide hall of ORPHEE where background levels were very low with virtually no fast and epithermal neutron background. At JNP on the contrary, HERMES is located in the same bunker as the proton beamline and the target station. During the neutron production, there is a very high fast neutron background (prompt pulse). This background decays quickly, but the moderation of fast neutrons in the bunker concrete creates a cloud of thermal neutrons, which decays only over mili-second timescales. In order to shield the detector from these unwanted neutrons, we designed and built an additional 20 mm borated polyethylene (BPE) shielding (see Fig. 4).

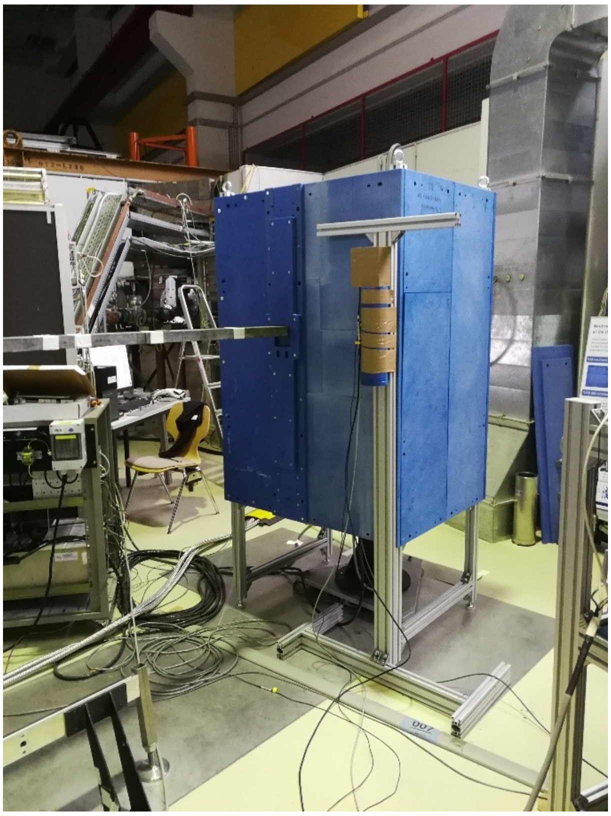

Figure 4: New borated polyethylene shielding added to the HERMES detector.

Background-to-signal ratio excluding the prompt pulse (ToF $\geq$ 2.5 ms, $\lambda \geq$ 1.4 Å) was reduced by 2 orders of magnitude from 3.10^{-3} to 4.10^{-5} just by the addition of the 20 mm BPE to the existing 10 mm of Boroflex. Although these values are still higher than the original values at ORPHEE, there is still a margin of progress in the accelerator and TMR shielding. The shielding proposed for ICONE and HBS would include an additional heavy concrete casemate separating the TMR station from the instruments.

The JNP represents an opportunity to test the operation of neutron scattering instrumentation at HiCANS. Its flexibility allowed us to test many critical features for future developments. Since the first neutrons were produced in 2022, several improvements were implemented to the platform, including additional shielding and the incorporation of a dedicated para-H_2 cold source for HERMES. The instrument's performance was vastly improved by these upgrades. The increase in proton current (Ip) followed by the spectrum shift towards colder neutrons allowed us to increase the reflectivity range of the instrument. This was also made possible by a reduction in background noise levels thanks to the added accelerator heavy concrete shielding and additional 20mm borated polyethylene added to the HERMES detector. If we focus on the results for the 40 nm Ni layer (Fig. 3), almost 3 orders in reflectivity were achieved in a 14h experiment with only 1 W into the target. Scaling these data to the 100 kW that is foreseen for a HiCANS, we should be able to achieve 6 orders in reflectivity for a 1 cm^2 sample in a 1 h measurement. If we extrapolate the last HERMES results at the JNP with the Monte-Carlo simulations for ICONE and HBS, we can envision that instrument performance at a HiCANS would match those that are currently operating at research reactors or spallation sources.

References

[1] M.A. Paulin, I. Pechenizkiy, P. Zakalek, K. Lieutenant, P. Kämmerling, A. Steffens, H. Kleines, U. Rücker, T. Gutberlet, S. Gautrot, A. Menelle, F. Ott, , EPJ Web of Conferences 286, 03003 (2023)

[2] O. Felden, N. Demary, N.-O. Fröhlich, R. Gebel, M. Rimmler, Y. Valdau, 22nd Int. Conf. on Cyclotrons and their Applications (2019)

[3] F. Cousin, F. Ott, F. Gibert, A. Menelle, Eur. Phys. J. Plus 126, 109 (2011)

[4] G. Battaglin, A. Menelle, M. Montecchi, E. Nichelatti, P. Polato, Glass Technol. 43, 203-208 (2002)

[5] D. Lairez, A. Chennevière, F. Ott, J. Appl. Crystallogr. 53, 464-476 (2020)

[6] B. Farnoux, D. Cribier, Phys. B+C 120, 31-36 (1983)

[7] T. Kai, M. Harada, M. Teshigawara, N. Watanabe, Y. Ikeda, Nucl. Instrum. Methods Phys. Res. 523, 398-414 (2004)

Stand-alone liquid para-H_2 moderator for beamline 3 of the JULIC Neutron Platform

U. Rücker, S. Eisenhut, M. Hannot, E. Rosenthal, F. Suxdorf, A. Schwab, Y. Bessler, M.-A. Paulin, P. Zakalek, J. Baggemann, T. Gutberlet, Th. Brückel

An important part of all instruments to be developed for HBS [1] will be the neutron moderators that deliver the neutron spectrum optimized for the requirements of the specific instrument. For the instruments dedicated to investigations of large-scale structures or for high-resolution spectrometers cold neutrons sources are required to deliver neutrons with long wavelengths and low kinetic energy.

Suitable moderator materials are e.g. liquid hydrogen, solid methane, ethane or mesitylene. In previous setups we have developed, built, and tested moderator cryostats for solid mesitylene [2], mixtures of liquid ortho- and para-hydrogen [3], and liquid or solid methane or ethane [4]. The methane / ethane cryostat is currently mounted in beamline 2 of the JULIC Neutron Platform. All these cryostats require external cooling (typically by supply of liquid helium) and have an open volume for the moderator material that needs to be connected to a reservoir outside of the moderator assembly, in most cases a pressurized gas cylinder. Most materials suitable as cold moderators are flammable carbohydrates, so that the supply is always a certain safety hazard.

Liquid para-hydrogen has a low scattering cross-section for cold neutrons, so that the mean free path for cold neutrons in para-hydrogen is more than one order of magnitude larger than for thermal neutrons. This property enables to build a one-dimensional moderator vessel that allows extraction towards a single beamline from a large moderator depth which is still efficiently fed from the surrounding thermal moderator. Para-hydrogen is the ground state of the hydrogen molecule at low temperatures, but the natural transition is strongly forbidden, so that it takes weeks to reach the ground state in a clean environment. A paramagnetic catalyst in the hydrogen circuit enables efficient conversion of liquid hydrogen into para-hydrogen.

In addition, liquid hydrogen at a temperature below 18 K is a suitable medium for heat transport without the necessity to use a cryostat with a separate cooling medium. For these reasons, we have decided to design and build a liquid para-hydrogen moderator with an enclosed hydrogen room temperature reservoir and a low-temperature circulation of the liquid hydrogen content. This cryostat is cooled by a closed-cycle cryocooler system, so that (once it is filled with the necessary hydrogen inventory) it only needs a connection of electricity and cooling water.

The cryostat system is split into three parts. The room-temperature part of the cryostat is the gas management panel and the hydrogen reservoir. It can be seen in figure 1 on the left side of the main cryostat. During initial operation, the valves together with a vacuum pump and a vacuum measurement system allow to evacuate the entire system to clean it from any contamination of materials that would freeze above 20 K and could block the circuit. Then, the system is filled with 800 l of hydrogen gas (at room temperature and standard pressure) which results in a room-temperature pressure of 12.5 bar in the room-temperature reservoir. Even if the entire contents of hydrogen is drained into the laboratory in case of an accident, the hydrogen concentration will quickly fall below the ignition limit at a few cm distance from the leak, which is an important safety feature of this system.

The second part is the cylindrical main cryostat that can be seen in figure 1 on the right side. This main cryostat is evacuated by a turbo pump and contains the cold head of the closed-cycle cryocooler system, the circulation pump, a mass flow measurement for the hydrogen circuit and several temperature sensors. In addition, a paramagnetic catalyst inside a section of the hydrogen tubing grants for the conversion into para-hydrogen.

The third part is the moderator volume that can be seen in figure 2. For operation, the moderator vessel is contained in a vacuum vessel which is mounted at the tip of an extraction plug. The extraction plug contains the vacuum connection and the hydrogen supply and exhaust tubes together with a neutron guide and shielding material around. This extraction plug has been mounted in beamport 3 of the JULIC neutron platform. Outside, the neutron guide is feeding the HERMES neutron reflectometer which has been set up and which is operated by our col-

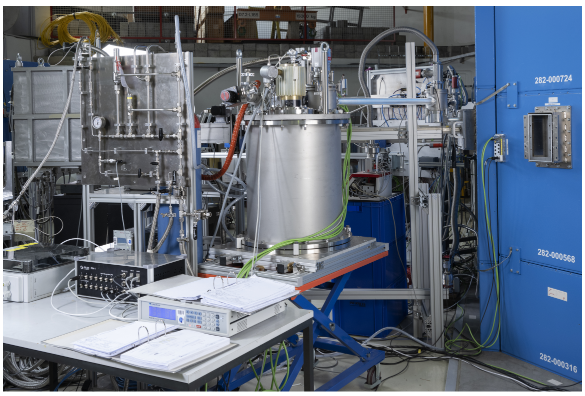

Figure 1: Main cryostat and gas management panel connected to the moderator plug inserted in beamline 3 of the JULIC Neutron Platform.

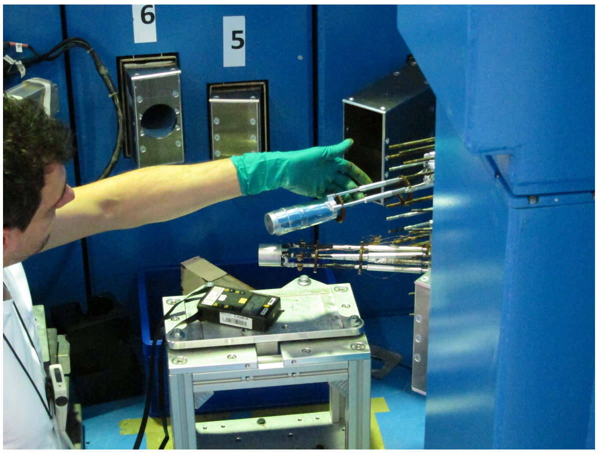

Figure 2: Liquid hydrogen moderator vessel (top) and solid methane (or ethane) moderator vessel (bottom) at their positions inside the shielding. For operation, the cold moderators are surrounded by an aluminium vessel for the thermal isolation vacuum and the thermal moderator (polyethylene) and reflector (lead) assembly.

leagues of LLB Saclay, France.
The moderator plug and the main cryostat are connected by a transfer line, where the thermal isolation vacuum and the hydrogen circulation lines are connected.

The operation of the cryostat has turned out to be very simple: When everything is assembled without leaks, the hydrogen system is properly evacuated and subsequently filled with hydrogen up to a system pressure of 12.5 bar. Then, the closed-cycle cooler is switched on and takes about three hours to reach a temperature below 100 K. At this temperature, the hydrogen density is sufficient to enable efficient circulation by the pump. When the circulation pump is switched on, the cooldown of the remaining circuit including the moderator vessel is started and at a temperature below 32 K condensation begins. The gas from the room temperature reservoir is successively condensed to fill the low-temperature circuit including the moderator vessel. After complete fill-up, which takes about another hour, the remaining pressure in the reservoir is 3 bar. After the end of the condensation process, the liquid is cooled down to 18 K, where an equilibrium between the cooling power of the cryocooler and the thermal intake of the hydrogen circuit is reached and stable operation over more than a week has been demonstrated. For shutdown, the cryocooler and the circulation pump are switched off and the hydrogen inventory evaporates and is stored in the room-temperature reservoir, where the pressure rises back to 12.5 bar. A restart can be done without any cleaning step and without addition of gas.
Figure 3 shows the neutron spectrum measured

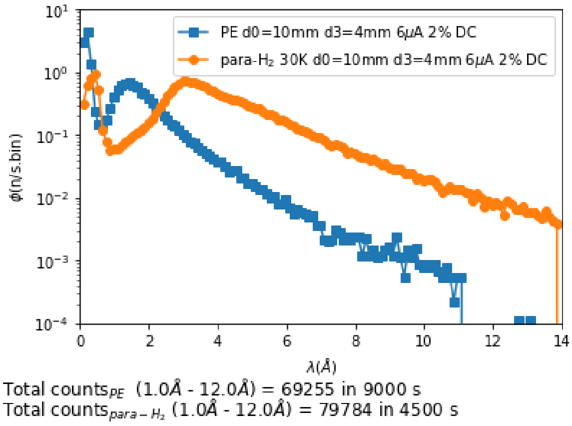

Figure 3: Neutron spectra measured at HERMES: thermal spectrum (blue) and cold spectrum emitted from the para-hydrogen moderator (orange).

at the detector position of HERMES without and with operation of the liquid para-hydrogen cold moderator. The maximum of the neutron spectrum shifts from 1.5 Å to 3.2 Å wavelength which offers improved resolution and Q range for the reflectivity measurements. In addition, the total intensity has increased by a factor 2.3 due to the improved extraction of cold neutrons from the para-hydrogen moderator and due to the improved transport of the cold neutrons in the neutron guide.

In conclusion, the stand-alone liquid para-hydrogen moderator has successfully been brought into operation at the JULIC Neutron Platform and has shown to be a perfect cold moderator serving the HERMES reflectometer with an appropriate spectrum of cold neutrons.

References

[1] Brückel, T., Gutberlet, T. (eds.): Technical Design Report High Brilliance neutron Source (HBS), Forschungszentrum Jülich (2023)
[2] M. Strothmann: Efficiency of a mesitylene based cold moderator system for a compact accelerator driven neutron source. Master thesis, RWTH Aachen University (2020)
[3] S. Eisenhut et al., EPJ / Web of Conf. **231**, 04001 (2020)
[4] A. Schwab: Design and manufacturing of a cryostat for a compact cryogenic neutron moderator for operating at temperatures below 10 K. Dissertation (submitted), RWTH Aachen University (2024)

Neutron Imaging Instruments at the JULIC Neutron Platform

N. Schmidt, P. Zakalek, E. Mauerhofer, A. Wolfertz, R. Kumar, A. Losko, T. Gutberlet

1 Introduction

Neutron imaging is a non-destructive analytic technique, which allows investigations of different kind of samples by the interaction of neutrons with the matter following the Beer-Lambert law:

$$I_x(E,t) = I_0(E,t)\, e^{\Sigma_x(E)\,\Delta x}, \tag{1}$$

where I_x is the intensity of the neutron beam observed at the detector after the interaction with the sample (s^{-1}), I_0 is the intensity of the incident neutron beam (s^{-1}), Σ_x is the macroscopic cross-section of the sample (cm^{-1}), and Δx is the thickness of the sample (cm).
Some of the scientific applications of this technique are: hydrogen in metals, energy conversion processes, strain phase mapping studies in engineering and energy conversion processes, archeological characterization, automotive and aerospace applications, or battery processes.
Five different neutron imaging instruments are planned for the HBS project [1]. For example, Figure 1 shows the layout of the cold neutron imaging instrument. To demonstrate the proof-of-principles regarding the neutron imaging technique, two different instruments were designed and developed at the JULIC Neutron Platform consisting of the target station prototype with 8 extraction channels setup at the Big Karl area.

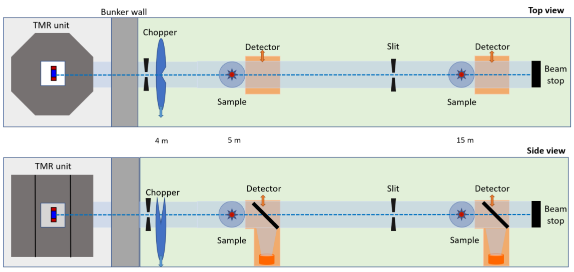

Figure 1: Proposed layout for the cold neutron imaging instrument at the HBS [1].

2 Instruments design

Following the target station prototype build at the JULIC Neutron Platform, two different collimators were designed: one for thermal neutrons at the extraction channel number 6, looking at the polyethylene moderator, and the other for fast neutrons at the extraction channel number 1, looking at the target. The diameters of the inner and outer holes of the collimator were chosen, in order to have a collimation L/D of 50 when the sample was placed at a distance of 2 m from the source. Figure 2 shows the design of the collimator for the fast neutron imaging.

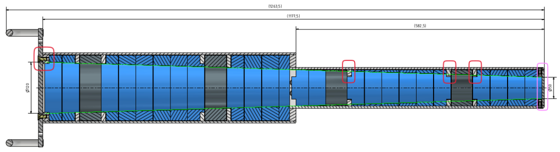

Figure 2: Drawing of the collimator designed for the fast neutron imaging instrument.

3 Experimental setup

For the thermal neutron imaging instrument, a TPX3Cam camera was used, which was provided by the Imaging Group of the Heinz Maier-Leibnitz Zentrum [3]. The samples were placed at the end surface of the collimator, and the camera was located just after the sample.
For the fast neutron imaging instrument, a detector developed by the detectors' group of the JCNS-2 institute was tested [2]. This detector was a commercial PerkinElmer (XRD-1642), which was modified by using a suitable scintillator for the detection of fast neutrons. The active area of the detector is 40 cm×40 cm and is divided into 1024×1024 pixels. A scintillator based on scintillating fibers was developed to improve the detection efficiency with an active area of 20 cm×20 cm. A photography with the experimental layout for the fast neutron imaging instrument is shown in Figure 3.

Figure 3: Picture of the experimental setup corresponding to the fast neutron imaging instrument.

4 Results

4.1 Thermal neutron imaging

The thermal neutron imaging instrument was used to investigate the possibility of probing biological samples and to perform time-of-flight measurements at a low-power source.

Figure 4: Cactus sample (left) and obtained neutron image (right).

Figure 4 shows the imaged cactus with a measurement time of 3600 s, which proves the feasibility of penetrating soil at just a power of a few watts.
The time-of-flight (ToF) option allows the selection of the neutron energy. For the imaged cactus it improved the signal-to-noise ratio as the large background during the proton pulse could be discriminated. For an imaged Cadmium sample which exhibits a large jump in absorption cross section at around 0.5 eV it allowed to select neutron energies that can penetrate the sample and thus look trough.

4.2 Fast neutron imaging

Different samples were studied, in order to characterize the spatial resolution of the fast neutron detector. In Figure 5, the results obtained for a lead brick with holes of different diameters are shown, with a measurement time of 200 s and the proton accelerator working in continuous mode.

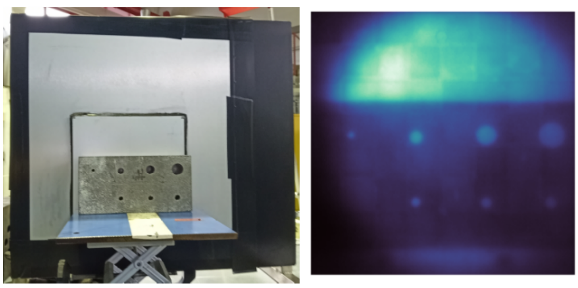

Figure 5: Lead brick sample (left) and the obtained neutron image (right) without white-beam normalization.

On the other hand, a graphite block with several holes was used as a sample, as shown in Figure 6. In this case, the measurement time was 5400 s, the frequency of the proton pulses was 10 Hz, and the proton pulse length was 3 µs.

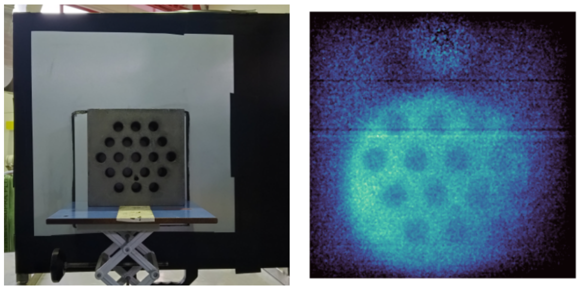

Figure 6: Graphite block with holes (left) and the obtained attenuation image (right) with white-beam normalization.

It was demonstrated that the fast neutron detector works correctly for the pulsed beam mode. Despite the images obtained could not be correctly analyzed due to the large amplitude of the signal corresponding to the electronic noise of the detector, with very low power at the target of just 1 W it was possible to resolve the minimum hole diameter of 2 mm.

5 Outlook

Thermal and fast neutron imaging are possible at low-power neutron sources. With an improved accelerator, which is foreseen for the HBS demonstrator, this technique would be more powerful, allowing proper images with measurement times of just some seconds.

References

[1] Gutberlet, T., Brückel, T., 2023. Technical Design Report HBS.

[2] Schumman, M., Engels, R.; Frank, M. ; Havenith, A.; Kemmerling, G.; Kettler, J.; Klapdor-Kleingrothaus, T. ; Mauerhofer, E.; Schitthelm, O., 2015. Performance Study of an aSi Flat Panel Detector for Fast Neutron Imaging of Nuclear Waste.

[3] Losko, A.S., Han, Y., Schillinger, B., Tartaglione, A., Morgano, M., Strobl, M., Long, J., Tremsin, A.S. and Schulz, M., 2021. Event-Mode Neutron Imaging Using the TPX3Cam-Breaking the Boundaries of Conventional Neutron Imaging Techniques.

A new Injector Timing System

O. Felden, K. Grigoriev*, Y. Valdau*

After a successful first beam on target in December 2022 additional 6 weeks of beamtime were granted in 2023 to the HBS-experiment, installed in the BIG-KARL-Experimental area, to investigate functionality of the shielding concept, neutron yields of the Ta-Target or different moderator concepts. Within these different tasks, the proton beam, hitting the Ta-target, needs to be pulsed with changing pulse-length or repetition rates, in combination with the extraction scheme from the cyclotron JULIC.

Fig. 1: Improved timing system.To cover the experimentalist needs as well as the COSY needs, a combination of two Quantum 9520 Pulse generators were foreseen to replace the old COSY timing system.

Starting with the COSY timing system, based on the HP 8116 PULSE/FUNCTION GENERATOR, which is very flexible, but tuned to the COSY-operation did not work. It showed very fast that this timing system isn´t capable of the experimental needs of variable repetition rates and pulse-length in its COSY-configuration. To overcome these problems a new timing system, consisting of two Quantum 9520 SERIES PULSE GENERATORS were designed (Fig. 1), capable of the COSY-timing-schemes as well as of the HBS-Timing needs .

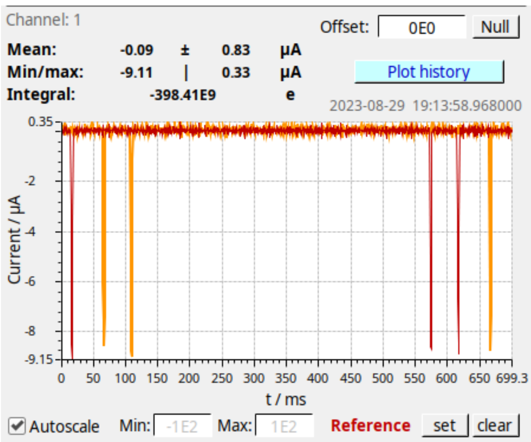

Fig. 2: Pulse trains at different times. The red line shows the pulse train at beginning of a measurement cycle (reference), while the orange line gives the moved pulse train after some minutes.

Unfortunately, the new timing system was not stable in operation and could not fulfil the expectations. First, the starting point of a pulse train wasn´t stable and moved within the given time frame (Fig. 2) causing loss of pulses after some time (Fig. 3). after some hours of operation the generators stopped working with bootrom failures.

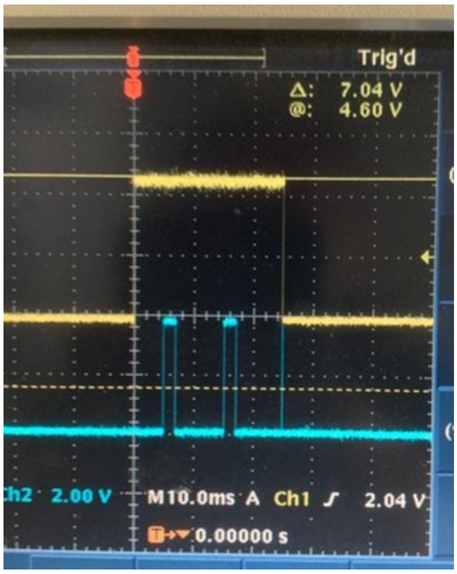

Fig. 3: Cut of the last pulse of a 3-pulse train.

To overcome these problems, the decision was drawn to decouple the HBS-timing from the COSY-timing and set up a standalone solution based on a Quantum 9530 SERIES PULSE GENERATOR acting on the ion source, JULIC injection- and extraction-system only.
The trigger signals for the ion source, the JULIC injection as well as JULIC extraction, diagnostic elements were cabled to the new Pulse generator for the HBS-experiments week exclusively and cabled back to COSY timing for following COSY-experiments. With the new timing system a stable operation (Fig. 4), covering the needs of the HBS experiment is fulfilled.
Fig. 4 shows the stability of the pulse trains after hours of operation with this new Quantum-9530 timing system.

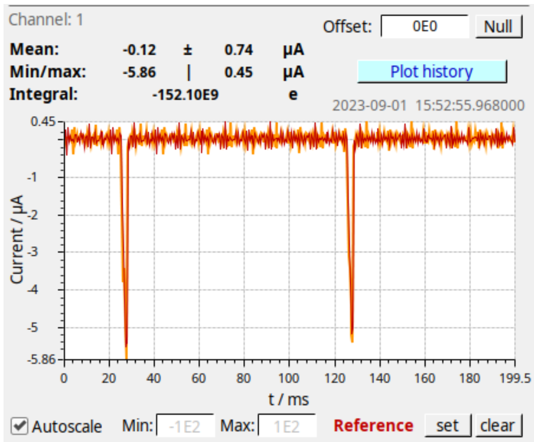

Fig. 4: Pulse trains at different times. The red line shows the pulse train at beginning of a measurement cycle (reference), while the orange line gives the pulse train, staying at the same position, after some hours.

* GSI Helmholtzzentrum für Schwerionenforschung GmbH, Planckstraße 1, 64291 Darmstadt

Polarization measurements with shiftable magnetic field

L. Kunkel [a,b,c], R. Engels [a,c], N. Hanold [a,d], C. Kannis [a,c,d], N. Faatz [a,b,c]

In the past, P.G. Sona developed a method to increase the nuclear polarization of atomic beams by altering the magnetic quantization axis. [1] This method exhibited an oscillation behavior dependent on the magnetic field configuration. We demonstrated that the transition method developed by Sona has the capability to alter the polarization of an atomic beam. When employing a sinusoidal magnetic field configuration with a single zero crossing, stimulated absorption and emission of photons occur, in addition to the exchange of pure states, leading to transitions between Zeeman states. [2]

In 2022, it was demonstrated that this new method is effective in generating polarization. In 2023, several experiments were conducted using such a transition unit, including one with movable coils. Fig. 1 illustrates possible movements, with this report focusing solely on the transverse displacement of the coil centers, as changes in wavelength have already been investigated previously.

The approximately sinusoidal field in the transition unit is induced by two coils at a variable distance through which the beam must pass. The magnetic fields act in opposite directions and can be shifted simultaneously, causing the center of the coil to move away from the beam axis. As atoms traverse the magnetic field in time, their relative movement induces a changing magnetic field, resulting in an electric field component, both radially and longitudinally. The stronger longitudinal component provides enough energy to split the energy levels of the atoms into substates of the hyperfine structure through the Zeeman effect, while the radial electromagnetic field induces transitions. The oscillating magnetic field facilitates the investigation of oscillating occupation numbers when the magnetic field components alter.

Figure 2 depicts the observed behavior for different coil positions where the center of the magnetic field deviates from the beam axis center. The beam position relative to the magnetic field center significantly influences the amplitudes of the field components. The field amplitude correlates with photon density, increasing the probability of atoms undergoing transitions with higher radial fields. However, changes not only in radial field amplitudes but also in the overall field lead to other effects influencing the measurement. The resulting graph demonstrates saturation with increasing distance from the center, possibly due to overlapping Lorentz peaks or other effects requiring further investigation.

As the spatial dimensions of the magnetic field change when the coils are moved, the wavelength also changes without varying the coil spacing. This is evident in the slight phase shift in Figure 2. Intentional changes in the wavelength result in more drastic peak shifts, as it was demonstrated in previous research.

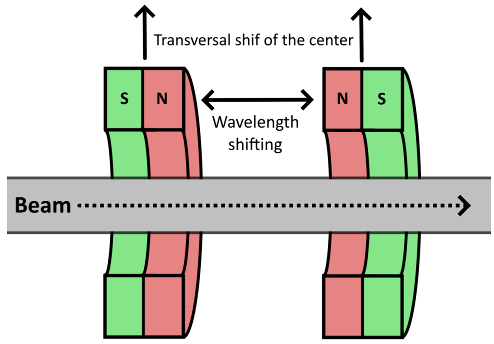

Figure 1: Schematic representation of the magnetic field configuration using the north and south poles and the directions of movement of the coils.

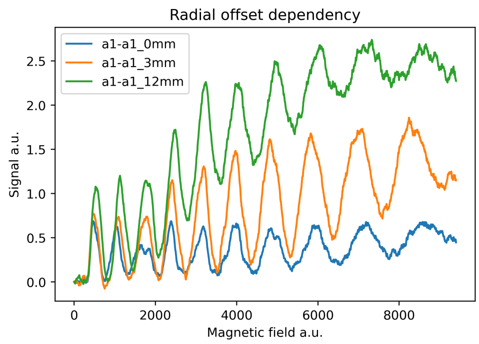

Figure 2: Changes in the occupation numbers of the α_1 states due to variation of the coil position as a function of the time-dependent magnetic field. The measurements were carried out with the same settings except for the distance to the beam. Two spin filters were used, one to define the incoming state and the second to measure the changes in its occupation number.

References

[1] P. G. Sona; Energ. Nucl. **14**, 295 (1967).
[2] R. Engels *et al.*; Eur. Phys. J D **75**, 257 (2021).

[a] Forschungszentrum Jülich GmbH, Institut für Kernphysik, Germany
[b] RWTH Aachen, Germany
[c] GSI, Darmstadt, Germany
[d] Institut für Laser- und Plasmaphysik, HHU Düsseldorf, Germany

Storage Cell Tests for the Polarized Target at LHCb@CERN

T. El-Kordy[a,b], R. Engels[b], K. Grigoryev[b], C. Kannis[b]

In the foreseeable future, the Large Hadron Collider beauty (LHCb) experiment at CERN is set to incorporate a polarized gas target, serving the purpose of enabling polarized fixed-target collisions for various spin physics experiments [1]. The objective of the LHCSpin project involves the integration of an atomic beam source (ABS) with a dedicated storage cell to enable the delivery of a polarized gas target for the unpolarized LHC beams.

Preserving the polarization of the incoming ABS beam is crucial for the storage cell. Hence, it is important to avoid using a ferromagnetic surface coating. Additionally, a hygroscopic coating, leading to the formation of a water layer, could hinder direct interaction between gas particles and the coating. Moreover, for vacuum compatibility, the outgassing rate needs to be minimal.

Using the former ANKE ABS, along with a Lamb-shift polarimeter (LSP), we investigated the polarization preservation and recombination behavior of a storage cell with a 200 nm thick amorphous carbon coating that was applied by the TE-VSC group at CERN.

Initially, hydrogen gas is introduced into the dissociator of the ABS. Following dissociation into atomic hydrogen, a conical shaped nozzle directs the beam into a Stern-Gerlach setup. Within this setup, two hyperfine substates of ground state hydrogen, characterized by the same electron spin projection, are filtered. The beam then passes through a set of transition units where, depending on the application, transitions into specific substates can be induced.

In the subsequent storage cell, the polarized atoms can recombine through surface-catalyzed recombination mechanisms, forming orthohydrogen (o-H_2). Simultaneously, an electron beam passing through the storage cell ionizes hydrogen atoms and molecules, while also dissociating a fraction of the molecules. Surrounding superconducting solenoids establish a strong magnetic field within the storage cell to prevent a loss in molecular polarization through wall collisions, attributed to the coupling between the rotational angular momentum J and nuclear spin I. Ions are subsequently accelerated out of the storage cell by a potential along the cell and directed into the LSP, where the polarization can be determined.

The Wien filter within the LSP can establish a proton beam comprising a fraction a of protons originating from the ionization of hydrogen atoms and a fraction $b = 1 - a$ from the dissociation of hydrogen molecules via electron impact. Their ratio depends on the recombination rate in the storage cell. Accounting for the distinct cross sections for both processes with the factor $k = \frac{\sigma(H_2 \to H^+ + H)}{\sigma(H \to H^+)} = 0.18$, the recombination rate c is expressed as:

$$c = \frac{2b}{ak + 2b}. \quad (1)$$

Due to the loss of the initial molecular polarization P_{m0} in weak fields, while the initial atomic polarization P_a is sustained, measuring the proton polarization P_p at various external magnetic fields B yields information on the recombination rate and on the number of wall collisions n. A fit on the measured data points, based on [2]

$$P_p(B) = aP_a + bP_m = aP_a + \frac{bP_{m0}}{1 + \frac{\tilde{n}}{ln(2)}\left(\frac{B_{c,m}}{B}\right)^2}, \quad (2)$$

considering the critical magnetic field $B_{c,m} = 5.4$ mT [3] for o-H_2 with $J = 1$, yields the fit parameters $a = 0.16 \pm 0.18$ and $n = 400 \pm 300$. The initial molecular and atomic polarizations, with $P_{m0} = 0.59$ and $P_a = 0.8$, were measured beforehand. Surprisingly, the recombination rate on an amorphous carbon coating lies in the region of $0.93 < c \leq 1$.

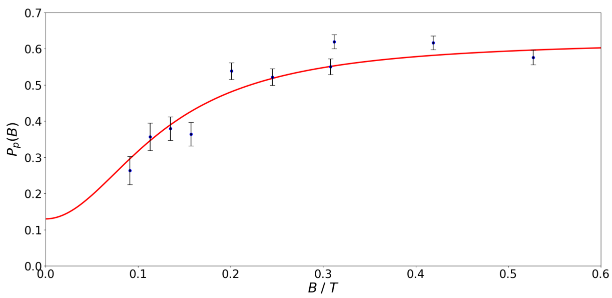

Figure 1: Proton polarization P_p for different storage cell magnetic field strengths B with associated fit.

Taking P_a and P_{m0} into account, the polarization preservation during recombination must fall within the range of 74%. Furthermore, the consistent presence of high recombination rates in all measurements indicates that there was no substantial water layer accumulation on the carbon surface, as water hinders recombinations. This renders amorphous carbon-coated storage cells suitable for delivering a polarized molecular gas target.

References

[1] B. Passalacqua *et al.*, IL NUOVO CIMENTO **45 C**, 121 (2022)

[2] R. Engels *et al.*, Phys. Rev. Lett. **115**, 113007 (2015).

[3] T. Wise *et al.*, Phys. Rev. Lett. **87**, 042701 (2001)

[a] FH Aachen - University of Applied Sciences
[b] GSI Helmholtzzentrum für Schwerionenforschung

Hyperfine dynamics of deuterium beams in sinusoidal magnetic fields

C. S. Kannis[a,*], R. Engels[a], N. Faatz[a,b], H. Sharma[a,c] and M. Büscher[d,e]

Nuclear spin-polarized deuterium (D) beams and targets serve as valuable tools across diverse disciplines. For instance, polarized deuterons find application in storage rings, particularly for research on the electric dipole moment. Additionally, beyond fundamental physics studies, polarized nuclear fusion is another notable application. In reactions involving deuterons and tritons or helions there is an increased efficiency by approximately 50% when the reactants are polarized in a parallel manner.

The predominant polarization techniques employed for D beams include atomic beam sources and spin exchange optical pumping. The former relies on the principles of the Stern-Gerlach experiment and the use of radio frequency transitions units to achieve the desired polarization. The latter follows a two-step process, where initially optical pumping induces polarization in a mediating species, and subsequently collisional exchange with ground-state atoms results in the establishment of nuclear polarization. Both techniques face limitations that restrict their production rates to levels below $\sim 10^{18}$ s^{-1}.

However, there is a demand for higher densities of polarized D beams or increased production rates in several applications, surpassing the capabilities offered by the conventional methods outlined. Our group has recently developed a novel technique [1] that effectively overcomes the limitations posed by these methods. A basic form of our polarizer involves the utilization of two opposing cylindrical coils. These produce a static field consisting of a longitudinal and a radial component. If the former is described by a sinusoidal function $B_z = -B_{z,max} sin(2\pi z/\lambda)$, the latter is given by $B_r = B_{z,max} cos(2\pi z/\lambda)\pi r/\lambda$, where z-axis is the direction of motion, $B_{z,max}$ represents the magnetic field amplitude of the longitudinal component, λ denotes the wavelength of the assumed sinusoidal function, and r corresponds to the radial distance from the z-axis. The combined effect of these magnetic fields creates Zeeman splittings between the hyperfine energy levels and simultaneously induces transitions between them. Specifically, the transitions are induced by the radial component, so none occur at $r = 0$ (on the z-axis). The experimental and theoretical investigations of this effect were conducted with an initially polarized metastable hydrogen beam [2, 3]. The spin dynamics were evaluated from the numerical solution of the Schrödinger equation and the results were compared to the measurements obtained using a Lamb-shift polarimeter. The direct comparisons enabled a comprehensive understanding of the induced transitions, ultimately giving rise to the conceptualization of this novel polarization method. The transition rates between the hyperfine states vary with the applied field strengths. This results in unequal occupation probabilities for the hyperfine states, which lead to uneven populations even in the case of an initially unpolarized beam. The hyperfine states, correlated to spin projections, determine the resulting polarization. The critical parameters for the optimization of the polarization of a particle beam are the wavelength λ, beam velocity, position, and distribution. Selecting an optimal current (or equivalently, $B_{z,max}$) the produced polarization can be maximized. Figure 1 illustrates an example of the variation of the average probabilities for the six hyperfine states of an equidensity D beam as a function of $B_{z,max}$.

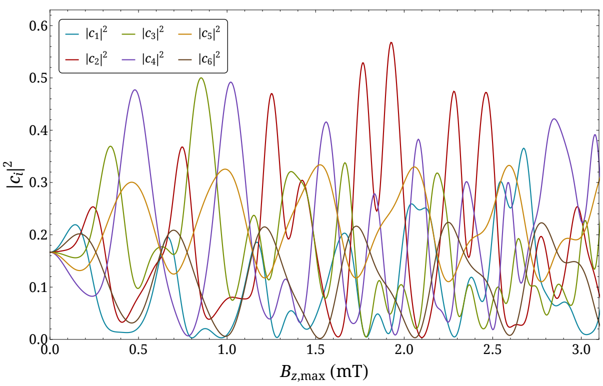

Figure 1: Average probabilities of the D hyperfine states as a function of $B_{z,max}$. They are computed over an equidensity beam profile with a diameter of 2 cm, where its center has an offset of 14 mm relative to the z-axis. The kinetic energy is set to 5 keV and the wavelength is assumed to be $\lambda = 45$ cm.

High asymmetries in the occupation number of the hyperfine states are indicative of high polarization degrees. In the specific example provided, the tensor polarization reaches a value of -1.44 when $B_{z,max}$ is set to 1.93 mT, considering the scenario with a high-field polarimeter following the polarizer.

References

[1] R. Engels *et al.*, arXiv:2311.05976.
[2] R. Engels *et al.*, Eur. Phys. J. D **75** (2021) 257.
[3] C. Kannis, Doctoral thesis, RWTH Aachen University (2023).

[a] GSI Helmholtzzentrum für Schwerionenforschung
[b] III. Physikalisches Institut B, RWTH Aachen
[c] FH University of Applied Sciences, Jülich
[d] Peter Grünberg Institut, FZ Jülich
[e] Institut für Laser- und Plasmaphysik, HHU Düsseldorf

[*]Present address: Institut für Laser- und Plasmaphysik, HHU Düsseldorf, Germany

Preliminary results of an improved automated polarization measurement with the lamb-shift polarimeter at the pulsed $\overrightarrow{\mathrm{H}}^-/\overrightarrow{\mathrm{D}}^-$ COSY Ion Source

S. Pütz[a,b], R. Engels[a], R. Gebel[a], K. Grigoryev[a], Y. Valdau[a]

Our polarized source delivers a nuclear polarized, pulsed H^- or D^- ion beam of 2 keV energy for stripping injection into the storage ring COSY. Before injection, nuclear polarization must be determined and optimized. For this purpose, a polarization measurement was carried out behind the source using a Lamb-shift Polarimeter (LSP). This method of polarimetry replaces the usually used Low Energy Polarimeter (LEP) because the LEP consumes a lot of energy and time, as it requires a pre-accelerated beam of 45 MeV from the JULIC cyclotron. After a successful proof of principle experiment showing that nuclear spin polarization measurements on H^- ion beams can also be performed with the LSP [1], we used a beam time in 2023 to test an improved automated data acquisition system.

The basic idea of the determination of the beam polarization is selecting certain conditions in the spin filter of the LSP in order to filter single hyperfine substates and compare their relative intensities. The spectrum is measured by a photomultiplier detecting Lyman-α photons produced by quenching the surviving metastable states into the ground state behind the spinfilter. For known magnetic field strengths, individual substates survive, which makes it possible to plot the intensity of the photons as a function of the B-field in order to determine the beam polarization by the relative difference of the peak heights. The quality of the spectra depends on the signal intensity and its relative uncertainty.

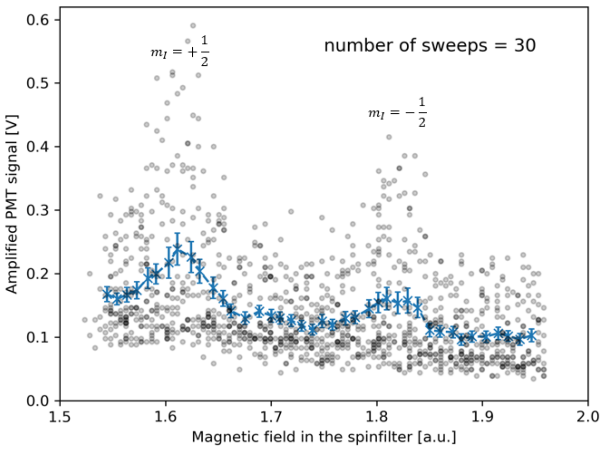

Figure 1: Lyman-α spectrum for positive polarization ($m_I = +\frac{1}{2}$ dominates). The gray dots show the raw data signals from the photomultiplier for 30 magnetic field sweeps. The mean values and their uncertainties are plotted in blue.

Analyzing these properties leads to the improvements demonstrated in the development from 2022 (Fig. 1) to 2023 (Fig. 2). This first version of the automized data taking is based on a computer-controlled ADC that simultaneously ramps the magnetic field in the spinfilter and receives the measured PMT signals as input, which can then be stored on the PC. The strong scattering and most values being close to zero turned out to be the result of the ADC's poor sample rate. The produced signals were too short for the ADC to measure them reliably.

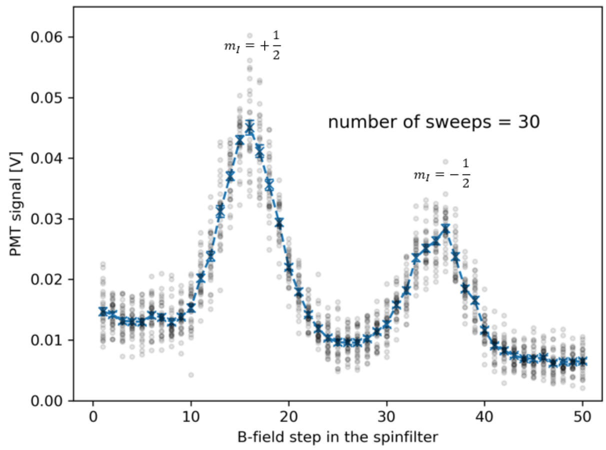

Figure 2: This plot illustrates a spectrum for positive beam polarization. The improved signal-to-noise-ratio is clearly recognizable, which is a result of the enhanced measurement precision.

Figure 2 shows a measured spectrum with the improved data acqusition setup. The ADC was replaced by an oscilloscope with a sufficient sample rate. The whole measurement was controlled by a python script that saved and averaged the data directly for plotting, allowing "live-tuning" of the polarized H^- source.

References

[1] S. J. Pütz *et al.;* Proc. Sci. **433** (2022) 029.

[a] GSI Helmholtzzentrum für Schwerionenforschung, Planckstraße 1, 64291 Darmstadt, Germany
[b] University of Cologne,
Zülpicher Straße 77, 50937 Cologne, Germany

Polarization, Acceleration and Polarimetry of $^3He^+$

J. Wirtz[a,b,c], M. Büscher[d,e], R. Engels[a,b], N. Faatz[a,b,c], O. Felden[a], R. Gebel[a,b], K. Grigoryev[a,b], A. Lehrach[a,c], C. Kannis[a,b], S. Pütz[a,b,f], H. Soltner[g] and C. Zheng[d,e]

Earlier experimental and theoretical studies proved that particles with a hyperfine structure can gain nuclear spin polarization when passing a specific magnetic field configuration [1]. An experiment was proposed and carried out to test this new polarization method for $^3He^+$ ions, where achieving nuclear polarization had been a challenging task so far. As a substitute for polarized neutron beams, ^3He is a promising probe for nuclear physics [2] and can also be used as a polarized fuel for nuclear fusion.

For this test an ECR ion source was installed at the source beamline, providing a $^3He^+$ ion beam of about 2 µA at 7 keV kinetic energy. This beam passes through a Wien-Filter, then a longitudinal magnetic field and finally two opposing solenoids. These solenoids provide a zero crossing of the longitudinal magnetic field component, which is expected to influence the beam polarization.

During a beam time in October/November it was planned to inject and accelerate these ions in the cyclotron JULIC with an expected final energy of around 70 MeV. Tests on injecting H_3^+ ions into the cyclotron proved unsuccessful at the normal operating point, most likely due the charge-to-mass ratio of 1/3 slightly exceeding the range of operation of the cyclotron. Instead, the acceleration was performed in the 9ω-mode [3], limiting the final energy to 14.2 MeV and the $^3He^+$ beam intensity to 0.7 nA. The final beam cross section is shown in figure 1.

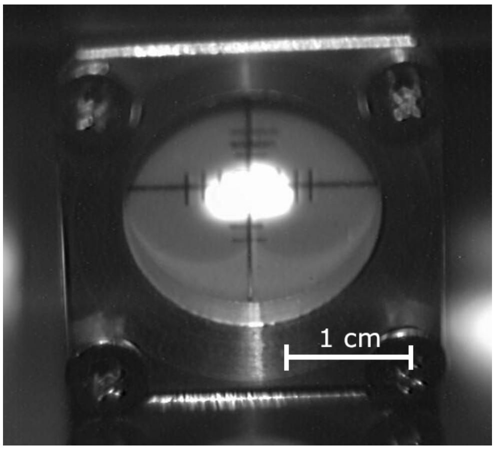

Figure 1: Final $^3He^+$ beam spot at the beam viewer in the Low-Energy-Polarimeter.

The beam polarization was measured with CH_2 and CD_2 targets installed in the existing Low-Energy-Polarimeter. The polarimeter is equipped with twelve plastic scintillator detectors covering polar angles between 25° and 75° and four different azimuthal angles. The known analyzing powers of both, the elastic scattering reaction p(^{3}He,p)^{3}He and the fusion reaction d(^{3}He,p)^{4}He, can be used to determine the beam polarization from measured azimuthal asymmetries. Additionally, peaks from the fusion reactions ^{12}C(^{3}He,p)^{14}N and respective excited states of ^{14}N were observed. At the reduced beam energy mainly protons are expected to reach the detectors, resulting in the measured spectrum shown in figure 2.

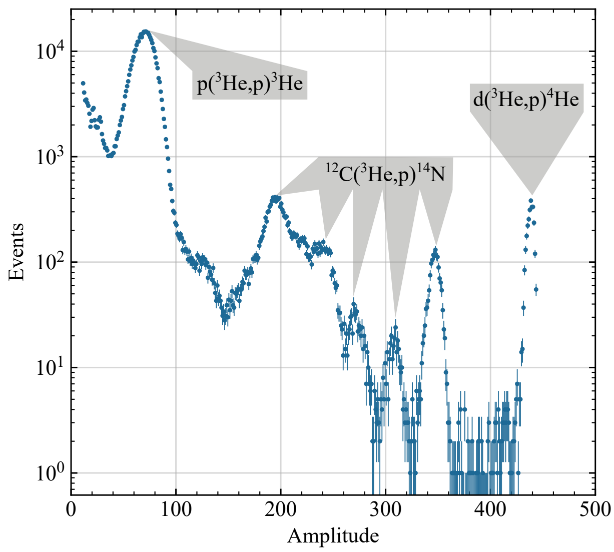

Figure 2: Spectrum from one hour of 0.7 nA $^3He^+$ ions on a 6.6 µm CD_2 + 8 µm CH_2 target at $\theta = 26°$.

The different reactions were identified using different targets, an energy calibration from known ^{12}C(p,p)^{12}C reactions and literature values for the expected cross sections. While the evaluation of the polarization is still ongoing, the transmission through the complicated beamline may have led to significant polarization loss.

References

[1] R. Engels et al., arXiv:2311.05976 (2023).
[2] T. B. Clegg, AIP Conf. Proc. 980, 37 (2008).
[3] W. Bräutigam et al., 9th Intl. Conf. on Cyclotrons and Appl., B29 (1982).

[a]Institut für Kernphysik, FZ Jülich
[b]GSI, Darmstadt
[c]III. Physikalisches Institut B, RWTH Aachen
[d]Peter-Grünberg-Institut 6, FZ Jülich
[e]Laser- und Plasmaphysik, HHU Düsseldorf
[f]Institut für Kernphysik, Universität zu Köln
[g]ZEA-1, FZ Jülich

Designing a transition-unit with oscillating transversal fields and testing

J. Steinhage[a,b], R. Engels[a], B. Klimczok[a], F. Van Maele[a,c],
N. Faatz[a], C. S. Kannis[a], M. Westphal[a,b], D. Tilli[d], C. Schoberer[b]

A Sona unit consists of two solenoids covering a beamline. The magnetic fields of these coils run in opposite directions. The longitudinal field lines establish a reference for the particle's spins. A particle beam with sufficient speed can pass through the crossing point between the solenoids without readjusting its nuclear spin projection. Furthermore, an atom passing through the radial fields of the solenoids will experience a waveform acting as a virtual photon. This process induces transitions in the hyperfine structure. By increasing the radial magnetic fields, the likelihood of these transitions will increase accordingly [1]. Transversal fields will be used as a substitute to maximize the radial fields. Two solenoids will be placed perpendicular to the beam axis for this setup. An additional pair of solenoids, running in the opposite direction, completes the waveform.

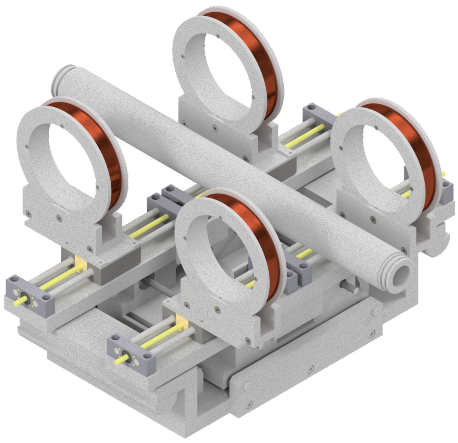

Figure 1: Design for a transition unit with transversal magnetic fields.

The maximum amplitude $B_{\max}$ of these solenoids is calculated with the equation for the magnetic fields in a Helmholtz constellation. This setup is established when the distance d between two solenoids equals their radius R. Under these circumstances, the two field lines connect without any losses. Since the diameter of the beamline is 50 mm, the chosen solenoid radius R is 60 mm. This leaves some options for adjustments afterward in case of discrepancies between the model and reality. The construction is aimed to produce fields of $B_{\max} = 10$ mT using $n = 70$ windings per solenoid and running on a current of $I = 10$ A. The idealized equation for the longitudinal magnetic field in the middle of two solenoids at a distance of $R/2$ is presented in the following equation [2].

$$B = \mu_0 \cdot \frac{8 \cdot I \cdot N}{\sqrt{125} \cdot R} \tag{1}$$

.

The closer this waveform resembles a sinusoidal, the more it becomes a virtual photon. The measurements in Fig. 2 present a rough approximation.

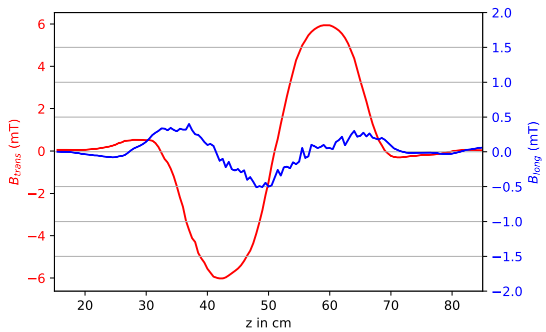

Figure 2: Measurements of the transitions units magnetic field along the beam axis with $B_{\max} = 5.5$ mT

Four linear modules allow for the individual alteration of the coil distances to the center of the beamline, as seen in Fig 1. This method will be used to shape the peaks of the transversal fields from square- to sinus-like.

The second important parameter is the distance between the pairs. This range influences the overlap and gradient of the two opposing peaks. The aluminum blocks underneath the coil pairs are loosely connected to the bottom plate via bolts. The connection includes a track to slide the blocks along, affecting the previously mentioned parameter. The screws at the bottom and the sides of the construction control the height of the installation.

Further magnetic field measurements and their tuning will follow. A first test to polarize metastable beams is foreseen in early 2024.

References

[1] P. G. Sona, Energ. Nucl. **14**, 295 (1967).
[2] P. Granum et al., Science Direct **1034** (2022), 166706.

[a] GSI Helmholtzzentrum für Schwerionenforschung, Germany
[b] Fachbereich Energietechnik, FH Aachen – University of Applied Sciences
[c] III. Physikalisches Institut B, RWTH Aachen University, Germany
[d] Department of Physics, Aristotle University of Thessaloniki

Production of polarized deuterium beam and its measurement

H. Sharma[a,b], R. Engels[b], S. Gass[c], C.S. Kannis[b,c], N. Faatz[b], V. Verhoeven[b], H. Xu[b], J. Wirtz[b,d]

After a successful production of nuclear polarization in beams of metastable hydrogen and deuterium atoms in $2S_{1/2}$ state with opposing coils[1], this method should be expanded to beams of ground state deuterium atoms. It was also concluded that the generation of polarization when flying through an oscillating longitudinal magnetic field depends on the speed of the atoms, the shape of the magnetic field, and its amplitude. Now, further experiments are being conducted to optimize and measure the nuclear polarization of a ground-state deuteron beam using a nuclear-reaction polarimeter.

To realize this measurement we need to perform a d+d→p+t fusion reaction. This process involves a beam polarized by the Sona unit and an unpolarized target made of CD_2 (deuterated polyethylene). The target foil has a thickness of 3.8 μm, which is sufficient to stop the deuteron beam and allows detection of the reaction products. The nuclear polarimeter consists of 6 silicon surface-barrier detectors placed at certain angles relative to the beam axis. These are calibrated with an alpha source containing Pu-239, Am-241 & Cm-244. Using studies that measured the angular distribution of vector and tensor analyzing power of the mirror d-d reaction products at low energies[2], the nuclear polarization value of the deuteron atom can be quantified. The counts of the products have an asymmetry in the amplitude at different angles which is taken as a ratio concerning the total amount of counts. The ratio of such quantity signifies the nuclear polarization of the products in the direction in which it is measured, in our case the beam direction is the spin-quantized axis, therefore the p_{zz} tensor polarization component can only be analyzed[3].

$$\epsilon(\theta) = \frac{n_{pol} N_{Apol}(1 - 1/4p^*_{zz}(3cos^2\phi - 1)A_{zz}(\theta)}{n_{unpol} N_{Aunpol}} \tag{1}$$

$$\frac{\epsilon(\theta_1)}{\epsilon(\theta_2)} = \frac{2 - p_{zz}A_{zz}(\theta_1)}{2 - p_{zz}A_{zz}(\theta_2)} \tag{2}$$

The tensor analyzing power (A_{zz}) amplitude differs over angles. Hence, the maxima and minima of the curve can be chosen and measurements can be performed. In addition to experimental measurements, the differential equation of the interaction of the hyperfine structure with the external magnetic field is derived and numerically analyzed. The quantum mechanics involved in the hyperfine transitions is theorized by time-dependent perturbation theory[4]. The system is studied in a stationary frame to focus on spin dynamics and avoid motion-related terms.

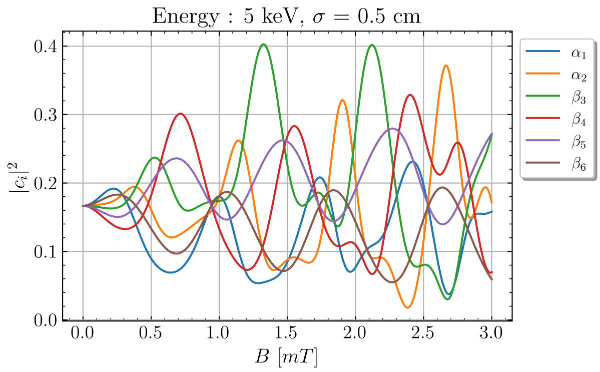

Figure 1: Probabilities $|c_i^2|$ of hyperfine states for a ground state deuteron atom for a radial gaussian beam of a diameter = 4 cm, σ = 5 mm, E_{kin} = 5 keV and wavelength of 45 cm as a function of the magnetic field inside the Sona unit.

The above figure illustrates an oscillatory behavior of the hyperfine substates as a function of the magnetic field for unpolarized ground-state deuterium atoms after leaving the Sona unit. In principle, this induced transition can be selected with dedicated magnetic and electric field configurations. Furthermore, the tensor polarization value in high fields ($B_{critical}$ > 11.7 mT) can be calculated using the following equation:

$$p^h_{zz} = |c_1|^2 - 2|c_2|^2 + |c_3|^2 + |c_4|^2 - 2|c_5|^2 + |c_6|^2 \tag{3}$$

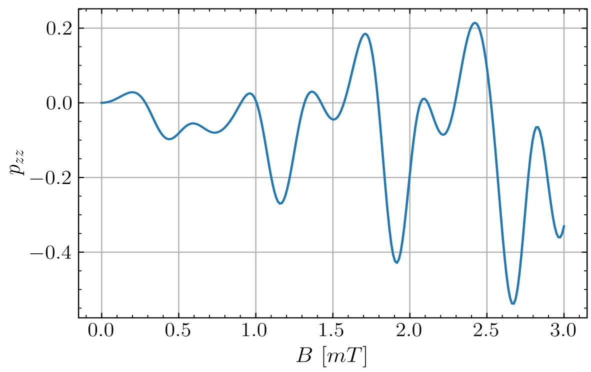

Figure 2: The plot computes tensor polarization (p_{zz}) produced when the beam passes through the Sona unit.

References

[1] R. Engels et al.; Eur. Phys. J. D **75**:257 (2021).
[2] Tagishi, Y. et al.; Phys. Rev. C 46, R1155–R1158 (1992).
[3] R. Engels, Diploma Thesis, Universität zu Köln (1997)
[4] C. Kannis, PhD Thesis, RWTH Aachen University (2023).

[a] FH University of Applied Sciences, Jülich, Germany
[b] GSI Darmstadt, Darmstadt, Germany
[c] Heinrich-Heine-Universität, Düsseldorf, Germany
[d] RWTH Aachen University, Aachen, Germany

A compact FEE and DAQ system for the nulcear-fusion polarimeter

H. Xu for the Polarized Atomic Beams Collaboration

Recently a new method to generate hyperpolarization has been investigated at IKP, FZ Jülich. The concept is to use a Sona transition coil, which generates oscillating magnet field, to polarize the beam particles. If this technique becomes feasible, there will be many applications, for example, polarized beams for tokamak or stellerator to increase their energy output or producing polarized tracer for increasing the MRI resolution. To find out the feasibility of this new method, one attempt is to measure the polarization of beam particles passing through the Sona coil.
In fact, a commissioning experiment measuring the beam polarization has been designed and carried out. The setup for such a measurement mainly consists of an ECR ion source, a Wien Filter, a Sona coil and a nuclear-fusion polarimeter. The ECR ion source generates a deuterium beam with an energy up to 10 keV, which can bombard a deuterium target. As a consequence, the nuclear fusion reaction, i.e., $d+d \rightarrow t+p$, can be measured. With the known analyzing power of the reaction, the beam polarization can be determined accordingly.
A polarimeter has been designed and constructed to measure the rate as well as the energy of the product of the nuclear fusion reactions. Fig. 1 shows an expected energy spectrum of the ~0.8 MeV $^3He^{2+}$, ~1 MeV triton and ~3 MeV proton, while an accompanying reaction, e.g., $d+d \rightarrow {}^3He+n$ is also occurring. To fulfill the requirements of the measurement the polarimeter was built on a standard double cross vacuum component. The deuterium target and silicon detectors are integrated on vertical and horizontal flanges, respectively. Six gold-silicon surface barrier detectors are currently employed and fixed on the horizontal plane as well as the vertical plane to measure the energy and the rates of fusion products, thus the analyzing power of a polarized beam.

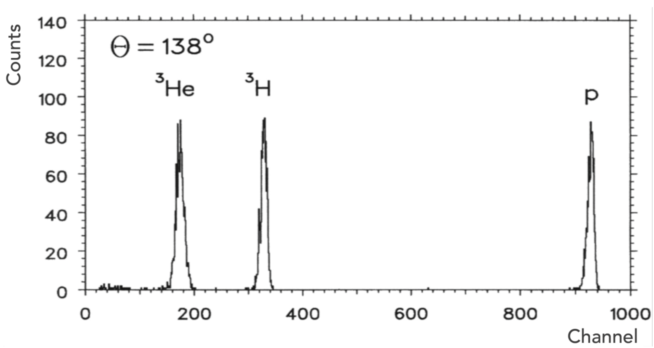

Fig. 1: Energy spectrum of the products of d+d fusion reactions.

A compact FEE and DAQ system has been established for this measurement. The sketch of the detector, FEE and DAQ system of the polarimeter is demonstrated in Fig. 2. A16-channel preamplifier, mesytec MPR16, has been employed for the readout of the silicon detectors. The mesytec shaping amplifier MSCF16 has been used for shaping the energy signal as well as offering the triggers for the data taking. Combined with VME bus, the 32-channel peak sensing ADC, i.e., MADC32, has been added into a VME crate for digitizing the amplitude of the energy signal of the fusion products. Benefitting from the integrated 16 channel electronics modules the FEE is very compact and can be extended up to 16 detectors without adding extra hardware. The only constraint is that all detectors must work at the same bias voltage. The software performing the data taking is the EMS system commonly used for experiments at COSY. The EMS system is running on a computer with Linux kernel. The raw data obtained by EMS can be processed for online display as well as for further offline analysis.

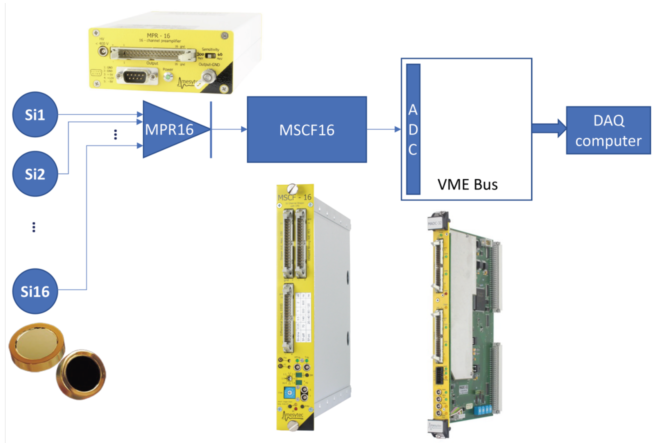

Fig. 2: Sketch of the FEE and DAQ system for the nuclear-fusion polarimeter.

The pilot measurement with unpolarized beam has been performed. With a beam energy of few keV, the event rate on a single detector was estimated to be at the order of few counts per hour. No fusion event has been observed. Few hits around the expected energy region were just some noise signals, because they appeared on different detectors simultaneously. After having tuned the ECR source to deliver a 10 keV D^+ beam as well as employing a CD_2 target, a new run is being performed. As indicated in the Fig. 3, with about 18 hours data taking, some desired protons of the fusion reaction have been observed on several detectors. Around 100 proton events were detected by the detector Number 7, which has a larger aperture than others. This is a very convincing achievement. The next attempt will be to measure the beam polarzation after particles go through the Sona coil.

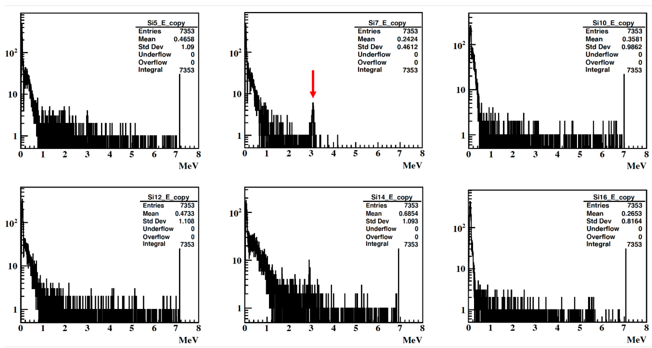

Fig. 3: Event candidates of the fusion products around 3 MeV.

Analyzing power measurement with a polarized COSY beam

D. Grzonka, P. Kulessa, D. Okropiridze, J. Ritman, V. Verhoeven, H. Xu, R. Yang, M. Zielinski, H. Zmeskal

In view of antiproton polarization studies at CERN, a measurement with a polarized proton beam from COSY has been performed [1]. The measurement was a test of the detection system to be used at CERN and aims at the determination of the analyzing power of the elastic pp-scattering in the Coulomb-Nuclear-Interference (CNI) region at a beam momentum in the few GeV range. A sketch of the detection setup and a photo of the installation in the TOF-area is shown in Fig.1. The system includes various detector components and has a length of about 4 m. The determination of the an-

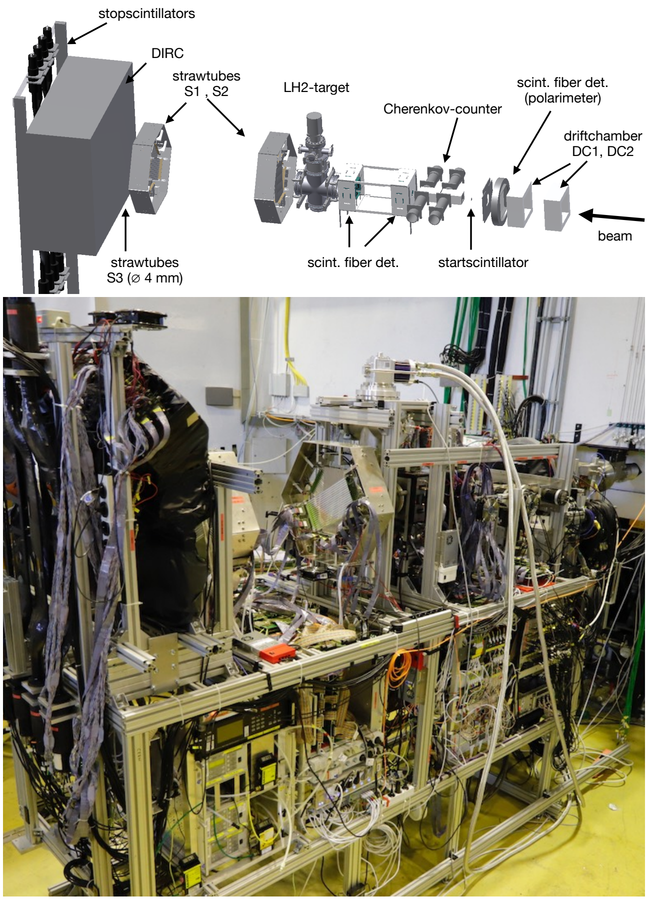

Fig. 1: Detection setup installed in the TOF-area.

alyzing power requires track measurements of the primary and the scattered particles which is done by a scintillating fiber detector with 0.5 mm and 1 mm thick fibers in front of a liquid hydrogen target for the primary beam particles and a set of straw tubes for the scattered particles. X- and y-coordinates in several planes were measured from which the scattering angle can be determined. A triggersignal was generated from the signals of the start- and stop-scintillators. The Cherenkov-counters were not necessary for the measurement at COSY with a pure proton beam. But they are important for a measurement at CERN at the secondary beam with 3.5 GeV/c momentum produced by the 24 GeV/c proton synchrotron where most beam particles are pions and have to be separated.

The COSY measurement requires an additional polarimeter to determine the beam polarization. It consists of a scintillating fiber array in x- and y-direction and a small plastic scintillator as scattering target in front of the polarimeter. Furthermore two drift chambers were used at the entrance of the system to determine the beam particle position at the polarimeter target.

For the measurement a beam momentum of 1.95 GeV/c was chosen in order to reduce the number of depolarizing resonances. A proof of beam polarization was done with the internal JEDI polarimeter. The absolute polarization value could not be extracted from these measurements but a clear asymmetry was observed which indicates a rather high polarization degree. A clear scattering asymmetry was also observed in the experiment setup which confirms the assumption of a high beam polarization. The determination of the polarization degree needs a detailed analysis which is now being performed.

In Fig.2 the beam profile in x- and y-direction is shown as measured by the first driftchamber DC1 and by the straw tube detector S3 located in a distance of about 3.5 m downstream. The histograms give the positions of the wires which have a distance of 10 mm in DC1 and 4 mm for S3. After calibration the expected position resolution will be in the order of 100 to 200 μm which will result in a precise reconstruction of the tracks and the scattering angle. The data are now under

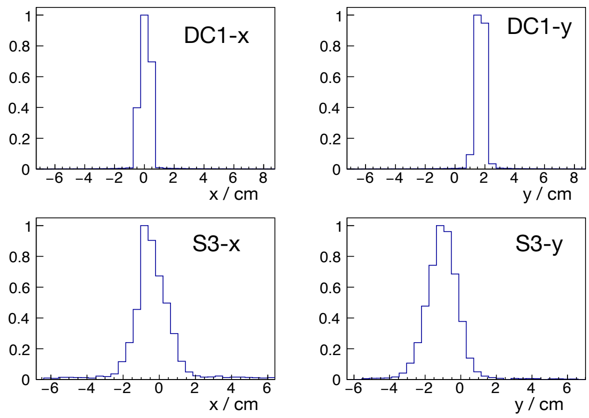

Fig. 2: Beam profile in x- and y-direction in DC1 at the entrance of the detector system and in S3 about 3.5 m downstream.

analysis and the results will allow a detailed planning of the antiproton polarization study which is foreseen in 2025.

References:

[1] COSY proposal D013.2, February 2023.

Investigation of proton irradiated SiPMs

V. Verhoeven, D. Grzonka, J. Ritman

Radiation hardness of Silicon photomultipliers (SiPMs) is a crucial property compared to conventional photomultiplier tubes. Therefore an irradiation study was performed at the Jülich cyclotron with a proton beam of about 39 MeV. A series of SiPMs were fixed on a plexiglas plate, as shown in the sketch of Fig. 1. and placed in the irradiation plane in such a way that, due to the beam profile ($d \approx 20$ cm), a factor of about 100 was obtained between the lowest and the highest radiation dose accumulated.

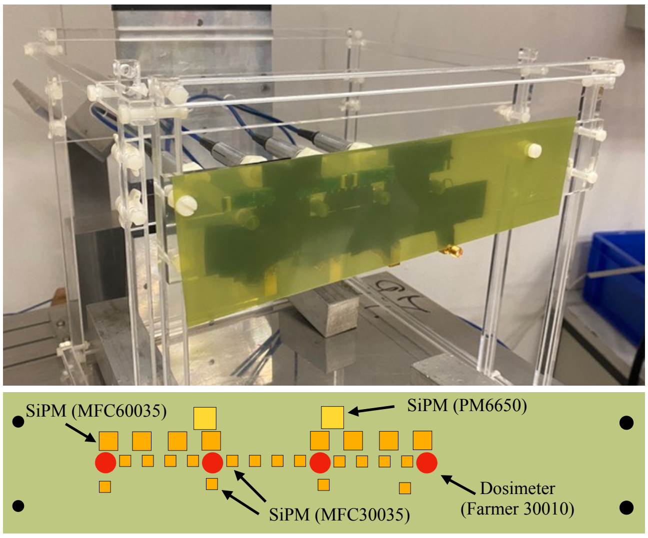

Fig. 1: Setup for the SiPM irradiation study. A sample of SiPMs were placed on a plexiglas plate as shown in the sketch. Radiation dose was measured by an irradiation foil and dosimeters attached to the plate.

SiPMs from OnSemi (orange squares) in 3x3 mm^2 (MFC30035) and 6x6 mm^2 (MFC60035) versions and from KETEK the 6x6 mm^2 type PM6650 (yellow squares) were used. The four SiPMs in the lowest row were light-tight covered by a thin black foil and taken into operation during the irradiation procedure to obtain online signals.
To determine the radiation dose, four dosimeters, Farmer chambers type 30010, were fixed to the plate with the SiPMs. The positions are indicated by the red dots in the sketch. In addition, the entire area was covered with a radiation-sensitive foil that darkens as the radiation dose increases. With the radiation dose measured in the dosimeters, the density of the foil can be calibrated as a function of the radiation dose and allows the determination of the dose absorbed by the individual SiPMs.
A first irradiation was performed with a dose rate of about 0.03 Gy/min. until the dosimeter with the highest dose had accumulated about 200 Gy, while the lowest dose was 0.33 Gy. The plate was then replaced with a new one prepared in the same way and the dose rate was increased to about 100 Gy/min. until the highest dose dosimeter had accumulated about 6,000 Gy.
With this irradiation study, a series of SiPMs is now available for detailed analysis.
A first indication of the SiPM performance is the dark current which is shown in Fig.2. Already at rather low irradiation levels a strong increase of the dark current by orders of magnitude is observed.

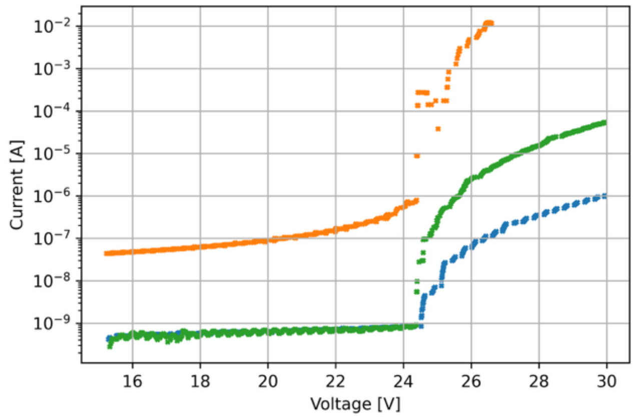

Fig. 2: SiPM current as a function of voltage for a new SiPM (blue), the least (green) and highest irradiated (orange) ones. The breakdown voltage is comparable at approx. 24.5 V. The voltage was stepwise ramped up and down and the related current was measured.

In Fig.3 typical signals of SiPMs coupled to a scintillator irradiated by a ^{90}Sr-source are shown. While a new SiPM gives clear signals, with increasing radiation dose the signals get worse until the separation of a single SiPM-signal is impossible at the highest radiation dose.

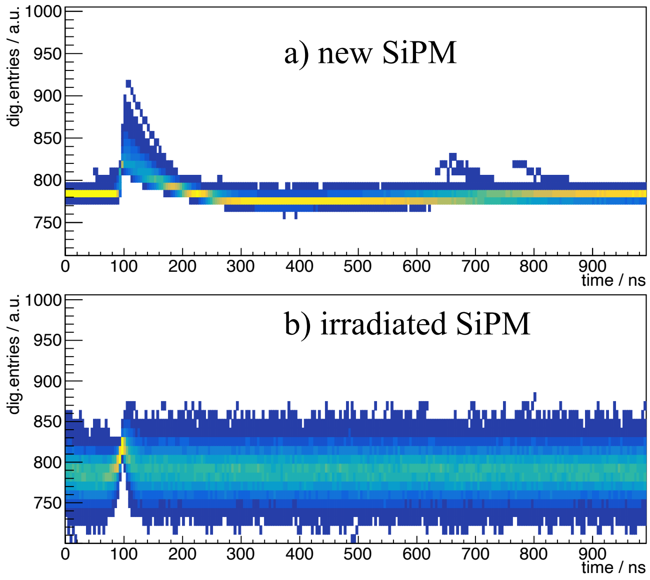

Fig. 3: Signals of a new SiPM compared to the highest irradiated one. Both SiPMs were coupled to a single scintillator and only coincident signals were recorded.

Presently the irradiated SiPMs are further investigated concerning parameters like dark count rate, breakdown voltage, after-pulse rate and response to different numbers of photons. Furthermore the recovering abillty with a bake-out procedure is studied.

M Poster Presentations

Contents

RUHR-UNIVERSITÄT BOCHUM

RUB

Study of the process $pp \rightarrow ppKK$ with Hades

V. Kladov[1,2], J. Ritman[1,2,3] and J. Messchendorp[2] on behalf of the HADES collaboration

[1]Ruhr-Universität Bochum
[2]GSI Helmholtzzentrum fur Schwerionenforschung GmbH
[3]Forschungszentrum Jülich

Motivation

- Search for intermediate resonances, both baryonic and mesonic, and study the strangeness production mechanism such as testing the OZI rule by comparing $\phi \rightarrow KK$ and $\omega \rightarrow KK$ cross sections.
- Improve $K^{\pm}$ identification at HADES, which is helpful in particular for cascade analyses with hyperons.

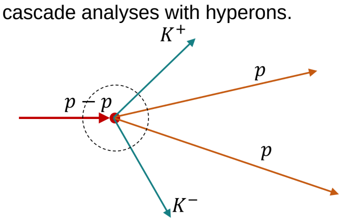

Process diagram. Protons with $E_k \approx 4.5\ GeV$ hit stationary hydrogen target (p). Lifetime of intermediate states is negligible.

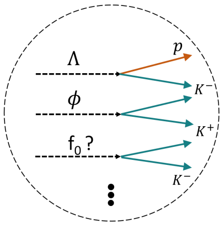

Main second-stage intermediate resonances decaying into final kaons and protons.

Experiment and selection strategy

Data available:

- Integrated luminosity $\mathrm{IL} = (6.47 \pm 0.1)\ \mathrm{pb}^{-1}$.

General Corrections:

- BeamTilt and E_{beam}.
- Energy loss.
- T_0 (adjust β_i when no start data available).

General cuts:

- Track quality flag.
- TOF "physics" trigger.

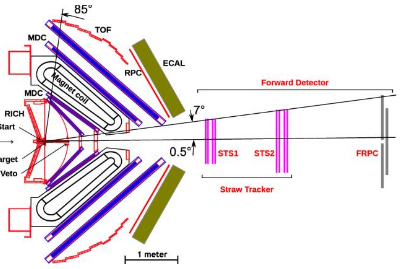

Hades detector layout for FEB22 p-p experiment.

Specific selections for $pp \rightarrow ppKK$:

- Multiplicity: $\mathrm{N_p} \geq 2, \mathrm{N_{K^+}} \geq 1, \mathrm{N_{K^-}} \geq 1$ in the main HADES.
- PID: NN-based, $\pi^{\pm}, \mathrm{K}^{\pm}, \mathrm{p}$ separation.
- Kinematic fit: χ^2 cut to account for 4-momentum (P) conservation.

Neural Network Particle Identification

- Domain adversarial NN (DANN) with half labeled (sim) and half unlabeled (exp) training dataset to compensate for the differences between experiment and simulation [1].
- NN takes as input a list of particle's parameters and predict a list of probabilities corresponding to particle types:
$P,\ Q,\ \theta,\ dE/dx_{MDC},\ dE/dx_{TOF},\ ToF,\ \beta,\ M^2 \rightarrow P_p,\ P_{\pi^+},\ P_{\pi^-},\ P_{K^+},\ P_{K^-}$

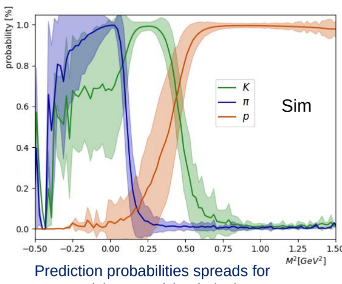

Prediction probabilities spreads for true particle types (simulation).

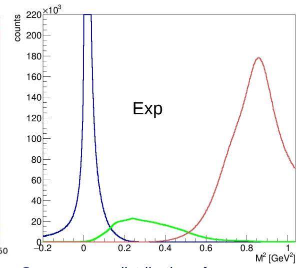

Square mass distributions for predicted particle types (experiment).

Kinematic reconstruction and fit

- Kinematic refit is the best tool in kinematically overdetermined measurement. It separates background and improves experimental resolution by adjusting measured parameters to strictly follow the physical process of interest.
- Fit minimizes $\chi^2 = (\vec{y} - \vec{\eta})^T V^{-1} (\vec{y} - \vec{\eta})$, where $\vec{y}$ and $\vec{\eta}$ are the vectors of measured and target particle's parameters, V is the correlation error matrix and $\vec{\eta}$ satisfies 4 momentum conservation $\sum P_i - P_{beam+target} = 0$ [2].
- Pull distributions are used as the main quality of fit metrics. $Pull_i = \frac{\eta_i - y_i}{\sqrt{\sigma^2(y_i) - \sigma^2(\eta_i)}}$ and ideally they follow normal distribution $N(0,1)$.

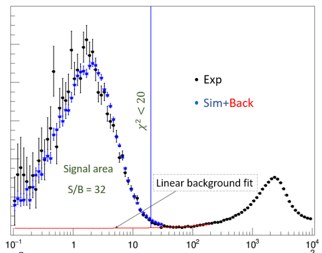

χ^2 probability distribution for 4C fit in logarithmic scale with linear approximation of experimental background (red).

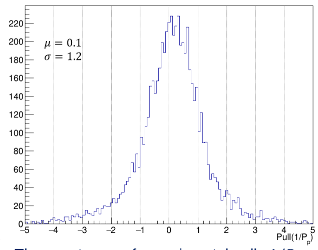

The worst case of experimental pulls $1/P_p$. Shift is due to difference in detector response in experiment and simulation.

Invariant mass distributions

Signal peak of $\varphi \rightarrow KK$ becomes clearly visible after applying kinematic reconstruction fit which suppresses background by 3 orders of magnitude with 80% efficiency.

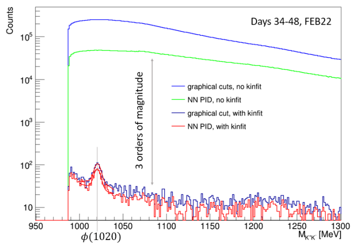

K^+K^- invariant mass distribution: $\phi(1020)$. $\mu = (1020.5 \pm 0.5) MeV$, $\sigma = (3.7 \pm 0.4) MeV$. Background is mostly a mixing of π with K.

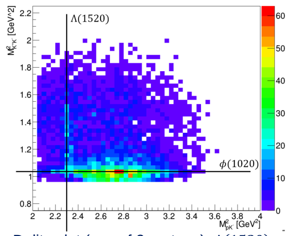

Dalitz plot (any of 2 protons): $\Lambda(1520)$: $\mu = (1519 \pm 3.7) MeV$, $\sigma = (11 \pm 3) MeV$. Peaked structure at $M_{pK^-} \approx 2.8 GeV^2$ corresponds to phase space distribution.

Conclusions

- NN PID with suppression of simulation systematics is implemented.
- Kinematic refit is applied and proved to be an essential tool in case of all final state particles being efficiently detected.
- Clear $\phi(1020)$ and $\Lambda(1520)$ peaks observed, parameters are consistent with PDG data within one standard deviation.
- ~1365 events found corresponding to $\phi(1020) \rightarrow KK$ decay for the full data set.
- Outlook: improve statistics by including forward detector in the analysis, improve PID by training on the new generation of simulation.

References

1. Ganin, Yaroslav, et al. "Domain-adversarial training of neural networks." The journal of machine learning research 17.1 (2016): 2096-2030.
2. Esmail, Waleed, et al. "KinFit-A Kinematic Fitting Package for Hadron Physics Experiments." arXiv preprint arXiv:2308.09575 (2023).

Physik und Astronomie
from matter to materials

GSI FAIR NRW-FAIR RUB

Development of Machine Learning Algorithms to Optimise the Detection of Low-mass Dileptons

Saket Kumar Sahu[1,2], Johan Messchendorp[2] and James Ritman[1,2,3]
[1]Ruhr-Universität Bochum, Bochum, Germany
[2]GSI Helmholtzzentrum fur Schwerionenforschung GmbH, Darmstadt, Germany.
[3]Forschungszentrum Jülich, Jülich, Germany

Motivation

- Radiative transitions and decays of hadrons provide insights in their electromagnetic structure.
- The radiative internal transition of the $\Delta^+ \to \Delta^+\gamma$ can be exploited to extract its magnetic moment μ_{Δ^+}.
- Large theoretical uncertainty in magnetic moment of the $\Delta^+, \mu_{\Delta^+} = 2.7^{+1.0}_{-1.3}$ (stat) ± 1.5 (syst) ± 3.0 (theo) μ_N [1] due to model ambiguities.

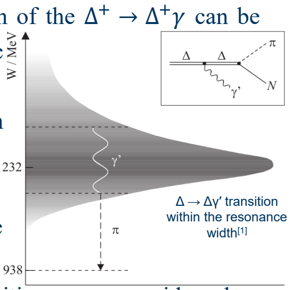

- Virtual photon (dilepton) transitions may provide a less model dependent extraction of the magnetic moment exploiting a measurement of the spin-density matrix elements.
- Studying exclusive reactions using elementary beams can be used to suppress the contribution of (virtual) bremsstrahlung.

Machine Learning

- Preliminary phase space studies show that ~64% of the dileptons have e⁺e⁻ opening angles < 4° and ~78% of the dileptons have e⁺e⁻ opening angles < 9.°
- Current HADES RICH ring reconstruction efficiency drops for low opening angles e⁺e⁻(<4°)[2].

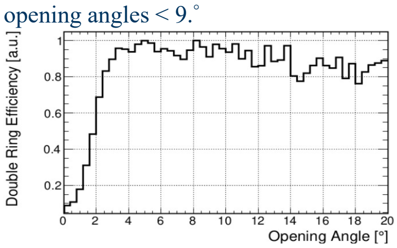

- Convolutional Neural Networks (CNN) show great performance in image analysis and thus can be used for ring reconstruction.
- Plan to train the CNN on the pixel hits of the Multi Anode PMT (MAPMT) of HADES.

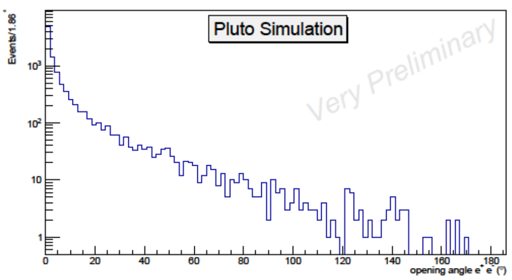

The HADES Experiment

- **H**igh **A**cceptance **D**i-**E**lectron **S**pectrometer at GSI Darmstadt.
- HADES designed for an excellent e+/e- reconstruction in hadronic reactions.
- Study the $p + p \to p + \Delta^+ \to pp\pi^0e^+e^-$ reaction from recent data taken at T_{beam}=4.5 GeV.

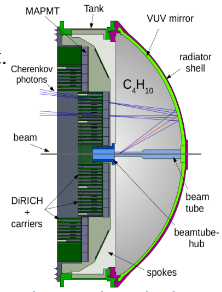

Side View of HADES RICH detector [2]

Event Generator

- Simulating the reaction process by extending the PLUTO framework for heavy ion and hadronic physics [3].
- Currently based on phase-space modelling of the $p + p \to p + \Delta^+ \to p + \Delta^+\gamma^* \to pp\pi^0e^+e^-$reaction.
- The $\Delta^+ \to \Delta^+\gamma^*$process sampled according to a relativistic Breit Wigner distribution.
- The $\gamma^* \to e^+e^-$decay accounting for a simplified $\frac{1}{m^2_{e+e-}}$ propagator term.

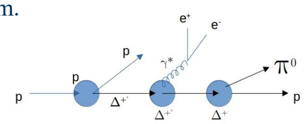

Outlook

- Include the proper angular distributions for the $\Delta^+ \to \Delta^+\gamma^*$ process.
- Study response of the RICH detector for the e⁺e⁻ pairs produced from this channel.
- Study the performances of various machine learning algorithm, including convolutional neural networks.
- Analyse the exclusive reaction using the recent proton data taken with HADES.

References

1. S. Schumann *et al.* (The European Physical Journal A 43.3 (2010), pp. 269–282).
2. J.H.Otto (PhD Thesis, http://dx.doi.org/10.22029/jlupub-7207).
3. I. Fröhlich, *et al.* (J. Phys. Conf. Ser. (2010)., 219, 032039.)

Contact: s.k.sahu@gsi.de

RUHR-UNIVERSITÄT BOCHUM

RUB

Track Finding for the Straw-Tube Tracker Using the Language Model

J. Kannika[1], T. Stockmanns[2], J. Ritman[1,2,3]
[1]Ruhr-Universität Bochum
[2]Forschungszentrum Jülich
[3]GSI Helmholtz Center for Heavy Ion Research

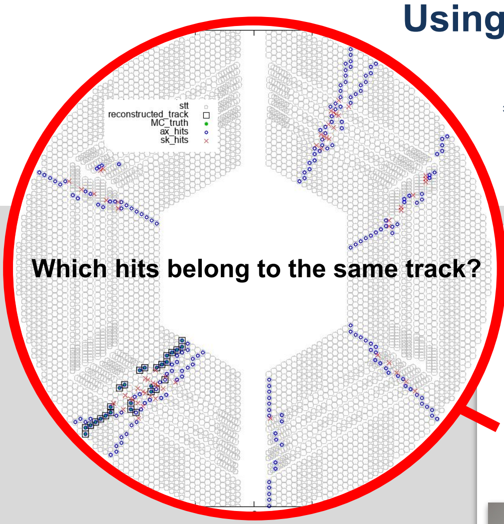

Introduction

In this research, we explore the uses of the language models to efficiently perform the track-finding task for the straw-tube tracker (STT) in the PANDA experiment at FAIR in Darmstadt.
The STT is a detector for tracking charged particles. It consists of densely packed straw tubes filled with gas that ionizes when the charged particle hits and sends the hit signal along the wire inside the straw tube.

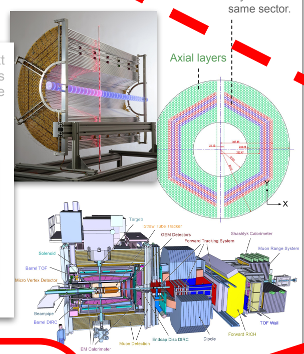

Tracking feature:

The angles between hits are not practical to use as a tracking feature for the STT due to the complexity of the geometry. We created the tracking feature called *relative moving vector* to represent data from the STT. Each word in this feature takes the form relative angle/distance/region tag, for example:

103/0.5/SKSK : 101/2.7/SKAX : 19/1.0/AXAX : -60/1.0/AXAX : 60/1.0/AXAX

This sample sentence consists of five words, and each word contains two parts:

- vector part (relative angle/distance)
- region tag part

The region tag gives the language model the context of the different areas in the STT.

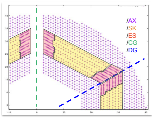

Language model

is a probabilistic model mainly used in natural language processing. The model contains series of words and their corresponding probabilities which calculated from frequency of the words in the training samples.

Language model (LM):			prob.
See	you	again	25%
See	you	tomorrow	25%
See	you	then	50%
See	you	then	

word history — next word (predicted)

The LM gives next word suggestions based on the learned sentences.

Train the LM by typing in sentences.

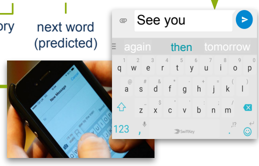

Feature extraction

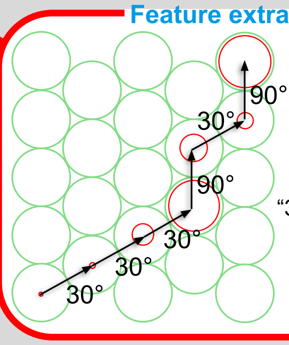

A series of angles were extracted from the hit data. This output string is equivalent to a sentence in natural language where each angle can be considered a word.

“30:30:30:90:30:90”

Note: this is just a simplified feature for demonstrating the idea.

Training

Language model:						prob.
30°	30°	30°	90°	30°	330°	25%
30°	30°	30°	90°	30°	30°	25%
30°	30°	30°	90°	30°	90°	50%
30°	30°	30°	90°	30°	90°	

word history — next word (predicted)

The probabilities of the possible next words are calculated from the training samples with shared hit history. This table filled with pairs of words and probabilities is called the language model.

Testing

The trained language model can suggest possible next hits based on the input hit history. This works in the same way as the next-word prediction program in natural language processing.

“30:30:30:90:30”
Input string

Language Model → {“330”: 0.25, “30”: 0.25, “90”: 0.5}
Output probability distribution

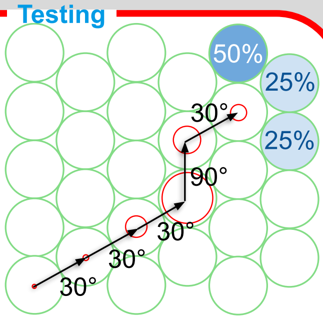

Track finding algorithm

Greedy algorithm

Input string → Next hit predictor → Reconstructed track

Language model

Input string → Track candidate generator → Track candidates → Track selector → Reconstructed track

Branching algorithm

The greedy algorithm tracks particles by following the suggestions with the highest probability from the language model. Meanwhile, the branching algorithm explores all possible paths and chooses the best path by considering a track performance parameter.

Results and discussion

Tracking algorithm	Avg. track completeness	Avg. track purity	Avg. track efficiency
Greedy	87%	95%	78%
Branching	91%	94%	86%

What are purity and completeness?

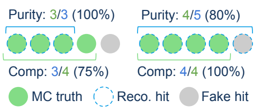

How is track efficiency calculated?

Testing samples:
- generating tracks: 4 π^+, 4 π^-.
- p_t: 0.2 - 2.5 GeV/c, θ: 25° - 100°
- 1000 tracks.

Found tracks must satisfy these conditions:
- primary track,
- completeness > 70% and purity > 70%
- track length > 5 hits,
- start tracking from 5 MC seeds (these are excluded from the evaluation).

The branching algorithm yielded a better track efficiency because the algorithm works by exploring all possible paths guided by the language model, in contrast to the greedy algorithm, which only follows the suggestions with the highest probability from the language model. This searching behavior tends to jump into the local optima where, in many cases, it fails to cross from the outer axial layers to the inner axial layers.

Summary

- The language model can be used for finding tracks in the discretized spaces, such as in the straw-tube tracker
- The greedy algorithm cannot effectively find optimal solutions for the track finding task
- The branching strategy helps to increase overall tracking accuracy

Outlook

- Compare the results with other tracking algorithms.

The Search for Charged Particle Electric Dipole Moments in Storage Rings

Achim Andres for the JEDI Collaboration - RWTH Aachen University & Forschungszentrum Jülich

Electric Dipole Moments (EDMs)

- Fundamental (vector) property of a particle aligned with the particles spin axis
- Requires $\mathcal{P}$ and $\mathcal{T}$ violation $\overset{CPT}{=}$ $\mathcal{CP}$ violation
- Close connection to **matter antimatter asymmetry**
- **Goal:** First direct measurement of the **deuteron** EDM
- Current neutron EDM limit $\sim 10^{-26}\,\mathrm{e\cdot cm}$ [1] → Measurement requires **precise** experiments

Technique Part I

- COSY @ Forschungszentrum Jülich: Magnetic Ring (184 m)

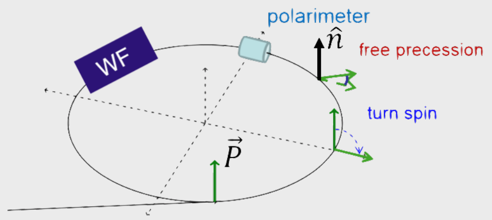

- Inject a **vertically polarized** deuteron beam
- Rotate the polarization into the **accelerator plane**
- Polarization starts to **precess** around the so-called Invariant spin axis $\hat{n}$ (ISA)
- Beam polarization is constantly measured by a polarimeter

Spin Dynamics

- **Main Idea:** Measure influence of EDM on Beam Polarization

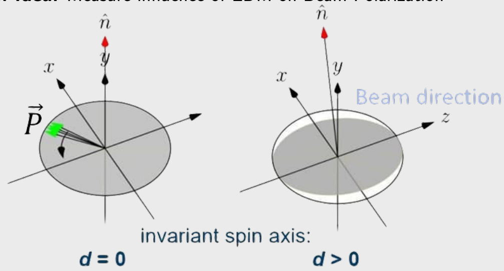

- In absence of an EDM & ideal accelerator: ISA $\perp$ accelerator plane
- Non zero EDM rotates the ISA $\hat{n}$ in radial (x) direction

$$\hat{n} = \begin{pmatrix} 0 \\ 1 \\ 0 \end{pmatrix} \overset{\mathrm{EDM}}{\Rightarrow} \begin{pmatrix} \sin\phi_0^{\mathrm{EDM}} \\ \cos\phi_0^{\mathrm{EDM}} \\ 0 \end{pmatrix} \approx \begin{pmatrix} \phi_0^{\mathrm{EDM}} \\ 1 \\ 0 \end{pmatrix}$$

- Magnet misalignment add additional systematics to the orientation of the ISA $\hat{n}$ in radial (x) and longitudinal direction (z)

$$\hat{n}_{\mathrm{meas.}} = \begin{pmatrix} \phi_0^{\mathrm{EDM}} + \phi_0^{\mathrm{COSY}} \\ 1 \\ \xi_0^{\mathrm{COSY}} \end{pmatrix}$$

- Simulations are needed to disentangle ϕ_0^{EDM} and ϕ_0^{COSY} (M. Vitz)
- **Goal:** Measurement of the orientation of the Invariant spin axis $\hat{n}$

References

[1] C. Abel *et al.*, *Measurement of the Permanent Electric Dipole Moment of the Neutron*, feb 2020.

[2] F. Rathmann, N. Nikolaev, and J. Slim, *Spin dynamics investigations for the electric dipole moment experiment*, Feb 2020.

Technique Part II

- The radio frequency (rf) Wien filter provides a vertical $\vec{B}$ and horizontal $\vec{E}$ field

$$\vec{E} \perp \vec{B} \perp \mathrm{Beam} \rightarrow \vec{F_L} = \vec{0}$$

- No influence on beam → Ideal Spin manipulator
- The Wien filter can be radially rotated around the beam pipe. The **magnetic field direction** of the Wien filter is given by

$$\hat{n}_{\mathrm{WF}} = \begin{pmatrix} \sin\phi^{\mathrm{WF}} \\ \cos\phi^{\mathrm{WF}} \\ 0 \end{pmatrix} \approx \begin{pmatrix} \phi^{\mathrm{WF}} \\ 1 \\ 0 \end{pmatrix}$$

- The rf Wien filter induces a **linear build up** of the vertical polarization
- The **build up** depends on the direction of the **magnetic field axis of the rf Wien filter** $\hat{n}_{\mathrm{WF}}$ and the orientation of **ISA** $\hat{n}_{\mathrm{meas.}}$ [2]

$$\begin{aligned} \epsilon^2\left(\phi^{\mathrm{WF}}\right) &\propto \left|\hat{n}_{\mathrm{WF}} \times \hat{n}_{\mathrm{meas.}}\right|^2 \\ &\propto \left(\left(\phi_0^{\mathrm{EDM}} + \phi_0^{\mathrm{COSY}}\right) - \phi^{\mathrm{WF}}\right)^2 + \epsilon_0\left(\xi_0^{\mathrm{COSY}}\right) \end{aligned}$$

- No build up if $\hat{n}_{\mathrm{WF}} \parallel \hat{n}_{\mathrm{meas.}}$

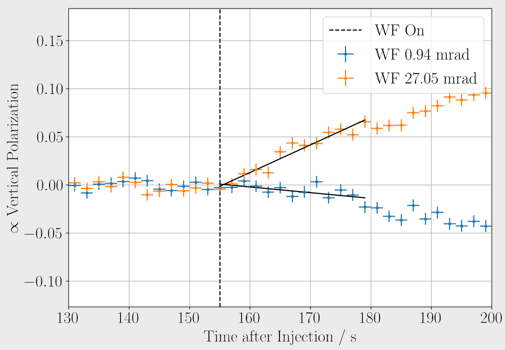

Preliminary Results

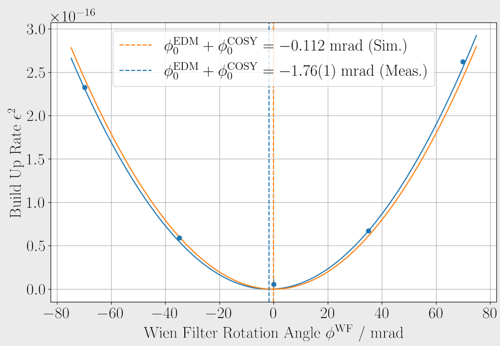

- Orientation of ISA in radial direction including ring systematics

$$\begin{aligned} \phi_0^{\mathrm{EDM}} + \phi_0^{\mathrm{COSY}} &= -\,1.76(1)\,\mathrm{mrad} \\ &\approx 10^{-17}\,\mathrm{e\cdot cm}\ \text{Upper Limit} \end{aligned}$$

- **Simulations** of the experiment (including magnet misalignments, steerer & magnet settings,..) **predict** radial angles **not larger than** $\mathcal{O}$**(0.1) mrad**.
- We are **missing systematics** of an order of magnitude
- Systematic Studies are ongoing

Contact: achim.andres@rwth-aachen.de

Towards axion searches with polarized hadron beams and targets at the GSI/FAIR storage rings

Daoning Gu

1. III. Physikalisches Institut B, RWTH Aachen University, Aachen, Germany, 2. Forschungszentrum Jülich, Jülich, Germany, 3. GSI Helmholtzzentrum für Schwerionenforschung, Darmstadt, Germany.

Motivation

- polarized hadron beams can be used to explore interactions that are not observable with unpolarized beams.
- axions are leading particle candidates for dark matter.
- axion like particles (ALP): similar properties as axions, but ALPs don't solve the strong QCD problem.

- in storage rings with polarized beams:

Axion/ALP field → Oscillating electric dipole moment (oEDM)

- first proof-of-principle experiment was performed with a polarized deuteron beam at COSY, Forschungszentrum Jülich.

Spin Motion in Storage Ring

$$\boxed{\frac{d\vec{s}}{dt} = \left(\vec{\Omega}_{MDM} + \vec{\Omega}_{EDM} + \vec{\Omega}_{wind}\right) \times \vec{s}}$$

$$\vec{\Omega}_{MDM} = -\frac{q}{m'} \qquad \vec{\Omega}_{EDM} = -\frac{1}{Sh} dc\vec{\beta} \times \vec{B}.$$

$$d = d_{DC} + d_{AC}\cos(\omega_a t + \varphi_o)$$

oEDM induced by axion field

- spin tune: $\nu_s = G\gamma$.
- spin tune spread:

$$\Delta\nu_s = G\Delta\gamma = G\gamma\beta^2\frac{\Delta p}{p} + \ldots$$

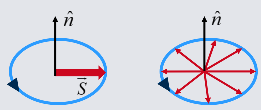

- spin coherence time (SCT):
  SCT = time after total polarization drops to 1/e.

G: the gyromagnetic anomaly.

Experimental Method

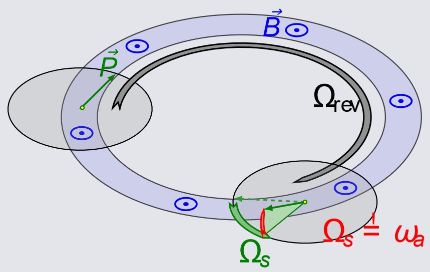

- store polarized hadrons.
- maintain precession in horizontal plane (long SCT).
- if $m_a c^2 \equiv \hbar\omega_a = \Omega_{MDM}\hbar$, polarization will turn out of the horizontal plane, resulting in a vertical polarization component.
- vertical polarization can be measured using a carbon target and a polarimeter.
- axion wind effect enhanced in storage rings when $v \approx c$.
- $\Omega_{MDM} = \gamma G \Omega_{rev}$, a wide mass range can be covered by:
  1) varying the three parameters γ, G and Ω_{rev},
  2) use additional electric field.

$$\vec{\Omega}_{MDM} = -\frac{q}{m}\left[G\vec{B} - \left(G - \frac{1}{\gamma^2 - 1}\right)\frac{\vec{\beta}\times\vec{E}}{c}\right]$$

Simulation

- CRYRING@ESR.
- spin tracking using the BMAD software library.
- betatron tune: $Q_x = Q_y = 2.42$

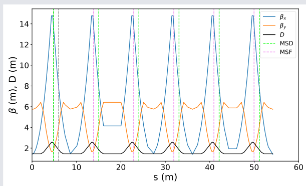

Two ways to optimize the SCT.

1. sextupole corrections:

$$\frac{1}{SCT} \propto \Delta\nu_s = |A + a_i l_i| \cdot \langle\Delta x^2\rangle + |B + b_i l_i| \cdot \langle\Delta y^2\rangle + |C + c_i l_i| \cdot \left(\frac{\Delta p}{p}\right)^2$$

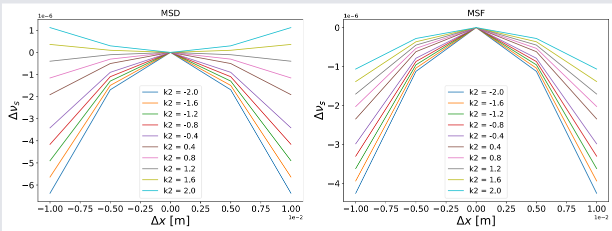

Minimum $\Delta\nu_s$ can be obtained by flattening the parabolas.

→at least 3 groups of sextupole are needed, and corrections are dependent on energy.

2. zero crossing shift induced by betatron tunes.
   Intrinsic spin resonances: $\gamma G = kP \pm Q_y$.

→unknown betatron tunes.

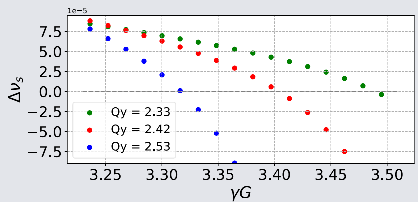

References

1. Stoehlker, T., et al. "Towards experiments with polarized beams and targets at the GSI/FAIR storage rings." 19th Workshop on Polarized Sources, Targets and Polarimetry (PSTP2022). 2023.
2. Chang, Seung Pyo, et al. "Axionlike dark matter search using the storage ring EDM method." Physical Review D 99.8 (2019): 083002.
3. Karanth, Swathi, et al. "First Search for Axion-Like Particles in a Storage Ring Using a Polarized Deuteron Beam." Physical Review X 13 (2023): 031004.

daoning.gu@rwth-aachen.de

RWTH AACHEN UNIVERSITY

JEDI

JÜLICH Forschungszentrum

Determination of the Invariant Spin Axis in a COSY model using Bmad

M. Vitz, A. Lehrach and J. Pretz, Institut für Kernphysik, Forschungszentrum Jülich, 52425 Jülich, Germany,
also at III. Physikalisches Institut B, RWTH Aachen University, 52056 Aachen, Germany
on behalf of the JEDI Collaboration

Motivation

The Electric Dipole Moment (EDM) is a fundamental property of a particle, similar to the Magnetic Dipole Moment (MDM). As a source of $\mathcal{P}$ and $\mathcal{T}$ violation ($\overset{\mathcal{CPT}}{=}$ $\mathcal{CP}$ violation) it is closely connected to **matter/antimatter asymmetry** [1].

As it has an impact on the spin rotation, the EDM of charged particles can be measured in a storage ring by determining the radial **tilt of the ISA** $\vec{n}_{\mathrm{ISA}}$ (Invariant Spin Axis).

Additionally, **systematic effects** $\phi_{\mathrm{Ring}}, \xi_{\mathrm{Ring}}$ caused by magnet misalignments etc. have to be disentangled from a potential EDM signal. Solenoidal fields ξ_{Sol} can directly influence the longitudinal tilt of the ISA.

$$\vec{n}_{\mathrm{ISA,\ ideal}} = \begin{pmatrix} \sin\phi_{\mathrm{EDM}} \\ \cos\phi_{\mathrm{EDM}} \\ 0 \end{pmatrix} \approx \begin{pmatrix} \phi_{\mathrm{EDM}} \\ 1 \\ 0 \end{pmatrix}.$$

$$\vec{n}_{\mathrm{ISA,\ real}} \approx \begin{pmatrix} \phi_{\mathrm{EDM}} + \phi_{\mathrm{Ring}} \\ 1 \\ \xi_{\mathrm{Sol}} + \xi_{\mathrm{Ring}} \end{pmatrix}$$

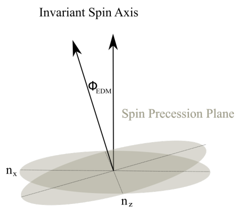

Methodology

A determination of the tilt of the ISA was performed at the storage ring **COSY** (Cooler Synchrotron) in Jülich by the JEDI (Jülich Electric Dipole moment Investigations) collaboration for the first measurement of the **deuteron EDM**.

To measure the tilt of radial and longitudinal ISA simultaneously, the so-called RF (Radio-Frequency) **Wien filter**, an RF device with radial electric E_x^{WF} and vertical magnetic field B_y^{WF} was implemented into COSY.

While the orbit in the center of this device is not perturbed, as the fields are set up so that the Lorentz force is zero, the particles receive a phase dependend spin kick each turn. The Wien filter is changing its fields on one of the harmonics k of the spin precession frequency ν_s.

$$E_x^{\mathrm{WF}} = E_0 \cos(2\pi f_{\mathrm{COSY}} |k + \nu_s| + \phi_{rel})$$
$$B_y^{\mathrm{WF}} = B_0 \cos(2\pi f_{\mathrm{COSY}} |k + \nu_s| + \phi_{rel}).$$

Using this device, the EDM signal can **accumulate over time**, resulting in a **build-up of vertical polarization** P_y if the Wien filter runs on resonance [2,3].

The build-up $\epsilon \propto \frac{d}{dt}P_y(t)$ depends on the orientation of ISA $\vec{n}_{\mathrm{ISA}}$ to the Wien filter fields $\vec{n}_{\mathrm{WF}}$ and the longitudinal fields by solenoids. By rotating the Wien filter is by an angle ϕ_{WF} around the beam it can be matched to the radial tilt of the ISA.

$$\epsilon^2(\phi_{\mathrm{WF}}, \xi_{\mathrm{Sol}}) \propto |\vec{n}_{\mathrm{WF}} \times \vec{n}_{\mathrm{ISA}}|^2 = \left| \begin{pmatrix} \phi_{\mathrm{WF}} \\ 1 \\ 0 \end{pmatrix} \times \begin{pmatrix} \phi_{\mathrm{EDM}} + \phi_{\mathrm{Ring}} \\ 1 \\ \xi_{\mathrm{Sol}} + \xi_{\mathrm{Ring}} \end{pmatrix} \right|^2$$
$$= ((\phi_{\mathrm{EDM}} + \phi_{\mathrm{Ring}}) - \phi_{\mathrm{WF}})^2 + (\xi_{\mathrm{Sol}} + \xi_{\mathrm{Ring}})^2$$

The dependence of the build-up ϵ on ϕ_{WF} and ξ_{Sol} is summarized by the **EDM resonance map**. Its minimum indicates the tilt of the ISA at the position of the Wien filter.

Another method to determine the longitudinal ISA can be used complementary. By observing the spin tune changes $\Delta\nu_s$ in dependency of the solenoidal strength B_{Sol} the **projection of the longitudinal ISA** c_{Sol} at position of the solenoid as well as the solenoid calibration factor k_{Sol}, giving the relation between solenoidal field B_{Sol} and spin kick $\xi_{\mathrm{Sol}} = k_{\mathrm{Sol}} \cdot B_{\mathrm{Sol}}$ can be measured [4].

$$\Delta\nu_s = -\frac{1}{\pi}\left(\cot(\pi\nu_s)\left(\cos\frac{k_{\mathrm{Sol}}B_{\mathrm{Sol}}}{2} - 1\right)\right) - c_{\mathrm{Sol}} \sin\frac{k_{\mathrm{Sol}}B_{\mathrm{Sol}}}{2}.$$

References

[1] A. Sakharov, "Violation of CP invariance, C asymmetry, and baryon asymmetry of the universe", *JETP Lett. Vol. 5*, 1967, pp. 24-27, doi:10.1070/PU1991v034n05ABEH002497.

[2] F. Rathmann, A. Saleev, and N. N. Nikolaev, "The search for electric dipole moments of light ions in storage rings", *Journal of Physics: Conference Series, Vol. 45*, 2014, pp. 229–233

[3] J. Slim *et al.*, "Electromagnetic Simulation and Design of a Novel Waveguide RF Wien Filter for Electric Dipole Moment Measurements of Protons and Deuterons", *Nuclear Instruments and Methods in Physics Research Section A: Accelerators, Spectrometers, Detectors and Associated Equipment, Vol. 828*, 2016, pp. 116-124

[4] A. Saleev *et al.*, "Spin tune mapping as a novel tool to probe the spin dynamics in storage rings", *Physical Review Accelerators and Beams 20*, 2017, 072801

[5] D. C. Sagan, "Bmad: A relativistic charged particle simulation library", *Nuclear Instruments and Methods in Physics Research A, Vol. 558*, 2006, pp. 356-359

Contact: Maximilian Vitz - m.vitz@fz-juelich.de

EDM Resonance Map and Solenoid Calibration

The measurement of the tilt of the ISA to determine the deuteron EDM was performed in 2018 and 2020 in the so-called **precursor runs**.

As a simulation is needed to disentangle a potential EDM signal from systematics a Bmad simulation using all known magnet strengths, misalignments and other systematic effects was written. By implementing the Wien filter an EDM resonance map was calculated [5].

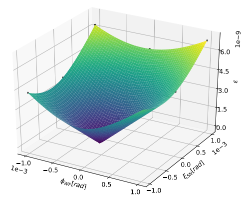

During the precursor runs also the projection of the longitudinal ISA was measured experimentally by performing **solenoid calibrations**. Two different solenoid have been used. One was the **Snake-Solenoid** (lower right graph), which also contributed to the EDM resonance map, the other one was the so-called the **2MeV-Solenoid** (lower left graph).

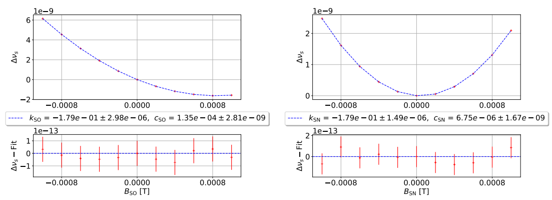

Method	ϕ_{WF}	ξ_{SN}	c_{SN}	c_{SO}
Precursor Experiments	-2.91(8) mrad	-5.22(7) mrad	-0.0612(9) mrad	-0.0585(5) mrad
Bmad Simulation	-0.1119(3) mrad	-0.3697(3) mrad	-0.006747(2) mrad	-0.135302(3) mrad

Unfortunately, simulation and experimental results differ by **one order of magnitude**. Reasons could be the **inaccuracy of the COSY model** to describe orbit and tune precisely, or the need for **correction factors** when the beam passes the devices with an angle.

Correction Factors

For an ideal lattice, the parameter ϕ_{WF}, ξ_{SN}, c_{SN} and c_{SO} are in perfect agreement with the tilt of the ISA $n_{\mathrm{WF},x}$, $n_{\mathrm{WF},z}$, $n_{\mathrm{SN},z}$ and $n_{\mathrm{SO},z}$ at their position. In case the lattice is **distorted**, a correction has to be applied.

This was investigated by giving an ideal lattice a random **vertical perturbation** via vertical steerers. The parameters were then compared with the real tilt of the ISA at their position for different sets of vertical perturbations.

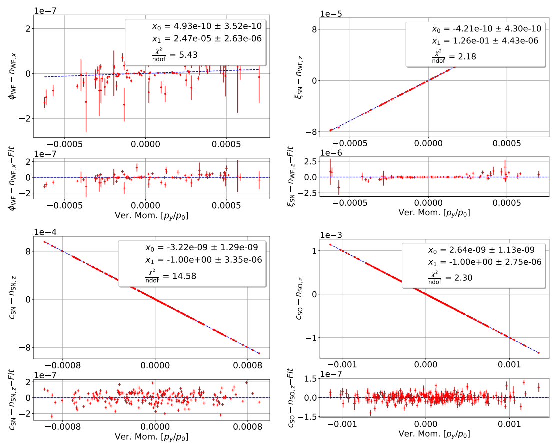

As expected, this correction depends on the **vertical angle** when passing through the devices. This is quite logical, as it reflects a transformation to the particles reference frame.

From a simulation point of view, it is now under investigation, whether further corrections are needed, if the horizontal orbit gets distortet additionally.

Member of the Helmholtz Association

SIMULATIONS OF BEAM DYNAMICS AND BEAM LIFETIME FOR THE PROTOTYPE EDM RING

Saad Siddique, on behalf of the JEDI and CPEDM Collaborations
III. Physikalisches Institut B, RWTH Aachen University, Germany
GSI Helmholtzzentrum für Schwerionenforschung GmbH Darmstadt, Germany
saad.siddique@rwth-aachen.de

Physics Case:

- Matter antimatter asymmetry can be explained by CP-violation.
- Permanent electric dipole moment (EDM) is fundamental property of particles (like mass, charge , magnetic moment)
- Existence of EDM only possible if violation of time reversal and parity symmetry.[1]

$$H = H_M + H_E = -\vec{\mu}\cdot\vec{B} - \vec{d}\cdot\vec{E}$$
$$P: H = -\vec{\mu}\cdot\vec{B} + \vec{d}\cdot\vec{E}$$
$$T: H = -\vec{\mu}\cdot\vec{B} + \vec{d}\cdot\vec{E}$$

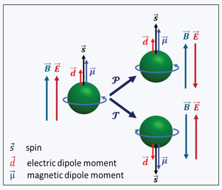

Methodology :

- Inject longitudinally polarized beam in the storage ring
- Radial electric field interacting with EDM (**torque**)
- Observe vertical polarization with time

Thomas-BMT-Equation

$$\frac{d\vec{s}}{dt} = \vec{\Omega}\times\vec{S} = (\vec{\Omega}_{MDM} + \vec{\Omega}_{EDM})\times\vec{S}$$

$$\vec{\Omega} = \frac{q}{m}\left\{G\vec{B} + \left(G - \frac{1}{\gamma^2-1}\right)\frac{\vec{\beta}\times\vec{E}}{c} + \frac{\eta}{2}\left\{\frac{\vec{E}}{c} + \vec{\beta}\times\vec{B}\right\}\right\}$$

Frozen Spin Idea

$$\vec{B} = 0 \text{ and } \left(G - \frac{1}{\gamma^2-1}\right) \equiv 0!$$

Magic momentum

[2]

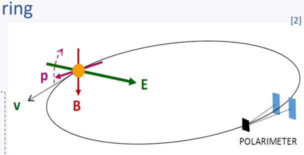

If G > 0 → pure electric ring
If G < 0 → combination of E-B

Strategy

1. Precursor Experiment @COSY Fz Jülich, Germany
2. Prototype Storage Ring
3. All Electric Storage Ring

Prototype Storage Ring :

- Beam injection with multiple polarization states and for longer time. (> 1000 sec)
- Develop key technologies beam cooling, deflector, beam position monitors, magnetic shielding….
- Perform EDM measurement

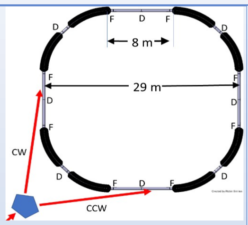

Ring will be operated in two modes:
a. Electrostatic bendings (at T=30 MeV)
b. Electromagnetic bendings (at T=45 MeV)

Beam Simulations :

Four Lattice with different focusing strength generated by MADX. [5]

- **Four different lattices studied**
  1. Strong Lattice with $\beta_{y-max} = 33\ m$
  2. Medium Lattice with $\beta_{y-max} = 100\ m$
  3. Weak Lattice with $\beta_{y-max} = 200\ m$
  4. Weaker Lattice with $\beta_{y-max} = 300\ m$

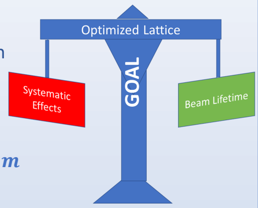

After generating these lattices, beam loss estimations were performed for all major effects and in two different scenarios, with residual gas only and with a carbon target.

Beam loss Estimations: [3]

1. Hadronic Interactions (HI)
2. Single Coulomb Scatterings (SCS)
3. Energy Loss straggling (ELS)
4. Intrabeam Scatterings (IBS)

$$\tau^{-1} = n\sigma_{tot} f_0$$

τ^{-1} = beam loss rate
n = target thickness or rest gas density
σ_{tot} = total cross section
f_0 = revolution frequency

Parameters

Gas composition $H_2 : N_2$ with 80:20

Gas density : n_g=5.30 × 10^5 $atoms/cm^3$

$P_{eq} = 2.8 \times 10^{-11}\ Torr$

Carbon target density:$n_t \sim 2\times 10^{12}\ atoms/cm^2$

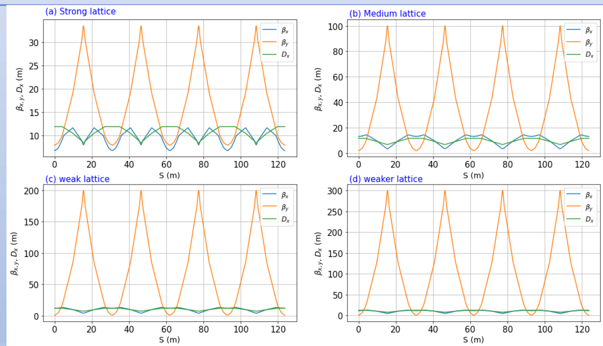

Results:

Total loss rate :

$$\left(\frac{1}{\tau}\right)_{Total} = \left(\frac{1}{\tau}\right)_{HI} + \left(\frac{1}{\tau}\right)_{SCS} + \left(\frac{1}{\tau}\right)_{ELS} + \left(\frac{1}{\tau}\right)_{IBS}$$

Lattice (β_{y-max})	H.I $10^{-6}\ s^{-1}$	SCS $10^{-4}\ s^{-1}$	IBS $10^{-4}\ s^{-1}$	τ^{-1} $10^{-4}\ s^{-1}$
33 m	2.7	7.6	2.34	9.47
100 m		27.3	2.10	27.5
200 m		94.6	1.99	90.0
300 m		208	1.90	195

Energy loss straggling isn't contributing theoretically in beam loss rates

Comparison b/w Analytical estimations and [4] Betacool Results

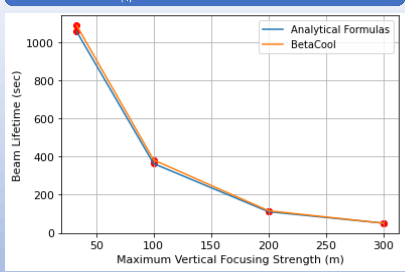

Summary

- Preliminary design of prototype EDM ring
- Most dominating effect is Single Coulomb Scatterings
- Lattice with $\beta_{y-max} \le 100\ m$ is preferable for longer beam lifetime.
- Analytical formulas and BetaCool results showing an agreement.

References:

1. Sakharov, A. *Violation of CP invariance, C asymmetry, and baryon asymmetry of the universe*, *JETP Lett. 1967* doi:10.1070/PU1991v034n05ABEH002497
2. Abusaif, Falastine *et al.*, *CERN Yellow Reports: Monographs, Vol. 3 (2021): Storage ring to search for electric dipole moments of charged particles: Feasibility study* doi:10.23731/CYRM-2021-003
3. F. Hinterberger, *Beam-target interaction and intrabeam scattering in the HESR ring*, Technical Report.
4. A.O. Sidorin, I. N. Meshkov, I. A. Seleznev, A. V. Smirnov, E. M. Syresin, and G. V. Trubnikov, *BETACOOL program for simulation of beam dynamics in storage rings*, Elsevier, 2006.
5. H.Grote and F.Schmidt *CERN MADX introduction* http://mad.web.cern.ch/mad/madx.old/ Introduction/doc.html

Determination of the Invariant Spin Axis in a COSY model using Bmad

M. Vitz, Institut für Kernphysik, Forschungszentrum Jülich, 52425 Jülich, Germany,
also at III. Physikalisches Institut B, RWTH Aachen University, 52056 Aachen, Germany
on behalf of the JEDI Collaboration

Motivation

Electric Dipole Moment (EDM) is a fundamental property of a particle, similar to the Magnetic Dipole Moment (MDM).

Source of $\mathcal{P}$ and $\mathcal{T}$ violation ($\overset{\mathcal{CPT}}{=}$ $\mathcal{CP}$ violation) and therefore closely connected to **matter/antimatter asymmetry** [1].

Impacts the spin rotation in a storage ring so EDM of charged particles can be measured by determining the radial **tilt of the ISA** $\vec{n}_{\text{ISA}}$ (Invariant Spin Axis).

Systematic effects $\phi_{\text{Ring}}, \xi_{\text{Ring}}$ induced by magnet misalignments etc. cause similar effects.

Additinally solenoidal fields ξ_{Sol} can be used to influence the longitudinal tilt of the ISA.

$$\vec{n}_{\text{ISA, ideal}} = \begin{pmatrix} \sin\phi_{\text{EDM}} \\ \cos\phi_{\text{EDM}} \\ 0 \end{pmatrix} \approx \begin{pmatrix} \phi_{\text{EDM}} \\ 1 \\ 0 \end{pmatrix}.$$

$$\vec{n}_{\text{ISA, real}} \approx \begin{pmatrix} \phi_{\text{EDM}} + \phi_{\text{Ring}} \\ 1 \\ \xi_{\text{Sol}} + \xi_{\text{Ring}} \end{pmatrix}$$

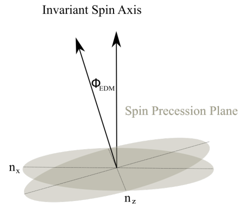

Methodology

Determination of ISA for **deuterons** was performed at the storage ring **COSY** (Cooler Synchrotron) in Jülich by the JEDI (Jülich Electric Dipole moment Investigations) collaboration.

Circumference 184 m.

Accelerates and Stores **Polarized**/Unpolarized **Deuterons** and Protons.

$p = 0.3 - 3.7$ GeV/c

Internal and External Experiments

Electron and Stochastic Cooling available

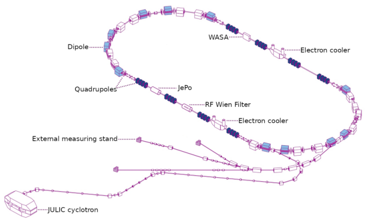

Operation Principle: injection of vertically polarized deuteron beam $\Rightarrow$ solenoid to rotate polarization into accelerator plane $\Rightarrow$ free polarization precession in accelerator plane around ISA $\Rightarrow$ polarization is constantly measured by a polarimeter.

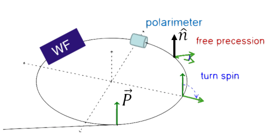

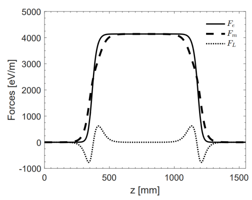

Measurement of ISA by operating the so-called RF (Radio-Frequency) **Wien Filter**.

The Wien Filter is an RF device with radial electric E_x^{WF} and vertical magnetic field B_y^{WF}.

Fields of RF Wien Filter are set up so Lorentz force is zero in its center and the orbit is not perturbated. Therefore its an ideal spin manipulator.

The Wien filter is changing its fields on one of the harmonics k of the spin precession frequency ν_s.

$$\begin{aligned} E_x^{\text{WF}} &= E_0 \cos(2\pi f_{\text{COSY}} |k + \nu_s| + \phi_{rel}) \\ B_y^{\text{WF}} &= B_0 \cos(2\pi f_{\text{COSY}} |k + \nu_s| + \phi_{rel}). \end{aligned}$$

This way a possible EDM signal can **accumulate over time**, resulting in a **build-up of vertical polarization** P_y if the Wien filter runs on resonance [2,3].

The build-up $\epsilon \propto \frac{d}{dn} P_y(n)$ depends on the orientation of ISA $\vec{n}_{\text{ISA}}$ to the Wien filter fields $\vec{n}_{\text{WF}}$ and the compensation of longitudinal fields by solenoids. No build-up occurs in case of $\vec{n}_{\text{WF}} \parallel \vec{n}_{\text{ISA}}$.

EDM Resonance Map

$$\epsilon^2(\phi_{\text{WF}}, \xi_{\text{Sol}}) \propto |\vec{n}_{\text{WF}} \times \vec{n}_{\text{ISA}}|^2 = \left| \begin{pmatrix} \phi_{\text{WF}} \\ 1 \\ 0 \end{pmatrix} \times \begin{pmatrix} \phi_{\text{EDM}} + \phi_{\text{Ring}} \\ 1 \\ \xi_{\text{Sol}} + \xi_{\text{Ring}} \end{pmatrix} \right|^2$$
$$= ((\phi_{\text{EDM}} + \phi_{\text{Ring}}) - \phi_{\text{WF}})^2 + (\xi_{\text{Sol}} + \xi_{\text{Ring}})^2$$

The dependence of the build-up ϵ on ϕ_{WF} and ξ_{Sol} is summarized by the **EDM resonance map**. Its minimum indicates the tilt of the ISA at the position of the Wien filter.

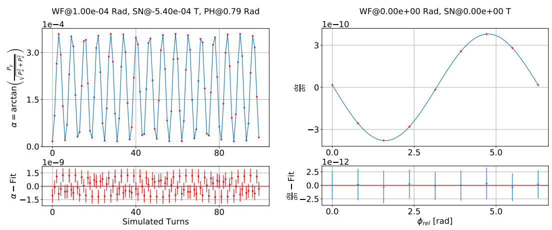

The measurement of the tilt of the ISA to determine the deuteron EDM was performed in 2018 and 2020 in the so-called **precursor runs** (Poster Achim Andres).

Simulations are needed to disentangle a potential EDM signal from systematics.

Therefore a Bmad simulation using all known magnet strengths, misalignments and other systematic effects was written [4].

Disagreement between simulation and measurement is currently under investigation.

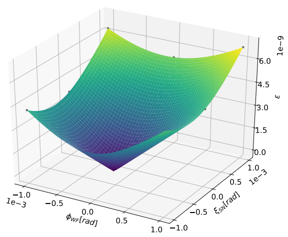

Method	ϕ_{WF}	ξ_{SN}
Precursor Experiments	-2.91(8) mrad	-5.22(7) mrad
Bmad Simulation	-0.1119(3) mrad	-0.3697(3) mrad

Correction Factors

As the EDM resonance map was derived for an unperturbated orbit, corrections have to be considered to $\phi_{\text{WF}}, \xi_{\text{SN}}$ in case the lattice is **distorted** to be in agreement with the tilt of the ISA $n_{\text{WF},x}$, $n_{\text{WF},z}$.

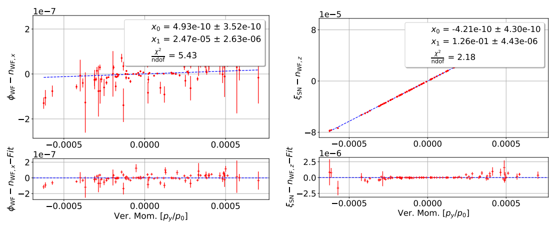

The vertical perturbation of the lattice leads to correction factor $A = \gamma - 1$ which has to be applied to the long. map minimum ξ_{SN}. Research about further corrections in progress.

$$\phi_{WF} = n_z(s_{WF}) \wedge \xi_{SN} = n_z(s_{WF}) - A \cdot p_y(s_{WF}/P_0)$$

References

[1] A. Sakharov, "Violation of CP invariance, C asymmetry, and baryon asymmetry of the universe", *JETP Lett. Vol. 5*, 1967, pp. 24-27, doi:10.1070/PU1991v034n05ABEH002497.

[2] F. Rathmann, A. Saleev, and N. N. Nikolaev, "The search for electric dipole moments of light ions in storage rings", *Journal of Physics: Conference Series, Vol. 45*, 2014, pp. 229–233

[3] J. Slim *et al.*, "Electromagnetic Simulation and Design of a Novel Waveguide RF Wien Filter for Electric Dipole Moment Measurements of Protons and Deuterons", *Nuclear Instruments and Methods in Physics Research Section A: Accelerators, Spectrometers, Detectors and Associated Equipment, Vol. 828*, 2016, pp. 116-124

[4] D. C. Sagan, "Bmad: A relativistic charged particle simulation library", *Nuclear Instruments and Methods in Physics Research A, Vol. 558*, 2006, pp. 356-359

Member of the Helmholtz Association

Optimization of Spin Coherence Time for Electric Dipole Moment (EDM) measurements in a storage ring

Rahul Shankar, *Anna Piccoli*, *Paolo Lenisa*

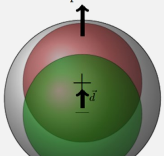

- An Electric Dipole Moment is a fundamental property of a particle:
  - → possible via CP violation
  - → closely correlated with the matter-antimatter asymmetry.
- EDM of charged particles can be measured using storage rings:
  - → Need **polarised beams**
  - → EDM can be measured via vertical precession induced using radial electric fields
- A new **Prototype** ring which uses a special combination of electric and magnetic fields can be used to "freeze" the horizontal precession of protons.
- But EDMs are expected to be very tiny:
  - → A precision experiment with **frozen spin** is needed!
  - → **Buildup of vertical polarisation** will be gradual.
  - → Particles in the bunch must remain aligned to each other for as long as possible
    - → High **Spin Coherence Time**! (time taken for the bunch polarization to fall below $^1/_e$)
- In this poster, a method to optimize the quadrupole and sextupole settings (beam optical settings) to maximize the spin coherence time is presented.

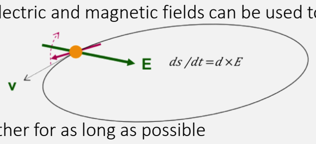

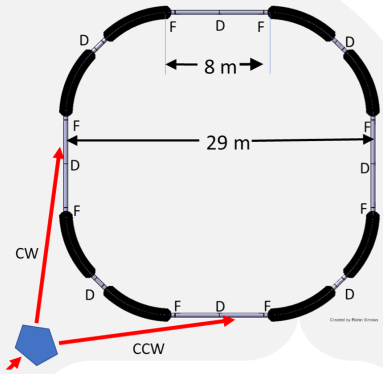

Combined E and B fields

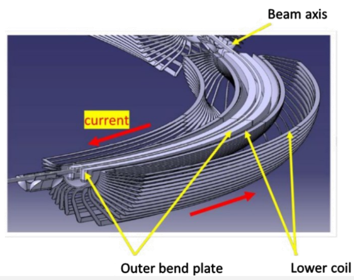

Simulations using BMAD:

A Software toolkit for charged particle and X-ray simulations

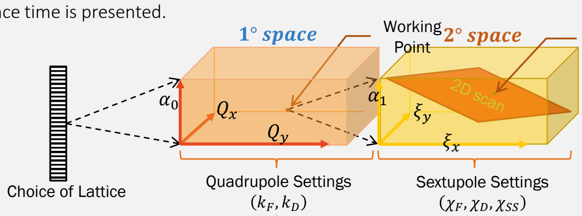

Preliminary Scans
- Scans of available working points
- Scan of phase slip factor and natural chromaticities
- Define the Observables of interest

Investigations into Decoherence
- Track polarisation vector magnitude and spin tune spread over time
- Extrapolate and measure the spin coherence time (τ) and average spin tune $\langle \Delta\nu_s \rangle$.

Grid Tests
- Track the variation of spin coherence time and average spin tune over the "space" of 2° optics.
- Devise the optimization strategy from data analysis

Lattice-wide Optimization Survey
- Optimized turns and grid resolution to maximize accuracy.
- 12 working points systematically optimized (optimized grid tests)

$$\vec{P}(t) = \frac{1}{n}\sum_{i=0}^{n} \frac{\vec{s}_i}{|\vec{s}_i|}$$

$$|\vec{P}(\tau)| = \frac{1}{e}|\vec{P}(0)|$$

Polarization vector; Individual particle spin; Number of particles in the bunch; Spin Coherence Time

$$\theta_x(t) = \tan^{-1}\left(\frac{P_x(t)}{P_z(t)}\right)$$

$$\langle \Delta\nu_s \rangle = \left\langle \frac{d}{dt}\theta_x(t) \right\rangle$$

$$\left\langle \frac{\Delta L}{L} \right\rangle = \alpha_1\delta_0^2 - \frac{\pi}{L}\epsilon_x\xi_x - \frac{\pi}{L}\epsilon_y\xi_y$$

Spin tune spread; Average spin tune of the bunch; Average increase in path length per turn; Square of initial momentum offset; Transverse Emittances; Chromaticities; second order momentum Compaction factor

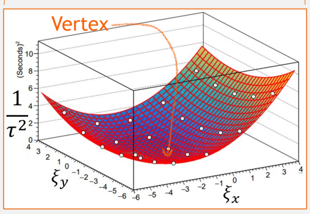

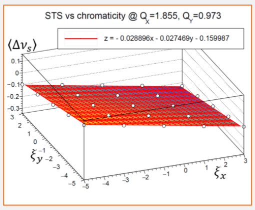

Q_x	Q_y	κ_F	κ_D	ξ_x^o	ξ_y^o	α_1^o	τ_{model}	τ_{low}	Δ_{1000}^{ξ}
1.855	1.095	0.077	-0.242	-1.271	-4.904	-0.0756	1473	1472	0.020
1.855	1.123	0.077	-0.247	-1.253	-5.036	-0.156	877	1614	0.016
1.855	1.223	0.079	-0.264	-1.167	-5.626	-0.211	3721	3237	0.013
1.823	0.723	0.036	-0.140	-1.483	-1.353	0.0543	677	676	
1.823	0.823	0.055	-0.177	-1.465	-2.389	0.0132	6105	4154	0.016
1.823	0.923	0.062	-0.201	-1.337	-2.983	-0.0573	5647	3870	0.019

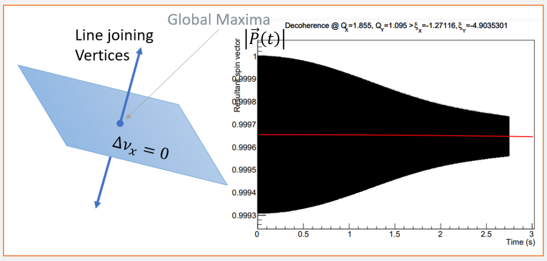

❖ **Conclusions:**

- ✓ Variation of SCT with 2° optical parameters follows definite pattern, influenced by the change in path length due to chromaticity and second order momentum compaction factor.
- ✓ **Decoherence virtually non-existent at optimized point.**
- ✓ **Average spin tune $\langle \Delta\nu_s \rangle = 0$, when path lenghtening effects exactly compensate the longitudinal phase-shift due to the distribution of momentum offset.**
- ✓ Optimized point occurs at the point where the line joining the local maxima crosses the plane of zero spin tune spread.
- ✓ **Global maximum SCT is sensitive to the optimized setting (more so at some working points than others).**

References
1. CPEDM Collaboration, "Storage ring to search for electric dipole moments for charged particles: Feasibility study," CERN Yellow Reports: Monographs, Geneva, 2021.

Università degli studi di Ferrara, Ferrara, Italy
Istituto Nazionale di Fisica Nucleare, Ferrara, Italy
Contact: shankar@fe.infn.it

JUNO's sensitivity to ^{7}Be, *pep*, and CNO solar neutrinos

Apeksha Singhal for JUNO Collaboration

IKP-2, Forschungszentrum Jülich GmbH, 52428, Jülich & Physikalisches Institut III B, RWTH Aachen University, 52062, Aachen, Germany

INTRODUCTION

Solar Neutrinos are the only carriers of information of energy production mechanism in the Sun's core and its chemical composition.

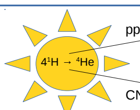

- Solar Metallicity Problem: High (HZ) or Low (LZ)?
- SSM predictions depend on Metallicity input [2].

Energy spectrum of solar neutrinos

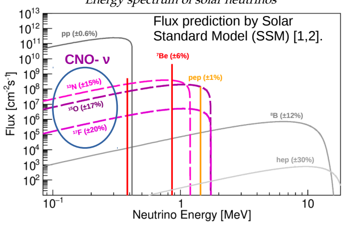

Species	HZ-Flux (cm^{-2}s^{-1})	LZ-Flux (cm^{-2}s^{-1})	% Difference
pp	$5.98(1 \pm 0.006)\times10^{10}$	$6.03(1 \pm 0.005)\times10^{10}$	-0.8
pep	$1.44(1 \pm 0.01)\times10^{8}$	$1.46(1 \pm 0.009)\times10^{8}$	-1.4
^{7}Be	$4.93(1 \pm 0.06)\times10^{9}$	$4.50(1 \pm 0.06)\times10^{9}$	8.9
^{8}B	$5.46(1 \pm 0.12)\times10^{6}$	$4.50(1 \pm 0.12)\times10^{6}$	17.6
^{13}N	$2.78(1 \pm 0.15)\times10^{8}$	$2.04(1 \pm 0.14)\times10^{8}$	26.6
^{15}O	$2.05(1 \pm 0.17)\times10^{8}$	$1.44(1 \pm 0.16)\times10^{8}$	29.7
^{17}F	$5.29(1 \pm 0.20)\times10^{6}$	$3.26(1 \pm 0.18)\times10^{6}$	38.3

Solar neutrinos are the perfect candidates to solve the metallicity problem!

Jiangmen Underground Neutrino Observatory Experiment

Under construction in southern China

First multi-kton (20 kton) liquid scintillator (LS) detector [3].

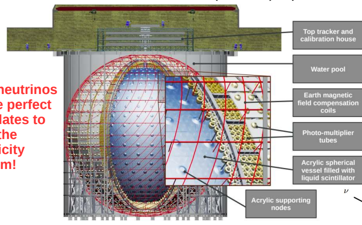

- Excellent energy resolution: 3% at 1 MeV.
- Large photocathode coverage (78%): 17612 20" PMTs and 25600 3" PMTs.
- 1% energy scale uncertainty, controlled by several calibration sources.

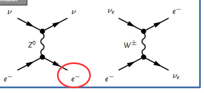

Solar neutrinos detected via elastic scattering of e-

METHODS

Region of Interest: 0.45-1.6 MeV

Internal Backgrounds
(^{210}Bi, ^{210}Po, ^{85}Kr, ^{40}K, ^{238}U & ^{232}Th chain)
Levels of Concentration:

- **High Background** : minimum requirement for NMO studies.
- **Medium Background**: 10x improvement from High Background.
- **Low Background**: 10x improvement from Medium Background.
- **Very Low Background**: Borexino Phase-III.

Cosmogenic Backgrounds (^{11}C, ^{10}C and ^{6}He)

$$\mu + {}^{12}\mathrm{C} \rightarrow \mu + {}^{11}\mathrm{C} + n$$

$$^{11}\mathrm{C} \rightarrow {}^{11}\mathrm{B} + e^+ + \nu_e$$

Identify cosmogenic backgrounds by finding space - time correlation between parent muon, ^{11}C decay and neutron capture using **Three Fold Coincidence Algorithm (TFC) [4]**.

TFC parameters:

Tagging Power (TP): percentage of correctly identified cosmogenic events.
Subtracted Exposure (SE): remaining exposure in ^{11}C depleted dataset.

Data is split using TFC:

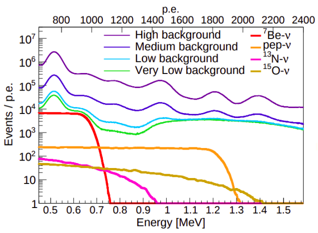

^{11}C depleted spectrum

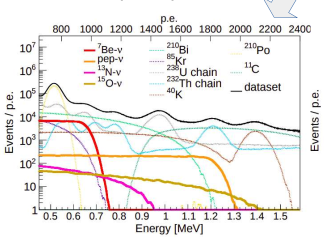

^{11}C enriched spectrum

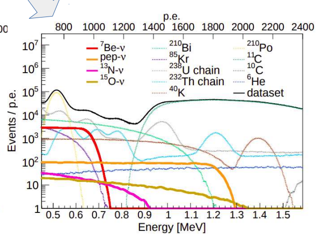

Toy MC approach to extract Sensitivity

Energy spectra from full Monte Carlo → Sampling → Thousands of pseuso-datasets (each species with expected rates) → Simultaneous Poisson Likelihood Fit → Best Fit Value; Fit Error (statistical only)

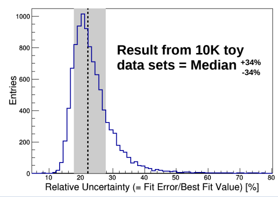

RESULTS

^{7}Be neutrinos

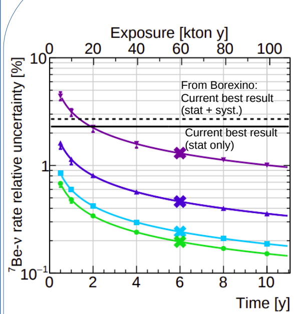

After 1 year of data-taking, JUNO can reach and overcome the current best result on ^{7}Be solar neutrino rate: 2.3% (stat.) and 2.7% (stat. +syst) from Borexino [5].

Critical backgrounds: ^{210}Po, ^{85}Kr, and ^{226}Ra

Impact of critical backgrounds levels

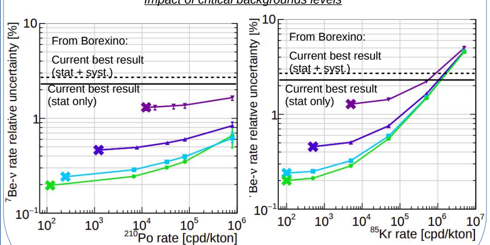

Measured ^{7}Be rate precision worsens as a function of increased backgrounds levels.

pep neutrinos

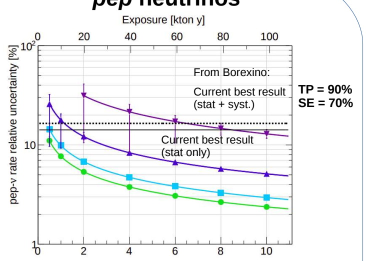

After 2 years of data-taking (except for the High background level) JUNO exceeds current best result : 14.2% (stat.) and 16.5% (stat. +syst.).

Impact of TFC-parameters – very low background level

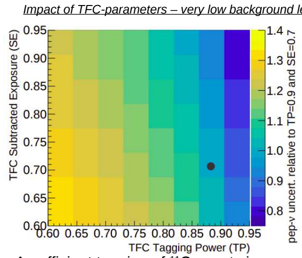

An efficient tagging of ^{11}C events is more relevant than having high fraction of exposure.

CNO neutrinos

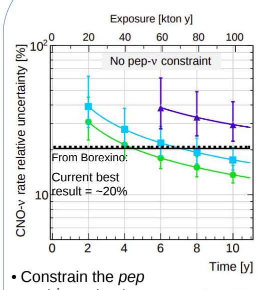

CNO spectral shape degeneracy with the *pep* neutrinos.

No CNO measurements possible for High background levels.

- Constrain the *pep* neutrino rate at 1.4% from theoretical and experimental info.
- JUNO can overcome the current best results (~20%) for long data-taking period (>6 years).
- No ^{210}Bi constraint used.

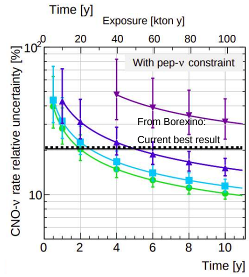

JUNO also has the potential to measure individually for the first time the rate of the two main components of the CNO flux, ^{13}N, and ^{16}O solar neutrinos, except in case of the High background level.

CONCLUSIONS

- After the first data-taking year, JUNO is able to provide unprecedented ^{7}Be and *pep* solar neutrino results (except for the High background scenario).
- JUNO is also able to provide the first simultaneous ^{7}Be, *pep* and CNO measurement for > 6 years of data taking in case of optimistic radio-purity scenario.
- Except for the High background scenario, JUNO will be highly competitive for the CNO measurements for long data-taking using *pep* constraint.
- The first separation of ^{13}N and ^{15}O neutrinos is also possible!

arXiv:2303.03910, accepted in Journal of Cosmology and Astroparticle Physics (JCAP)

REFERENCES

[1] John N. Bahcall et al, "New Solar Opacities, Abundances, Helioseismology, and Neutrino Fluxes" , 2005 ApJ 621 L85
[2] Vinyoles et al. , A New Generation of Standard Solar Models , Astr.J. 835 (2017) 202.
[3]A. Abusleme et al., JUNO physics and detector, Progr. Part. Nucl. Ph. 123 (2022) 103927.
[4] M. Agostini et al.,Identification of the cosmogenic ^{11}C background in large volumes of liquid scintillators with Borexino, Eur. Phys. Journal C 81 (2021) 1075.
[5] M. Agostini et al., "Comprehensive measurement of pp-chain solar neutrinos," Nature, vol. 562, pp. 505–510, Oct 2018.

JUNO Sensitivity to Geoneutrinos

Cristobal Morales Reveco
GSI Helmholtzzentrum für Schwerionenforschung, RWTH Aachen, and Forschungszentrum Jülich, Germany
email: c.i.moralesreveco@gsi.de

Introduction

Jiangmen Underground Neutrino Observatory

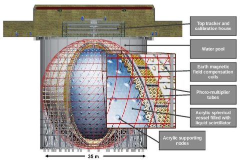

- Largest liquid scintillator neutrino experiment
- Under construction at the Jiangmen region, China
- Near two nuclear power plants at 52.5 km
- Rock overburden of 650 m
- 20 kton Liquid Scintillator target
- Detector with diameter of 34.5 m
- Energy resolution of 3% at 1 MeV

- **Main objective:** determine the Neutrino Mass Ordering [3] with reactor anti-neutrinos. Precise measurement of oscillation parameters with subpercent precision [2]
- Potential in other topics: Atmospheric neutrinos, **Geoneutrinos**, Solar neutrinos, Supernova neutrinos, and many others

This work aims to update previous results published [1,4]:
- Refined geological model around JUNO - latest in [5]
- Reactor spectrum and uncertainty
- Updates on detector response and backgrounds
- Impact of oscillation parameters
- Full MC approach including reconstruction

Geoneutrinos

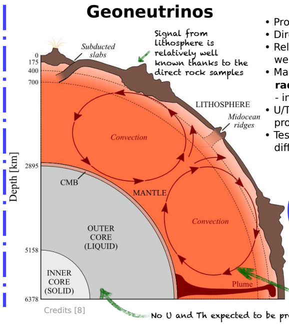

- Product of Earth's decay of longlived radioactive elements
- Direct probe of the deep Earth
- Released heat from the decays and geoneutrino flux is in a well known ratio
- Main goal is to **measure the contribution of the radiogenic heat to the total Earth's surface heat flux** - in particular radiogenic heat of the mantle
- U/Th ratio provides insights about the Earth's formation process
- Testing mantle homogeneity by measuring geoneutrino at different locations [7,8]

Measured by JUNO

$$^{238}\mathrm{U} \rightarrow {}^{206}\mathrm{Pb} + 8\alpha + 8e^- + 6\bar{\nu}_e + 51.7\,\mathrm{MeV}$$

$$^{232}\mathrm{Th} \rightarrow {}^{208}\mathrm{Pb} + 6\alpha + 4e^- + 4\bar{\nu}_e + 42.8\,\mathrm{MeV}$$

$$^{40}\mathrm{K} \rightarrow {}^{40}\mathrm{Ca} + e^- + 1\bar{\nu}_e + 1.32\,\mathrm{MeV}$$

Low energy < 1.8 MeV

Signal Signature

Inverse Beta Decay

$$\bar{\nu}_e + p \rightarrow e^+ + n$$

Delayed signal: thermalize and captured ~ 200µ

Prompt signal: Quick anihilation into two 511 MeV gammas

$$E_{prompt} \approx E_{\bar{\nu}} - 0.782\,\mathrm{MeV}$$

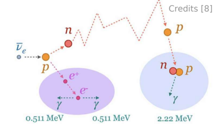

IBD candidate: correlated prompt-like with a following delayed-like event

Procedure

Toy MC approach with the software **Julich nUsol Sensitivity Tool (JUST)** [6]

Rates of each process

	Energy Range 1.8 ⩽ E ⩽ 12 MeV	Rate [cpd x kton]	Rate unc.	Shape unc.
IBD events	Geoneutrinos	1.2	-	6.7%
	Reactor Neutrinos	43.18	-	Daya Bay
Non-IBD events	Accidentals	0.8	1%	-
	Li/He	0.8	10%	13.4%
	(alpha,n)	0.05	50%	67%
	Fast Neutrons	0.1	100%	27%
	World Reactor	1	5%	6.7%
	Atmospheric	0.16	50%	67%

Number of toyMC

PDFs

Experiment Exposure

JUST: Configuration

Normilized processes shape

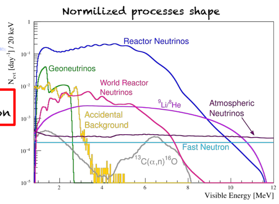

JUST: Sampling and Fitting

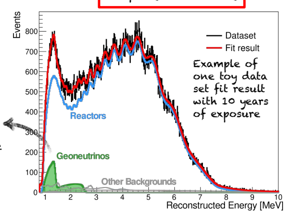

Example of one toy data set fit result with 10 years of exposure

Toy data sets generated by randomly sampling the PDFs and stastically fluctuate the injected rate

Fitting characteristics:
- Energy rage: 1.8-12 MeV
- Pearson χ^2
- Minimization using Minuit
- Rate uncertainty introduced as constrain and addtional pull term in χ^2 for other backgrounds
- Shape uncertainties modify the χ^2 definition

$$\chi^2 = \frac{(y-n)^2}{y + (\sigma_{shape} \cdot y)^2} + \text{Pull Terms}$$

- PDFs are fluctuated given the shape uncertainty on every fit
- Fitting errors provided by minimizer
- Fixed oscillation parameters

Fit Error

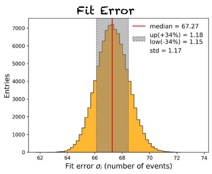

Analyze fits: 100k Output results

Fit Value

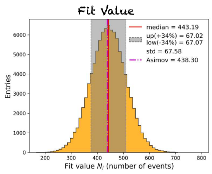

Fit Error / Fit Value

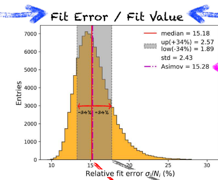

Asimov data set can also be produced and fitted, where a single toy is produced without any statistical fluctuation

- Median from toy approach agrees closely to asimov fit
- Toy approach provides extra information: 68% C.I.

$$\text{Sensitivity} = \text{median}^{+34\%}_{-34\%}$$

Results

Geoneutrinos Precision

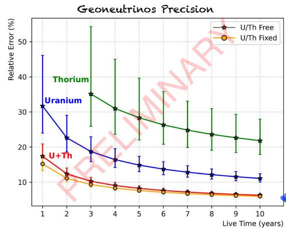

Two measuring schemes:

1. U/Th Fixed: Signal ratio U/Th is fixed and the total geoneutrino signal is fitted. The ratio assumed is 0.29 corresponding to abundances from CI chondrites

2. U/Th Free: The PDFs of U and Th are fitted independently. Provides the possibility of measure the observed Th/U ratio and their correlation

Combined U+Th signals offer a comparable result to U/Th fixed

$$\sigma(U+Th) = \sqrt{\sigma_U^2 + \sigma_{Th}^2 + 2\sigma_U\sigma_{Th}\rho}$$

Th/U Ratio Precision

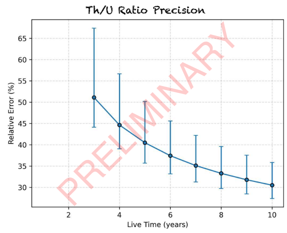

Correlation of U and Th

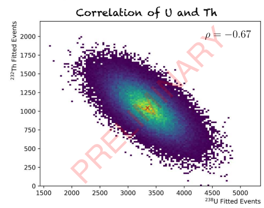

Background Impact Analysis

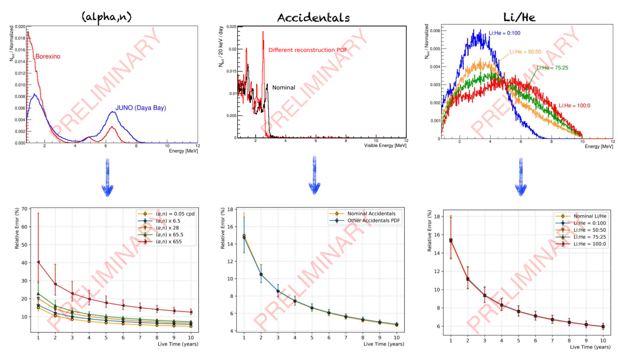

- Different radiopurity scenarios considered
- Borexino (alpha,n) PDF
- **Most critical background**, after reactor neutrinos
- Current works on improved spectrum and rate estimation

- Test with a PDF with a different reconstruction for accidentals
- Rate constrain of 1%
- Constrain will be from real data
- **No impact**

- Generate Li/He PDF using different contribution ratio of Li and He
- Contribution varies with the experiment - dependance with the overburden
- Test Li/He with different PDF
- **No impact**

Conclusions

- **Highest geoneutrino statistics:** JUNO with just 1 year will collect more events (~400) than other experiments, e.g: KamLAND ~ 170 events in 18 years [7] and Borexino ~ 50 events in 10 years [8]
- Biggest challenge is to **disentangle geoneutrinos from reactor neutrinos.** A **understanding of the radiopurity** for the (alpha,n) background contribution is needed
- **Precise measurement of total geoneutrino signal** can be achieved for both U/Th fixed and free. JUNO could also be sensitive to measuring Th/U signal ratio

Next Plans

- **Update PDFs** with new MC production - better detector knowledge
- **Geological crust model** - refined rates and spectrum. Ongoing work of updated geomodel
- **Mantle signal sensitivity and precision** to different models
- Overhaul of **(alpha,n) background** - new generator and rate estimation
- Inclusion of neutrino **oscillation parameters**

References

[1] Juno Collaboration. (2016). Neutrino physics with JUNO. Journal of Physics G: Nuclear and Particle Physics, 43(3), 030401. https://doi.org/10.1088/0954-3899/43/3/030401
[2] A. Abusleme et. al. (JUNO Collaboration). Sub-percent precision measurement of neutrino oscillation parameters with JUNO. Chinese Physics C, 46(12):123001, dec 2022
[3] JUNO Collaboration. JUNO physics and detector. (2022). Progress in Particle and Nuclear Physics, 123, 103927. https://doi.org/10.1016/j.ppnp.2021.103927
[4] Han, R., Li, Y.-F., Zhan, L., McDonough, W. F., Cao, J., & Ludhova, L. (2016). Potential of geo-neutrino measurements at JUNO*. Chinese Physics C, 40(3), 033003. https://doi.org/10.1088/1674-1137/40/3/033003
[5] Gao, R., Li, Z., Han, R., Wang, A., Li, Y., Xi, Y., Liu, J., Mao, X., Sun, Y., & Xu, Y. (2020). JULOC: A local 3-D high-resolution crustal model in South China for forecasting geoneutrino measurements at JUNO. Physics of the Earth and Planetary Interiors, 299, 106409. https://doi.org/https://doi.org/10.1016/j.pepi.2019.106409
[6] Göttel, A., Ludhova, L., Meraviglia, A., Pelicci, L., & Settanta, G. (2021). JUST: A neutrino fit software for JUNO's solar analysis and sensitivity. Nuovo Cim. C, 45(1), 9. https://doi.org/10.1393/ncc/i2022-22009-8
[7] Abe, S., Asami, S., Eizuka, M., Futagi, S., Gando, A., Gando, Y., et al. (2022). Abundances of uranium and thorium elements in Earth estimated by geoneutrino spectroscopy. Geophysical Research Letters, 49, e2022GL099566. https://doi.org/10.1029/2022GL099566
[8] Agostini, M., & et. al. (2020). Comprehensive geoneutrino analysis with Borexino. Phys. Rev. D, 101(1), 012009. https://doi.org/10.1103/PhysRevD.101.012009

JUNO's NMO sensitivity

Mariam Rifai[1,2] on behalf of JUNO collaboration

1. Forschungszentrum Jülich GmbH, Nuclear Physics Institute IKP-2, Jülich
2. III. Physikalisches Institut B, RWTH Aachen University, Aachen

JUNO detector

Jiangmen Underground Neutrino Observatory is the first multi-kton liquid scintillator (LS) detector ever built. Construction in south China to be completed by the end of 2023.

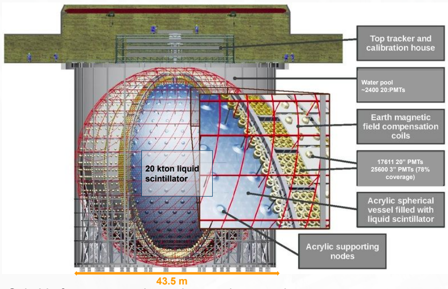

Suitable for reactor anti-neutrinos and many other measurements (atmospheric neutrinos, solar neutrinos, geo-neutrinos, supernova …)

Neutrino Mass Ordering (NMO) in JUNO

Combining reactor and atmospheric neutrino oscillations has the potential to maximize JUNO's total sensitivity.

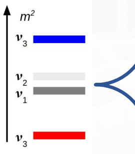

Normal Ordering: $m_3 > m_2 > m_1$

Inverted Ordering: $m_3 < m_2 < m_1$

Reactor neutrinos: 3σ in 6 years vacuum oscillation pattern independent of δcp and θ_{23}

Reactor oscillated spectrum of reactor anti-neutrino events

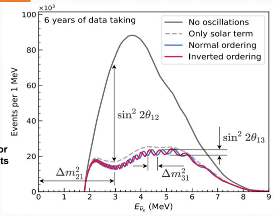

Atmospheric neutrinos: provide additional independent sensitivity to NMO via oscillation in matter

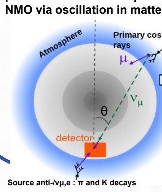

Sensitivity region to NMO:
- E~ [3, 10] GeV
- cos θ [-1, -0.8]

Survival oscillation probability in the matter $P_{\nu\mu \to \nu\mu}$

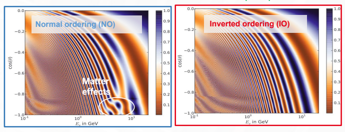

Oscillation probabilities in matter depends on neutrino energy *E*, direction, and electron density N_e in matter

Reactor oscillated spectrum and backgrounds

- **Detection channel:** Inverse Beta Decay (IBD): $\bar{\nu}_e + p \rightarrow e^+ + n$

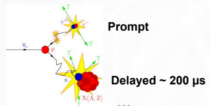

IBD event selections [3]

Type	Value
Prompt Energy	$E_p \in [0.7, 12.0]$ MeV
Delayed Energy	$E_d \in [1.9, 2.5]$ MeV ∪ [4.4, 5.5] MeV
Fiducial Volume	$R < 17.2$ m
Time difference between prompt and delayed signal	$\Delta T_{p-d} < 1$ ms
Distance between prompt and delayed signal	$\Delta R_{p-d} < 1.5$ m

Chin. Phys. C 46(2022)no.12, 123001

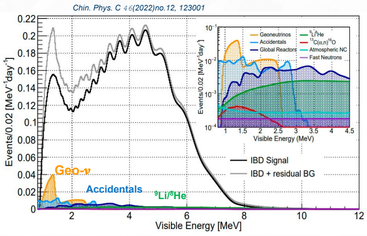

IBD and residual backgrounds

Event type	Rate [/day]	Relative rate uncertainty	Shape uncertainty
Reactor IBD signal	60 → 47	-	-
Geo-ν's	1.1 → 1.2	30%	5%
Accidental signals	0.9 → 0.8	1%	negligible
Fast-n	0.1	100%	20%
^{9}Li/ ^{8}He	1.6 → 0.8	20%	10%
$^{13}C(\alpha, n)^{16}O$	0.05	50%	50%
Global reactors	0 → 1.0	2%	5%
Atmospheric ν's	0 → 0.16	50%	50%

J. Phys. G 43:030401 (2016) → this update

Analysis requirements: [1,2]

- Excellent energy resolution: 3%/√E(MeV)
- 1% energy scale uncertainty, controlled by calibration strategy encompasses multiple sources
- High photon yield (10^4 photons/MeV)

- Other detectors related to JUNO under construction:
  - The OSIRIS detector: [4]
    - Monitors radiopurity of the liquid scintillator during filling.
  - Satellite detector TAO (Taishan Antineutrino Observatory): [5]
    - 2.8 ton Gd-loaded liquid scintillator detector at ~30 m baseline from the Taishan (1 reactor core).
    - Energy resolution < 2% at 1 MeV.
    - Reference reactor spectrum for JUNO.

Calibration

1D, 2D, 3D scan systems, controlled by γ/α/β, UV-laser, and light pulses sources.

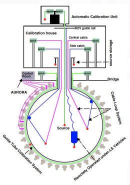

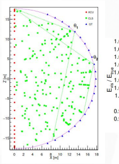

250 calibration points in a half vertical plane of the JUNO CD

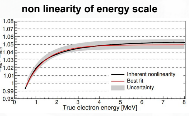

J. High En. Phys. 3 (2021) 4

Reactor sensitivity to NMO

3σ (reactors only) @ ~6 yrs * 26.6 GW$_{th}$ exposure

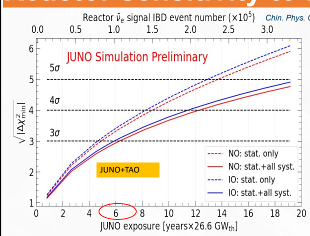

doi: 10.5281/zenodo.6683749
doi: 10.5281/zenodo.6775075

	$\Delta\chi^2_{min}$
Statistics	11.3
Stat.+Flux error	-0.6
Stat.+Backgrounds	-1.4
Stat.+Nonlinearity	-0.4
Stat.+Others	< -0.05
Total	9.0

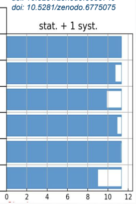

Neutrino oscillation parameters

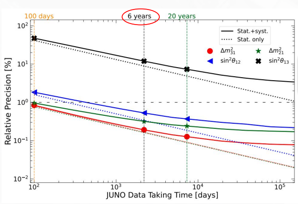

Chin. Phys. C 46 (2022)no.12, 123001

	Δm^2_{31}	Δm^2_{21}	$\sin^2\theta_{12}$	$\sin^2\theta_{13}$
JUNO 6 years	~0.2%	~0.3%	~0.5%	~12%
PDG2020	1.4%	2.4%	4.2%	3.2%

JUNO will measure $\sin^2\theta_{12}$, Δm^2_{13}, and Δm^2_{12} with < 1% precision level

Atmospheric sensitivity to NMO

Previously estimated NMO Sensitivity, based on toy MC simulation:

JUNO sensitivity to NMO with atmospheric neutrinos:
- **0.75 ~1.4 σ with 6 yrs exposure.**
- **Detector response was based on estimations**

To be combined with the 3σ in 6 yrs with reactor neutrinos.

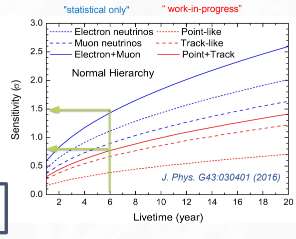

A new realistic study is carried out based on event reconstruction and Particle Identification(PID).

	Design (J. Phys. G43:030401 (2016))	New estimation [6]
Event selection	Hadron-to-total energy ratio < 0.5	-
Direction	Constant resolution: $\sigma_{\theta_\mu} = 1^\circ$, $\sigma_{\theta_\nu} = 10^\circ$	$\nu_e/\bar{\nu}_e$ ($\nu_\mu/\bar{\nu}_\mu$): $\sigma_{\theta_\nu} < 10^\circ$ at E>4(3) GeV
Energy	Visible energy: σ_E=1%@1GeV	Neutrino energy: σ_{E_ν}=10%@1GeV
PID (ν/ν̄ discrimination)	-	Efficiency: 70%-85%
PID (ν_e-CC/ν_μ-CC/NC discrimination)	Idealistic assumptions	Efficiency>80%

Work in progress

JUNO's NMO sensitivity from atmospheric neutrinos will be significantly improved

- Statistics increased by ~30% (due to event selection removal).
- Improved direction reconstruction performance.
- ν/ν̄ separation

Conclusions

- **JUNO construction in south China to be completed by the end of 2023.**
- **Neutrino mass ordering: 3σ in about 6 years with reactor antineutrinos**
- **Joint analysis with atmospheric neutrinos will enhance the sensitivity**
- **Measurement of $\sin^2\theta_{12}$, Δm^2_{13}, and Δm^2_{12} witch sub-percent level in 6 years.**

References:

[1] JUNO physics and detector, Progr. Part. Nucl. Ph. 123 (2022) 103927
[2] Yellow Book: J. Phys. G: Nucl. Part. Phys. 43 (2016) 030401
[3] Sub-percent Precision Measurement of Neutrino Oscillation Parameters with JUNO, *Chin. Phys. C 46 (2022)no.12, 123001*
[4] OSIRIS, Eur. Phys. J. C 81 (2021) 973.
[5] TAO Conceptual Design Report: A Precision Measurement of the Reactor Antineutrino Spectrum with Sub-percent Energy Resolution, arXiv:2005.08745 (2020)
[6] Prospects for atmospheric neutrino measurements in JUNO, EPS-HEP conference 2023 https://indico.desy.de/event/34916/contributions/147008/

Accelerator R&D for the High Brilliance Neutron Source (HBS)

A. Lehrach[1], T. Gutberlet, Forschungszentrum Jülich, Jülich, Germany
R. Gebel[2], GSI Helmholtzzentrum für Schwerionenforschung, Darmstadt, Germany
H. Podlech[3], Johann Wolfgang Goethe-Universität Frankfurt, Frankfurt, Germany
[1]also RWTH Aachen University, Aachen, Germany, [2]also Forschungszentrum Jülich, Jülich, Germany
[3]also Helmholtz Research Academy Hesse for FAIR (HFHF), Frankfurt, Germany

Introduction

- The High Brilliance Neutron Source (HBS) belongs to the class of High Current Accelerator based Neutron Sources (Hi-CANS) [1].
- The linac has to deliver proton beams at 70 MeV with 100 mA [2].
- The High Energy Beam Transfer (HEBT) [3] distributes the beam to three different targets via a multiplexer system [4].
- Each proton pulse has a specific time structure.

Design Philosophy and Beam Parameter

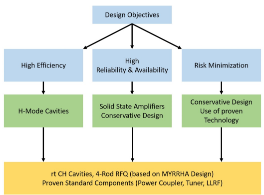

Required	Specifications	Unit	Detail/Comment
Particle type	Protons	N/A	User requirement
Accelerator type	RF Linac	N/A	
Beam current	100	mA	Output current
Final energy	70	MeV	User requirement
Beam duty factor	6 (up to 20)	%	User requirement
RF duty factor	8 (up to 25)	%	Required for cavity filling
Pulse length	208/208/833	μs	User requirement
Repetition rate	96/96/24	Hz	User requirement
Average beam power	420 (1400)	kW	can be upgraded
Peak beam power	7	MW	
Availability	>95	%	During scheduled operation
Maintainability	Hand-on	N/A	
Life time	>25	Years	

Overall Layout

The layout is determined by the location and arrangement of the HBS target stations in three experimental halls, based on the space requirements of the neutron targets, instruments and the corresponding building locations and dimensions.

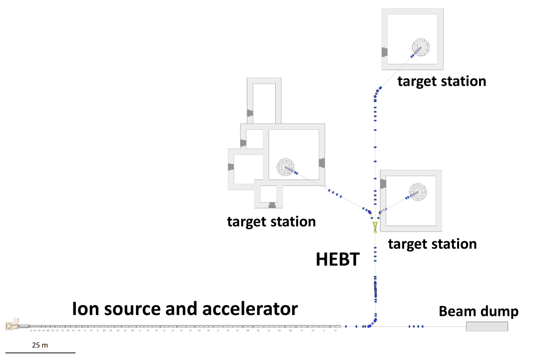

Schematic top view of the HBS, including front end, linac, beam dump and HEBT beamline to individual target stations.

RFQ and CH-Linac

The linac has to deliver proton beams at 70 MeV with 100 mA

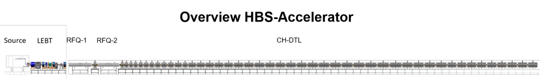

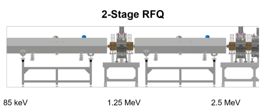

CH-DTL

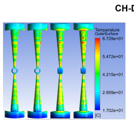

Parameter	Specification
No. of cavities	45
Aperture diameter	35 mm
Shunt impedance	19 – 51 MΩ/m
Voltage	0.5 – 2.4 MV
Gradient	1.5 – 2.4 MV/m
Total power per cavity	70 – 405 kW
Thermal load	8 – 25 kW/m

Beamline Layout

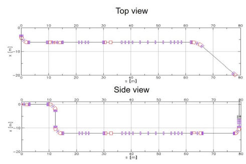

Top and side view of the straight HEBT beamline. The drawing shows the three different sections, the beam dump, and the respective quadrupole (pink), dipole (red), and scanner dipole magnets (black).

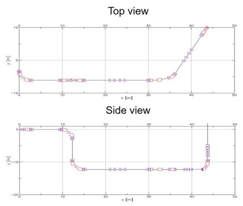

Top and side view of the left HEBT beamline. The drawing shows the three different sections and the respective quadrupole (pink), dipole (red), and scanner dipole magnets (black).

Beamline Optics

Beam parameters at the entrance of HEBT:

- Transverse beam size: $\sigma_{x,y} = 1.6\,\text{mm}$,
- Beam emittance: $\epsilon^g_{x,y} = 2.54\,\text{mm mrad}$ (rms, geom.),
- Momentum spread: $\Delta p/p = 0.5\,\%$,
- Optical functions: $\beta_{x,y} = 1.1\,\text{m}$, $\eta_{x,y} = 0\,\text{m}$.

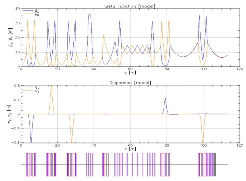

Horizontal and vertical Beta function $\beta_{x,y}(s)$ (upper plot), and dispersion function $\eta_{x,y}(s)$ (middle plot) versus longitudinal position s. In the lower plot quadrupoles are shown in pink, dipoles in red, and scanner dipole magnets in black (straight beamline).

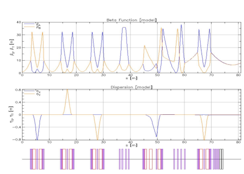

Horizontal and vertical Beta function $\beta_{x,y}(s)$ (upper plot), and dispersion function $\eta_{x,y}(s)$ (middle plot) versus longitudinal position s. In the lower plot quadrupoles are shown in pink, dipoles in red, and scanner dipole magnets in black (left beamline).

References

[1] T. Brückel, T. Gutberlet (Eds.), Conceptual Design Report: Jülich High Brilliance Neutron Source (HBS), Schriften des Forschungszentrums Jülich, Reihe Allgemeines, vol. 8, 2021, ISBN 978-3-95806-501-7.
[2] H. Podlech et al., Conceptual Design of the Proton Linac for the High Brilliance Neutron Source HBS, in Proc. 10th Int. Particle Accelerator Conf. (IPAC'19), Melbourne, VIC, Australia, MOPTS027, May 2019, pp. 910-913.
[3] A. Lehrach et al., Beam Dynamics Studies for the Target Beamlines of the High Brilliance Neutron Source, Proc. of the International Acclerator Conference (IPAC 2023), TUPA145, to be published in IoP Conf. Series.
[4] M. Rimmler et al., Developments of a multiplexer system for the High-Brilliance Neutron Source HBS, Journal of Neutron Research, Volume 23 (2-3), Sept. 2021, pp. 143-156.

Acknowledgements: Work supported by the Innovation Pool project on "High Current Accelerator Systems for Future HBS", Research Field Matter of the Helmholtz Association (HGF), Germany.

Contact: Andreas Lehrach - a.lehrach@fz-juelich.de

Member of the Helmholtz Association

Design and Production of the Fast HESR-Injection Kicker Magnets

Yury Valdau[1,2], R. Gebel[1,2], R. Tölle[2], N. Bongers[2], C. Ehrlich[2], S. Hamzic[2], M.Retzlaff[2], P. Chaumet[3], F.M. Esser[3], H. Jagdfeld[3], F. Jordan[3], F. Klehr[3], B. Laatsch[3], W. Lesmeister[3], L. Reifferscheidt[3], G. Schyns[3], L. Semke[3], O. Maulat[4], O. Cosson[5], F. Forest[6], L. Rambaud[6], P. Jivkov[6], J.-C. Le Douarin[6], P. Boeher[6], V. Sigalo[6], D. Ramaugé[6], W. Beeckman[6], N. O. Fröhlich[2,7]

[1]GSI Helmholtzzentrum für Schwerionenforschung GmbH, 64291, Darmstadt, Germany
[2]Forschungszentrum Jülich, Institut für Kernphysik, IKP4, 52428, Jülich, Germany
[3]Forschungszentrum Jülich, Zentralinstitut für Engineering und Technologien, ZEA-1, 52428, Jülich, Germany
[4]JEMA France, 1, Boulevard Hélène Boucher, 67500 Haguenau, France
[5]Normandy Hadrontherapy, 1, rue Claude Bloch, 14000 Caen, France
[6]SigmaPhi, Rue des frères Montgolfier, F-56000 Vannes, France
[7]now at Deutsches Elektronen-Synchrotron DESY, 22607 Hamburg, Germany

Abstract

The injection kicker system been build for the High Energy Storage Ring (HESR). The system consist of four magnets, located in the specially developed vacuum tanks, and semiconductor based (IGBT) pulsers connected using coaxial cables. Produced system fully meets designed injection pulse parameters and can be used for the injection of protons, antiprotons and charged ions in the HESR storage ring.

Requirements

- Deflection angle 1.6 mrad/magnet
- Integral magnetic field 57.8 mT
- Field homogeneity 1.5%
- Maximal puls current 4 kA
- Rise/Fall time <200 ns

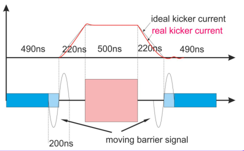

System Design

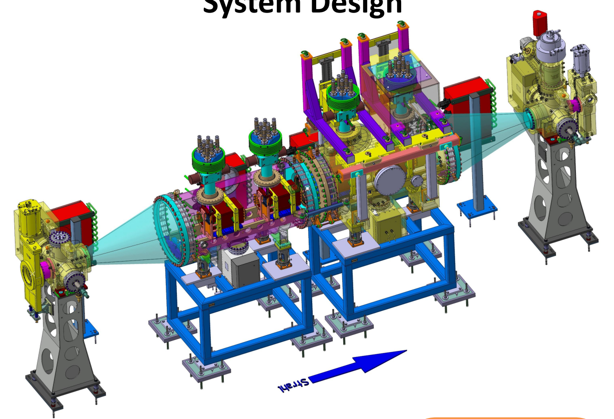

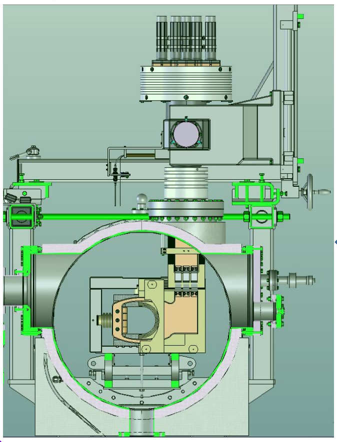

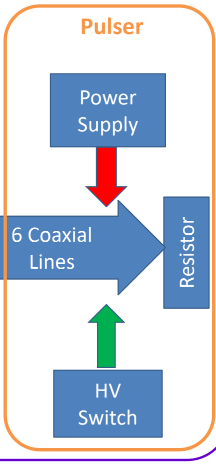

Kicker Pulse

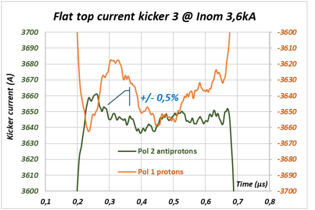

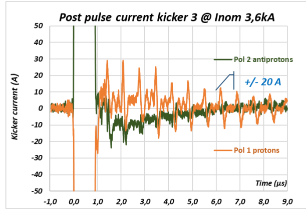

Flat-top and after-puls fluctuations about 0.5% of I_{max}

Magnet Field Measurements

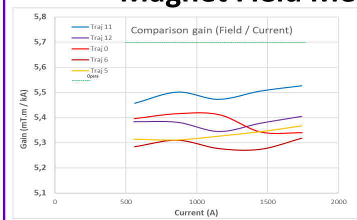

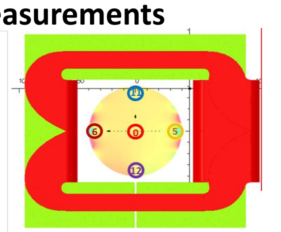

Integrated mean field factor 1.5% homogeneous over 5 trajectories

Produced System

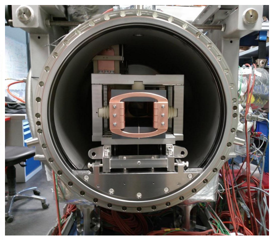

Produced System Parameters

- Deflection angle 6.4 mrad
- Rise/Fall time <220 ns, Current fluctuations <0.5% of I_{max}
- UHV compatible and bake-able system
- 4 Kicker magnets: single winding, ferrite yoke (CMD5005)
- 6 Coaxial cables per magnet
- One semiconductor based (IGBT) pulser per magnet

IPAC´23 THPA167

Contact: y.valdau@fz-juelich.de

Development of a Combined Element with an Electric and Magnetic Fields for the JEDI Experiment

Kirill Grigoryev[1,2], R. Gebel[1,2], M. Schubert[1,2], Yu. Valdau[1,2], N. Bongers[2], N. Demary[2], G. Langenberg[2], F. Scheiba[2], H. Zens[2], J. Böker[2,3]

[1]GSI Helmholtzzentrum für Schwerionenforschung GmbH, 64291, Darmstadt, Germany
[2]Forschungszentrum Jülich, Institut für Kernphysik, IKP4, 52428, Jülich, Germany
[3]now at Medical Systems Particle Therapy GmbH, 53842 Troisdorf, Germany

MOTIVATION

The precursor experiments to measure the proton and deuteron permanent Electric Dipole Moment (EDM) at the Cooler Synchrotron COSY in Jülich led to a new ring concept with combined magnetic and electric field elements. The high-stability electric and magnetic field deflector is one of the technical challenges of this project.

PROTOTYPE RING PARAMETERS

Conditions	E [MV/m]	B [mT]	HV [kV]
E Field 30MeV	6.67	-	400
E×B Field 30MeV	4.56	28.5	274
E×B Field 45MeV	7.00	32.7	400

SMALL SCALE SETUP

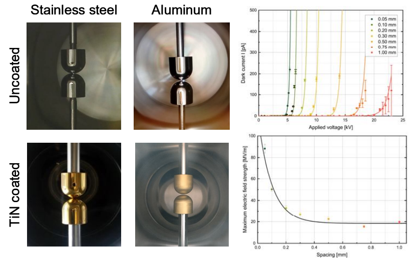

- TiN coated aluminum is the best material choice.
- The maximum electric field strength of 17 MV/m can be reached.

K. Grigoryev, et.al., RSI 90, 045124 (2019)

THE LARGE SCALE SETUP

MAGNET	
B_{max}	1.6 T
Mass	64 t
Gap height	200 mm

DEFLECTOR	
Length	1020 mm
Height	90 mm
Displacement	20 – 120 mm

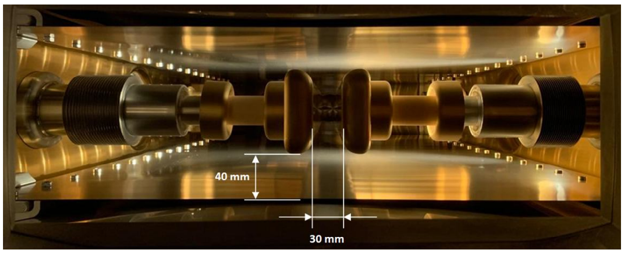

DESIGN and SIMULATION

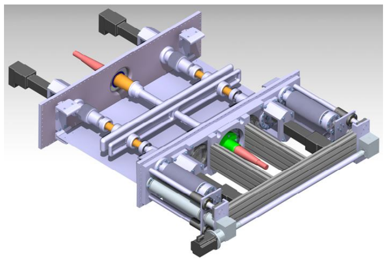

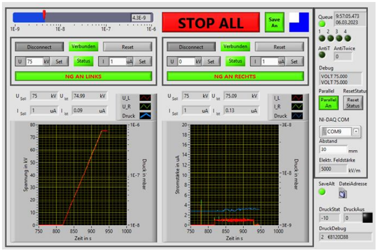

Electron trajectories simulation

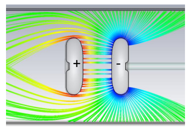

B-field: 0 T

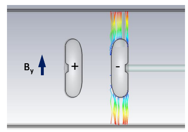

B-field: 0.15 T

Electrons energy: 50 eV
Voltage: ±100 kV → 4MV/m

POWER CONVERTER	
$Voltage_{max}$	200 kV
$Current_{max}$	2 mA
Stability U/I	< 10 ppm

MEASUREMENTS and RESULTS

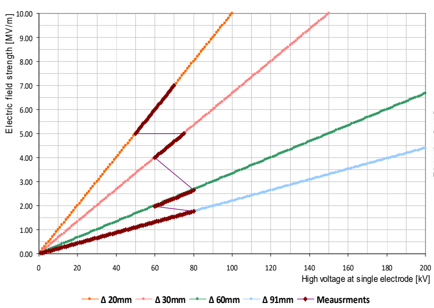

Measurements at high electric field

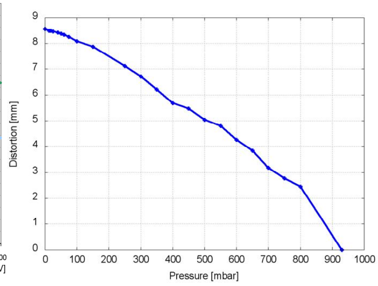

Chamber deformation

OUTLOOK

The electrodes were aligned along the flanges with an accuracy of 50 µm.

A large-size vibration-free ultra-high vacuum system was used to test the deflector prototype.

Security interlock and remote control have been integrated into the existing accelerator systems.

7 MV/m is achieved in the presence of 150 mT magnetic field at various electrode distances.

During the measurements at high electric fields the dark current did not exceed 100 nA.

References:
F. Abusaif, et.al., "Feasibility Study for an EDM Storage Ring", arXiv:1812.08535 (2019).
F. Abusaif, et.al., "Storage Ring to Search for Electric Dipole Moments of Charged Particles - Feasibility Study," CERN Yellow Report 257 (2021).
K. Grigoryev, et.al., "Electrostatic deflector studies using small-scale prototype electrodes", Rev. Sci. Instrum. 90 045124 (2019).

Contact: k.grigoryev@gsi.de

IPAC'23 THPA189

Improved Waveforms for Barrier-Bucket Systems

Bernd Breitkreutz*, GSI Darmstadt, Germany | Rolf Stassen, Forschungszentrum Jülich, Germany

At each revolution, barrier-bucket cavities apply a short, typically single sine-period shaped, accelerating/decelerating pulse to the beam. Reducing the field between these pulses to zero is challenging. Conventional approaches use signal predistortion and do not overcome the problem of the low-pass characteristics of the power amplifiers. This problem is addressed here by investigating more suitable signals than sinusoidal bursts.

Low-pass filtered sine bursts

Sinusoidal bursts are not differentiable at their edges. This results in an infinite set of harmonics (blue). Therefore, applying a low-pass filter creates an unavoidable ripple (green). It also increases the width *w* of the barrier.
Example: An intended barrier width of α = 20 %, low-pass filtered to the 9th harmonic, results in a ripple of r = 5.4 % and an actual barrier width of w = 22 %.

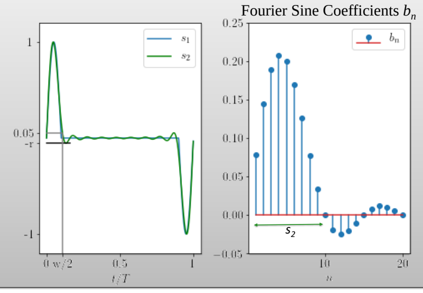

Comparison of different barrier shapes

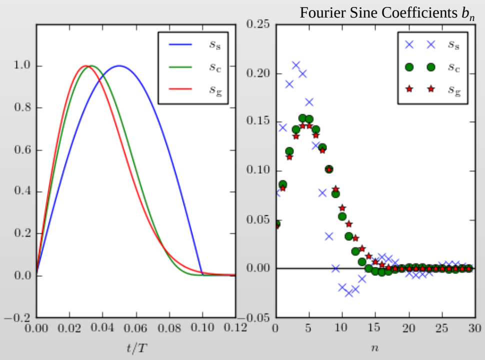

Sinusoidal burst

$$s_s(t) = -\sin\left(\frac{1}{\alpha}\cdot 2\pi\,\frac{t}{T}\right)\,\Pi_\alpha\left(\frac{t}{T}\right) \quad \text{for} \quad |t| \le \frac{T}{2}$$

Raised-cosine window

$$s_c(t) = s_s(t)\cdot\frac{1}{2}\left(1+\cos\left(\frac{1}{2\alpha}\cdot 2\pi\,\frac{t}{T}\right)\right)$$

Gaussian pulses

$$s_g(t) = \exp\left(-\frac{1}{2}\left(\frac{t/T-\sigma}{\sigma}\right)^2\right) - \exp\left(-\frac{1}{2}\left(\frac{t/T+\sigma}{\sigma}\right)^2\right)$$

Ripple r after low-pass filtering to the h^{th} harmonic

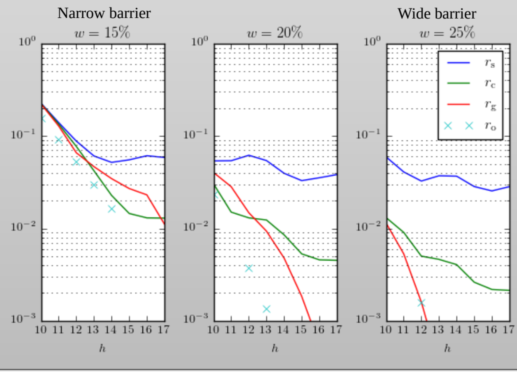

The ripple of sinusoidal bursts s_s is compared to three other barrier shapes, i.e. a raised-cosine window function s_c, a pair of Gaussian pulses s_g and the best solution found by an optimizer s_o.
As expected, the soft-edged barrier types produce less ripple in the bucket after low-pass filtering. Typically, the Gaussian pulses have the best characteristics. However, especially for small values of h, the raised cosine window sometimes gives even better results.
The limit can be pushed further with an optimizer, if the number of available harmonics is limited and the effort is justifiable.
For the HESR barrier bucket system, the double Gaussian proved to be a simple and satisfactory approach to meeting the specifications.

Example: FAIR HESR Barrier-Bucket cavity

- Air-cooled magnetic-alloy cavity (Magnetec Nanoperm)
- Twelve 500-watts Barthel power amplifiers
- Signal shape: double Gaussian pulse

Revolution Frequency	494 kHz
Pulse Width	16.6 %
Harmonics	20
Ripple (measured)	3 %
Gap voltage (measured)	7 kVpp

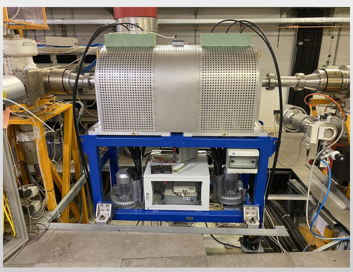

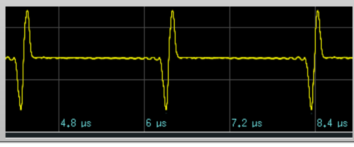

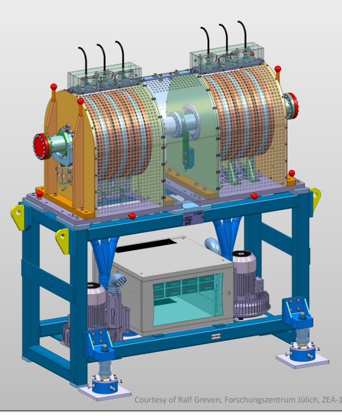

Injection Optimization via Reinforcement Learning at the Cooler Synchrotron COSY

A. Awal[1,2], J. Hetzel[1], J. Pretz[2,3]
[1]GSI Helmholtzzentrum für Schwerionenforschung, Germany
[2]III. Physikalisches Institut B, RWTH Aachen University, Germany
[3]Institut für Kernphysik, Forschungszentrum Jülich, Germany

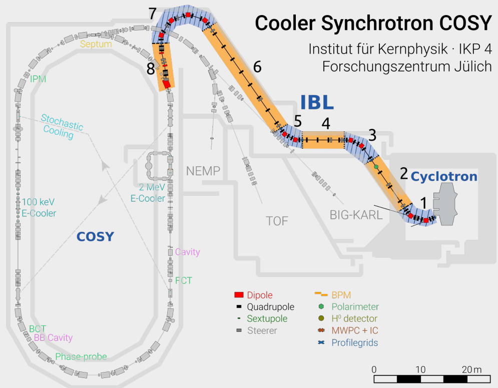

Objective

The Cooler Synchrotron (COSY) is used to store and accelerate charged hydrogen and deuteron ions for various research applications. We aim to control and optimize the injection process at COSY to increase the beam intensity and reduce the setup time using Reinforcement Learning (RL) agents. The focus is the injection beam line (IBL) for transporting pre-accelerated ions from the cyclotron to the storage ring.

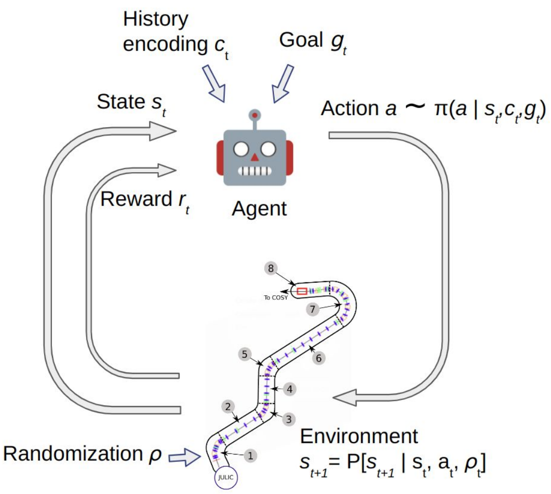

The Agent

- An actor-critic agent (SAC) is used due to its sample efficiency and to improve generalization by optimizing the action entropy along with the expected return.
- Encoding of the observed history c_t is added. The critic models the value function as $Q(s_t, c_t, a_t, g_t, \varrho_t)$.
- The environment dynamics are randomized through a set of randomization parameters ϱ_t.
- Domain randomization parameters include: initial beam angle, magnets strength, observation noise, bunch offset, offset of the magnets values, observation noise, number of bunches within a bunch, offset of the buch location

Control in Simulation and Live

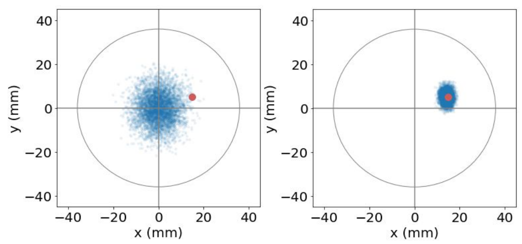

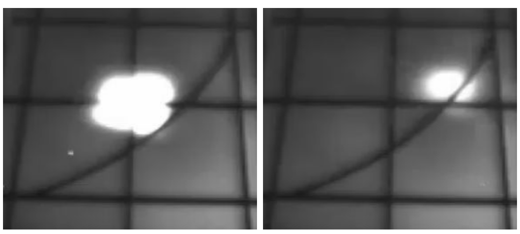

Agent Training Anatomy

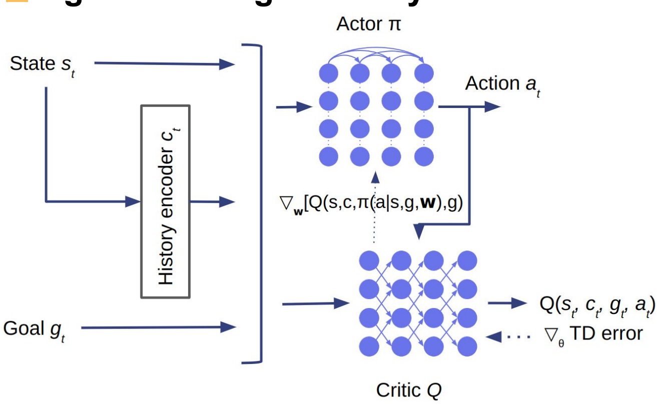

IBIC23 MOP001

Current Status of the HESR Beam Instrumentation

C. Böhme *, A. Halama ‡, V. Kamerdzhiev ‡, G. Koch ‡, K. Laihem ‡, K. Reimers ‡
*IKP, Forschungszentrum Jülich GmbH, Jülich, Germany
‡GSI Helmholtzzentrum für Schwerionenforschung, Darmstadt, Germany
Author contact: c.boehme@fz-juelich.de

Introduction

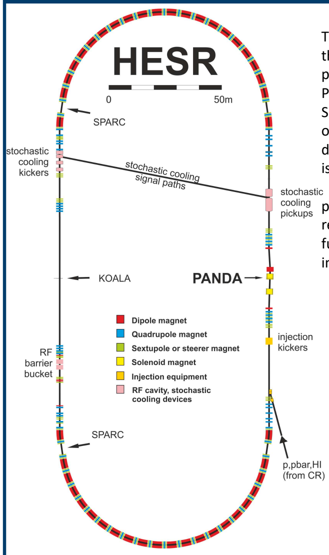

Abstract

The High Energy Storage Ring (HESR), within the FAIR project, will according to current planning, provide anti-proton beams for PANDA and heavy ion beams for i.a. the SPARC experiment. Manufacturing for most of the envisaged beam instrumentation devices in vacuum is completed and testing is well underway. The overall status update of the beam instrumentation devices is presented, with a focus on the test-bench results of the BPMs. In addition, the planned future timeline of the HESR beam instrumentation is briefly reported.

Technical Details

- Circumference 574 m
- Momentum range 1.5 – 15 GeV/c

Beam Instrumentation (selection)

- 63 BPMs Shoe-Box Design
- 2 Beam Current Transformers
  - 1 NPCT
  - 1 FCT
- 1 In-Gap particle measurement
- 118 BLMs
- 2 Ionization Profile Monitors
- 5 + 1 Viewer (Ring + Inj. Beamline)
- 2 Scraper (2 plain each)
- Schottky Pick-Up
- Dynamical Tune-Meter
- Phase Pick-up

Ionization Profile Monitor

In cooperation with GSI

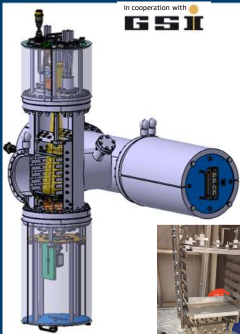
Picture: M. Maubach, IKP, Forschungszentrum Jülich

- 2 IPMs are envisaged for HESR & 15 for high energy beam transport (HEBT)
- Joint work with GSI based on the FAIR prototype
- Re-Design for HEBT and HESR with 150 mm width of the E-field cage
- Two identical devices rotated by 90° for measuring both plains
- Top: UV-lamp for relative calibration of MCPs
- Bottom: Data acquisition with GigE-camera
- 1st of series in production

Manufactured E-field-box

Wiring of the IPM between the multipin-feedthroughs and the intermediate terminals. Not only the top- and base-plate of the E-field-box, the MCPs and the phosphor screen are connected individually, but also all 6 side electrodes of the E-field-box

Viewer

Produced RF cage

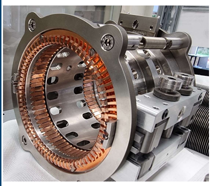

Viewer

- 45° scintillation screen
- Read out based on GigE camera
- Pneumatic drive
- If the viewer is not used, a RF cage will be moved into its place to minimize the overall impedance of the accelerator
- In production

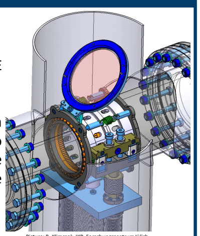
Picture: B. Klimczok, IKP, Forschungszentrum Jülich

Summary

Significant progress was recently achieved with manufacturing and testing of BI components for the HESR.

- IPM and viewers are well underway
- Current measurement, scrapers are completed.
- BPM production (but 1) finished, 75% tested
- Other BI components still to be designed

Scraper

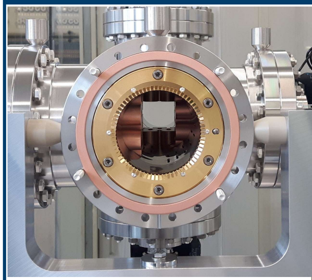
Picture: R. Tölle, IKP, Forschungszentrum Jülich

Look into the scraper in the beam plane

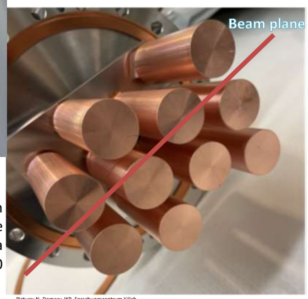

Picture: N. Demary, IKP, Forschungszentrum Jülich

One jaw consisting of 10 copper rods, which are placed in an alternating manner and are each 25 mm in diameter. This layout assures a particle will be slowed down by at least 50 mm of material

BPM

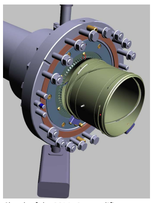
Sketch of the BPM. Preamplifiers are directly connected to the pick-ups
Picture: F. Klehr, ZEA, Forschungszentrum Jülich

Pick-Up

- Diagonal cut design
- Inner diameter of 89 mm and 78 mm length for one plain
- 47 tested, add. 14 delivered, 1 to be produced.

Test Bench Measurements

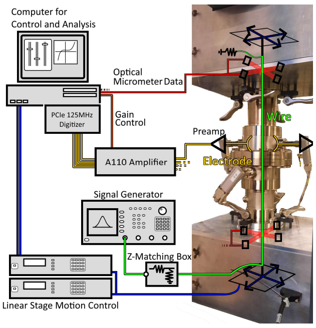

- Schematic setup of the test bench
- The probe wire is controlled by two independent units
- High precision reference pins on the BPM vacuum flanges align the two units

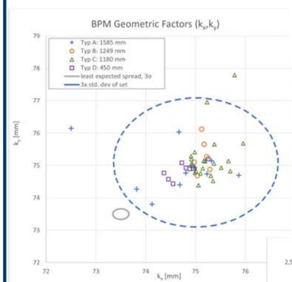

- Notable spread and outliers result from the real statistical characteristic of the individual BPM, systematic errors on the test bench as well as measurement uncertainties
- One major identified source of deviations is the capacitance of the vacuum feedthroughs, which have large deviations

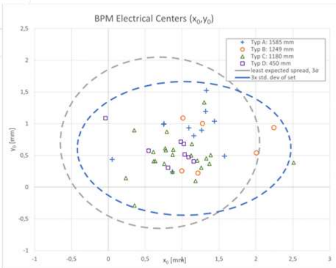

- Grey ellipse shows the expected value region by only taking the statistical error of the capacitance-deviations of the feedthroughs into account
- Blue ellipse is the 3σ–deviation of the measured values
- Simulations predict a deviation of the geometrical to the electrical center

Signal Chain

- Head-on Amplifier with 500 kΩ input impedance and 20 dB amplification
- A110 pre-amplifier, which features an amplification range of +60 dB to -60 dB
- Libera Hadron from I-Tech, Slovenia was chosen for FAIR project.
- Direct 250 MHz 16 bit signal digitization with all digital signal processing .

Member of the Helmholtz Association

ICALEPCS23 TUPDP028

Challenges of the COSY Synchrotron Control System upgrade to EPICS

C. Böhme *, C. Deliege*, V. Kamerdzhiev ‡ , R. Modic§, M. Simon*, M. Thelen*, Ž. Oven§
* IKP, Forschungszentrum Jülich GmbH, Jülich, Germany
‡ GSI Helmholtzzentrum für Schwerionenforschung, Darmstadt, Germany
§ Cosylab d. d., Control System Laboratory, Ljubljana, Slovenia

JÜLICH Forschungszentrum

COSYLAB Advancing humanity. Engineering remarkable.

Author contact: c.boehme@fz-juelich.de

Introduction

Cooler Synchrotron COSY

Circumference 183 m

- Momentum range 0.3 – 3.7 GeV/c
- Protons, Deuterons
- Polarized & unpolarized beams
- Electron and stochastic cooling
- Ultra-slow extraction
- Internal targets

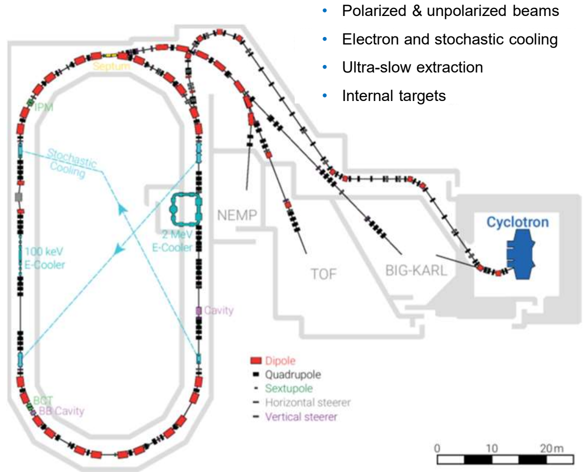

Before-upgrade Situation

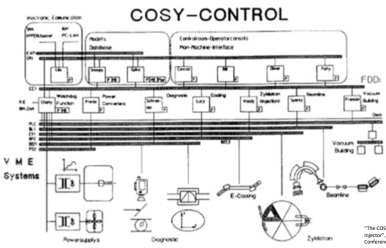

Figure 1: Cosy Control Hierarchy

- Analog Controls
- PLC
  - Siemens Simatic S5/S7/1500
- Self-developed Control System SCSR
  - **S**ingle **C**ommand **S**ingle **R**esponse
  - Based on Ethernet and Tcl/Tk

"The COSY Control System, a Distributed Realtime Operating System: First Practical Experience at the COSY-Injector", *M. Stephan, U. Hacker, K. Henn, A. Richert, K. Sobotta, A. Weinert,* 1991 IEEE Particle Accelerator Conference, Accelerator Science and Technology.

Upgrade Motivation

The upgrade is driven by:

- New requirements on the RMS beam orbit deviation introduced by Jülich Electric Dipole moment Investigations (JEDI)
- New BPM readout system commissioned

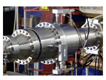

- Beam-based alignment of BPMs further improved orbit correction

A decision was made to upgrade the control system in a step-wise manner

- The following considerations were taken into account:
  - Add a logging and archiving capabilities
  - Save & Restore of machine settings
  - Use software developed and supported by a larger community
- EPICS was chosen as new control system environment.

Outlook

- Further projects might benefit from the experience, e.g.
  - HBS (High Brightness Neutron Source), FZJ, Jülich
  - FAIR (Facility for Antiproton and Ion Research), GSI, Darmstadt

Timeline of Upgrades

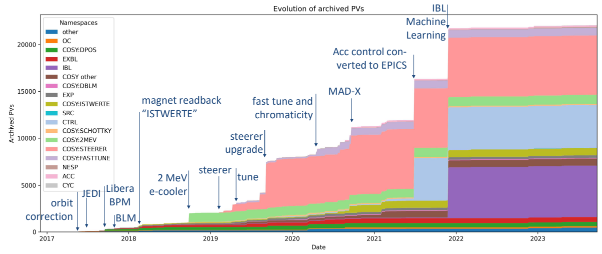

Enabled Developments

Beam Loss

I. Bekman et. al., Experience and Prospects of Real-Time Signal Processing and Representation for the Beam Diagnostics at COSY, ICALEPCS'17, Experience and Prospects of Real-Time Signal Processing and Representation for the Beam Diagnostics at COSY

- Red Pitaya: Xilinx Zynq-7010 SoC + 2x 14-bit ADC (125 MS)
- + 16x GPIO pins FPGA used for fast parallel signal processing
- Custom firmware and EPICS device support
- Tested for up to 30MHz input rates, counting scheme allows for dead-time free operation and is mainly limited by the scintillator speed and pile-up
- CAEN EPICS-ready multichannel power-supply

Slow Controls

- Magnet & BCT readback, BPM gain control
- Usage of EtherCAT, Beckhoff Modules
- EPICS integration with DIAMOND[1] EtherLab EPICS integration
- Stepper motor control with iThemba LABS extension

[1]U. Pedersen et. al., Use of AreaDetector and EtherCat at Diamond beamlines, EPICS collaboration meeting 2012, https://epics.anl.gov/meetings/2012-10/program/1023-B4_Use_of_AreaDetector_and_EtherCat_at_Diamond_beamlines.pdf

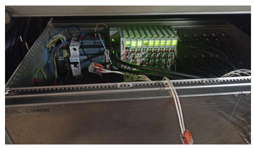

Example of an EtherCAT installation for magnet control & readback

Orbit Correction

- An integrated orbit measurement and orbit correction GUI was developed in close collaboration with COSYLAB
- Software based
- 2 second iteration cycle, based on (old) magnet controller response time

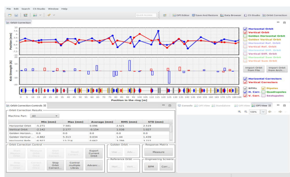

Tune Monitoring

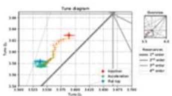

P.J. Niedermayer et. al., Development of a Fast Betatron Tune and Chromaticity Measurement System for COSY, IPAC2021, https://doi.org/10.18429/JACoW-IPAC2021-MOPAB319

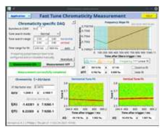

- Based on the bunch-by-bunch beam position data
- Allows for a discrete tune measurement within a few milliseconds, as well as continuous tune monitoring during beam acceleration.
- Also enables determination of the beam chromaticity.
- integrated into the control system.

Machine Learning

- Optimization of the injection process at COSY
- Use of Reinforced Learning agents
  - An actor-critic agent (SAC) is used due to its sample efficiency

A. Awal et. Al., Injection Optimization via Reinforcement Learning at the Cooler Synchrotron COSY, IPAC'23, https://doi.org/10.18429/JACoW-IPAC2023-WEPA098

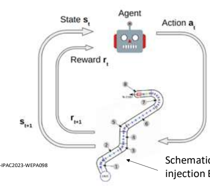

Schematics of the injection Beamline

Member of the Helmholtz Association

KICKER FOR THE CR STOCHASTIC COOLING SYSTEM BASED ON HESR SLOT-RING COUPLERS

R. Stassen†, R. Greven, H. Schneider, J. Wolters, Forschungszentrum Jülich, 52425 Jülich, Germany
B. Breitkreutz, GSI Helmholtzzentrum für Schwerionenforschung GmbH, 64291 Darmstadt, Germany

Abstract
A 'light' version of the HESR stochastic cooling system was already successfully tested in the Cooler Synchrotron COSY. There the stochastic cooling system was operated together with the original PANDA cluster jet target from University Münster. The system layout includes all components as planned for the HESR like low noise amplifier, switchable delay-lines and optical notch-filter. The robust slot ring design has been proven. Hence it was decided to use this concept for the CR kicker as well. Therefore the parameters need to be adapted for the CR cooling system. However, the significantly higher RF power requires a new water cooling concept. First simulations and measurements show that using heat pipes could be a possible solution. At COOL23 main parameter as well as the promising results achieved at COSY will be presented.

HESR Stochastic Cooling

Installation in COSY:

One Pickup fully used. One Kicker two groups used for transvers cooling, one group used for longitudinal cooling. Successful cooling against PANDA cluster jet target, target thickness: 1E15 atoms/cm²

Pick-up for the stochastic cooling system of HESR – tank and structure with slot rings

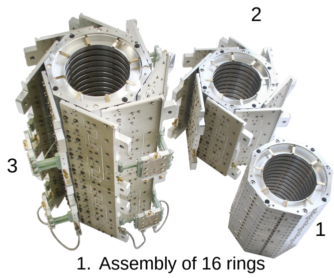

1. Assembly of 16 rings
2. Single structure with 16 rings
3. Stack of two structures (32 rings)

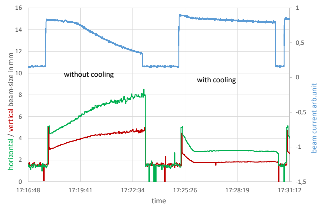

Beam current and beam size with (right) and without stochastic cooling (left).

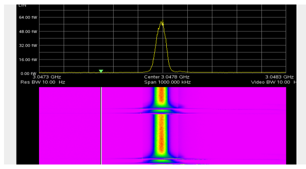

Schottky signal of 1500th harmonics with stochastic cooling, barrier bucket and target

Differences HESR – CR Kicker

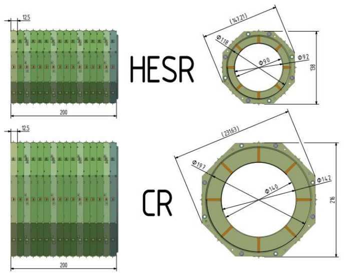

	HESR Kicker	CR Kicker
Aperture	90 mm	140 mm
Frequency range	2 – 4 GHz	1 – 2 GHz
Nominal power loss / tank	60 W	960 W
Nominal power loss / combiner-board	2 W	15 W
Max. power loss / tank	800 W	6 kW
Max. power loss / combiner-board	25 W	94 W

Combiner-boards

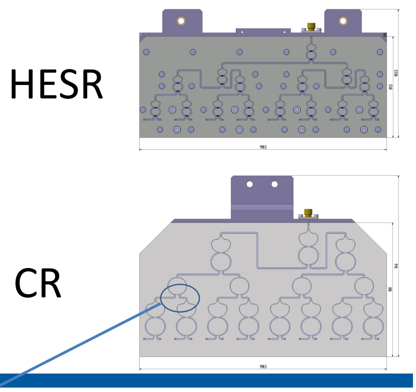

Simulations

EM Simulation of scaled HESR Structure

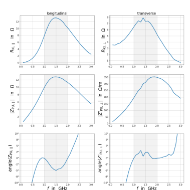

Longitudinal (left) and transverse (right) kicker shunt impedance (top) and pick-up transfer impedance (middle and bottom row) for antiproton cooling (β = 0.97). All values are for one single ring, with four of the eight electrodes in use.

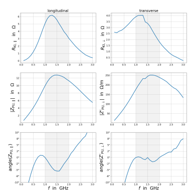

Longitudinal (left) and transverse (right) kicker shunt impedance (top) and pick-up transfer impedance (middle and bottom row) for isotope cooling (β = 0.83). All values are for one single ring, with four of the eight electrodes in use.

Simulation of thermal behavior including every single transition

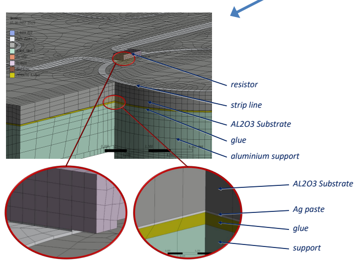

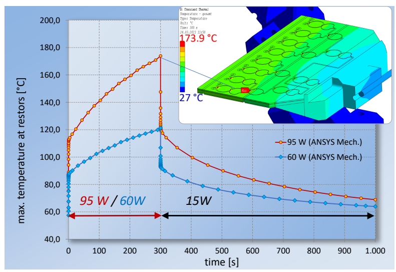

ZEA-1 | ENGINEERING AND TECHNOLOGY
Technology for Excellent Science

Mitglied der Helmholtz-Gemeinschaft

An optimized optical delay line with temperature compensation

N. Shurkhno, A. Kononov, GSI, Darmstadt, Germany
R. Stassen, FZ Jülich GmbH, Jülich, Germany

The poster shows the design and development of a low-loss, low-latency optical delay line that provides temperature stability within a given temperature range. Such delays are of particular interest for stochastic cooling systems, where they are used to synchronize a system's correction pulse and in a feedforward loop of optical comb filters. However, commercially available optical delay lines have certain disadvantages for stochastic cooling - large intrinsic delay, high and non-constant optical attenuation, and overall delay drift due to temperature-dependent optical fibers. To mitigate these problems, an optimized optical delay line has been developed for the stochastic cooling systems of the COSY (FZ Jülich, Germany) and HESR (FAIR, Germany) accelerator facilities

Motivation :

- No commercially available optical delays with large delay range and small resolution, only separate stepped and motorized precise delays
- Attenuation varies when switched to a different state
- Temperature dependence of stepped delays (SMF ~40ps/km/K or >1ps/K for a typical delay)
- Commercially available devices usually provide large intrinsic delay and/or large insertion losses

As a result, when used in stochastic cooling systems (system and comb filter delays), it is required to re-adjust the parameters during the day and after every step change in stepped delay.

Optical delay 0-128ns (OPDM-128)

Precisely and shortest possibly cut stepped delay

Attenuator

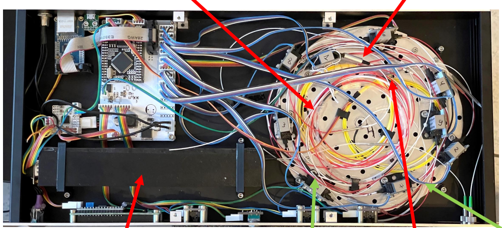

Precise motorized optical delay (left)

Temperature sensor

Optical 1x2 switches for stepped delay, cherry-picked to have smallest possible insertion losses

At higher steps a phase-stabilized optical fiber (yellow) is used to mitigate temperature dependence

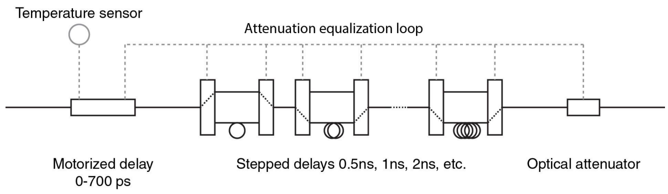

General layout of developed optical delay

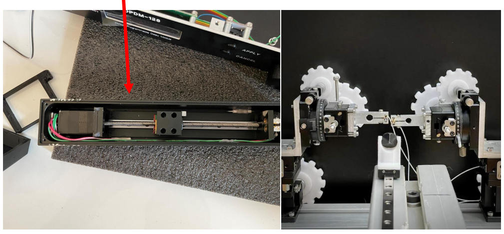

Opened motorized optical delay (left) and alignment tool, created to adjust input and output fibers in the delay

Relevant parameters:

Optical delay range	0 to 128 ns
Optical delay resolution	±0.001 ps
Optical delay accuracy	±0.01 ps
Optical delay repeatability	±0.01 ps
Latency (own delay)	<14 ns
Insertion loss	<5.5 dB
Insertion loss variation	±0.1 dB
Operating temperature	10 °C to 40 °C

4 developed optical delays used at COSY accelerator as system and filter delays:

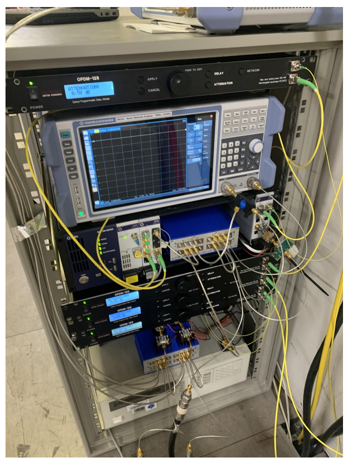

Summary :

Developed optical delays provide precise optical signal delay in range 0 to 128 ns with 1 fs resolution. The instrument has low optical insertion loss and reduced delay latency of less than 14 ns. A unique feature of the instrument is an internal equalization of delay and attenuation. Together with temperature compensation of the delay it results in nearly constant insertion loss and delay accuracy over the whole delay and temperature ranges

JÜLICH Forschungszentrum   COOL23   FAIR GSI

How to adjust stochastic cooling systems

N.Shurkhno, GSI, Darmstadt, Germany

The poster summarizes techniques and algorithms for adjustment of stochastic cooling systems, that have been developed and tested at the COSY accelerator facility (FZ Jülich, Germany). An overall goal was to automate typical time-consuming manual adjustment routines. As a result, a set of algorithms based on a theoretical description of the stochastic cooling process has been developed, which allows accurate and fast automatic adjustment of main system's parameters. The methods have been elaborated and used at COSY during development and testing of stochastic cooling systems for HESR and are planned for further use at the FAIR accelerator complex (GSI, Germany). The methods are quite universal and can be applied or adapted to any similar system.

Introduction

- An adjustment of a stochastic cooling system is bringing its broadband frequency response to its instantaneous optimum
- Common parameters for adjustment are system gain and delay and optionally a comb filter if it is used
- The developed adjustment techniques for both gain and delay are based on calculating the system transfer function from open loop measurements and using it in Focker-Planck or single particle equations to obtain the optimum values, while the comb filter is adjusted simply iteratively

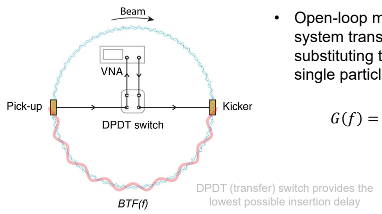

- Open-loop measurements produce direct product of beam and system transfer functions, so the latter can be obtained by substituting the BTF and then used in the Fokker-Planck and/or single particle equation to calculate optimum gain and delay:

$$G(f) = \frac{OLM(f)}{BTF(f)} \quad \rightarrow \quad \frac{dx}{dt} = F(G,x,t) + \frac{D(G,x,t)}{x}$$

System delay adjustment

- System delay synchronizes kick with the measured particles and defines the phase slope of the system transfer function
- Flattened phase is a good starting point, but not an optimum, need to correlate phase flatness with amplitude
- Optimum delay can be calculated directly from cooling force after OLM (+ comb filter):

$$F_{cool} \sim f_p \cdot Re\sum_n \frac{G}{1 - G \cdot BTF} e^{i2\pi n f_p T_{pk}(f_p)} = f_p \cdot Re\sum_n n \cdot OLM \cdot e^{-i2\pi n f_p T_{pk}\frac{\eta_{pk}}{\eta}\frac{f_p - f_0}{f_0}}$$

- The developed method for is universal and proved to be robust and accurate
- Adjustment time depends only on the OLM:

  ~1 s when adjusted from scratch, and ~100-200 ms if only fine-tuning needed

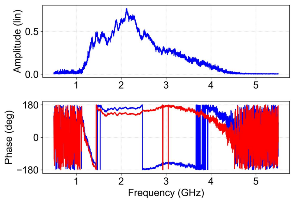

Amplitude and phase of vertical OLM for optimum delay (blue) and flattened phase (red)

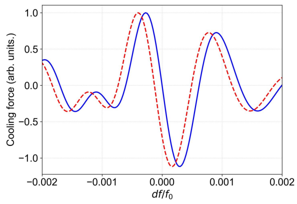

Cooling force calculated with Eq. (2) for optimum delay (blue) and delay, that flattens the phase (blue)

System gain adjustment

- System gain controls cooling rate and final equilibrium state of the parameter being cooled by balancing the cooling and heating forces
- Optimum gain provides instantaneous fastest cooling rate, but worse final state, and equilibrium gain provides smallest equilibrium, but slower cooling
- Both gain immediately calculated if diffusion due to hardware noises is negligible. Otherwise, it must be estimated from measurements:

$$D_{th} = \frac{1}{2} f_0^2 k(T_{pu} + T_{amp})Z_0 \sum_n \left|\frac{G_{cl}}{Z_p}\right|^2 \rightarrow \bar{A}\sum_n |G_{cl}|^2 \qquad \boxed{\frac{dx}{dt} = F + \frac{D_{Sch}}{x} + \frac{\bar{A}}{x}\sum_n |G_{cl}|^2 + C_{IBS}}$$

- The developed technique for gain adjustment provides accurate enough results, but may require some adaptation to a specific setup and goal

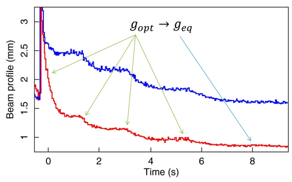

Horizontal (blue) and vertical (red) beam profiles during transverse cooling with stepped gain changing. Each step the gain is reduced by ~3 dB.

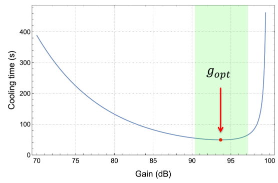

Cooling time vs gain. The resulting accuracy typically should not exceed 1 dB, making the calculation very tolerable to possible errors.

Comb filter adjustment

- Adjustment is done without the beam, which makes it much easier
- The notch frequency is adjusted iteratively by measuring the current frequency and subsequent delay correction. The notch depth is also adjusted iteratively by varying the attenuation and using a binary search to find the optimum value with a given precision.
- Due to dispersion and mismatch in the filter components both the depths and positions of the notches vary, so these distributions should be measured and used in system delay and gain calculations
- Filter adjustment is fully automatic, adjustment time ~ few seconds if adjusted from scratch and <1 s for fine-tuning

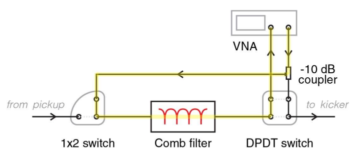

Layout for OLM and additional loop (yellow) for remote comb filter tuning during operation

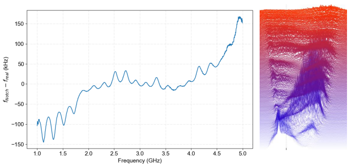

Notch frequency mismatch in the passband (left) and its influence on the Schottky bands filtering (right) if dp/p is small

Conclusion

The developed techniques for system gain, system delay and comb filter adjustments significantly simplify, improve, and speed up the set-up of the stochastic cooling system. Full adjustment can be done automatically in a few seconds or less if only fine-tuning is required. While the system gain adjustment may require some adaptation to a specific setup and goal, the techniques for the system delay and comb filter adjustments are sufficiently universal to be applied to any similar system

N IKP Annual Reports since 1977

For manual access, please use `http://hdl.handle.net/<hdl>` or `http://dx.doi.org/<doi>`.

2023	doi: 10.34734/FZJ-2024-01973
2022	doi: 10.34734/FZJ-2024-01948
2021	hdl: 2128/34179
2020	hdl: 2128/28809
2019	doi: 10.34734/FZJ-2024-01943
2018	doi: 10.34734/FZJ-2024-01960
2017	hdl: 2128/20196
2016	doi: 10.34734/FZJ-2024-01961
2015	doi: 10.34734/FZJ-2024-01940
2014	doi: 10.34734/FZJ-2015-03234
2013	doi: 10.34734/FZJ-2014-01786
2012	doi: 10.34734/FZJ-2024-01962
2011	hdl: 2128/4619
2010	hdl: 2128/4426
2009	hdl: 2128/3832
2008	doi: 10.34734/FZJ-2020-02317
2007	hdl: 2128/4386
2006	hdl: 2128/2636
2005	hdl: 2128/2548
2004	hdl: 2128/576
2003	hdl: 2128/2581
2002	hdl: 2128/219
2001	hdl: 2128/217
2000	hdl: 2128/24123
1999	hdl: 2128/23912
1998	hdl: 2128/4444
1997	hdl: 2128/22371
1996	hdl: 2128/21842
1995	hdl: 2128/21611
1994	hdl: 2128/21283
1993	hdl: 2128/20084
1992	hdl: 2128/19303
1991	hdl: 2128/19135
1990	hdl: 2128/18882
1989	hdl: 2128/25033
1988	hdl: 2128/13356
1987	hdl: 2128/24791
1986	hdl: 2128/24744
1985	hdl: 2128/13573
1984	hdl: 2128/13641
1983	hdl: 2128/13729
1982	hdl: 2128/13801
1981	hdl: 2128/13233
1980	hdl: 2128/13167
1979	hdl: 2128/13118
1978	hdl: 2128/13073
1977	hdl: 2128/13051